Rare-earth elements based Perovskites: Bulk and Low-Dimensional Superlattices

A Thesis Submitted to
Indian Institute of Technology Guwahati

Doctor of Philosophy in Physics

by

Shaona Das

Roll no: 186121102

Department of Physics
Indian Institute of Technology Guwahati
Guwahati-781039, India

June 2023

Dedicated to my beloved parents, Maa and Baba

INDIAN INSTITUTE OF TECHNOLOGY GUWAHATI

Department of Physics

Guwahati- 781039

Declaration

"Rare-earth elements based Perovskites: Bulk and Low-Dimensional Superlattices" is the result of my own doctoral research work. This work was carried out under the supervisions of Dr. Subhash Thota and Dr. Pankaj Kumar Mishra at the Department of Physics, Indian Institute of Technology Guwahati. To the best of my knowledge, the work presented in this thesis has not been submitted to any other Institute/University for the award of any degree.

Shaona Das
Research Scholar
Roll No: 186121102
Department of Physics
Indian Institute of Technology Guwahati
Guwahati-781039
India.

INDIAN INSTITUTE OF TECHNOLOGY GUWAHATI

Department of Physics

Guwahati- 781039

Certificate

It is certified that the work described in this thesis, entitled "Rare-earth elements-based Perovskites: Bulk and Low-Dimensional Superlattices", done by Ms. Shaona Das, a Ph.D. student of Department of Physics, Indian Institute of Technology Guwahati, for the award of degree of Doctor of Philosophy has been carried out under my supervision. This work has not been submitted elsewhere for the award of any degree.

21/6/2023

Dr. Subhash Thota
Professor
Department of Physics
Indian Institute of Technology Guwahati
Guwahati-781039, India

Dr. Pankaj Kumar Mishra
Assistant Professor
Department of Physics
Indian Institute of Technology Guwahati
Guwahati-781039, India

Synopsis report

Since the discovery of the mineral calcium oxide ($CaTiO_3$) in Russian Ural Mountains by Gustav Rose in 1839 and named after Russian mineralogist Lev Perovski, Perovskites have become a classic compound for the research because of their vast potential applications in magneto-electronics. Among various classes of perovskite compounds the *d*- and *f*-block transition metals-based perovskite have gained widespread attention due to the strong correlation between the electron-electron and electron-lattice interaction. The general chemical formula used to describe the perovskite materials is ABX_3, where A and B are cations with A larger than that of B and X is the anion usually oxides or halogens. In general, the rare-earth perovskites have the form $RCrO_3$ and R = Ce structure where R symbolized as rare earth elements. Usually, each corner of the unit-cell is shared by BO_6 octahedral with 12 coordinated A cation, each A site cations are occupied at the corners of the cube, B cations sit at the body centered sites and Oxygen at the face centered positions. The unique physical properties of perovskite materials have gained a huge research attention in recent past because of their applications in many of the magneto-electronic, optoelectronic and photovoltaic devices. Properties such as charge-ordering, large magnetic entropy change, long-range ambipolar charge transport, bipolar exchange bias, multiferroic behaviour make them even more attractive for the applications as well as fundamental research point of view. Apart from all the above characteristics the recent research trends reveal that alkali-halide and organometal halide perovskites can be considered as key materials for photovoltaic applications. Moreover, negative magnetization (NM) and magnetic compensation phenomena has become central theme of research in the rare-earth perovskites. The utilization of the NM and magnetization reversal phenomena in perovskites have opened-up a constructive approach in designating next generation switching devices especially in the field of volatile magnetic memory storage, thermo-magnetic switches, femtosecond optical laser induced high speed read/write magnetic memories, thermally assisted magnetic random-access memory (TAMRAM), etc. Motivated by such novel features and their exquisite applications here in this thesis we report a detailed study of rare-earth perovskites both in the form of bulk and thin-films superlattices. In what follows we present a detailed structure of the PhD thesis which is mainly divided into seven Chapters.

Chapter 1 deals with the introductory concepts including the basic crystal structure of perovskites followed by their intriguing characteristics and their applications. This chapter also deals with different magnetic exchange and related phenomena linking the strongly correlated aspects of the rare-earth perovskites which is very useful in understanding the key results discussed in the subsequent chapters of the thesis. This chapter also provides a brief discussion of some of the novel physical phenomenon like magnetocaloric effect, exchange bias, magnetocrystalline anisotropy, negative magnetization, *etc.* Finally, this chapter provides the the key motivation and the central idea of the research problem undertaken in this thesis which is followed by the outline of the subsequent chapters.

Chapter 2 provides a detailed discussion pertaining to the experimental procedure including the

synthesis of the proposed systems and their characterization. This chapter also provides some of the standard thin films' fabrication methods such as pulsed laser ablation method, sputtering techniques etc. Further we discuss about the details of various characterization techniques employed in the current work such as X-ray diffraction, X-ray photoelectron spectroscopy, Atomic force microscopy, Raman spectroscopy, *dc*-magnetization measurements using VSM based Physical property measurement system.

Chapter 3 demonstrates the role of epitaxial strain on the atomically flat interfaces of PLD grown LSMO/LCO bilayers. In this chapter we provide a systematic analysis of on the basis of the terminating lattice planes and tuning the interfaces across the proposed heterostructures. Emphasizing on these aspects, here we employ a novel strategy of engineering the interfaces through the layer stacking sequence and degree of strain to probe the changes occurring in the local atomic environment at the interfaces, magnetic behaviour, and electronic properties. We find that the bilayer sequence LCO (15 nm)/LSMO (5 nm) (BL2) exhibits large magneto-crystalline anisotropy ($K_u \approx 4.7 \times 10^4$ erg/cc) and weak anti-FM coupling across the interface of the two FM constituents. Partial compensation of the magnetic moment was noticed in these bilayers within a specific temperature window ($\Delta T = 184 - 82$ K) revealing the dominant AFM coupling at low-temperatures. However, at low-temperatures the FM superexchange interaction between the trivalent Co high-spin and low-spin states. The magneto-dynamic features probed by the frequency dependent FMR on this system yield the gyromagnetic ratio ($\gamma/2\pi \sim 29.22$ GHz/T), demagnetization fields ($4\pi M_{eff} \sim 3770$ Oe), and effective damping constant ($\alpha_{eff} \sim 0.0143$) for the BL2 configuration. However, the strength of the nearest-neighbour exchange interaction J_{eff} in the BL2 configuration appears to show a linear falloff with the increasing LCO layer thickness (2 nm $\leq t_{LCO} \leq$ 18 nm). This scenario is also consistent with the variation of the effective number of spins available per unit volume [10 $cm^{-3} \leq N_V(\times 10^{22}) \leq 2$ cm^{-3}] with increasing t_{LCO}. For small t_{LCO} values (< 2 nm), the magnitude of J_{eff}/k_B attains a maximum of ~ 5.47 K (for LCO) and 21.93 K (for LSMO), which is in good agreement with $J_{eff}/k_B \sim 5 \pm 2$ K (20 ± 2 K) for highly epitaxial LCO (LSMO) single layers. With these studies we establish that the layer sequence control of magnetic coupling across the interfaces can be used for exploring the novel magneto-electronic devices.

In Chapter 4 we investigated the texture/orientation dependent growth characteristics along with the other physical properties including the electronic structure, magnetic and magneto-transport, and vibrational excitations in atomically flat interfaces of $[La_{0.7}Sr_{0.3}MnO_3/LaNiO_3]_{10}$ superlattices coherently grown on (001/011/111)-$SrTiO_3$ substrates by the PLD technique. Initial studies pertaining to the X-ray reflectometry confirms the periodic superlattice stacks from the Kiessig interference fringes and well-defined even interfaces between the nickelate and manganite layers. A complex local atomic environment across the interfaces was noticed, yet trivalent La, divalent Sr, and mixed valent $Ni^{2+/3+}$ and $Mn^{3+/4+}$ electronic states prevail at the core level with enhanced relative intensity ratio of the Mn ions in the superlattices grown on (111) oriented $SrTiO_3$.

Our results on the temperature dependence of electrical resistivity $\rho(T)$ reveals the prevalence of 3D variable range hopping mechanism: $[\rho(T) = \rho_0 \exp(T_0/T)^{1/4}]$ of electronic transport with large magnitude

of hopping energies (≥ 40 meV) for the SL-111 system. The investigated system exhibits high energy gap between the localized states owing to the presence of inherent disorderness across the interfaces which contains the polar layers. Moreover, all superlattice systems exhibit reduced ferromagnetic ordering temperatures ($67 \leq T_C \leq 110$ K) with a low-temperature anomaly ($11.4 \leq T^* \leq 22$ K) and a substantial enhancement in the effective exchange interaction ($J_{eff} \sim 3.52$ meV) with ground state spin configuration S = 1/2 different from S = 3/2 usually noticed in $La_{0.75}Sr_{0.25}MnO_3$. On the other hand, the SL-011 system exhibits large anisotropy field $H_K \sim 18$ kOe and cubic anisotropy constant $K_1 \sim 9.3 \times 10^3$ J/m^3 in comparison to the other two orientations. Finally, the Raman spectroscopy results demonstrate the appearance of second order two-phonon interaction driven by the local polaronic distortion. Substrate-induced effects and highly oriented epitaxial growth pattern and their role on two distinct modes ν_4 (326 cm^{-1}) and ν_8 (728 cm^{-1}) have been have been investigated for SL-111 superlattices.

In Chapter 5 we probed the role of Ce substitution on the crystal structure, temperature and field dependence of magnetic characteristics and phonon instabilities of $DyCrO_3$ polycrystalline compounds. All the investigated compounds exhibit distorted orthorhombic crystal structure with a distortion factor of $d_{Oct}/d_{Cell} \sim 6 \times 10^{-3}/3.5$ ppm (for $x \sim 0.2$) for *Pbnm* space group that follows Vegard's law. The bonds between apical oxygen atoms (O_{A1}) and Cr atoms stand more rigidly in comparison with the basal oxygen atoms (O_{B1}/O_{B2}) resulting the octahedral distortion and thereby causing the changes in phonon modes. The CrO_6 octahedral tilt angle θ rotates with respect to the Miller pseudocubic axis [101] which varies from 10.36° (x = 0.1) to 12.25° (x = 0.5) and significantly influences the $A_g(5)$ phonon stability by 3% for a change in A-site mean radius from 1.095 Å to 1.141 Å for x = 0.1 and 0.5, respectively.

Monophasic polycrystalline bulk $Dy_{1-x}Ce_xCrO_3$ perovskite oxides of compositions x = 0.1 – 0.5 have been successfully investigated using various characterization techniques. Firstly, the crystal structure analysis performed by means of Rietveld refinement of the X-ray diffraction data reveals that all the compounds exhibit orthorhombic structure (of space group *Pbnm*) with moderate lattice distortion and enhanced tolerance factor with the substitution of higher ionic radius (1.07 Å) trivalent Ce than the Dy^{3+} (0.912 Å). These results demonstrate that the octahedral distortion is associated with the elongation and compression of the bond lengths of basal O_{B1} and O_{B2}, respectively with more rigid apical O_{A1} pertaining to the Cr atoms in the CrO_6 octahedra. The pristine compound $DyCrO_3$, the Néel temperature, T_{N_1} was found to be around 145 K, however, with Ce substitution T_{N_1} increases to ~260 K. Also, the low temperature phase transition in this system occurs at 2 K to $\Gamma_{25}, C_y^R, G_x^R, A_y^R$ whereas with the inclusion of Ce, we observed another transition between 31 and 45.5 K with $\Gamma_2(F_x, C_y, G_z)$ configuration. The magnitudes of exchange parameters, J_S and D_{AS} in Ce substituted compounds increase by one order compared to the parent system $DyCrO_3$. Moreover, a significant enhancement in the overall magnetic entropy change (ΔS_M) was observed with improved RCP (~360 J/kg) for 10% Ce substituted $DyCrO_3$ system measured at T = 5 K (for ΔH = 40 kOe), whereas, the previous studies on $DyCrO_3$ reported 256 J/kg under same conditions. All the compositions exhibit G-type AFM character with $\Gamma_4(G_x, A_y, F_z)$ spin-configuration and undergoes a phase-

transition across T_{PC} ($< T_{N_1}$) with $\Gamma_2(F_x, C_y, G_z)$ spin configuration through a mechanism involving the variation in total free energy change which is associated with the induced local effective field caused by strong coupling between the trivalent Cr and rare-earth ions Ce/Dy. The low-temperature spin-reorientation transition T_{SR} (3.5 K − 16.8 K) significantly supresses for higher composition ($x \geq 0.4$) and a weak ferromagnetic character (of Γ_2 configuration) emerges due to the Dy spins. On the other hand, the AFM character in these perovskites are interpreted in terms of antisymmetric (Dzyaloshinskii–Moriya) exchange interaction between the trivalent cations which increases progressively with the extent of Ce substitution. These magnetic characteristics probed by the dc-magnetization studies are complemented by the temperature and field dependence of heat-capacity data C_P(T) which reveals the Debye temperature Θ_D to be at 390 K. Finally, we present the phonon spectroscopy which reveals that the phonon modes $A_g(5)$ and $A_g(3)$ exhibit opposite trend in their position (~ 3.09 ± 3 cm^{-1}) with increasing the Ce content. Such changes are associated with the CrO_6 octahedral tilt angles (θ, ϕ) around pseudocubic Miller axes [101] and [010] which is quite different in comparison to the other perovskite family of oxides. In the present case the phonon spectra are quite complex in region between 470 cm^{-1} and 490 cm^{-1} which essentially consists of the three modes $A_g(6)$, $B_{2g}(3)$ and $B_{3g}(2)$, all of them collapses into a single phonon mode $A_g(6)$ at higher compositions ($x \geq 0.4$).

Chapter 6 emphasizes the magnetization of the combination of two most promising rare earth chromate systems namely, $GdCrO_3$ and $SmCrO_3$. We mainly focus on the structural, temperature dependent Raman spectroscopy and field and time dependence of *dc*- magnetization of these system. In this work we examine the effect of 10, 50 and 90 atomic % of Sm substitution at the A-site of $GdCrO_3$ termed as GSO1, GSO5 and GSO9, respectively. The main purpose of choosing $GdCrO_3$ as pristine compound for the study was lying in the fact of interesting features like complex exchange interaction of Cr^{3+}-Cr^{3+} and R^{3+} (Gd^{3+}, Sm^{3+})-Cr^{3+} which play important role in deciding the presence of multiple T_{Comp} throughout the broad temperature regime. We found the strong correlation between the structural and magnetic properties based on the combined study of XRD, Raman and *dc*-magnetization. In particular we find that the Sm doped $GdCrO_3$ undergoes a G-type AFM phase transition at T_N = 197 K (for GSO1) - 201 K (for GSO9) with Cr^{3+} along with Gd^{3+} and Sm^{3+} ions aligned in Γ_4 (G_x, A_y, F_z) configuration. All the three compositions GSO1, GSO5 and GSO9 show multiple zero-crossovers in magnetization versus temperature under ZFCW, FCC and FCW measurement protocols. For T< 40 K, the exchange interaction between the rare-earth and trivalent Cr ions rotates the AFM component along *z*-axis from the easy axis resulting the change in the magnetic phase to Γ_2 (F_x, C_y, G_z) configuration. The Sm rich compound (GSO9) shows the interesting characteristics of magnetic field driven short range metastable frozen state of simultaneous existence of both Γ_2 (F_x, C_y, G_z) and Γ_4 (G_x, A_y, F_z) phases. This particular feature occurs as a consequence of clustering of the FM in the background of AFM matrix which not evident in FCW case at higher magnetic field. Raman spectra reveals a clear anomaly near the magnetic transition temperatures indicating a direct spin-phonon coupling. Further we found the gradual hardening of the A_{1g} (5) mode at around 563 cm^{-1} with respect to temperature which suggests the Cr^{3+}-Cr^{3+} AFM coupling accompanied by exchange-striction effect. The variation of the tilt angles as calculated from refined structural parameters of XRD reveals the presence of

quasi-harmonic effect due to Gd^{3+}-Cr^{3+} exchange interaction which soften the A_{1g} (3) mode. Across the different substitution levels, the GSO shows multiple magnetic compensations under the ZFCW, FCC and FCW cases as well. Overall, the intriguing characteristics explored under the substitution of trivalent Sm in the $GdCrO_3$ making it a potential candidate for the applications in the field of tunable thermo-magnetic switching devices, magnetic sensors and non-volatile magnetic memory storage devices.

The final Chapter 7 presents a brief summary of important findings of our experimental results. In this chapter we also identify some open issues which are potentially interesting for the future studies.

List of Publications:

[1] "Substrate orientation dependent characteristics of half-metallic and metallic superlattices $[La_{0.7}Sr_{0.3}MnO_3/LaNiO_3]_{10}$"
S. Das, R. G. Tanguturi, S. Ghosh, R. K. Dokala, R. Medwal, S. Gupta, Z. Yan, Y. Qi, R. S. Rawat and S. Thota,
J. Appl. Phys. **131**, 125305 (2022).

[2] "Effect of Ce substitution on the local magnetic ordering and phonon instabilities in antiferromagnetic $DyCrO_3$ perovskites"
S. Das, R. K. Dokala, B. Weise, R. Medwal, R. S. Rawat, P. K. Mishra and S. Thota,
J. Phys.: Condens. Matter **34**, 345803 (2022).

[3] "The role of epitaxial strain on the electronic and magnetic structure of $La_{0.7}Sr_{0.3}MnO_3/LaCoO_3$ bilayers"
S. Das, S. Ghosh, R. G. Tanguturi, R. Medwal, S. Gupta, R. K. Dokala, R. S. Rawat, S. Das and S. Thota,
AIP Advances **11**, 125115 (2021).

[4] "Phonon scattering and magnetic manifold switching in $(GdSm)CrO_3$"
S. Das, R. K. Dokala, B. Weise, P. K. Mishra, R. Medwal, R. S. Rawat and S. Thota,
Phys. Rev. Mater. (2023) – *To appear in.*

[5] "Elastic strain control of electronic structure, and magnetic properties of $[Pr_{1-x}Ca_xMnO_3/SrTiO_3]_{15}$ superlattices"
R. K. Dokala, **S. Das**, D. C. Joshi, S. Ghosh, Z. Yan, Y. Qi, S. Das and S. Thota,
J. Appl. Phys. **127**, 175303 (2020).

[6] "Magnetization reversal, field-induced transitions and H–T phase diagram of $Y_{1-x}Ce_xCrO_3$"
R. K. Dokala, **S. Das**, B. Weise, R. Medwal, R. S. Rawat and S. Thota,
J. Phys.: Condens. Matter **34** 065801 (2022).

[7] "Magnetic ordering in Ce Substituted Zirconite Nanostructures: Focus on Tunable Energy Bandgap and Local-atomic Environment"."
R. K. Dokala, **S. Das**, P. K. Mishra and S. Thota,
Phys. Scr. (2023)- *Under review.*

[8] "Irreversible Metamagnetic Transitions in Orbital-Ordered $(Pr_{0.45-x}Yb_x)Sr_{0.55}MnO_3$"
R. K. Dokala, **S. Das**, G. Jangam, P. K. Mishra and S. Thota,
Appl. Phys. Lett. (2023)- *Under review.*

Work presented in international/national conferences and workshops:

[1] Poster presentation on "Field and path induced magnetization switching and spin reorientation phenomenon in Ce substituted $SmCrO_3$" at **Perovskite Society of India Meet (**March 2023**)**, IIT Roorkee Department of Physics and Center for Flexible and Smart Energy Devices, a Conference at IIT Roorkee

[2] Poster presentation on "Magnetic glass signature and evolution of multiple magnetic polarity switching in Gd doped polycrystalline $SmCrO_3$" at 9th Forum on New Materials, **CIMTEC** (June 2022) at Perugia, Italy.

[3] Poster presentation on "Tunable spin-reorientation transition in Canted antiferromagnetic $Dy_{1-x}Ce_xCrO3$" at National Conference on Quantum Condensed Matter, **QMAT** (December 2021) at TIFR Mumbai.

[4] Poster presentation on "Structural and vibrational excitations in the magnetic phase $Dy_{1-x}Ce_xCrO_3$ solid solutions" at **MRSI** –Annual General Meeting, (December 2021) at IIT Madras.

[5] Poster presentation on "Electronic structure studies of $[La_{0.7}Sr_{0.3}MnO_3/LaAlO_3]_{15}$ Superlattices" at National conference on progress in Material science research, **PMSR** (February 2020) at Dibrugarh University.

[6] Poster presentation on "Evidence for Field induced phase transition and Enhanced Long-range ordering in Fe doped $MnCo_2O_4$ spinel" at **INUP Familiarization** workshop organized by CeNSE, (May 2019) at IISc Bangalore.

Acknowledgements

I would like to acknowledge my supervisors Dr. Subhash Thota and Dr. Pankaj Kumar Mishra for the guidance and supervision throughout the journey. I would like to express my thankfulness to them for giving me the opportunity to work under their supervision. I would like to thank them for their patience, enthusiasm and encouragement for new ideas and encouragement towards work. I would like to thank my DC committee members, Dr. Ashwini Kumar Sharma (DC chairman), Dr. Tapan Mishra, Dr. R. Anandalakshmi and Dr. Kanhaiya Pandey for reviewing the research work and their valuable suggestions. I would also like to thank the former HoD. Dr. Subhradip Ghosh and present HoD. Dr. Perumal Alagarsamy for their huge support by providing me with all the necessary facilities to carry forward the research work. I would also like to acknowledge the Physics office staffs for their help with the information whenever I need.

I would also express my sincere acknowledgement towards Dr. Sujit Das, Dr. R. G. Tanguturi, Dr. R. Medwal, Dr. S. Gupta, and Dr. R. S. Rawat for their immense help and important suggestions for the superlattice and bilayer work. I would also thank to Dr. R. Rawat and Dr. R. J. Choudhary for helping with the electrical and magnetic measurements. I am expressing my acknowledgement to the funding program DST FIST-I (XRD), DST FIST-II (PPMS) and the Central Instruments Facility (CIF) for supporting my research work. I am grateful to IIT Guwahati, and Govt. of India, Ministry of Education for the financial support.

I would like to thank my seniors from the lab Pratibha Di and Sayan Da for their friendship and important suggestions to make the research days easier. I would like to thank my current post-doctoral senior Priyanka Di for her suggestions and friendship. I would like to thank my juniors Maruthi, Arpita, Harshita and Arijit for their company. I would also like to thank the project students Shourya, Swati, Shalini, Ayush, Shashank, Bhupesh, Joya for their never-ending talks and amazing company. I would like to thank Ravi for his constant support, motivation and friendship. I can declare that he made the PhD journey worth cherishing with his out-of-the world ideas, discussions and always availability for sharing concerns. I would like to thank him for his technical help throughout in writing the thesis.

Next, I would like to thank my childhood friends who encouraged me to pursue the research career and stayed with me throughout my journey and helped me to stay focused and making me stress-free with their company. I would also like to thank my friends from my previous University who stood with me in my bad days. I would like thank Pratibha, Laxmipriya, Manaswini, Debraj, Nurul, Ayushman for their memorable friendship. I would like to thank Zahid for encouraging me to choose the research world. I would like to thank my current hostel friends Sampriti, Rumela, Krishna for their invaluable friendship and encouragement. I would thank Sampriti for her help whenever I need her support. I can doubtlessly say that without them it would be very difficult to stay sane during the PhD days. I would like to thank my batchmate Sampreet for wonderful company and help with all sorts of technological support starting from course work to till date.

Now, most importantly, I would love to show my deepest sincere acknowledgement towards my parents, Maa and Baba for their constant love and support. It is an honour to be their daughter and I am the luckiest to have them beside me guiding me constantly and for providing me the safest place to reach in my down times. Their immense love and sacrifices are beyond acknowledgement. Giving thanks won't be enough to show my gratitude towards them. And lastly, I would like to thank and show my ultimate gratitude towards the Almighty without whom it won't be possible for me to stay well-being and motivated.

Shaona Das

Contents

List of Figures

Chapter 3

Chapter 5

Chapter 6

List of Tables

$\theta_{\mathrm{NM-FCC}}$ (K), and $H_{\mathrm{int-FCC}}$ (Oe), respectively obtained from the NM fit Eq. 6.10 under FCC condition. Magnetic contribution from Cr-sublattice, CW temperature, and induced internal magnetic field, $M_{\mathrm{Cr-FCW}}$, (emu/mol), $\theta_{\mathrm{NM-FCW}}$ (K), and $H_{\mathrm{int-FCW}}$ (Oe), respectively obtained from the NM fit Eq. 6.10 under FCW condition. Saturation magnetization, M_{S} (emu/mole), magneto-crystalline field, H_{K} (Oe), and magneto-crystalline anisotropy constant, K_1 (J/m^3) obtained from LAS fit.

List of Abbreviations and Symbols

XRD	–	X-ray diffraction
XPS	–	X-ray Photoelectron spectroscopy
MCE	–	magnetocaloric effect
Eg	–	band gap energy
T_N	–	Néel temperature
T_{MG}	–	Magnetic-Glass temperature
h	–	hours
ZFC	–	Zero-Field Cooled
FCC	–	Field Cooled Cooling
FCW	–	Field Cooled Warming
FM	–	Ferromagnetic
AFM	–	Anti-ferromagnetic
PM	–	Paramagnetic
B. E	–	Binding energy
Å	–	Angstrom
χ	–	Magnetic susceptibility
K	–	Kelvin
M	–	Magnetization
H	–	Magnetic field
T	–	Temperature
U	–	Coulombic parameter
μ_B	–	Bohr magnetron
DM	–	Dzyaloshinskii-Moriya

Chapter 1
Introduction

Since the discovery of the mineral calcium oxide ($CaTiO_3$) in Russian Ural Mountains by Gustav Rose in 1839 and named after Russian mineralogist Lev Perovski, Perovskites have become a classic compound for the research because of their vast potential applications in magneto-electronics [1–4]. Among various classes of perovskite compounds the *d*- and *f*-block transition metal based perovskites have gained wide attentions due to the strong correlation between the electron-electron and electron-lattice interaction leading to diverse properties like charge-ordering, bipolar exchange-bias, large magnetic entropy change, long-range ambipolar charge transport, low exciton-binding energy, high-absorption coefficient, high dielectric constant, intriguing multiferroic characteristics, *etc.* [5–8]. The perovskites have an acquiescent tendency of accommodating various cations leading to the structural distortions and thus making them more interesting and novel. It is well known that to fabricate any electronic device on the basis of the specific structure one has to tailor the physical properties (such as exchange-bias, multiferroicity, variable coercivity, magnetization reversal, superconductivity, magnetic ordering *etc.*) by various parameters such as compositions, strain, magnetic field and temperature. The perovskite material provides a perfect platform for all the above discussed characteristics [9–13]. The perovskite with Jahn-Teller distorted (Mn) Rare earth shows a large number of variations in the physical phenomenon, like, spectroscopy, stereochemistry and crystal chemistry. These materials are highly applicable in the field of spintronic and specifically in magnetic random-access memory (MRAM) and disk drives due to their large exchange-bias [14,15].

On the other hand, the effects of unconventional spin-orbit coupling leads to the Giant magnetoresistance (GMR) highlighting the close link between the charge transport and magnetic structure. It is now quite well established that the GMR property can be considered as the cornerstone for the devices like, disk read/write heads, biosensors, microelectromechanical systems (MEMS), *etc.* [9–15]. On the other hand, the Rare earth perovskites exhibit quite good light absorption properties which is very advantageous for the photocatalytic devices and for the energy conversion as well as in solar cells [16]. Magnetization reversal, being a significant property of these materials, has been the key ingredient for many of the electronic devices, such as, magnetic storage devices, thermally assisted magnetic random-access memory (TAMRAM), magnetic field, and temperature driven magnetic switches, *etc.* [17,18]. Interestingly, the Rare earth elements like, Nd, Dy, Gd, Sm, hold quite high magnetic moment and thus can be considered as perfect candidate for the giant magneto-caloric effect (MCE) which in-turn is the most important feature for magnetic refrigeration technology. Such features have been currently being used as environment friendly application in covariation to the conventional vapour-compressed refrigeration [19,20].

Apart from these properties the compounds comprising the Rare earth element exhibit half-metallic properties which is an essential ingredient for the spintronic devices [20]. These oxide perovskite hetero-structures containing Ni as the transition element (e.g. $LaNiO_3$), exhibit one of the most unusual

characteristics which is the change of magneto transport property from insulator to highly conducting depending on the thickness of the layer, grain size, and the atomic environment [21,22]. Since last few decades the research on these perovskites have reached to the new level recently after the invention of Nano hyperthermia treatment where these non-toxic magnetic nanoparticles have been used in order to destroy the cancer cells by optimizing the temperature that arises in different regions [23–26].

In this chapter, first we present a detailed crystal structure of different class of perovskites. It is followed by a brief description of different magnetic and electronic behaviour of various perovskite systems. Following this some theoretical background like crystal filed theory and Jahn-Teller effect have been discussed. Further, we present details of various magnetic interactions usually present in the perovskites (Direct exchange, Superexchange, Double exchange, Ruderman-Kittel-Kasuya-Yosida (RKKY) interaction and Dzyaloshinskii–Moriya (DM) interaction). Next, we provide a brief discussion pertaining to the intriguing magnetization features of the perovskite systems like exchange-bias, negative magnetization, magnetic glass, magnetocaloric effect. We finally end the chapter with the motivation and brief description of the research problem presented in the subsequent chapters.

1.1 Crystal geometry and Lattice structure:

After the name of Count Lev Alslseevich Perovski, the compounds holding the similar structure as $CaTiO_3$ have been named as Perovskites. This general group of materials possess the chemical formula of ABX_3 with A representing a positive charged ion (valency +1, +2, +3) with relatively smaller ionic radius than that of B which is also a cation (valency +3, +4, +5) and X depicting as the smallest ions with negative polarization (of valency -2)[27]. In the simple cubic structure, the unit cell consists of the largest B cation resides with single occupancy, whereas, the A cations reside on the six corners of the cell, and share the $^1/_{4^{\text{th}}}$ space of the octahedral with twelve-fold coordination number (ten). On the other hand, the six small anions (having coordination number ten) frame the B cations and share $^1/_{6^{\text{th}}}$ of the octahedral space. The reason behind the flexibility of accommodating other cations at A- or B- site is the rigidity of edge sharing of BX_6 octahedra. Here X can be either Halogen (Halide perovskite Fig. 1.1(a)) or oxygen (Oxide Perovskites Fig. 1.1(b)). The representative schematic structure of these compounds is presented in the Fig. 1.1(a) and 1.1(b). The halide perovskites can be divided into two sub-groups: (i) Alkali-Halide perovskites and (ii) Organic Halide perovskites. Any kind of Perovskites can be either intrinsic (primeval) or doped (mixed) chemically. However, the halide perovskite is generally formed with X = I, Cl *etc.* and A= Cs^+, RNH^{3+} *etc.* Among them, the ones containing Pb or Sn are used more in thin films.

Usually, the perfect cubic crystal structure deviates from its ideal shape due to the free rotation and tilting of the octahedra in three dimensions inside the crystal [28]. The most common structures available are: (i) Rhombohedral: $R3c$ (ii) Orthorhombic: $Pbnm$ (with crystallographic axis c longer) or $Pnma$ (with crystallographic axis b longer) and (iii) hexagonal: $P6_3cm$ (iv) cubic bixbyite: $Ia3$. The ideal cubic structure contains A-site cation (2a) at $(0,0,0)$, B-site cation (2a) at exact corner of the *fcc* cube at $\left(\frac{1}{2},\frac{1}{2},\frac{1}{2}\right)$

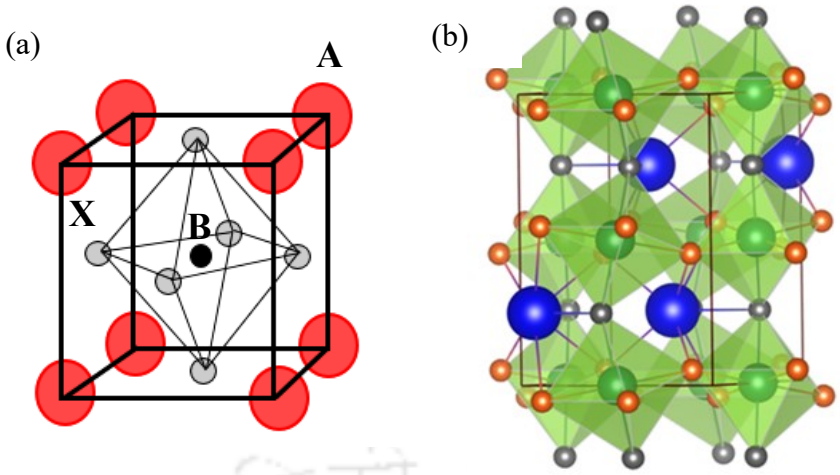

Fig. 1.1. (a) General crystal structure of a Perovskite system (ABX_3) and (b) the rare earth perovskite with A= La, B = Mn and X = O.

coordination and X-anion (6b) at $\left(\frac{1}{2},\frac{1}{2},0\right),\left(\frac{1}{2},0,\frac{1}{2}\right),\left(0,\frac{1}{2},\frac{1}{2}\right)$ position. $YAlFeO_3$ is one such example invented long back in 1927 [29]. The rhombohedral structure arises due to the rotation of the octahedra involving B-cation and the oxygen which deviates from the ideal cubic symmetry. Here the A-cation resides at $\left(0,0,\frac{1}{4}\right)$, while the B-cation resides at the center of the unit cell $(0,0,0)$, and X or O-anion occupies at $\left(x,0,\frac{1}{4}\right)$ co-ordinates. The most relevant example of such crystal structure is $LaAlO_3$ with the least deviation from ideal cubic structure in comparison with the rest [30]. The most common and diversified structure is orthorhombic with moderate distortion parameter and twice in size of the cubic unit cell (see Fig. 1.1(b)).

The investigated compound in the thesis $DyCrO_3$ is a typical example of such distorted orthorhombic structure [31]. With the increasing distortion in the BX_6 octahedra the structure gets converted into hexagonal pattern with modified coordination number of A-site cation being VII and that of B-site cation being V. Here, the structure deviates from the perovskite system with two kind of A-cation and four different O-anion and therefore find good similarity with the garnet group of crystals. First type of A-site cation with Wyckoff position (2a) occupies (0, 0, z) co-ordinates and second category of A-site cation resides at $\left(\frac{1}{3},\frac{2}{3},z\right)$ with Wyckoff position (4b). The B-site cations of Wycoff position (6c) fill $(x,0,z)$ coordinates, while, OA1 and OA2 anion (6c) reside at $(x,0,z)$. On the other hand, OB1 anion with (2a) is present at $(0,0,z)$ and the OB2 anion with (4b) is situated at $\left(\frac{1}{3},\frac{1}{3},z\right)$ position [32]. Lastly, the structure with the maximum distortion and size difference in cubic bixbyite structure consists of almost equivalent A-site and B-site cations. For such interesting structure, any of the A-site or B-site cation holds the Wykoff position of 8b with fixed co-ordinates $\left(\frac{1}{4},\frac{1}{4},\frac{1}{4}\right)$, and another one of these two cations reside at $\left(x,0,\frac{1}{4}\right)$ crystallographic position with (24d) Wycoff location. Usually it is very difficult to predict any difference between the apical and basal

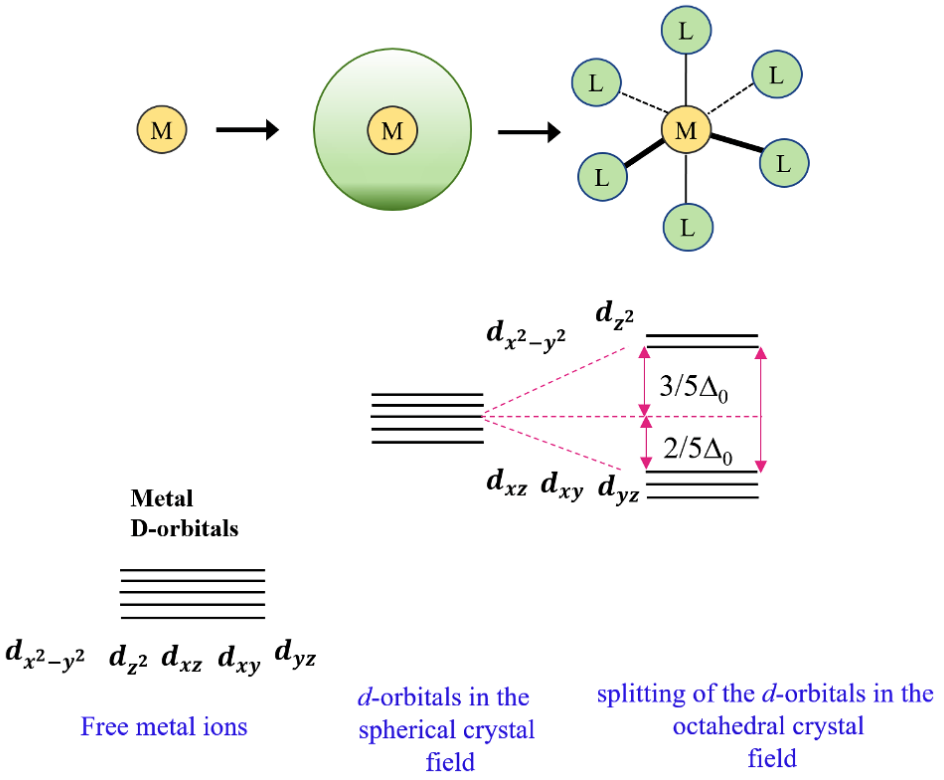

Fig. 1.2. The *d*-orbital splitting in an octahedral crystal field.

oxygens with Wycoff location (48e) and their corresponding lattice position in the unit cell [33]. The parameter pertaining to the distortion from ideal cubic structure due to the dislocation of the larger A-site cation or the tilting of the BX_6 octahedra can be calculated using the Goldschmidt tolerance factor:

$$t = \frac{R_A + R_X}{\sqrt{2}\,(R_B + R_X)} \tag{1.1}$$

$$\mu = \frac{R_B}{R_X} \tag{1.2}$$

where, R_A , R_B, R_X are the radii of the A-site, B-site cation and X-anion, respectively, in which the magnitude of t =1 represents the ideal cubic structure. The necessary value for the t has to be maintained within 1.00 and 1.13 to retain the hexagonal symmetry, while, for t = 0.75 – 0.9 indicates the stable orthorhombic symmetry which generally holds the lower symmetry groups. On the other hand, the value of μ remains within 0.44-0.90 for the orthorhombic halide perovskites. As for an example $SrTiO_3$ carries t value 1.00 exhibiting perfect cubic structure [34]. After this detailed description of the typical crystal structure of the perovskites, now we turn our focus on the theoretical concepts pertaining to various strongly correlated mechanism, such as crystal field theory, Jahn-Teller effect, magnetic interactions, *etc.*

1.2 Crystal field theory and Jahn- Teller Effect:

Starting from the molecular orbital theory with the same approximation as of the ligand field theory, the crystal filed theory (CFT) demonstrates the added approximation of neighbouring orbitals and suggests whether the magnetic ion be part of the low-spin state or high spin state [35]. The electric field produced due to the interaction between the ligand and the central ion as well as due to their overlap, generally giving rise to the CFT which remarkably depends on the local environment symmetry. The fivefold 3*d* orbitals consists of three planes based t_{2g} orbitals (namely d_{xy}, d_{xz} and d_{yz}) and two axes oriented e_g orbitals (namely d_{z^2} and $d_{x^2-y^2}$) for the neighbouring atoms with vacant p - orbitals that lower the electrostatic energy in case of overlapping with t_{2g} orbitals. However, the electrostatic energy gets enhanced in case of overlapping with the crystallographic axis pointed e_g orbitals. Now considering the point charge residing at the centre of an octahedral, the ligands reside on the axis centres or at $(\pm x, 0, 0), (0, \pm y, 0), (0, 0, \pm z)$. Due to this the electrostatic interaction between the t_{2g} orbital and the ligands reduces the columbic energy as compared to that of with e_g orbitals. The point charge at the centre of a tetrahedra with ligands on the corner of the cube, results decrease in the columbic energy for the interaction with the e_g orbitals than that of with the t_{2g} orbital [35]. In general, the splitting of the orbitals takes place on basis of the variation of the energy under different symmetry environment as depicted in Fig. 1.2. Upon considering this feature, one may find that the transition element Mn have two interchanging oxidation states, namely, trivalent (3+) and tetravalent (4+) act differently in the octahedral and tetrahedral symmetry environment. For this case, t_{2g} orbital gets filled first in the tetrahedral symmetry and e_g orbitals have low energy, hence, have the priority first when filling up with electrons in the octahedral symmetry. The sequence of filling up the orbitals depends on the competition between the CFT and the electrostatic paring energy (PE). For weak field limit (CFT < PE) (Fig. 1.2) the orbitals first have the single occupancy before getting paired up. In contrast to it, for the strong field limit (CFT > PE) the system allows the double occupancy first to the lower energy states. For Mn^{3+} the energy gap between the t_{2g} and e_g states is around $\Delta E_{CFT} \sim 1$ eV. However, the difference between the ground state and the t_{2g} is around ~ 0.4 eV and ~ 0.6 eV for the e_g electrons. The 3*d* electrons with lower ΔE_{CFT} possess high spin values than 4*d* and 5*d* electrons acquiring typically low spin values.

Apart from the effect of the local environment symmetry, the distortion in the lattice itself also known as Jahn-Teller effect (JT) can have impact on the local environment which in turn significantly influence the magnetic properties of the system. The spontaneous distortion saves some of the electrostatic columbic energy by the increment in the elastic energy. This phenomenon observed by Jahn and Teller in 1937. In general, it refers to the minimum in one directional positive (i.e. negative slope of the potential energy surface) for the high-symmetry cases of electronic degeneracy that results in further splitting of the CFT energy states. The schematic representation of the energy levels and the effect of JT on them is depicted in the Fig. 1.3(a) The JT leads to deprivation of energy, $\Delta E_{JT} \sim 0.1$ eV lower than to the magnitude of ΔE_{CFT}. For Mn^{3+} with electronic configuration of [Ar] $3d^4$ the permanent JT distortion can be observed but for Mn^{4+}

with [Ar] $3d^3 4s^2$ electron structure the distortion is absent as the e_g energy level remains empty as no reduction of resultant energy is possible by re-arrangement [36].

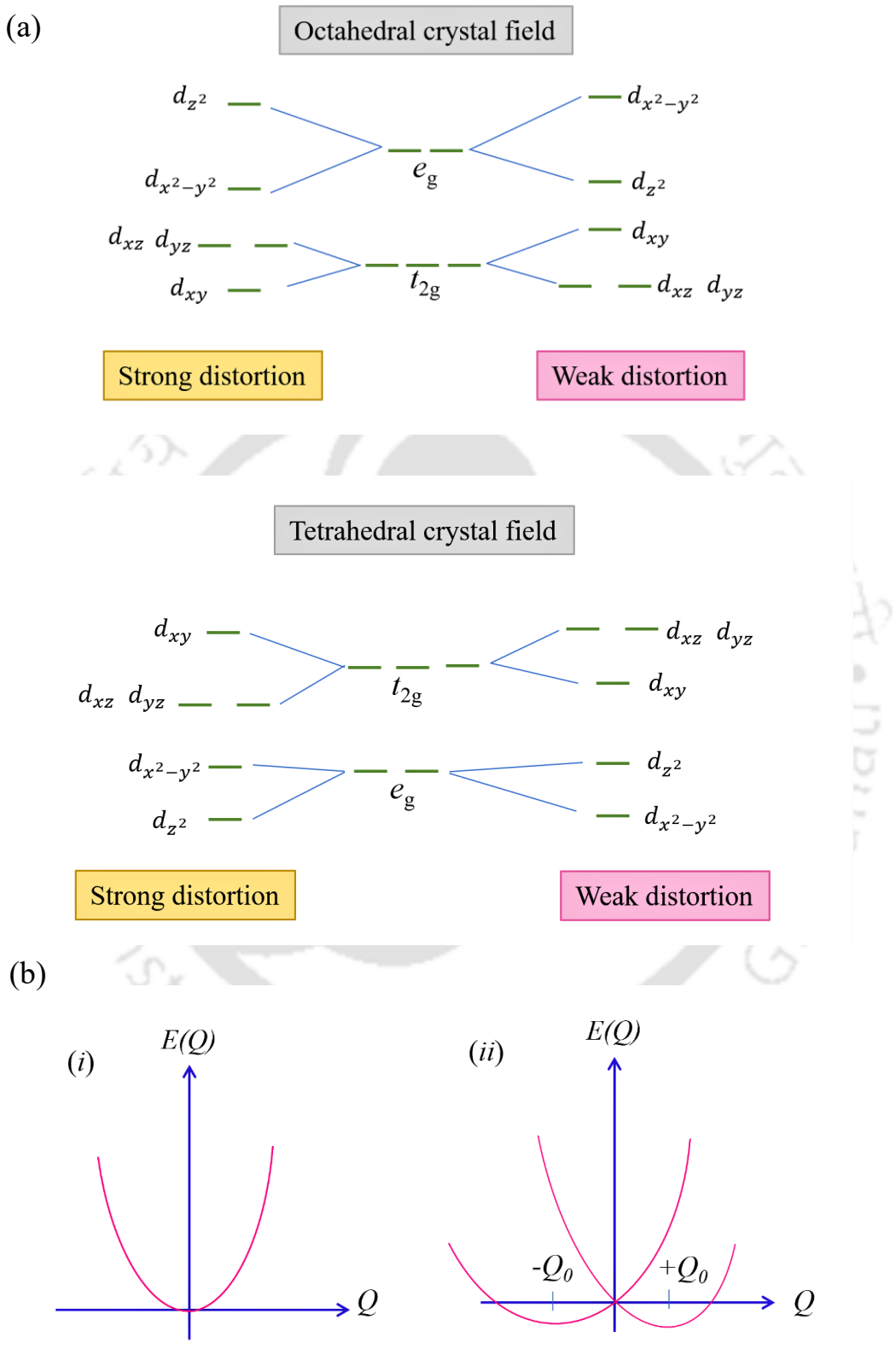

Fig. 1.3. (a) The Jahn-Teller distortion in octahedral and tetrahedral crystal field both under the effect of strong and weak distortion. (b) The energy of an octahedral complex as a function of the distortion Q with (i) minimum orbital energy and (ii) a given energy of ± BQ.

Considering the energy E as a function of distance r which relates the position of the distortion with respect to a proper normal mode co-ordinate system and m denoting the electron mass and ω referring to the angular frequency related to the respective normal mode the energy is given by:

$$E(r) = \frac{1}{2}m\omega^2 r^2 \tag{1.3}$$

as shown in Fig. 1.3(b) Here, for the partially filled orbitals, the distortion can be added with the linear term of the Taylor series expansion of the extra distortion assuming the distortion is very small ($\pm$ Br) where B is suitable constant. The corresponding energy can be written as:

$$E(r) = \frac{1}{2}m\omega^2 r^2 \pm Br \tag{1.4}$$

$$E_{min}(r) = \frac{-B}{m\omega^2} \tag{1.5}$$

Note that here we take account of the fact that the net energy can be preserved by automatic structural distortion. Such JT distortions are limited to the fixed octahedral axis and position for Mn^{3+}. For a system where a Mn oxidation states interchange in between 3+ and 4+, the extra electron resides at the lattice site of e_g energy level causing the JT distortion. In addition, hopping of the electron from one site to another site gives rise the dynamical JT distortion [35]. Therefore, we find that the JT can be predicted as one of the intrinsic tools for the crystal to monitor the magnetic and other optical properties. Next, we discuss the different class of strongly correlated systems used in the thesis.

1.3 Strongly Correlated Systems:

The metals and most of the semiconducting fermi-systems consist of non-interacting electrons which can be considered as the free particles as the outermost valence electrons mostly decide the physical, magnetic, and optical properties of the corresponding systems. The other important category of materials is the strongly correlated system where the interrelation between the electrons plays a major role within the atoms. First time the indications of such systems were given by Steglich and his colleagues in 1970 [37]. In Fig. 1.4, we present the schematic diagram of the two classes of such strongly correlated systems [38]. The wave function for the free electron with charge concerted in a sphere of radius R and the distance between the nuclei of two similar spheres d can be represented as

$$\Psi = \frac{1}{\sqrt{N}}\, e^{ikr} \tag{1.6}$$

where N is the normalization factor, r is the position vector of length r, and $R \sim d$, valid for the s- and p-orbitals. For the system with strong correlation between the ions, they overlap with each other and for $R \ll d$ the wave function gets modified as

$$\Psi = \frac{1}{\sqrt{N}} \sum_i e^{ikR_i}\, \Psi_0\,(r - R_i) \tag{1.7}$$

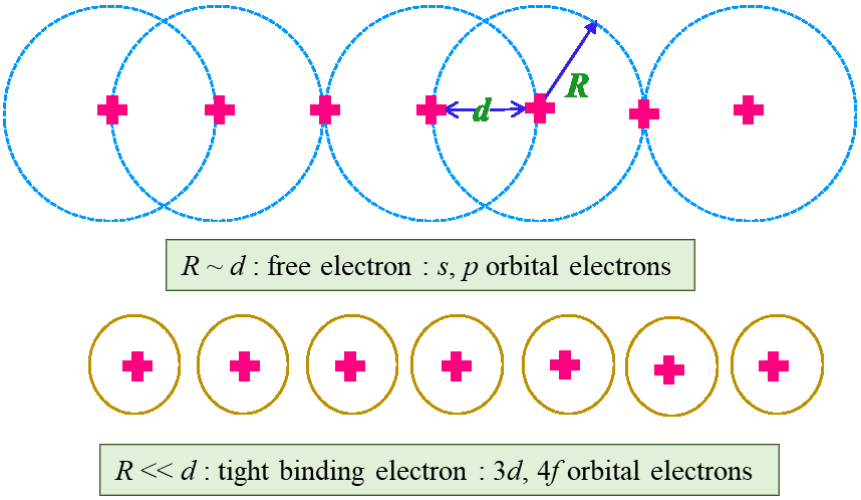

Fig. 1.4. The two cases of atomic structure for free electron and for tight binding electrons or strongly corelated atomic electrons.

where r is the position coordinate, valid for 3d and 4f orbitals. The atomic like structure due to the strong binding can be controlled by the electron hopping amplitude (h_a) and the charge carrier density (d_c). The compounds attaining narrow energy bands generally show strong magnetic characteristics (e.g. Rare earth metals, transition metals and their respective compounds Gd, CuO, $SrTiO_3$, $BaTiO_3$, MnO, Cr_2O_3 *etc.*). The highly discussed Mott-insulators are the product of competition between the h_a and the Coulomb repulsion energy. The electron localization occurs as a result of the balance between the atomic site in a lattice and the number of atoms. The Mott transition occurs when the threshold value reaches for the ratio of Columbic energy over h_a which makes the system to show the metallic feature [39]. The Rare earth perovskite oxides as a perfect candidate of such strongly correlated systems can be probed as per applicative intention to attain the optimum range of parameters.

1.4 Magnetic exchange interactions:

Magnetic exchange interactions among the atoms with the interplay between their e^- spin and orbitals decide the type and range of magnetic ordering. Transitions metals with different possible oxidation states make this phenomenon more exotic among the strongly correlated oxide systems. Since 1928, Exchange interactions responsible for the different magnetic behaviour in the materials as proposed by Heisenberg have given the adequate theoretical base to the experimental magnetization observation and their analyses. On the hand the model of magnetic dipole interactions and exchange interactions explain the long-range ordering in most of the magnetic materials and thus have become the prime model to explain the magnetic interaction of many of these strongly correlated materials. To comprehend these phenomena, we consider the two-electron wave function with spatial co-ordinates $\boldsymbol{r_A}$ and $\boldsymbol{r_B}$ and their corresponding states $\Psi_1(\boldsymbol{r_A})$ and $\Psi_2(\boldsymbol{r_B})$, respectively. The resultant wave function can be overall antisymmetric with either symmetric spatial part (case 1) or antisymmetric spatial state (case 2):

Case 1: $$\boldsymbol{\Psi'} = \frac{1}{\sqrt{2}}[\Psi_1(\boldsymbol{r_A})\Psi_2(\boldsymbol{r_B}) + \Psi_1(\boldsymbol{r_B})\Psi_2(\boldsymbol{r_A})]\,\xi_A \quad (1.8)$$

Case 2: $$\boldsymbol{\Psi''} = \frac{1}{\sqrt{2}}[\Psi_1(\boldsymbol{r_A})\Psi_2(\boldsymbol{r_B}) - \Psi_1(\boldsymbol{r_B})\Psi_2(\boldsymbol{r_A})]\,\xi_S \quad (1.9)$$

Where the ξ_A and ξ_S are the antisymmetric (S = 0) and symmetric (S = 1) spins states respectively. The energies corresponding to the $\boldsymbol{\Psi'}$ and $\boldsymbol{\Psi''}$ states are given as:

$$E' = \int \boldsymbol{\Psi'^*}\hat{\mathrm{H}}\boldsymbol{\Psi'}\,d\boldsymbol{r_A}\,d\boldsymbol{r_B} \quad (1.10)$$

$$E'' = \int \boldsymbol{\Psi''^*}\hat{\mathrm{H}}\boldsymbol{\Psi''}\,d\boldsymbol{r_A}\,d\boldsymbol{r_B} \quad (1.11)$$

Evaluating the difference of the two energy states and inserting the values of the triplet and singlet spin states of S_1 and S_2, the exchange integral can be equated like:

$$J = \int \Psi_1^*(\boldsymbol{r_A})\Psi_2^*(\boldsymbol{r_B})\hat{\mathrm{H}}\Psi_1(\boldsymbol{r_B})\Psi_2(\boldsymbol{r_A})\;d\boldsymbol{r_A}d\boldsymbol{r_B} \quad (1.12)$$

And the conclusive normalized Hamiltonian of the system can be written as:

$$\hat{\mathrm{H}}^{Spin} = -2J\boldsymbol{S_1}.\boldsymbol{S_2} \quad (1.13)$$

where $\boldsymbol{S_1}$ and $\boldsymbol{S_2}$ are the spins of two spin-1/2 particle. Following the above relation between the magnetic orientation and spatial position of the electron can be decided. As $J > 0$ the two electrons residing inside the same atom while for the neighbouring atoms, J becomes negative in order to kinetically favour the energy [35]. Exchange interactions can be of two types: (*i*) Direct exchange interaction and (*ii*) Indirect exchange interaction.

1.4.1 Direct Exchange Interaction:

For the electrons involving different atoms from neighbourhood, the direct exchange interaction takes charge in the absence of any mediatory paths or atoms intermediate. This interaction seems to be very weak and somewhere impractical when the strongly localized electrons of 4*f* and 3*d* orbitals near to the nucleus are considered due to the negligible probability of coupling paths with another electrons. The localized wave functions of the left (ϕ_L) and the right atoms (ϕ_R) can be written as

$$\phi_L = \frac{1}{N}(\Psi_1 + g\Psi_2) \quad (1.14)$$

$$\phi_R = \frac{1}{N}(g\Psi_1 + \Psi_2)\; where\; g = \frac{-1 + \sqrt{1 - S^2}}{S} \quad (1.15)$$

where Ψ_1 and Ψ_2 are the Bloch wave functions for metals, N is the normalization constant and S is the overlap integral, $\int \Psi_1^*(r)\Psi_2(r)\,d^3r$.

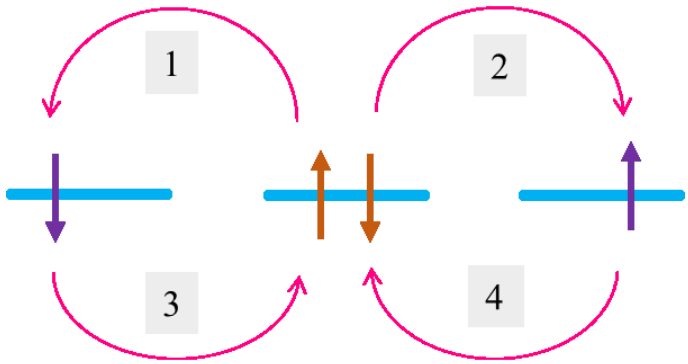

Fig. 1.5. The possible pathway of Direct Exchange Interaction.

respectively, as ϕ_L and ϕ_R and S is the combined product of the integral of the two wave functions Ψ_1 and Ψ_2 [39]. Among four possibilities of wave-functions, considering two of them being doubly generated, the h_a can be calculated as:

$$h_a = \int \phi_R^*(r)\phi_L^*(r')\hat{H}(r,r')\phi_L(r)\phi_R(r')d^3rd^3r' \tag{1.16}$$

$$J_d = \int \phi_L^*(r)\phi_L^*(r')\hat{H}(r,r')\phi_R(r)\phi_R(r')d^3rd^3r' \tag{1.17}$$

This interaction can mediate both FM and AFM interaction with the Hamiltonian including the direct exchange interaction for multi electron system can be simplified to:

$$\hat{H}_D = -\sum_{ij} J_{ij}\, S_i S_j \tag{1.18}$$

The simplified demonstration of the direct exchange possible pathway is given in Fig. 1.5.

1.4.2 Super Exchange Interaction:

In the case of magnetic materials containing transition metal ions sharing their nearest neighbourhood with non-magnetic oxygen atoms, magnetic properties cannot be explained by the Heisenberg Direct exchange interaction mechanism. In such situations, Indirect exchange interactions consist of the super exchange and double exchange interactions play a decisive role in many of the complex oxide perovskites where manganese and some other transition metal ions dictate the long-range ordering. Most of the exchange interactions generally explains the magnetic behaviour of the magnetic metals in contrary to those, Kramer proposed a new kind of interaction in 1934 to illuminate the spin dynamics of paramagnetic salts. Anderson extended the theory for the antiferromagnetic systems by modifying it later in 1950 which again got renewed in 1959 by Anderson [40].

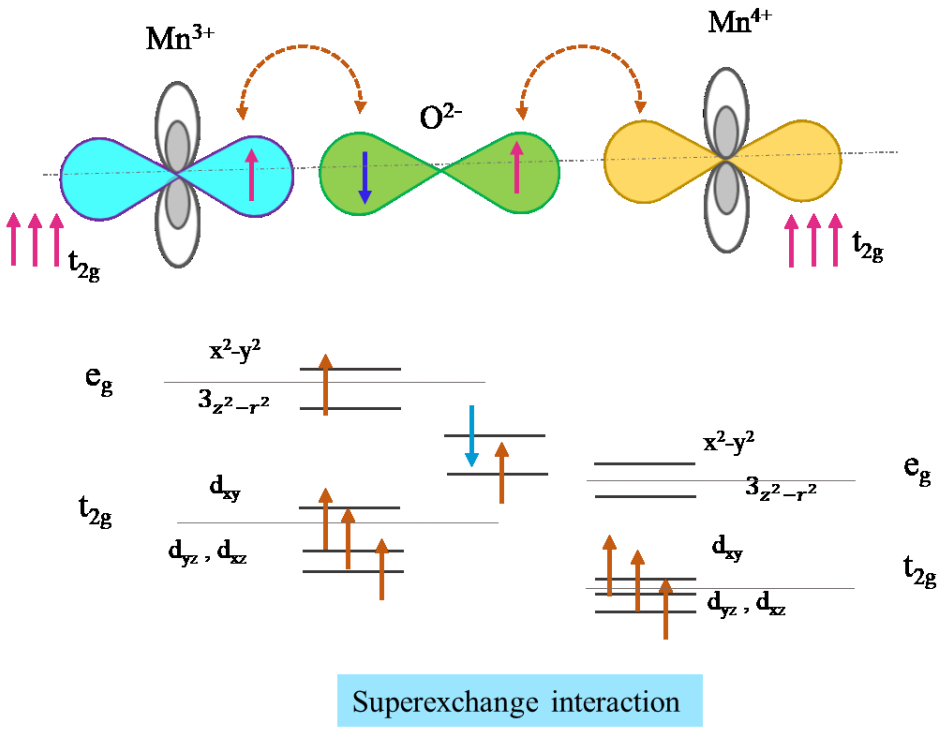

Fig. 1.6. Super exchange interaction between Mn^{3+} with $3d^4$ and $Mn^{4+}$with $3d^3$ electronic configuration.

Superexchange interaction is one of an indirect exchange interaction that is very common for the explanation of charge ordering or anti ferromagnetic insulating phenomena in the complex oxide manganite systems. In this case, the electrons are actually shared between the Mn e_g and *O*-2*p* orbitals reducing the Mn-O bond length. As the two Mn^{3+} e_g orbitals interact through the oxygen, the half-filled e_g electron of Mn^{3+} participating in the semi-covalent bond with oxygen aligns parallel to its corresponding t_{2g} electrons due to the strong intra-site Hund's coupling. However, these two Mn^{3+} ions in the Mn-O-Mn bond aligns antiferromagnetically with each other (as shown in the Fig. 1.6) making the super exchange interaction antiferromagnetic and localises the shared electrons making the system insulating in a long range. Similarly, the single electron shared between the O-*p* orbital and Mn^{4+} hybridised e_g orbital aligns AFM with the other Mn^{4+} located on the other side of O-atom following the Hund's rule. Even the Mn^{3+}-O-Mn^{4+} superexchange interaction leads to the FM coupling is also possible in certain situations. The AFM coupling with the superexchange interaction brings the total effective energy down rather than the FM coupling. Due to the involvement of both *f* and *p* orbital, the SE interaction is explained by the second-order perturbation theory by which the SE integral which can be expressed as [41]:

$$J \sim \frac{4h_a^2(\boldsymbol{S_1}.\boldsymbol{S_2})}{U} \tag{1.19}$$

considering two magnetic spins S_1, S_2 of *p* orbital and *U* being the Coulomb energy. In order to concise the SE interaction some rules are supposed to be maintained. Firstly, for unpaired 3*d* electrons with the lobes on the axis leads antiferromagnetic coupling with robust magnitude. Secondly, the *d*- orbitals of rare earth system holding cubic symmetry prefers the FM alignment via SE interaction. Lastly for the unpaired 3*d*

orbital electrons interacting with another vacant or filled *d*- orbitals, the SE assists the weak FM coupling. The transition metal oxides (*d*- block) elements attains the h_a value of nearly ~ 0.1 eV and the Coulomb energy of the order of ~ 4 eV approximately. Tolerance factor, Jahn-teller distortions, crystal symmetry, external fields and some other factors can affect the super exchange interactions.

1.4.3 Double Exchange Interaction:

Indirect superexchange interaction could not explain the transport properties of the complex oxide systems where the hopping of electron takes place and gives rise to a metallic character for the complex oxide systems. To explain the e^- high mobility character the double exchange interaction has been proposed for the manganite systems and some other systems as well. The indirect exchange interaction mediated by the oxygen with the 2*p*-orbital valence electrons enable the interaction between the Mn^{3+} and Mn^{4+} atoms containing the half-filled e_g orbital and empty e_g orbital by transfer of electrons. This transfer of electrons in the Mn^{3+}-O-Mn^{4+} chains explicitly explains the metallic nature of the system. The localised t_{2g} electrons align ferromagnetically with the half-filled e_g electron in the case of Mn^{3+} and pairs antiparallelly with the O-2*p* electron following the Pauli exclusion principle. The t_{2g} electrons of the Mn^{3+} and Mn^{4+} aligns ferromagnetically and makes the ordering more preferable as it contains the lower energy. If it doesn't have to flip the spins then the kinetic energy of the hopping electron gets saved and hence it prefers the

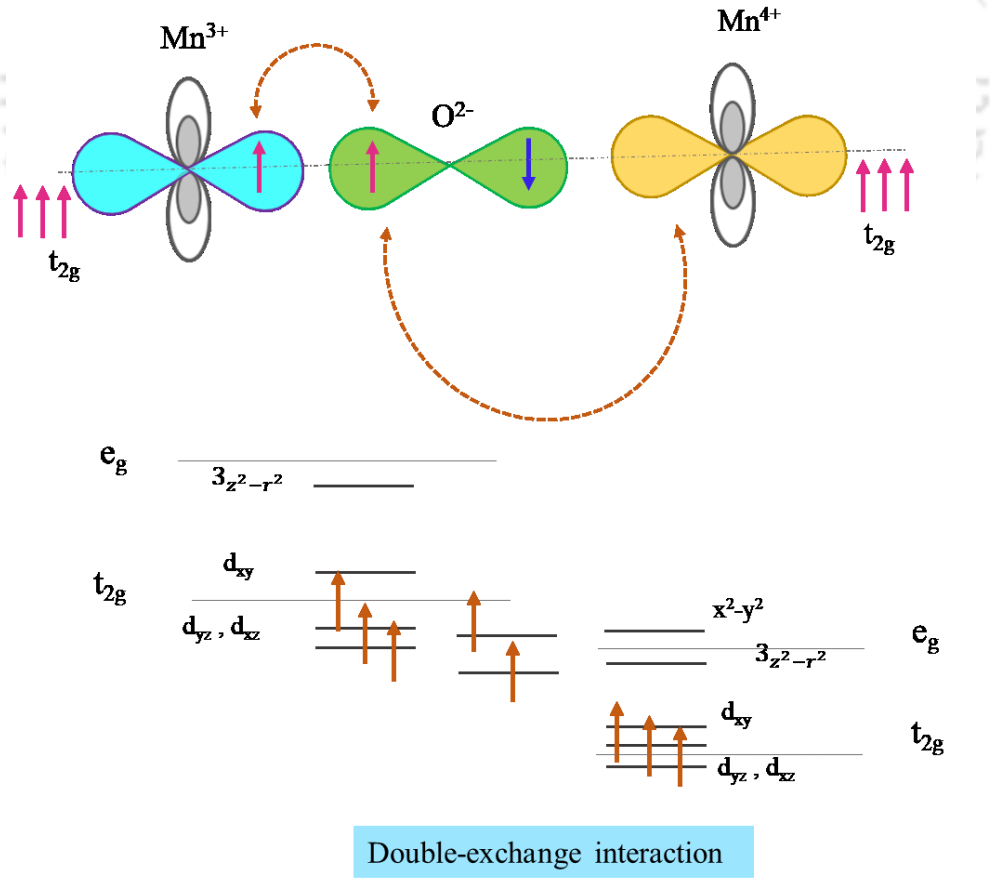

Fig. 1.7. Double exchange interaction between Mn^{3+} with $3d^4$ and $Mn^{4+}$with $3d^3$ electronic configuration

ferromagnetic ordering more favourable. The streamlined schematic for the DE is shown in Fig. 1.7 Electrons choosing to occupy the narrow t_{2g} energy state singly according to the Hund's rule and the last electron goes to the broad e_g band can be clearly observed in DE interactions. Thus, DE or electron hopping to the nearest vacant energy state is possible only if the spins are ferromagnetically aligned to each other otherwise overcoming the huge energy barrier generated due to the antiferromagnetically alignment the spins states cannot be affordable following Hund's interaction rule [35]. The Hamiltonian considering the DE interaction ($\hat{\mathrm{H}}_{DE}$) into account can be expressed as follows:

$$\hat{\mathrm{H}}_{DE} = -j \sum_{n=0}^{\infty} J_n(S) \, (\boldsymbol{S_1}.\boldsymbol{S_2})^n \tag{1.20}$$

with j being the transfer integral and the angle between the neighbouring FM spins S_1 and S_2 with θ being the variation of j related to θ by cos (θ/2) and $j = 0$ for θ = Π indicating towards the necessary condition of the spins to be directed ferromagnetically and $J_n(S)$ being the coupling constant [42]. Some of the most extensively studied perovskite system showing the DE interaction are $La_{1-x}Sr_xMnO_3$, $La_{1-x}Ca_xMnO_3$, $Pr_{1-x}Ca_xMnO_3$, and $Pr_{1-x}Sr_xMnO_3$ etc. with Mn^{3+} and Mn^{4+} mixed oxidation states, Fe^{2+} ($3d^6$) and Fe^{3+} ($3d^5$) on octahedral sites.

1.4.4 RKKY Interaction:

The indirect interaction involving the spin-polarized mobile electrons by magnetic moments via hyperfine interactions correlates two nuclear spins without coming into direct influential contact to each other. The name was given of four discovers of the very interaction: Ruderman (R), Kittel (K), Kasuya (K) and Yosida (Y). This generally corresponds to the *d* or *f* orbital conducting electrons. It was first used to explain the spin dynamics of the electron gas where the perturbation is of the order of delta function dispersed over the nuclear volume, whereas, in theoretical prototype second order perturbation is actually considered. The magnetization gets induced and passed by localized moments to another moment inside electron gas. For RKKY interaction, both FM and AFM coupling favours the minimum energy usage protocol. Here, the exchange interaction (J_{sf}) between the 4*f* shell localizes the magnetic moment with intrinsic spin $\boldsymbol{S}$ and the movable electron of spin $\boldsymbol{\sigma}$ is given by the relation $\propto (-J_{sf}\boldsymbol{S}.\boldsymbol{\sigma})$. It has been observed that the resistivity or the inverse of the metallic character increases proportionally with r^3 with periodically fluctuating polarization when the doping of another material is introduced in the parent compound. The added impurity is mainly responsible for the oscillation in long-range ordering. The effective exchange coupling value can be expressed as:

$$J_{\text{eff}} \sim \frac{9\pi J_{sf}^2 \, v^2 F(\varphi)}{64 \, e_f} \tag{1.21}$$

with $\frac{\varphi}{r} = 2k_F$ (k_F denotes the Fermi vector), e_f represents Fermi energy, $F(\varphi) = \frac{(sin\varphi - \varphi cos\varphi)}{\varphi^4}$ with v denoting moving electron no. per atom [39].

1.4.5 Dzyaloshinskii - Moriya Interaction:

The magnetoelectric effect has been popular after it was nomenclatured by Landau and Lifshitz in the year of 1957 with the basic theory of induction of magnetization in particular magnetic compounds by the help of an external electric field. In 1960 Dzyaloshinskii proposed the applied version of the theory by means of symmetry relations to predict the spin mechanism of weak Ferromagnetic component of some magnetic compounds like Cr_2O_3 [43]. In the same year along with Moriya the weak Ferromagnetism in α – Fe_2O_3 was explained named as Dzyaloshinskii- Moriya (DM) interaction considering the spin-orbit coupling between the excited state electron and the ground state electron using the second-quantization based perturbation theory which later described various interesting phenomena like magnetic frustration, skyrmions *etc.* [44]. Taking only two spins into account the Hamiltonian involving the DM interaction has the form as:

$$\hat{H}_{DM} = \boldsymbol{D_{12}}.(\boldsymbol{S_1} \times \boldsymbol{S_2}) \tag{1.22}$$

where $\boldsymbol{S_1}$ and $\boldsymbol{S_2}$ are the two interacting spins and $\boldsymbol{D_{12}}$ is the vector in-between them and shown in Fig. 1.8(a) and 1.8(b) The interaction vector $\boldsymbol{D_{12}}$ ceases to exist for the system having perfect inversion symmetry. So, considering a perovskite system like $DyCrO_3$ the Cr-Cr bonds undergo a distortion forming the Cr-O-Cr angles canted and aligned antiferromagnetically. The inversion and rotational symmetry break down due to the distortion. Hence, the $\boldsymbol{D_{12}}$ vector can be inward or outward to the horizontal plane depending on the interaction path and the route of symmetry breaking but perpendicular to the plane. Let's assume both the spins $\boldsymbol{S_1}$ and $\boldsymbol{S_2}$ are oriented ferromagnetically or parallel to each other at the first sight which in turn persuades a spin-orbit coupling leading to the DM interaction. The resultant unit vector connecting the $\boldsymbol{S_1}$

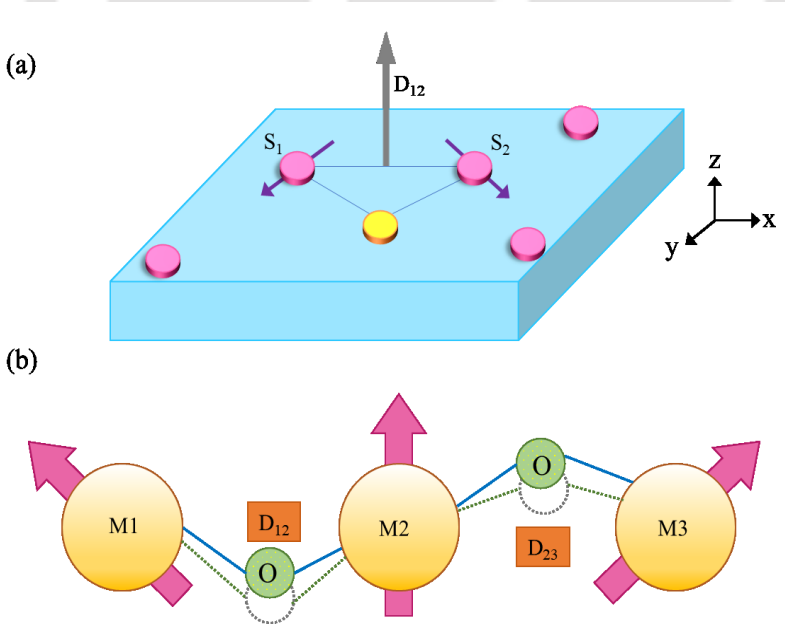

Fig. 1.8. (a) The schematic representation of the interfacial DM interaction for two spins and (b) a graphical flowchart of the asymmetric DM interaction due to the bond bending where the D_{ij} vector lies perpendicular to the M (metal ion) axis as well as to the oxygen displacement vector and the dotted lines represent the probable virtual displacements due to the interaction.

and $\boldsymbol{S_2}$ spins namely $\boldsymbol{r_{12}}$ which can be parallel or perpendicular to the $\boldsymbol{D_{12}}$ in order to put the system in equilibrium by attaining the minimum energy level. The approximated value of $\boldsymbol{D_{12}}$ can be evaluated using first order approximation:

$$\boldsymbol{D_{12}} = \eta \boldsymbol{r_{12}} \times \boldsymbol{t_0} \tag{1.23}$$

with $\boldsymbol{t_0}$ as the deviation magnitude of the O-ions due to distortion and η is the coefficient. The quantity can be calculated using second order approximation as well [44] where, for a perfect cubic lattice $\boldsymbol{D_{12}}$ will vanish but for a distorted orthorhombic crystal structure with reduced symmetry $\boldsymbol{D_{12}}$ magnitude as well as the direction will differ with respect to the Cr-O-Cr bond angle. Hence, the overall Hamiltonian counting the Heisenberg interaction term in along with the DM interaction for two-spin system can be expressed as:

$$\hat{\mathrm{H}} = \sum \{ J_{12}\, \boldsymbol{S_1}.\boldsymbol{S_2} + \boldsymbol{D_{12}}.(\boldsymbol{S_1} \times \boldsymbol{S_2}) \} \tag{1.24}$$

where J_{12} represents the Heisenberg exchange interaction coefficient.

1.5 Magnetocaloric effect:

The Magnetocaloric effect (MCE) was first predicted by William Thomson in 1860 which was later experimentally evaluated by Weiss and Piccard for Ni showing a temperature change of 0.7 K when the field was varied of the order of 15000 Oe [45]. In the very recent time of the year of 1976, G. V. Brown developed the first magnetic refrigerator using the MCE of 47 K temperature difference with the help of Gadolinium metal [46]. The simplified version of the theoretical explanation of MCE is related with the increasing and decreasing behaviour of the spin-ordering degree via external magnetic field which in turn raise or bring down the temperature of the system without any help of compressor. To explain MCE in Figs. 1.9(a) and 1.9(b) we show a schematic representation of both the thermal compression and magnetic field driven refrigeration.

In what follows we discuss the details of MCE process. Let's consider a system in absence of external field (H_{DC} = 0) where the paramagnetic spin state persists with maximum entropy (S_1). For the sudden increase of H_{DC} to some constant magnitude, the system undergoes an adiabatic change with the scattered spins orientated in a particular direction making the S_1 to vanish (S_1 = 0). However, the other related entropy of the system namely lattices entropy (S_2) and electronic entropy (S_3) adjust accordingly. Hence the change in entropy becomes as $\Delta S_1 < 0$. Following the energy conservation law, the total entropy before and after the field change should remain equal which implies

$$\Delta S_1 + \Delta S_2 + \Delta S_3 = 0 \tag{1.25}$$

$$\Rightarrow \Delta S_2 + \Delta S_3 > 0 \quad (as\ \Delta S_1 < 0) \tag{1.26}$$

In turn the increased entropy arising from electronic and lattice contribution raise the temperature of the system. Now, similarly with the adiabatic removal of the field again (H_{DC} = 0) the whole system loses the heat energy by increasing the S_1 to positive quantity leaving the spins randomized.

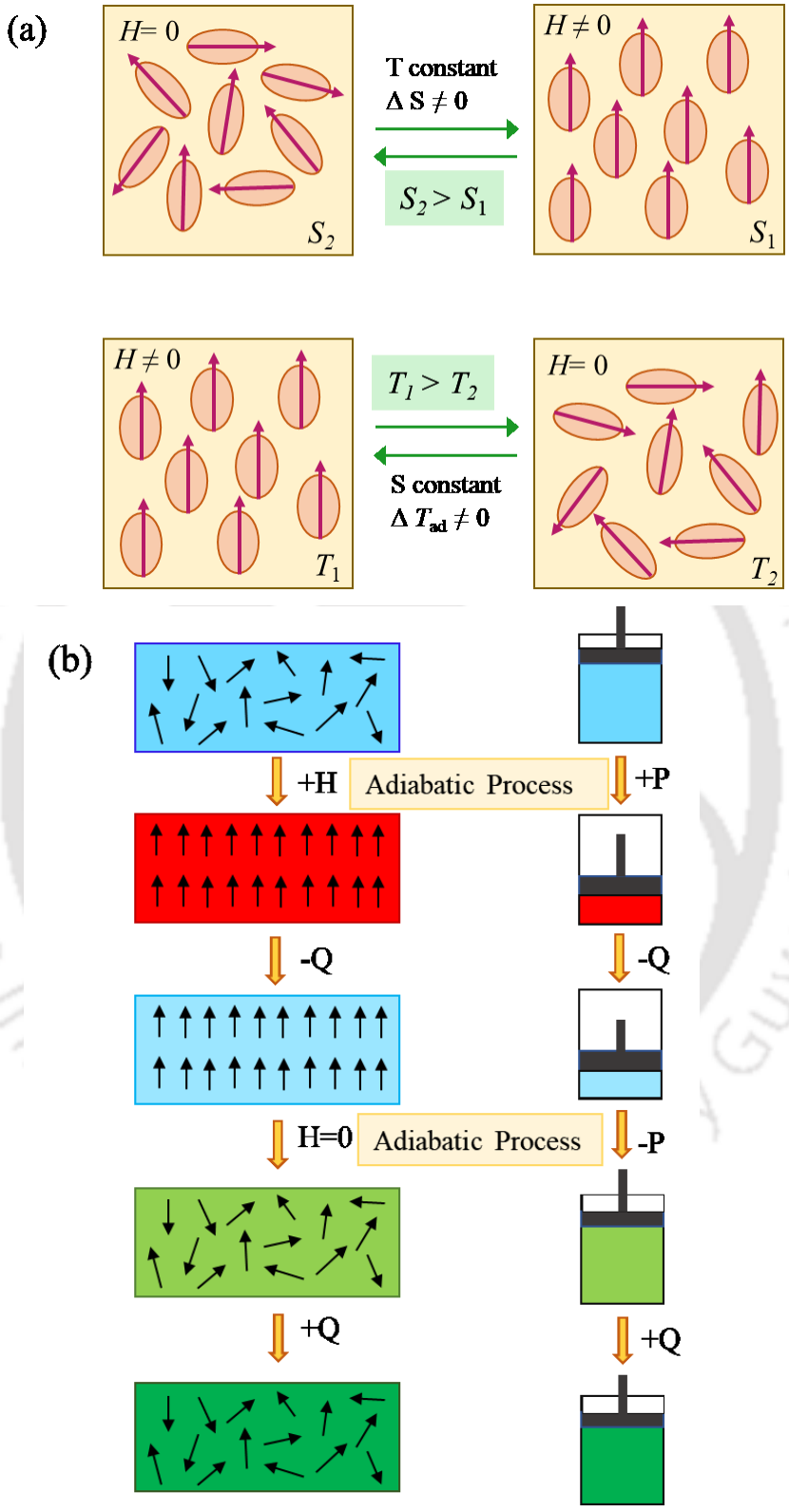

Fig. 1.9. (a) Schematic diagram portraying the two basic processes of the magnetocaloric effect when a magnetic field is applied or removed in a magnetic system considering the isothermal process, (leading to an entropy change) and the adiabatic process (resulting temperature variation). (b) Schematic diagram of the magnetic (left) and vapor-based (right) refrigeration cycles.

The change in temperature ΔT_{ad} during the whole cycling process of application and removal of the field indicates the cooling degree of the particular material. Referring the H_{DC} as H, temperature as T, magnetization as M and overall entropy as S using the Maxwell's relation:

$$\left(\frac{\delta S\ (T,H)}{\delta H}\right)_T = \left(\frac{\delta M\ (T,H)}{\delta T}\right)_H \tag{1.27}$$

$$=>\ \Delta S_1(T,\Delta H)\int_{H_1}^{H_2}\left(\frac{\delta M\ (T,H)}{\delta T}\right)_H dH \tag{1.28}$$

And the refrigeration cooling capacity (RCP):

$$RCP = \int_{T_1}^{T_2}\Delta S_1(T,\Delta H)\,dT \tag{1.29}$$

Where T_1 and T_2 are the temperatures with the difference of ΔT_{ad} [47].

1.6 Exchange Bias:

Another intriguing feature of the perovskite systems is the exchange anisotropy or exchange bias (EB) phenomenon invented by W. H. Meiklejohn and C. P. Bean in the year of 1956 while working with the single domain transition metal Cobalt along with its innate oxide CoO which is AFM in nature [48]. This property occurs only at the interface of FM (ordering temperature-T_C) and AFM (ordering temperature-T_N) layers where $T_C > T_N$. The common observation of Fig. 1.10(a) for $Y_{0.9}Ce_{0.1}CrO_3$ polycrystalline sample describes the lateral shift of hysteresis loop for FC case than that of ZFC case as the rotational hysteresis loss (I_r) remains intact and of larger value even if the H_{DC} is of the range of ~ 16kOe. For the mechanism of the EB, we need to cool the investigated system consisting of FM and AFM domains from a temperature between T_C and T_N to the temperature of measurement which is necessarily be lower than T_N in the presence of an H_{DC} of a definite value. With the H_{DC}, the FM spins start to get aligned towards the field while the temperature below the AFM ordering keeps the AFM spins in the paramagnetic region (Fig. 1.10(b)) until the temperature is brought below T_N and the AFM domains direct themselves in antiparallel orientation with the FM ordering at the interface of the FM and AFM zone reaching the maximum moment (saturation magnetization). Now, as the field direction is reversed, the FM domains try to align themselves in the opposite direction. On the other hand, the AFM spins hold their positions in the previous orientation with the interfacial torque of the AFM spins experienced by the FM moments at the boundary. This unidirectional FM anisotropy competes with the torque created by the AFM domains, hence, the magnitude of the reverse field needed is more in order to completely orient the FM and AFM in their respective stable direction called as exchange bias (the microscopical field induced acts as biasing). The hysteresis loop completes its path the way back as we bring the field direction to the starting direction and the FM spins feel free to move towards the reversed filed due to the push from the interfacial AFM spins at the same direction. The energy involved in the EB process relates the anisotropy constant k and the cosine of the angle (θ) created by the saturation magnetization and direction of H_{DC}:

$$E = -kcos\theta \tag{1.30}$$

The EB recently have been found in some unusual different categories of materials like mixture of fine particles of oxides: Ni-NiO, Fe-Fe_2O_4, nitrides: Fe-Fe_2N, materials without defined FM/AFM edge of $Cu_{1-x}Mn_x$, $Au_{1-x}Fe_x$, FM coated AFM single crystals of FeF_2, NiO *etc.* [49]. Most importantly the exchange bias is very interestingly studied in the manganite and chromite complex oxide perovskites such as $La_{1-x}Sr_xMnO_3$, $Y_{1-x}Pr_xCrO_3$, $Y_{1-x}Ce_xCrO_3$ systems *etc.* [50–52].

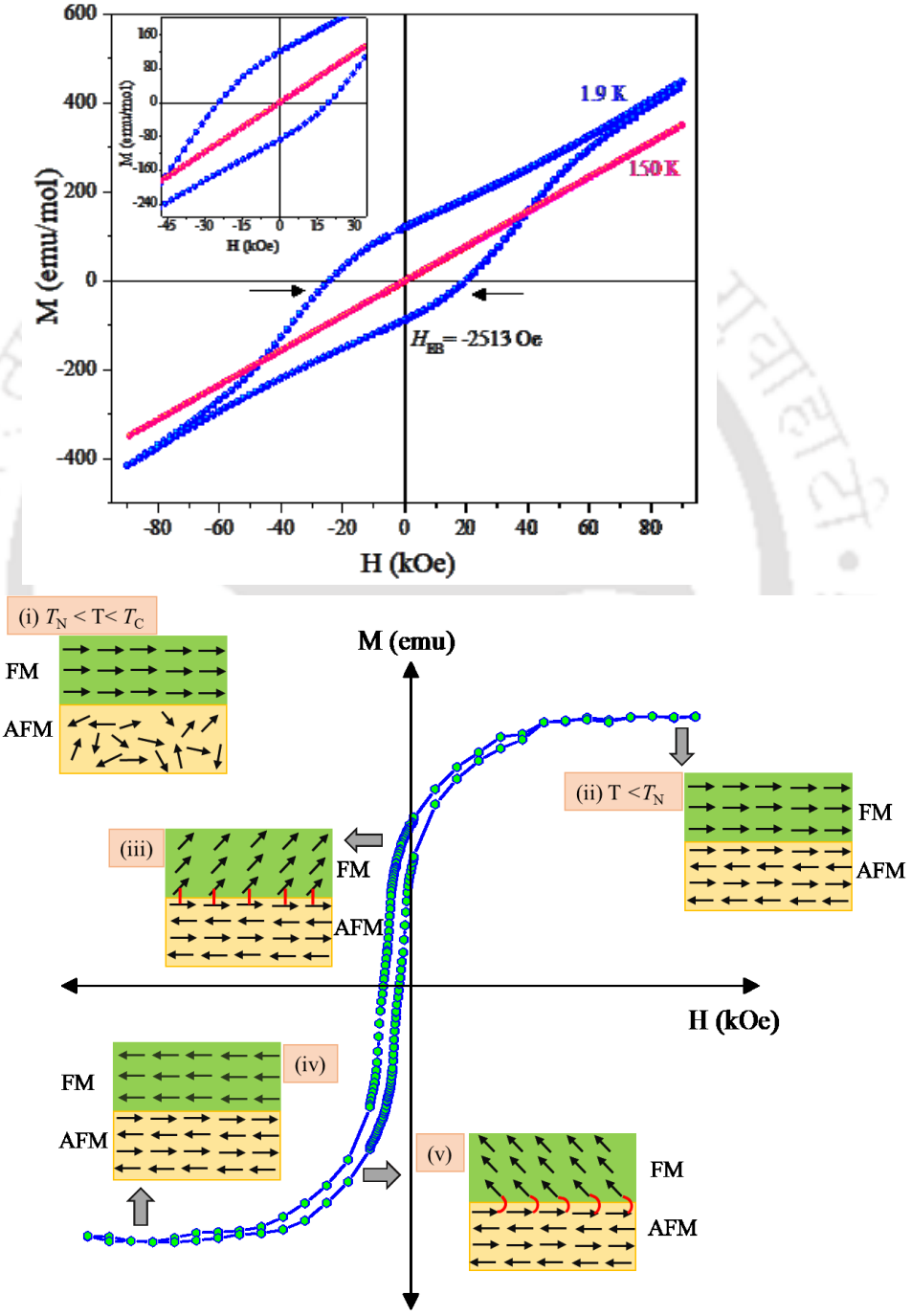

Fig. 1.10. (a) The horizontal (*x*-axis) shifting of the hysteresis loop of $Y_{0.9}Ce_{0.1}CrO_3$ polycrystalline sample measured under 1.9 K termed as exchange bias whereas the loop shifting is not present for the curve measured at 150 K. The inset shows the zoomed view of the exchange bias. (b) The schematic visualization of the spin configuration of a FM/AFM bilayer at different stages (i)-(v) of an exchange biased hysteresis loop.

1.7 Negative magnetization and compensation phenomena:

The change in magnetization polarity from positive to negative under the application of positive cooling field is often called as magnetization reversal or the negative magnetization (NM). The observation was first recommended by L. Néel in the year of 1948 by theoretical interpretation and it was experimentally realized with the help of spinel ferrite compound after two years in 1950 [53]. The material with NM has positive susceptibility ($\chi = \partial M/\partial H$) which is different from the diamagnetic or superconducting materials that shows negative susceptibility. Consequently, the particular temperature associated with the zero magnetization after which the magnetization goes to negative value is termed as compensation temperature (T_{Comp}). The NM feature can be generalized to be observed in five cases: (a) where two FM sublattices interrelates via negative exchange interaction: e.g. Co_2VO_4, $Li_{0.5}Fe_{2.5-x}Cr_xO_4$ ($1.0 \leq x \leq 1.6$), Fe_2MoO_4, $Bi_xCo_{2-x}MnO_4$ ($x = 0, 0.1, 0.3$) *etc.* (b) where both the sublattices are AFM in nature and interact via negative exchange interaction: e.g. $SmVO_3$, $CaMn_{0.96}V_{0.04}O_3$, $BiFe_{0.5}Mn_{0.5}O_3$, $Ni(HCOO)_2 \cdot 2H_2O$ *etc.* (c) where one of the sublattice is either FM or AFM and the other is PM and they interfere via negative exchange interaction: *e.g.* $La_{0.25}Gd_{0.75}MnO_3$, $ErCo_{0.5}Mn_{0.5}O_3$, $Gd_{1-x}Ca_xMnO_3$ ($0.2 \leq x \leq 0.4$), $GdCrO_3$ *etc.* (d) where the sublattice inherits the spin and orbital interacts which counter each other : e.g. Sm_2Al, $SmNiAlH_{1.17}$, $(Sm_{1-x}Gd_x)Al_2$ ($0.01 \leq x \leq 0.026$), $(Sm_{0.974}Gd_{0.026})Al_2$ *etc.* (e) where the exchange interaction occurs at the interface of the FM and AFM counterparts: e.g. Ni-FeF_2 multilayers, $YFe_{1-x}Mn_xO_3$ ($x = 0.4$, 0.45, and 0.5), $LiFeTiO_4$, $YFe_{1-x}Mn_xO_3$ ($x = 0.4$, 0.45, and 0.5) *etc.* [54]. The first category of materials having two FM sublattices namely A and B possess the molecular field at their respective sites [55]:

$$H_A = \eta\,(\alpha M_A - M_B) \tag{1.31}$$

$$H_B = -\eta\,(M_A - \beta M_B) \tag{1.32}$$

where, M_A and M_B are the magnetization of A and B sublattices respectively, η is the molecular field parameter associated with the exchange integral of the A and B sublattices, α and β are the respective molecular field parameters. So, the magnetization of the two sublattices depends on temperature which relation with the Brilliouin function can be expressed as:

$$M_A = \lambda N g \mu_B S_A B_A \frac{g\mu_B S_A\,(H + H_A)}{k_B T} \tag{1.33}$$

$$M_B = \gamma N g \mu_B S_A B_A \frac{g\mu_B S_A\,(H + H_B)}{k_B T} \tag{1.34}$$

where N is the number of unit volume magnetic moment, S_A and S_B corresponds to the spin-angular momenta of respective sublattices A and B, λ and γ represent magnetic ions molar fractions, k_B is the Boltzman's constant and g is g-factor. NM can occur when, α is larger than β which ranges between 0 and -1. The resultant magnetization occurs along the A sublattice below the AFM ordering temperature. Our investigated systems fall under the third case. Here, the PM sublattice experiences an induced field due to the other magnetic (FM/canted AFM) counterpart which can be expressed as [56]:

$$M_{Net} = M_A + \frac{(H_1 + H_{ext})C_B}{T} \tag{1.35}$$

Where, M_A represents the magnetization of the PM sublattice, H_1 being the induced field due to the magnetic B sublattice, C_B denoting the Curie constant of B sublattice cation and H_{ext} being the external magnetic field. Here, the net magnetization attains negative value when the second term becomes negative and that is only possible when the H_1 surpasses H_{ext} in negative magnitude [55].

1.8 Magneto-crystalline Anisotropy:

The direction dependence of magnetization as well as other magnetic properties is generally referred as magnetic anisotropy [57]. This property hugely affects the magnetization and the shape of the hysteresis (M-H) loop. It is pronounced ann-eye-SOT-rope-ee which makes the phenomenon very important in designating the commercial magnetic materials. This can be an intrinsic character of the particular magnetic material due to its crystallographic shape or the manual processing of the material. The most important and vital category of magnetic anisotropy is magneto-crystalline anisotropy which is very active in our working materials.

Magneto-crystalline anisotropy or shape anisotropy is the common propensity of magnetization to get aligned in the favoured crystal direction. The energy difference required to magnetize the sample along the easy (along which the magnetization of the crystal is easy) and the hard axis (along which the magnetization is hard) per unit volume is termed as the magneto-crystalline anisotropy energy whereas the anisotropy field H_K is defined as the field needed to saturate the magnetization in the hard direction. For example: bcc Fe has the [100] as the easy and [111] as the hard axis in contrast to fcc Ni which has [111] as the easy and [100] as the hard axis. Now, assuming Co as the sample, the magneto-crystalline energy can be written as [35, 39]:

$$E = K_1 sin^2\theta + K_2 sin^4\theta \tag{1.31}$$

with K_1 and K_2 as the highly temperature dependent anisotropy constant in the form of energy densities measured in terms of J m^{-3} and θ being the angle between the magnetization and the stacking direction of the hexagonally close packed planes. It is interesting to note that the symmetry of the magneto-crystalline anisotropy is always the same as that of the crystal structure. The equation can be considered for the system where the magneto-crystalline energy depends on a single axis angle thus not valid for cubic field systems. The magneto-crystalline energy for a cubic system can be expressed with $m = (m_x, m_y, m_z)$ as:

$$E = K_1\left(m_x^2 m_y^2 + m_y^2 m_z^2 + m_z^2 m_x^2\right) + K_2 m_x^2 m_y^2 m_z^2 + \cdots (higher\ orders) \tag{1.36}$$

Now in spherical coordinate the equation can be modified like:

$$E = K_1\left(\frac{1}{4} sin^2\theta\ sin^2 2\phi + cos^2\theta\right) sin^2\theta + \frac{K_2}{16}\ sin^2 2\phi\ sin^2 2\theta\ sin^2\theta \tag{1.37}$$

This energy actually originates from the spin-orbit interaction ranging in magnitude within 10^2 - 10^7 J m^{-3} referring to the atom wise energy of the value of 10^{-8} – 10^{-3} eV. The orbital which is generally strongly

coupled within the lattice also requires to be reoriented along with the electron spin direction under the application of external field. For the 4*f* group rare earth elements possessing higher mass affirms the high spin-orbit coupling hence the magneto-crystalline anisotropy. This magneto-crystalline energy varies in high magnitude for low symmetry magnetic ions and low magnitude for high symmetry ions.

1.9 Motivation:

Some of the striking results such as observation of superconductivity $[LaNiO_3(2uc)/La_{0.7}Sr_{0.3}MnO_3(3uc)]_{20}$ grown on (001) $SrTiO_3$ due to the interface driven antiferromagnetic coupling triggered us to look into the particular compositions [58]. The temperature dependence of the electrical resistivity ρ(T) for the $La_{0.7}Sr_{0.3}MnO_3$ (LSMO)/$LaNiO_3$ (LNO) superlattices between 300 K and 2 K which displays the superconducting transition with a detection current of 5×10^{-3} mA. Another remarkable property that gave motivation to take-up this research problem is the thickness dependence of exchange bias as well as metal-insulator (MI) transition reported by Zhou et al. in the superlattices of $La_{0.7}Sr_{0.3}MnO_3$ (LSMO)/$LaNiO_3$ (LNO) [59,60]. Large coercivity (H_C) and exchange bias (H_{EB}) are the key features of these systems. Since, $La_{1-x}Sr_xMnO_3$ crystal itself shows remarkable compositional dependence of electrical and magnetic properties, it is worth to discuss its crystal structure variation with the doping of Sr at the La site [60]. The crystal structure at room temperature changes from orthorhombic (space group: *Pbnm*, Z = 4; $x < 0.175$) to rhombohedra (space group *R3*c, Z = 2; $x \geq 0.175$) along with the resistivity while the ferromagnetic transition is absent for lower compositions and robust change in resistivity has been observed across T_C. For doping amount more than $x = 0.175$, metallic character was observed (for $T \leq T_c$).

Another interesting system that motivated us to work on this research problem is the $LaNiO_3$ thin films (deposited on $SrLaAlO_4$ (100) and $SrLaAlO_4$ (001) single crystal substrates) in which the thin films oriented in the direction of 100, independent of thickness, they all show semiconducting insulating behaviour which fits well with the Variable Hopping Model (VRH) within the temperature range of 40 K to 260 K. Typically, the systems which exhibit VRH model follows the resistivity expression $\rho = \rho_0 \exp\left(\frac{T_0}{T}\right)^{1/4}$ where $T_0 = 5.7\alpha^3/k_B N(E_F)$, $N(E_F)$ is the density of states at the Fermi level and α^{-1} is the localization length. On the contrary, the thin films oriented along (001) direction, showing insulating behaviour throughout the whole temperature range for the film of thickness 50 nm, where 100 nm thick thin film being the break point in exhibiting the starting point of conducting property, above which the higher thicknesses show metallic behaviour. Below 100 K, the resistivity data shows a localized character which in turn has the very same origin as observed in samples grown on (100) substrates [61,62]. On the other hand, $LaCoO_3$ exhibits the nonmagnetic insulator to the PM semiconductor transition attracts numerous spintronic applications along with the very specific characteristic holding strain induced FM spin orientation in the ground state in the thin films whereas nonmagnetic feature for polycrystalline with singlet ground state of Co^{3+} [62]. The compound being very sensitive towards the oxygen deficiency, it changes the degree of distortion in tetragonal structure so the magnetic ordering for the thin films grown on $SrTiO_3$ indicating towards the long-range ordering persisting in the system [63].

Another study showed that the for T < 300 K, the magnetic frustration between the antiparallel orientated spins hinder the AFM ordering in the system and the long-range FM ordering persist at lower field like ≤ 100 Oe higher to which the system biases towards the AFM characteristic connecting to the reduction of the Co-O-Co bond angle [64].

Coming to the polycrystalline perovskite part of the work, the rare-earth doped $CeCrO_3$ finds its own class of applications which motivated us to work in this area. Some of the interesting results of $CeCrO_3$ will be proper to discuss as the reason of the inspiration of our work. The main motivation lies in the magnetization switching in $CeCrO_3$bulk systems [65]. Cao et.al reported totally opposite behaviour of ZFC and FC magnetization under the application of 100 Oe external field, as with cooling in FC shows AFM transition around 260 K along with magnetic-compensation temperature of 133 K. For T < 30 K, these authors noticed further increment in magnetization in negative range with a maximum at 16 K. In contrary, the M_{ZFC} shows completely mirror symmetry with M_{FC} curve with respect to *x* axis. According to the authors, a small thermal hysteresis between field-cooled-cooling (FCC) and field-cooled-warming (FCW) around T_N was raised due to first order phase transition. Again, for FCC under 1.0 kOe field, the magnetization value changes from the most negative around 37 K to positive again below 16 K. This zero-magnetization crossing temperature can be denoted as the second compensation temperature T_{comp2}. Interesting features can be observed in case $DyCrO_3$, another chosen rare earth chromate oxide which exhibits significant change in the magnetic entropy changes ΔS_M (T, H) ~ 8.1 J kg^{-1} K^{-1} at 12K for a change in the magnetic field ΔH~3T. Some studies reported that ΔS_M (T, H) ~ 8.4 J kg^{-1} $^{-1}$K at 15 K for ΔH ~ 4T which are higher than other rare-earth chromates confirming its application in magnetic refrigeration within the range of 10 to 80 K. $DyCrO_3$ also exhibits unusual temperature dependence of coercivity due to the two different contributions coming from AFM Cr^{3+} and paramagnetic Dy^{3+}. At low temperature (2.5 - 10 K), the paramagnetic signal becomes intense where at higher temperature the canted AFM behaviour evident. The coercive field (H_C (T)) increases with the decrease of temperature below 146 K and saturates with further lowering of temperature H_C (T) peak at 80 K and then decreases proving the paramagnetic contribution to it. The above literature results are the main motivation in choosing Ce as one of the substituents in the parent compound in the present study [66].

Another two interesting rare earth oxide chromates $GdCrO_3$ and $SmCrO_3$ exhibit NM under unique field cooling conditions, one under FCC and another ZFC which are quite rare in the literature of perovskite systems. Gd^{3+} hold high magnetic moment of 7.94 μ_B at room temperature and hence attain higher saturation magnetization. The proper reason of the origination of the peculiar characteristics of the NM spanning a region of ~110 K and almost 35 times higher in negative magnitude than that of the positive value makes the compound interesting. The compound possesses two stable isotopes Gd^{155} and $Gd^{157}$with energy band gap of 0.0281 eV and 0.0312 eV respectively. Apart from this $GdCrO_3$ is considered as one of the potential candidate of the key ingredient of magnetic refrigeration having entropy ($-\Delta S_m$ ~ 36.9 J kg^{-1} K^{-1}) and RCP

of the order of 542 J kg^{-1} which is higher than other Gd-compounds of $GdAlO_3$ of 209 J kg^{-1} or $Gd(HCOO)_3$ of 503 J kg^{-1} [67]. Along with $GdCrO_3$, $SmCrO_3$ also go under several magnetic phase transitions with respect to temperature. The $-\Delta S_m \sim -24$ J kg^{-1} K^{-1} and 11×10^{-2} J kg^{-1} K^{-1} at temperature 191 K and 32 K makes the system interesting due to their polarity change with respect to temperature. The most fascinating characteristic that $SmCrO_3$ holds is the metastable magnetic glass like feature within a feasible range of temperature. The path dependent magnetization is proved to be sensitive for $SmCrO_3$ as the system doesn't exhibit Nm under higher external field. The polycrystalline shows both ZFC-EB and FC-EB and training cycle effect making us biased towards the investigation of the sample [68].

1.10 Gaps in the literature:

A systematic study related to the $La_{0.7}Sr_{0.3}MnO_3/LaNiO_3$ superlattice and $La_{0.7}Sr_{0.3}MnO_3/LaCoO_3$ bilayer structure deposited on $SrTiO_3$ is not initiated in the literature till now. In particular, a detailed study related to both orientation and thickness dependence of magnetization and electronic properties are still scarce in the literature. Therefore, we choose these systems for the current PhD research plan. Nevertheless, a detailed study Raman spectroscopy, Interface-morphology, electronic transport studies still lacking in the literature. Elaborated studies are very important to understand the nature of magnetic interactions in this class of compounds.

On the other hand, a detailed research on Dy doped $CeCrO_3$ (i.e. $Dy_{1-x}Ce_xCrO_3$ (DCCO)) with variable dopant concentrations is a new idea and not implemented in the literature till now. This combination fills the gap in the literature. A detailed spectroscopic and morphological study linking with the magnetic and electrical transport properties are very much needed to understand the magnetic ground state of this system. Since $CeCrO_3$ exhibits prominent negative magnetization characteristics which play a key role in the magneto electronic device applications, it is worth to initiate this study. Moreover, $DyCrO_3$ can be very high in demand due to its efficient application in magnetic refrigeration technology. Other than this $CeCrO_3$ can be doped with other rare-earth materials to have a balanced survey on the entire family. Doping with various elements can be used for comparative studies. Along with this, another idea that can be readily implemented in this study is the substitution of other rare-earth elements at the Ce site in CCO to probe the anomalous changes occurring across the morphotropic phase boundary. Hence, being a new compound the DCCO is expected to be surveyed throughout the course of this study with appropriate doping the concentration. Along with this, a thorough investigation of the newly prepared combination of $GdCrO_3$ and $SmCrO_3$ with variable doping concentration (GSO) is missing in the literature. An elaborated structural and electronic analysis is required to fill the gaps in the literature for this particular system. A comprehensive study for temperature, field and time dependent dc-magnetization can be helpful as well. Due to the observation of NM for both of the compounds, it can be very interesting to examine the mixed composition.

1.11 Layout of the thesis:

We have planned to study the coherently grown [$La_{0.7}Sr_{0.3}MnO_3/LaCoO_3$] bilayer system on (001) $SrTiO_3$ single crystal substrate by varying the thickness of LCO and exchanging the sequence of deposition

on the substrate. We analysed the local atomic features with the help of x-ray photoelectron spectroscopy measurements and the magnetic spin environments with respect to temperature and field for different bilayers and the dominating characteristic for each one connecting to the nearest-neighbour effective exchange constant (J_{eff}) for both the systems of thickness variant bilayers and the corresponding effective number of spins available/unit volume (N_A) (chapter 3). The systemic study on Pulsed Laser Deposited $[La_{0.7}Sr_{0.3}MnO_3/LaNiO_3]_{10}$ superlattices on three different orientations of (001), (011) and (111) $SrTiO_3$ has been done. With the help of electrical resistivity characterization, we explored the thermal dependence of the electrical resistivity authenticating the 3D and 2D Variable Range Hopping models and the corresponding hopping energy and density of states. In order to connect the electronic properties with the magnetic spin dynamics, *dc*-magnetization (T, H) experiments has been executed to know further about the anisotropy field and anisotropy constants of the superlattice system along with the Raman mode analysis to conclude the direction-oriented biasness of the superlattices (chapter 4). The single phase $Dy_{1-x}Ce_xCrO_3$ with x = 0.1–0.5 with the help of solid-state reaction has been prepared and have been in detailed invigilated by the means of crystal structure, electronic properties and Raman mode analysis. The multiple magnetic phase changes and the overall ascendency of phases with respect to temperature and the doping percentage or average cationic radius value. The effect of Ce substitution at the Dy site on the structural distortion combine with the Raman shift and order-disorder and spin reorientation have been discussed (chapter 5). We prepared $Gd_{1-x}Sm_xCrO_3$ polycrystalline with x = 0.1, 0.5 and 0.9 with the special investigation on x = 0.5 doping aiming the unusual magnetic features depending on temperature and time. The magnetization reversal is given importance and the high temperature antiferromagnetic ordering is focused. The temperature dependent Raman mode shifts of the chosen composition can bring the anomaly between the magnetic and structural co-dependency along with the expectation of multiple T_{Comp} making the sample appropriate for magnetic memory-based devices (chapter 6).

Chapter 2
Experimental Methodology

In this chapter we will illustrate the experimental methodology adopted for the preparation and characterization of different perovskite compounds used in this thesis work. As our analysis mainly revolve around the structural, magnetic, electrical and optical properties of these rare earth thin film and polycrystalline perovskites we provide a very brief discussion on some of the related state-of-the art tools and techniques being used in the field. We begin our discussions with some of the key techniques, such as, solid state reaction method for polycrystalline and Pulsed Laser Deposition method for thin-film preparation which is followed by the brief outline of tools and techniques for the structural, magnetic, electronic, optical properties of the samples.

2.1 Synthesis methods:

2.1.1 Pulsed Laser Deposition:

We prepare the thin-film heterostructure Perovskites using one of the conventional techniques popularly known as Pulsed Laser Deposition (PLD). The procedure of preparing a superlattice or bilayer begins with the deposition of thin film on the single crystal substrate with the help of a high-power laser beam precisely focused on the target by gradual process of interaction as shown in Fig. 2.1. The different stages of the procedure in general have following steps (see Fig. 2.2(a) – (c)):

- First target is exposed with high intensity power laser beams for short period of time.
- The target reaches its melting point followed by the vaporization with the gradual heating with the laser beam.
- The vapour starts getting transformed in the form of plasma due to the photon–electron ionization blending.
- The plasma starts to inflate slowly reaching far from the target.
- The hot grown plasma drops down on the substrate in the form of thin film.

The first step of the procedure depends highly on the material chosen for deposition as the vibrational states of the material coming from the free electrons that decides the interaction with photon energy. For metals the free electron mediated absorption of the photon energy is given away to the lattice atoms following the thermal diffusivity as $\sqrt{Ds}$ where D stands for the diffusivity constant and s is the time of laser exposure on the target. The typical approximate time for the heat energy goes from targeted region to the lattice atoms is ~ 10^{-12} seconds. The plasma frequency following the expression of $\omega_F = \sqrt{\frac{Ne^2}{m\varepsilon_0}}$ plays a major role (N, m and ε_0 being the density, mass and free space permittivity of electron) as the irradiated laser with

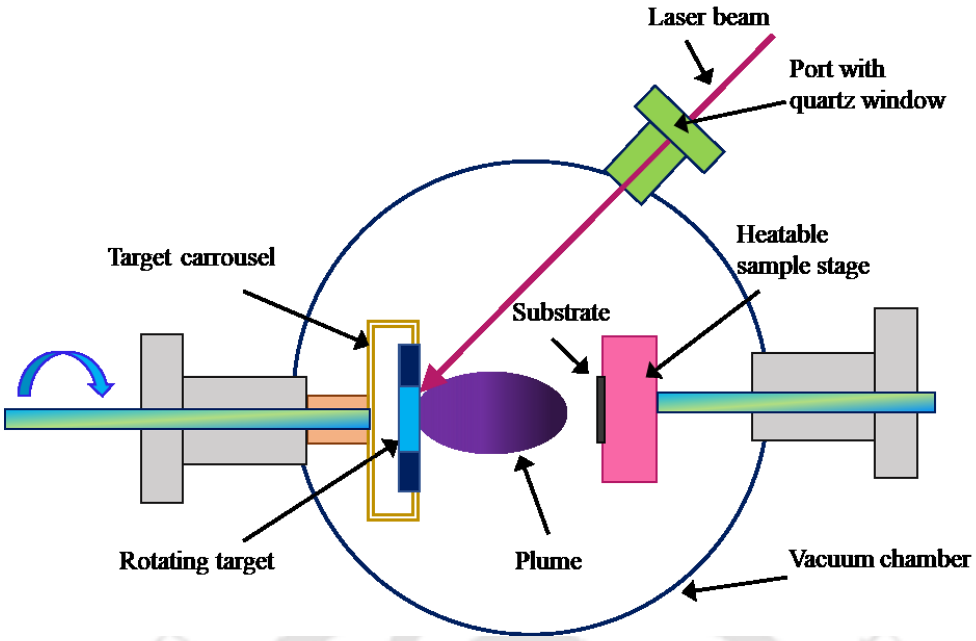

Fig. 2.1. The schematic diagram of a Pulsed Laser Deposition instrument.

frequency $\omega > \omega_F$ are only capable to penetrate the plasma. The next stage is about the increased temperature due to the frequent enhancement in the lattice vibration for the consumption of the heat energy. In order to change the physical phase of the target, the critical power is happened to be ~ 10^8 W/cm^2 below which the target gets heated without changing its phase. The vaporization of the target comes next which depends on the thermal conductivity and the flux density which are in proportion with each other for the vaporization of the target apart from heat capacity of the material which follows the 1D equation of heat flow:

$$t_F = \frac{\pi \rho k C_p \Delta T}{4F^2} \tag{2.1}$$

with t_F = time required to reach the meting point, F = density of laser flux, C_p= heat capacity, ρ = density and k = thermal conductivity of the material. The plasma gets formed next where the ionization needs to takes place via electron impact ionization procedure where kinetic energy transferred after the collision with the electron and the particles of the vapour necessarily occurs to be greater than ionization potential. The time required (μs) for the plasma to grow is higher than the irradiation time (ns) of the laser. For the case of the plasma expansion in the vacuum, the case can be expected to be adiabatic whereas in the presence of gas, the system can behave in two different ways depending on the pressure. Under the pressure range < 1 Pa, the system is considered as vacuum and the plume expansion rate reduces significantly with the presence of shock wave arising from the particles under higher pressure in the experimental atmosphere. The deposition of the plume in the form of thin film can be formed like (a) stacks of monolayer on the substrate (Frank-van der Merwe growth) (b) scattered islands attaining multiple single layer thickness (Volmer-Weber growth) (c) both monolayer and islands together (Stranski-Krastinov growth) [69].

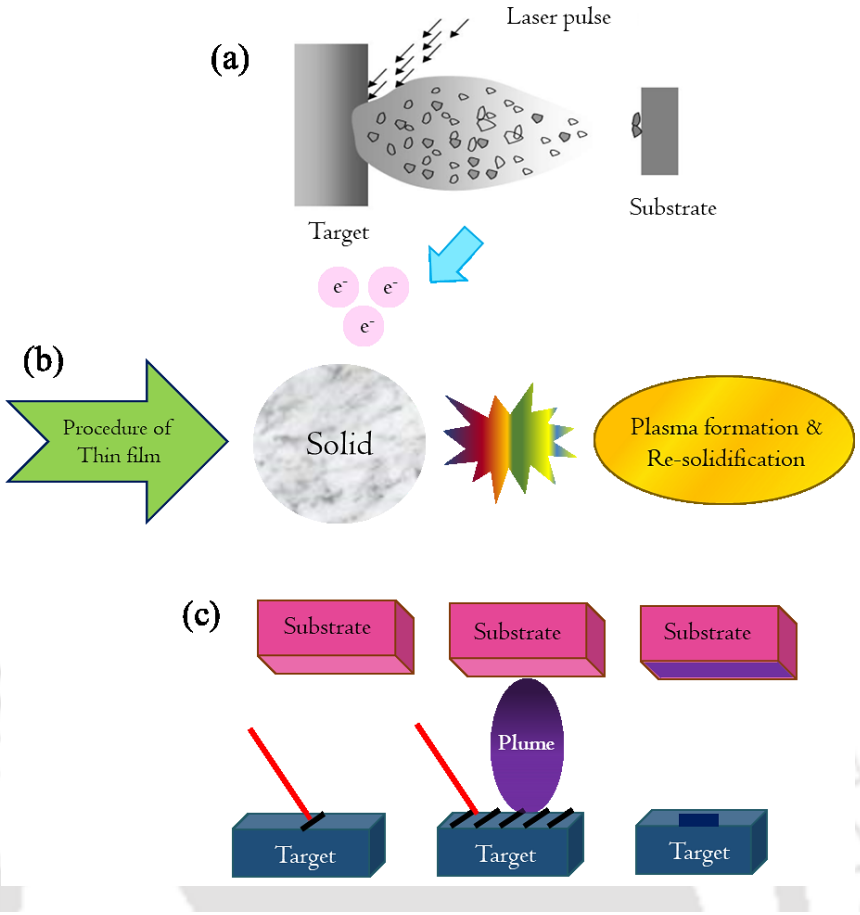

Fig. 2.2. The flow chart [(a)- (c)] of the step by step formation and deposition of thin film on the substrate.

Here, for our investigated systems the superlattices of [$La_{0.7}Sr_{0.3}MnO_3$ (LSMO)/$LaNiO_3$(LNO)] were prepared using a 248 nm wavelength KrF laser as the source of irradiation with 10 times of periodicity. The LSMO of thickness 4.2–4 nm being the first monolayer on the $SrTiO_3$ substrate of three different orientations: (001): SL-001, (011): SL-011 and (111): SL-111. After one layer of LSMO, single layer of LNO with thickness 3-2.6 nm is chosen to be deposited on the top of it. The energy fluence has been kept 2 J/cm^2 during the ablation process where the $SrTiO_3$ was maintained at 700° C. The plume was formed under the presence of oxygen with partial pressure 0.2 mbar followed by the post annealing procedure with oxygen of 400 mbar pressure.

For the bilayer systems, the same laser has been used for ablation process with energy fluence of 1.5 J/cm^2. Here, on the (001) oriented STO, single layer of $La_{0.7}Sr_{0.3}MnO_3$ of fixed thickness 5 nm is deposited which has been coated with $LaCoO_3$ (LCO) monolayer of thickness 15 nm and this combination is termed as BL1. The sequence of deposition of LSMO and LCO with the same thickness has been reversed and named as BL2. The chamber is kept at vacuum of pressure 10^{-6} mbar and STO temperature at 700°C. The top layer is deposited in the presence of oxygen of partial pressure 0.4 mbar. At the end of the deposition procedure, the samples are annealed in oxygen atmosphere of pressure 600 mbar for 30 min.

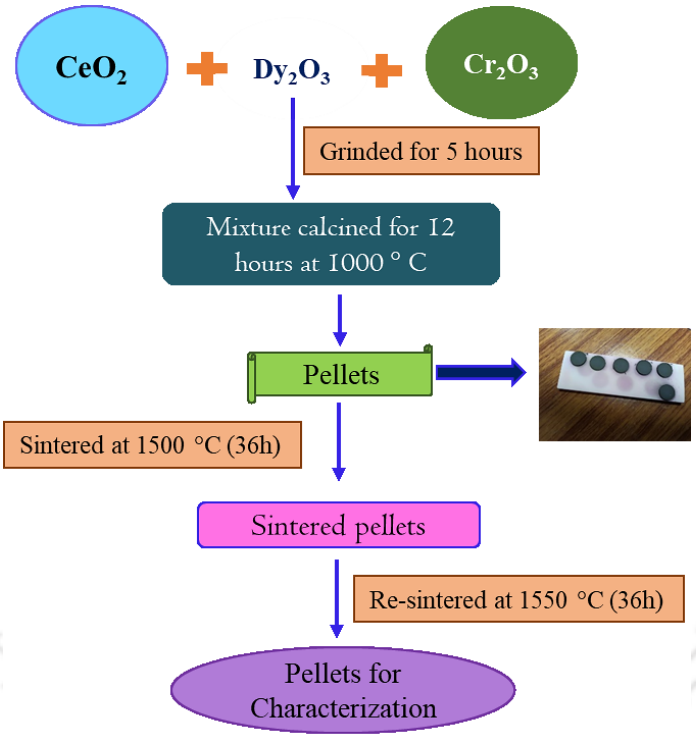

Fig. 2.3. The flow chart of the synthesis of polycrystalline sample with solid state reaction method and the freshly sintered pellets of $Dy_{1-x}Ce_xCrO_3$ are shown.

2.1.2 Polycrystalline method:

The polycrystalline samples are those which consists of small grain size crystals with the randomly oriented crystallographic axis. In the bulk work we have prepared the polycrystalline samples by the standard high temperature solid-state reaction method. This method is low cost and easily synthesized part from being thermodynamically stable. Here, the grains diffuse through the boundaries under high temperature in the span of time varying from few days to weeks to grow out the boundary regions. We synthesised $Dy_{1-x}Ce_xCrO_3$ (x = 0.1- 0.5) (DCCO) and $Gd_{1-x}Sm_xCrO_3$ (x = 0.1, 0.5, 0.9) (GSO) following the solid-state reaction method. We have demonstrated the flow chart for $Dy_{1-x}Ce_xCrO_3$ solid solution in Fig. 2.3. We have taken the stoichiometric amounts of the $DyCrO_3$, CeO_2, Cr_2O_3, Gd_2O_3 and Sm_2O_3 as precursors with 99.9 % purity from Alfa-Aesar GmbH. We have mechanically ground the raw chemical ingredients for 5 hours with the help of agate mortar to make the mixture homogeneous. We have kept the mixed sample in oven with 100°C in the means time of the mixing multiple times to ensure the phase purity and avoid the materials become deliquesced. After the grinding was completed we have kept the mixture into alumina crucibles and calcination was done using a muffle furnace at 1273 K for 12 hours for both the compositions for 12 hours in air followed by a regrinding of 2 hours again. The calcined powders were pressed with 60 kN/m^2 pressure using a hydraulic press in order to make 13 mm cylindrical shaped pellets. The pellets were next sintered at 1823 K for DCCO system and at 1473 K for GSO system for 36 hours in air to achieve high density and cooled by natural cooling of rate 2.8°/ min to room temperature. At the end of the sintering dark and light green samples were collected for the respective sample composition which were further tested for phase purity and other physical properties.

2.2 Characterization Details:

Here, we will discuss about the precise descriptions of the various characterization techniques used in our work. Starting with structural characterization, we will move towards the depiction of electronic, Raman and magnetization measurements.

2.2.1 Structural characterization:

After the investigated samples were prepared, we executed X-ray diffraction (XRD) technique to check the phase purity, atomic arrangement, unit cell dimensions and the crystal structure. The instrument used for the structural characterization of polycrystalline samples is shown in Fig. 2.4(a) This characterization is eligible to bring important information about many crystallographic parameters like strain, grain size and defects. X-rays coming from the source laser diffract from the plane or the interface of the investigated material. The Bragg's law defines a relation between the angle of incidence (θ), atomic plane spacing (d) and the wavelength of the incident laser (λ): $n\lambda = 2d \sin\theta$ [70] stated as, the constructive interference occurs between the incident rays falling on the uppermost plane and the consecutive lower plane of the material if the path covered by the ray is a finite integer (n) times wavelength and shown in Fig. 2.4(b) The incident ray and the diffracted ray being denoted as K and K' vector follow the relation:

$$G = \Delta K = K' - K \tag{2.2}$$

with G being the diffraction vector. As the polycrystalline compounds do not possess any specific direction between the crystallites and the G vector, the diffraction data is gathered considering the total atomic planes. For generalization, we consider here a bulk polycrystalline sample with triclinic structure with h, k, l being the Miller indices, V, a, b, c, α, β, γ as the volume and lattice parameters of the unit cell respectively following the equation:

Fig. 2.4. (a) The XRD instrument.

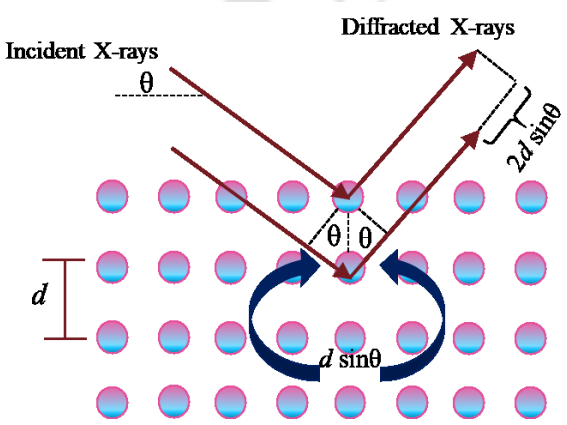

Fig. 2.4. (b) The schematic diagram presenting the X-ray diffraction from lattice planes to satisfy the Bragg's law.

$$\frac{1}{d^2} = \frac{t_{11}h^2 + 2t_{12}hk + t_{22}k^2 + 2t_{23}kl + t_{33}l^2 + 2t_{13}hl}{V^2} \quad (2.3)$$

with V = $\sqrt{(abc)^2(1 - cos^2\alpha - cos^2\beta - cos^2\gamma)}$ and $\sqrt{t_{11}} = bcsin\alpha$, $\sqrt{t_{22}} = acsin\beta$, $\sqrt{t_{33}} = absin\gamma$.

Apart from this, the destructive interference occurs for a cubic structure as an example when the rays diffracted from (001) and (002) planes in spite of following Braggs condition separately they fail to make constructive interference as they meet out of phase with each other making the resultant intensity zero. For single atoms, similar effect can be observed as a result of diffracted rays coming from several orbitals in the atom meeting out of phase [71]. In our work we used X-ray powder diffractometer from Rigaku model: TTRAX III at room temperature of 18 kW power source using $CuK_{\alpha 1}$ radiation (λ = 1.540 56 Å). Slow measurement scan of speed 2-degree min^{-1} within the Bragg angle range of 10º and 90º with step angle of ~ 0.02 for qualitative analysis. These XRD patterns were refined using Rietveld method with the help of FullProf suite in order to evaluate the corresponding crystallographic parameters for all the compositions.

2.2.2 Electronic characterization:

After checking the cell dimensions and the distortions occurred in the monophasic samples, we next performed the X-ray photoelectron spectroscope (XPS) at room temperature to ensure the electronic structure and oxidation sates of the materials present in the composition. The instrument used for this particular experiment is shown in Fig. 2.5(a). This technique is also known as the s Electron Spectroscopy for Chemical Analysis (ESCA) which is much useful for quantitative study on atomic compositions. The basic principle of XPS lies in the Nobel winning theories of Photoelectric effect by Albet Einstein and Photoemission by Kai Siegbahn. The sample irradiated with X-rays comprised of k-alpha radiation with energy hυ, ejects an electron of binding energy (B.E.) named as photoelectron with the kinetic energy (K. E.) and work function ϕ, following the relation [72];

$$K.E = h\upsilon - B.E. - \phi \quad (2.4)$$

Generally, the energy of the ejected electrons is measured by the detector and no emission happens if $h\upsilon < \phi$. Each element of a composition has different value for K. E for core level electrons providing chemical state information of the detected elements, such as distinguishing between sulphate and sulphide forms of the element sulphur. The XPS technique is able to measure (a) Surfaces (3 atomic layers) using XPS and angle resolved XPS (ARXPS) (b) Ultra-thin films (3-30 atomic layers) using XPS and angle resolved XPS and finally (c) Thin films (3-600 atomic layers) using XPS in combination with sputter etching for profiling. This can be used to measure (i) elemental composition of the surface (top 1–10 nm usually), (ii) empirical formula of pure materials, (iii) elements that contaminate a surface, (iv) chemical or electronic state of each element in the surface, (v) uniformity of elemental composition across the top surface (or line profiling or mapping) and (vi) uniformity of elemental composition as a function of ion beam etching (or depth profiling).

The XPS instrument consists of:

- Ultra-High Vacuum (UHV) system
- X-ray source
- Electron analyser
- Ion gun

The internal construction of standard XPS instrument is shown in Fig. 2.5(b). The UHV is required in order to achieve longer photoelectron path along with keeping the surface away from the contaminations to

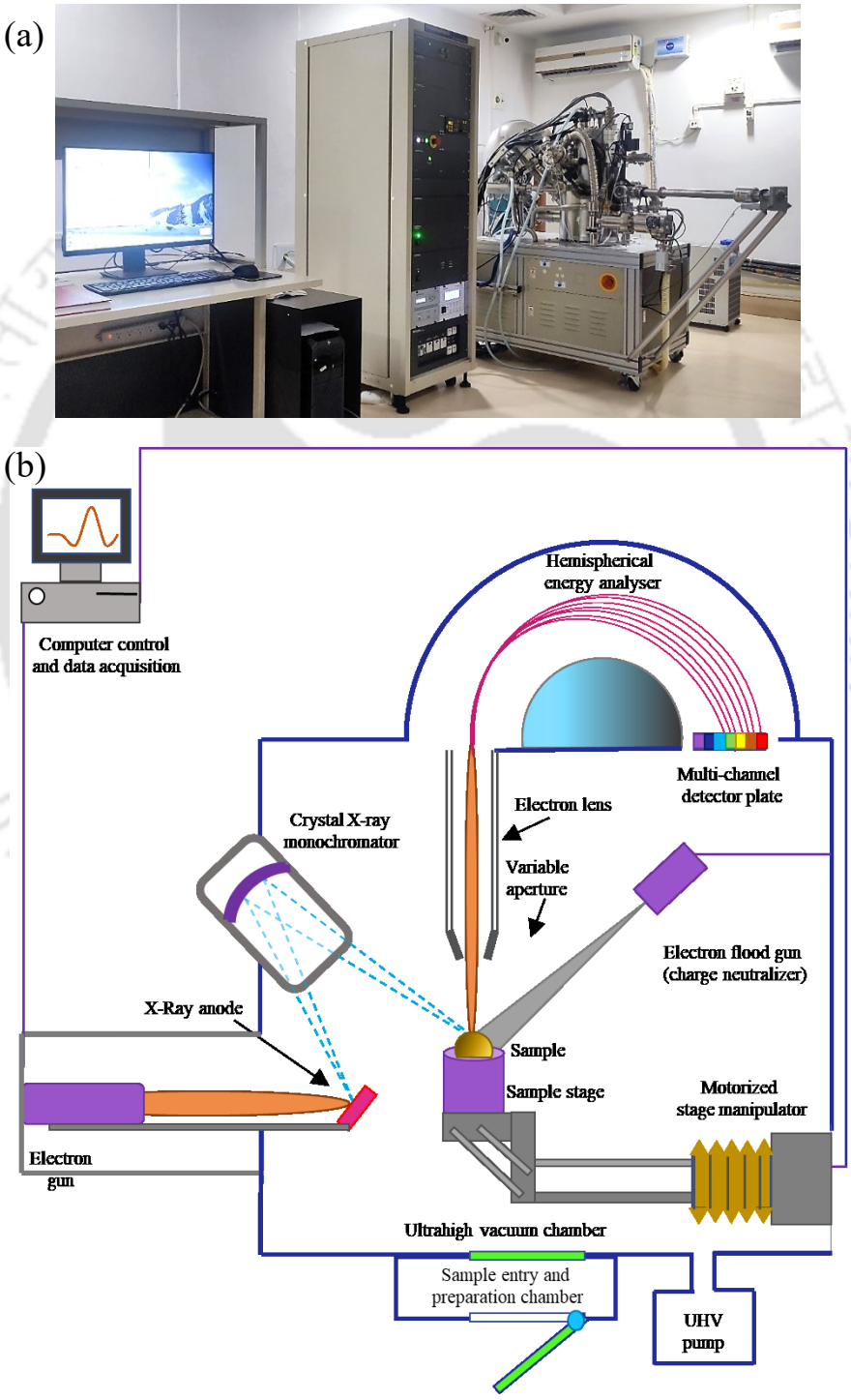

Fig. 2.5. (a) The XPS instrument. (b) The schematic diagram presenting the interior of X-ray photoelectron spectroscopy instrument.

generate X-ray signal. The pressure maintained is ~10^{-8} Torr with the help of roughing pump, turbo pump and Ion pump. Dual anodes are generally used as X-ray source for example Mg $_{K\alpha}$ of energy 1253.6 eV or Al $_{K\alpha}$ of energy 1486.6 eV along with monochromatic quartz crystal. Another important part is comprised of lens system to collect photoelectrons, Analyzer to filter electron energies and Detector to count electrons. Ion guns are used (widely used Ar^{+}) to clean the sample or in case of analysis related to depth profile (To remove surface contaminations or find elemental distribution throughout the film thickness). The separation between the two peaks are named spin orbital splitting. The values of spin orbital splitting of a core level of an element in different compounds are nearly the same and the peak area ratios of a core level of an element in different compounds are also nearly the same. When an atom makes a bond with another atom, the valence electron density changes resulting in an adjustment of the electrostatic potential affecting the core electrons. Change in the binding energies of the core electrons cause shifts in the corresponding photoelectron peaks. Here we have used the high resolution XPS from Kratos Analytical Ltd (model: AXIS Supra+) having Al $_{K\alpha}$/Ag $_{L\alpha}$(2984.2 eV) as lab source for Superlattice, bilayer and DCCO system and Scanning XPS microprobe of model: PHI 5000VVersaProbe III and Al Kα (544 eV) as lab source. The core-level X-ray photoelectron spectra was calibrated with C-1*s* binding energy 282.6 eV for GSO system. The spectra were fitted with the Lorentzian–Gaussian distribution after calibrating with C-1*s* binding energy 282.6 eV and subtracting the background by using Tougaard method.

2.2.3 Raman spectroscopy:

Apart from the structural and electronic analysis of the investigated systems, we performed Raman spectroscopy measurements in order to acquire the knowledge of the corresponding phonon modes as the XRD provides the information about the unit cell parameters and atomic level statistics. Named after C. V. Raman being invented in the year of 1928 [73], the analysis is very important for determination of metal-ligand bonds giving information about the composition, structure and stability of the complex compounds. The instrument used for Raman characterization can be identified in Fig. 2.6(a). The basic theory of spectroscopy lies in the light interacting with matter in different ways, transmitting through some materials, while reflecting or scattering off others. Raman spectroscopy is an analytical technique where scattered light is used to measure the vibrational energy modes of a sample. When light is scattered by molecule, the oscillating electromagnetic field of a photon induces a polarization of the molecular electron cloud leaving the molecule in a higher energy state with the energy of the photon transferred to the molecule. Now, this can be considered as the formation of a very short-lived complex between the photon and molecule which is commonly called the virtual state of the molecule which is not stable and the photon is re-emitted almost immediately, as scattered light. Two different conditions can arise in the scattering phenomenon: (a) Rayleigh Scattering (elastic): in the majority of scattering events, the energy of the molecule is unchanged after its interaction with the photon keeping the energy as well as the wavelength of the scattered photon equal to that of the incident photon, (b) Raman scattering (inelastic): in some of the rare cases the scattering occurs with the with a transfer of energy between the molecule and scattered photon with the possibility of

molecule gaining the energy from the photon and evolved in the next higher vibrational level with the scattered photon losing energy giving rise to its wavelength named as Stokes Raman scattering (see Fig. 2.6(b)). On the contrary, the other possibility lies for the molecule to lose energy by relaxing to a lower vibrational level of lesser energy, while the scattered photon gains the corresponding energy and its wavelength decreases named as Anti-Stokes Raman scattering. However, with an ensemble of molecules, the majority of molecules will be in the ground vibrational level (Boltzmann distribution) and Stokes scatter is the statistically more probable process making the Stokes Raman scattering more intense than the anti-Stokes scattering. Hence, almost always the measured spectra in the Raman spectroscopy are the Stokes lines. The Raman scatter position is therefore converted to a Raman shift away from excitation wavelength:

$$\Delta\bar{\upsilon} = \left(\frac{1}{\lambda_0} - \frac{1}{\lambda_1}\right) \tag{2.5}$$

where λ_0 and λ_1 are the consecutive wavelengths of the respective energy states. In the classical theory, we can refer to the Raman effect as the effect of polarization of the dipole moment. The electric field experienced by a molecule upon radiation of frequency υ is:

$$E = E_0 \sin 2\pi\upsilon t \tag{2.6}$$

which polarizes the molecule and makes it to oscillate with the same frequency generating the induced dipole moment indicating towards Rayleigh scattering:

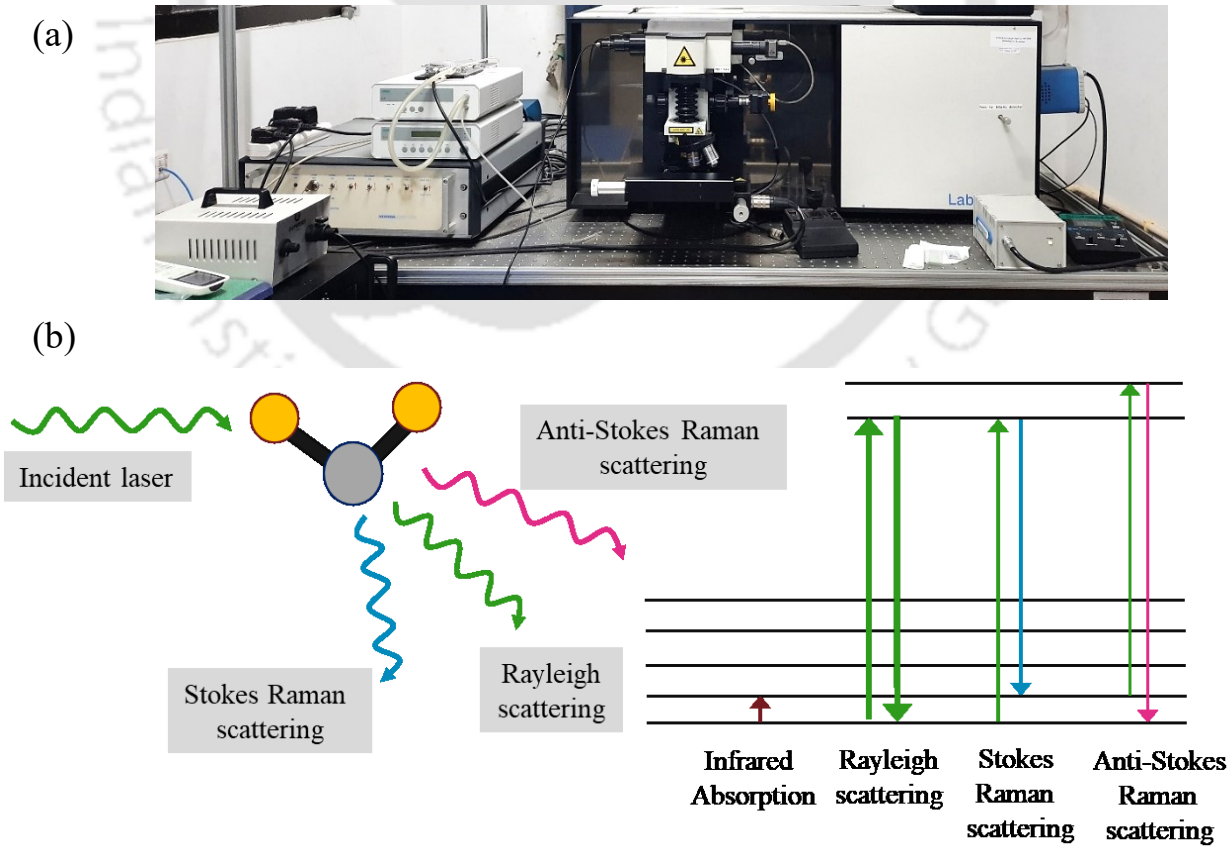

Fig. 2.6. (a) The Raman instrument. (b) The schematic diagram presenting the interior of X-ray photoelectron spectroscopy instrument.

$$\mu = \alpha\, E_0\, \sin 2\pi\, \upsilon t \tag{2.7}$$

Whereas, If the molecule undergoes rotation or vibration also (Raman Scattering), then the polarizability of it changes, hence the emitted frequencies also to υ_{vib}:

$$\alpha = \alpha_0 + \beta \sin 2\pi \upsilon_{vib}\, t \tag{2.8}$$

with α_0 being the equilibrium polarizability, β being the rate of change of polarizability with vibration. Hence, the induced dipole moment can be written as:

$$\mu = \alpha_0 E_0\, \sin 2\pi\, \upsilon t + \frac{1}{2}\, \beta\, E_0[cos2\pi\, (\upsilon - \upsilon_{vib})t - cos2\pi\, (\upsilon + \upsilon_{vib})t] \tag{2.9}$$

where the second term refers to the anti-stokes Raman line and the third term indicates the stokes Raman line.

The instrumentation for the Raman analytical measurement consists of:

1) Source: Generally, lasers as high intensity is required to produce Raman scattering of sufficient intensity to be measured with a reasonable signal-to-noise ratio. Argon, krypton, He-Ne ion sources that emit in the blue, green and red region is preferable as the intensity of the Raman spectrum varies with the fourth power of the frequency.
2) Sample illumination: All liquid, solid and gas samples are examined with the help of Raman spectroscopy though the liquid samples are the easiest to handle because of water is weak Raman scattered medium.
3) Raman Spectrometers: Mostly double grating spectrometers are used to minimize the spurious radiation reaching the transducer (photomultipliers are used as transducers).

Raman spectra were recorded to characterize the vibrational excitation using a HR Raman spectrometer (model: LabRam HR) from Horiba JobinYvon using monochromatic radiation discharged by 632.8 nm He-Ne laser (20mW laser power) operating under backscattering geometry at room temperature. Temperature dependent study was performed within the temperature range 80 K-300 K covering the Neel temperature (T_N) by attaching the THMS600 module to the stage [74].

2.2.4 Ferromagnetic resonance measurement:

In order to probe the magnetization dynamics and the corresponding anisotropy for the bilayer system, we measured the ferromagnetic resonance (FMR) for the both systems. Since the discovery of FMR by V. K. Arkad'yev while observing the absorption of ultra-high frequency radiation by FM materials in 1911, it has been widely used as a standard tool for probing spin waves and spin dynamics which was later modified by Ya. G. Dorfman in 1923 by the means of optical transitions due to Zeeman splitting. FMR arises from the precessional motion of a FM material in an external magnetic field. The magnetic field puts a torque on the magnetization which causes the magnetic moment to precess. The precession frequency depends on the orientation of the material and the strength of the magnetic field. The standard FMR instrument has been shown in Fig. 2.7.

Assuming the FM substance containing only one ellipsoidal domain to determine the magnetic resonance of frequency ω under the application of *dc*-field applied along the *z*-axis is:

$$\hbar\omega = g\mu_B\sqrt{[(H + D_x - D_z)M][(H + N_y - D_z)M]} \tag{2.10}$$

where D_x, D_y and D_z are the demagnetization factors in the x, y, z directions respectively, g refers to the spectroscopic splitting factor (Lande factor) and $\mu_B = e\hbar/2m_e$ defines the Bohr magneton. Considering S to be the total spin of the FM polarized under a *dc*-magnetic field and the energy sates are distributed according to the Zeeman frequencies following the magnetic selection rule: $\Delta m_S = \pm 1$, the investigated FM substance experience very high amplitude transverse susceptibility components χ' and χ'' as magnetization observed in case of FM domains with the application of external magnetic field is much higher than that of electronic paramagnetic samples. Another interesting feature to observe for the FM is the decreased dipolar contribution to the line width as a result of the strong exchange interaction among the FM spins making the FM resonance lines very sharp in turn. The related important parameters for FMR study are:

Resonance Field: The resonance field is the field value at which the maximum of absorption occurs for some excitation frequency. The internal field depends on the shape of the sample and on the atomic interaction between nearest neighbours. The motion of the magnetization around its equilibrium position is described by the Landau-Lifshitz-Gilbert equation of motion:

$$\frac{dM}{dt} = -\gamma(M \times H_{eff}) - \frac{\lambda}{M^2}(M \times M \times H_{eff}) \tag{2.11}$$

Fig. 2.7. The FMR instrument.

with M is the magnetization and H_{eff} is the effective field that includes the *dc* external field, H_{eff} = -$\nabla_M E$ and finally λ is a relaxation frequency related to the viscous damping of the magnetization due to the interaction between magnetic moments.

Linewidth: The linewidth of the absorption spectrum is related to the relaxation times of the magnetization. The contributions to the linewidth are conduction mechanism and fundamental relaxation, surface-interface effect, magnetic impurities *etc.* altering the magnetic anisotropy and the locally dispersing the anisotropy axes. The FMR linewidth can be written as:

$$\Delta H = \Delta H_1 + \Delta H_2 \tag{2.12}$$

The first term here refers to the inhomogeneous line-broadening due to the presence of defects and inhomogeneities whereas the second term depicts homogeneous line-broadening due to the intrinsic conduction mechanisms [70]. In our work we have implemented the FMR experimental procedure at various frequencies ranging from 5 GHz to 20 GHz at 300 K for both the bilayer systems.

2.2.5 Magnetic characterization:

We executed the *dc*-magnetization measurements of all the systems in order to investigate the magnetic phases, transitions and other magnetic parameters of corresponding compositions and are elaborated in this section. We have used both superconducting-quantum-interference-device (SQUID) as shown in the Fig. 2.8(a) based magnetometer from Quantum-Design and physical property measurement system (PPMS) as depicted in Fig. 2.9(a) with vibrating-sample-magnetometer (VSM) from Quantum-Design extensively in the dissertation [75].

SQUID magnetometer is more sensitive in order to detect low magnetic moments with very high resolution (> 10^{-7} emu) and very small magnetic field using the Josephson junctions. Now what follows we discuss about the DC Josephson effect. There is an electrical direct current flowing through a Josephson contact even in the absence of an external voltage. This current is given by $I = I_0 \sin\delta = I_0 \sin(\theta_2 - \theta_1)$, where δ is the phase difference of the Cooper pairs in the superconducting material wave functions on both sides of the Josephson contact and I_0 is the maximum supercurrent. The concept is portrayed in Fig. 2.8(b). However, the AC Josephson effect could be realized by applying a direct voltage $V > V_C$ (c = critical voltage) on the Josephson contact an oscillating current flow is generated with the frequency $\omega = 2eV/\hbar$ [76]. SQUID consists of two Josephson junctions connected in parallel on a closed superconducting loop. The superconducting rings carry a basic feature of enclosing flux in multiples of a universal constant called the flux quantum ϕ_0. This is a very important quantum condition which plays a crucial role in understanding the functionality of SQUID. In other words, an external magnetic field can penetrate a superconductive loop if the magnetic field is an integer multiple of the magnetic flux quantum ϕ_0:

$$\phi_0 = \frac{h}{2e} = 2 \times 10^{-15}\, Wb \tag{2.13}$$

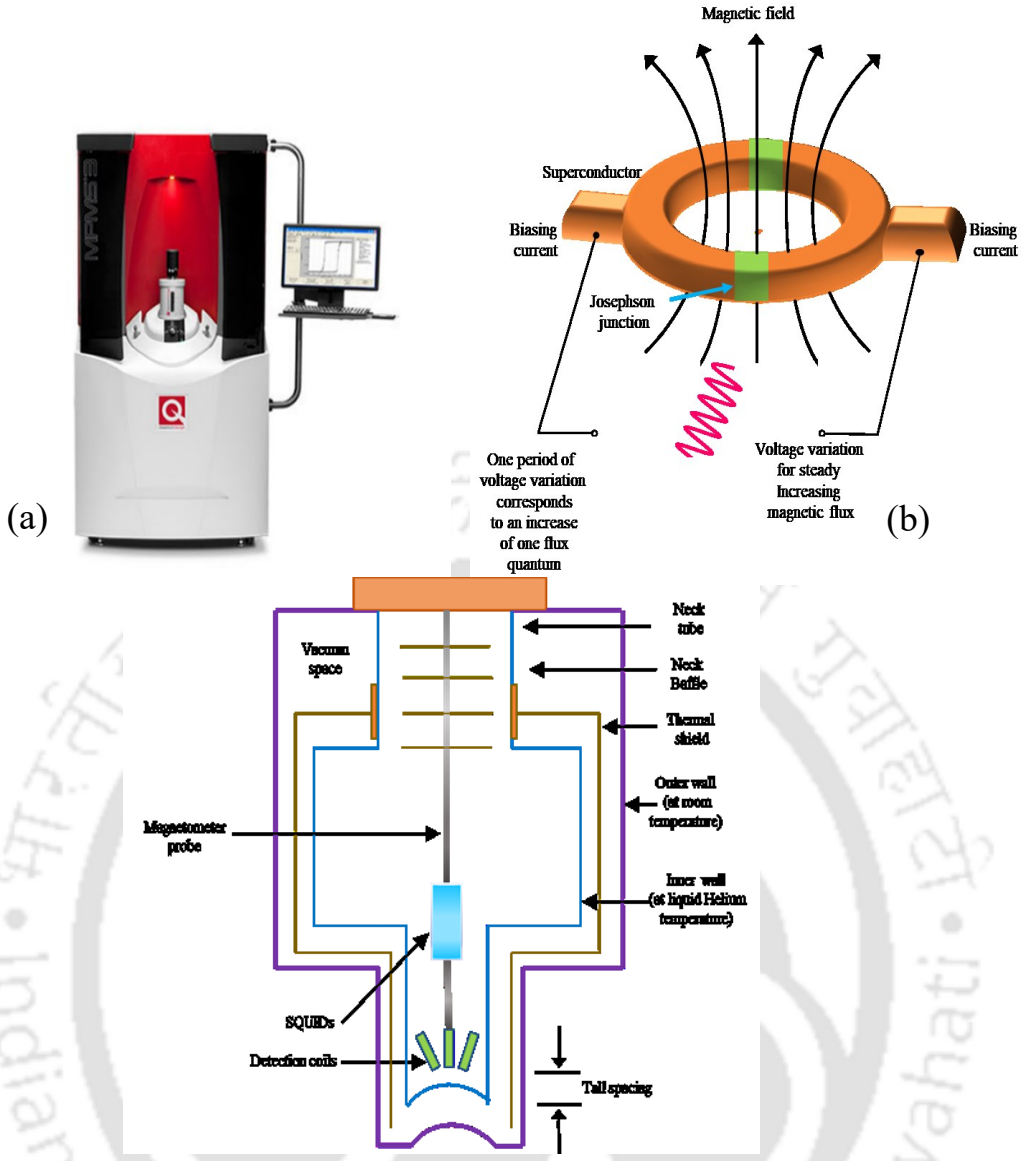

Fig. 2.8. (a) The SQUID instrument. (b) The pictorial form of a superconducting ring consisting with two Josephson junctions inside the SQUID magnetometer. (c) The schematic flow chart of a SQUID interior.

Because the flux quantum is the smallest quantity of the magnetic flux, this physical effect can be exploited to produce an extraordinarily sensitive magnetic detector known as SQUID. If we consider that a constant current, known as a bias current, is passed through a SQUID, the SQUID being symmetrical and the junctions identical, the bias current will split equally, half on each side. A *dc* SQUID is generally represented schematically as shown in Fig. 2.8(c) where a supercurrent flows through the SQUID, as long as the total current flowing through it does not exceed the critical current of the Josephson junctions, possessing a lower critical current than the rest of the superconducting ring. The critical current is the maximum zero– resistance current which the SQUID can carry, or the current at which a voltage across it develops. When the two junctions in the SQUID are identical, the loop is symmetrical, and the applied field is zero giving rise to the same voltage in the both junctions simultaneously. Hence, the critical current of the SQUID is simply twice the critical current of one of its junctions.

Coming to the working procedure of the SQUID, we assume the SQUID biased with a current well below its critical current. Then, if we apply a tiny magnetic field to the SQUID, the magnetic field wants to change the superconducting wave function. Therefore, the superconducting loop opposes the applied magnetic field by generating a screening current I_S, flowing around the loop. The screening current creates a magnetic field equal but opposite to the applied field, effectively cancelling out the net flux in the ring. The applied magnetic field has lowered the critical current of the SQUID. The reason behind this is the screening current superimposing itself on top of the bias current so that the critical current of the top junction decreases with the quantity of I_S and the critical current of the bottom junction has to decrease also with I_S, in order that the bottom junction to be in the superconductive state. As a consequence, bias current (I_{bias}) decreases with double magnitude ($2 \times I_S$) [77,78].

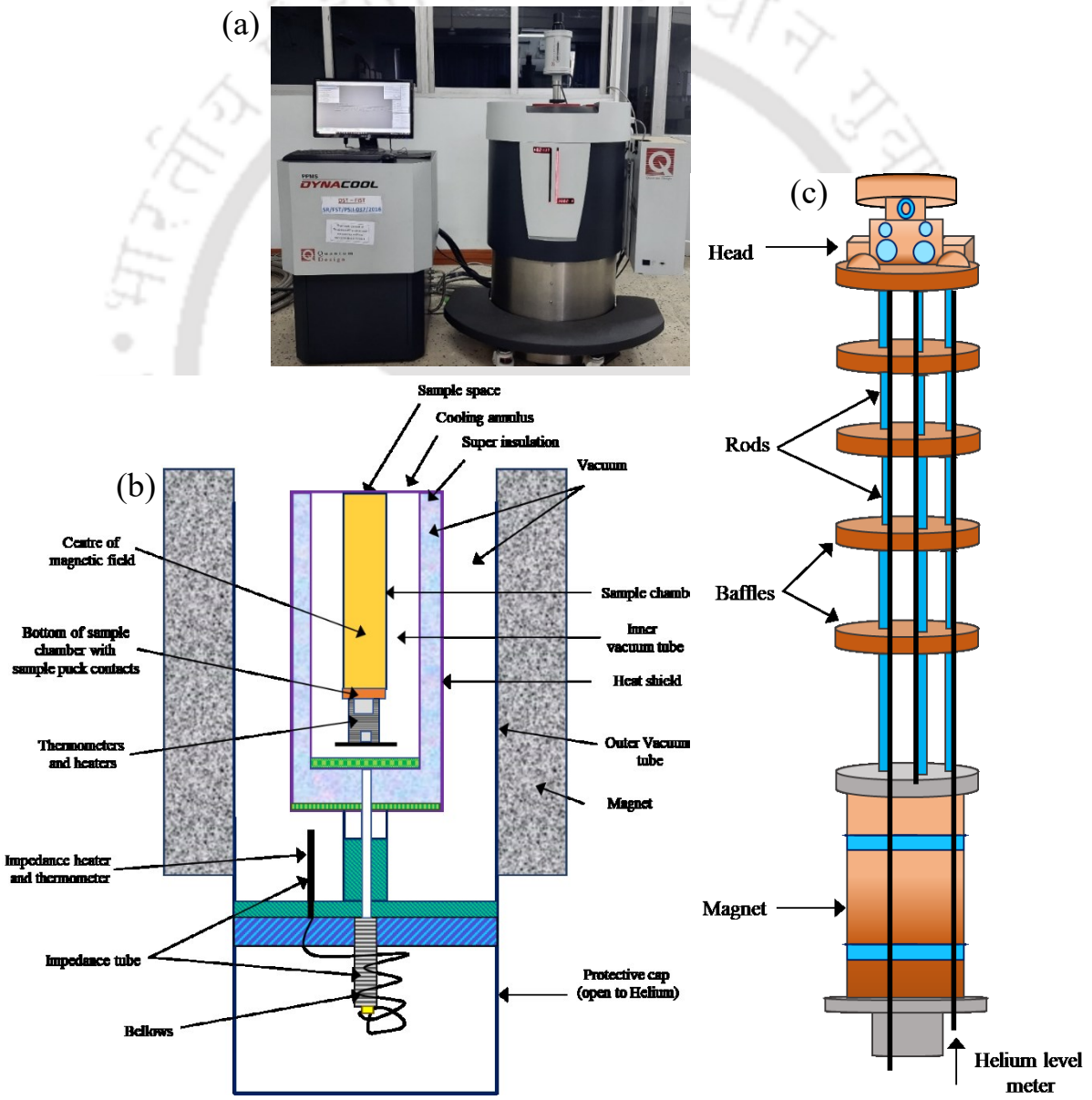

Fig. 2.9. (a) The PPMS instrument. (b) The schematic flow chart of PPMS interior. (c) The schematic diagram of the interior of the Probe inside PPMS.

PPMS consists of a chamber maintaining temperature of the range of 1.9 K to 400 K with the help of liquid He in Dewar and magnetic field varying between +90 kOe to -90kOe and superconducting magnetic coils to keep the temperature low in the required region. The internal construction of the PPMS instrument is demonstrated with the help of Fig. 2.9(b) and Fig. 2.9(c). Temperatures below 4 K are possible by arrangement compress the boiled-out liquid He out of Dewar capturing it in the vicinity of the he kept inside a closed loop system which aims to reduce the waste of He in the process of purging and the leakage via seals. Hence, a stream of ultra-high pure He in gas form is complemented to it keeping the He level upheld. High power supply helps the magnetic coils to keep in the superconducting region by controlling the magnetic field which consists of one superconducting component which has to be kept below the transition temperature along with the superconducting coils. The charging and discharging of the magnet are regulated by heating the superconducting element above the transition temperature termed as persistent switch and the cooling process is followed by current from the power supply targeted to the coil. The current applied to the coil is the measuring parameter of the magnetic field as magnetic field sensors are not used in this particular system. The magnetic flux pinning sites of the of the type-II superconducting coil moves in the process of charging and discharging of the magnet and even slide to the centre of the coil. The shifting of the flux sites conventional refrigeration cycle on the liquid He at the cold head of the cryostat. The Evercool rotational is negligible for the case of high magnetic field but very significant for the zero field hence a particular method of the discharging is followed to achieve the precise zero magnetic field value. This method includes the magnetic field attaining 2 T followed by the damped oscillation of 8 cycles reaching zero magnetic field which in turn eradicates the left out remanent magnetization of the coil during discharging. The Vibrating sample magnetometer (VSM) attached to the system for *dc*-magnetization measurements. Inside the PPMS sample chamber, one pick-up coil is mounted where the sample is then suspended from a linear motor into the coil. The sample is easily vibrated with the help of this motor by two independent, counter-wound pick-up coils in and out of the coil. As a result of Faraday induction phenomenon, the magnetization of the vibrated sample induces a current in the coil which is measured along with the speed of the oscillation of the sample to evaluate the corresponding magnetization. The signal is detected and measured with the help of a lock-in amplifier. Partial vacuum of ~ 40 Torr is of gaseous He in the sample chamber mediates the thermal contact between the suspended sample and the chamber. A postponement of the measurement by few minutes is maintained to confirm the thermal conduction to begin and the sample to reach the temperature of the chamber. For pellets: we have used the tiny solid pellet of weight between 5 mg to 60 mg wrapped in a insulating Teflon paper carefully and placed inside the plastic capsule and that is placed in the mid position of sample holder rod in PPMS chamber. For thin films: we have coated the thin-films in insulating Teflon after multiple times of cleaning in ethanol using a 230 V ac 50 Hz ultrasonicator. Then the film is placed in-place orientation for the measurement.

Using this VSM setup in the PPMS from Quantum Design (Model: Dynacool), we measured the temperature dependence, field dependence and time dependence of the magnetization of the associated systems. Throughout the works, we have used the M-H and M-T measurement sequences under ZFCW

(ZFC), FCW (FC) and FCC conditions. For hysteresis loops, we have measured the five-cycle magnetization of 0 kOe → +90 kOe → 0 kOe → -90 kOe → + 90 kOe at fixed temperatures with "no overshoot" protocol. The ZFC and FC measurements of the M-T case, the magnetization was recorded by cooling the sample from room temperature with or without the presence of external field to the lowest 1.9 K under "settle" mode or "sweep" mode (without giving time to the sample to stable in the particular temperature) and measuring while heating back or cooling accordingly. We have used the PPMS system for DCCO and GSO work completely and part of the superlattice work whereas the complete bilayer work has been investigated with the help of VSM and partially PPMS.

Specific heat: We have executed the measurements of specific heat (C_p) for some chosen compounds using PPMS with heat capacity accessory. We know, heat capacity is defined by dQ/dT where Q is the heat required to affect a change in temperature. A precise amount of heat is provided to the sample at fixed power and fixed time in each individual measurement cycle followed by a cooling time period of equal time. Figure 2.10 describes the schematic of thermal connections to the sample and the platform in PPMS.

A heater and a thermometer are attached at the bottom of the sample stage. The sample is attached on the stage by thin layer of Apiezon N Grease which helps to make thermal contact between sample and the sample-platform. Highly sensitive wiring system is connected with the heater and thermometer to provide electrical and thermal connections. Usually, the additional measurements are performed before the C_p (T) measurement of the sample, which consists of measuring the C_p of the sample holder. In the additional run, a thin layer of Apiezon N Grease is placed on the sample stage and the measurement is taken. After the completion of additional run, the sample is carefully attached with the grease without disturbing it. The measurement is performed once more and the correct value of the C_p of the sample is determined by subtracting the C_p of the sample holder from the total magnitude.

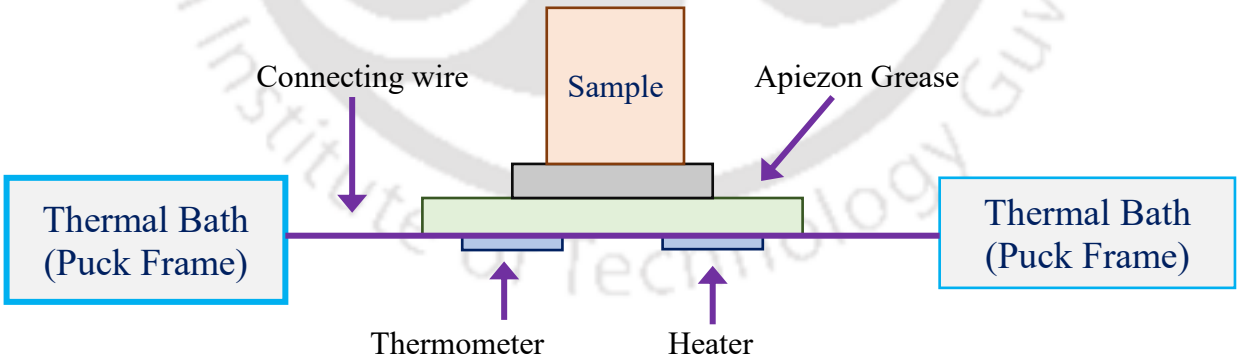

Fig. 2.10. The schematic of C_p measurement instrumentation and connections.

Chapter 3
Electronic and magnetic structure of $La_{0.7}Sr_{0.3}MnO_3/LaCoO_3$

This chapter deals with electronic and magnetic structure of ferromagnetic bilayers $La_{0.7}Sr_{0.3}MnO_3$ (LSMO)/$LaCoO_3$ (LCO) grown by the pulsed laser deposition technique. Here we focus our study mainly on the role of epitaxial strain on the structural, electronic, optical and magnetic properties of LSMO/LCO bilayers. Realizing atomically flat interfaces between the ultrathin perovskite oxides is a challenging task, which usually possess different chemical environments. In this chapter we provide a systematic analysis of on the basis of the terminating lattice planes and tuning the interfaces across the proposed heterostructures. Emphasizing on these aspects, here we employ a novel strategy of engineering the interfaces through the layer stacking sequence and degree of strain to probe the changes occurring in the local atomic environment at the interfaces, magnetic behaviour, and electronic properties. First, we provide a brief introduction of the system and outline the experimental techniques in the similar line as discussed in the last chapter. Following this we present a detailed description of the results pertaining to the electronic and magnetic properties of LSMO/LCO bilayers followed by the brief summary of important findings.

3.1 Introduction:

In this chapter, we consider the bilayer (BL) heterostructures of FM lanthanum manganite (LSMO) and lanthanum cobaltate (LCO) where their functionalities are tuned by interchanging the stacking layers. Here, both the ferromagnetic constituents (LSMO and LCO) exhibit perovskite crystal structures, and they obey the typical requirements of epitaxial growth of 2D heterostructures [79–83]. In addition, the need for 2D ferromagnetic layers with 100% spin polarization of carriers (half-metallic) is very much needed to develop sophisticated spintronic devices involving the magnetic junctions in which one can manipulate the functionalities using both the charge and spin of the layers [84–94]. Our main motivation in choosing the LSMO layer is that it exhibits tunable metal-to-insulator phase transition due to the band filling, large negative magnetoresistance (MR) across the Curie temperature (T_C), and induced planar uniaxial anisotropy with a moderate anisotropy field (≈100–500 Oe) grown on the variety of substrates at room temperature [89, 95–106]. Multilayers of manganites and cobaltites exhibit recorded magnitudes of MR in which the stacking order of layers plays a major role in the spin polarization of the electrons [86,107,108]. On the other hand, depending on the ambient pressure, substrate induced strain, and heat-treatment conditions during the synthesis stage, LCO exhibits unusual electronic and magnetic properties. Otherwise, LCO is a non-magnetic semiconductor with a low-spin $Co^{3+}(d^6)$ ground state configuration $t_{2g}^6 e_g^0$ [109]. Nevertheless, LCO gained significant scientific attention in the recent past due to its FM characteristics with $T_C \approx 85$ K [109]. Such FM behaviour arises because of the strain driven suppression of the Jahn–Teller distortion with the altered ground state spin configuration ($t_{2g}^5 e_g^1$, S = 1 and $t_{2g}^4 e_g^2$, S = 2) of trivalent Co between different ranges of temperatures [95]. Density-functional theory (DFT) studies by Kushima *et al.* reported that the lattice strain

influences the oxygen-vacancy formation and oxygen adsorption, which, in turn, mediates the magneto-elastic and elastoplastic effects in LCO [110]. These authors proposed that the elastic stretching of the Co–O bond alters the band structure and local relaxations in high strain states create stronger Co–O bonds, trapping the lattice oxygen, which, in turn, plays a major role in the spin configuration from S = 0 to either S = 1 or 2 [110]. In addition, the orientations [(100), (110), and (111)] of the single crystal substrates, such as $LaAlO_3$ (LAO) and $SrTiO_3$ (STO), significantly influence the strain directions of the CoO_6 octahedron and mean bond length of Co–O in LCO [111]. This overall process changes the crystal field splitting and binding energies of Co^{3+} and Co–O, respectively, and shrinks the energy bandgap of 2D thin-film nanostructures of LCO [111]. Similarly, the significant enhancement of saturation magnetization (M_S) [varying from 0.26 μ_B (T_C ~ 40 K) to 0.8 μ_B (T_C ~ 80 K) for LCO thickness changing from ~1.5–9.45 nm] of LCO has been reported when combined with STO in the form of multilayers comprising LCO/STO grown on the single crystal substrates, such as $Sr_{0.7}La_{0.3}Al_{0.65}Ta_{0.35}O_3$ (LSAT) and STO[112]. However, in the case of single layer LCO, the FM order vanishes below ~6 nm [112]. Recent studies based on DFT calculations by Wang *et al*. reported that the substitution of larger elements, such as Ba (1.35 Å), at the La (1.03 Å) site in LCO can efficiently introduce strain, prompting the occupancy into e_g orbitals modulating the spin configuration [113]. Interestingly, experimental studies based on the temperature-dependent soft x-ray reflectivity measurements and DFT calculations by Izquierdo *et al*. reveal that the charge-disproportionation in the single crystals of LCO can be induced by laser irradiation [97].

Laser irradiation treatment also alters the metal to insulator transition temperature in LCO [97]. Moreover, the metallization process can be established by laser irradiation, and the subsequent optical transitions stabilize the metallic state in LCO single crystals in which Co exists in the high-spin configuration [97]. Nonetheless, neutron diffraction studies and superconducting quantum interference device (SQUID) magnetometry experiments reveal a crossover from strong to weak antiferromagnetic correlations across 40 K in the larger nanoparticles of LCO; otherwise, they show FM behaviour predominantly [114]. The FM ordering in the LCO nanoparticles depends on the amount of the secondary phase (Co_3O_4), which prompts tensile strain on the LCO lattice [114]. Additionally, recent studies reveal that the energy conversion efficiency and oxygen reduction/evolution reaction activity of LCO can be enhanced by controlled charge transfer between a LCO thin film and an active layer under the film[115]. All these studies motivated us to investigate the bilayer combination of LSMO and LCO in which one can expect interesting magnetic behaviour in the range of 350 – 360 K and 80 – 90 K in the vicinity of T_C of LSMO and LCO, respectively [103–106]. Since the mixed valency of the cations is very much essential to attain unique magneto-transport properties and robust magnetic behaviour in the multilayer systems, in the present work, we bring both trivalent and tetravalent manganese (Mn^{3+}/Mn^{4+}) and trivalent cobalt (Co^{3+}) ions together in a single entity by considering the bilayer configuration of LSMO and LCO systems with different stacking orders [116]. In the following we provide the experimental details pertaining to the growth of the bilayer configuration using PLD technique and provide a detailed characterization technique.

3.2 Experimental Details:

Two different bilayer (BL) configurations discussed below are fabricated using a multitarget pulsed excimer laser (KrF; wavelength λ = 248 nm and fixed fluence = 1.5 J/cm^2) ablation technique on (001) oriented STO single crystal substrates. First, the chamber is evacuated to the lowest base pressure of 10^{-6} mbar and 5 nm LSMO is grown on STO at a substrate temperature of 700 °C (T_S) in the presence of 0.2 mbar oxygen partial pressure (P_{O2}). On this LSMO bottom layer, we deposited a 15 nm LCO top layer with (P_{O2}) = 0.4 mbar at the same T_S. A similar procedure is adopted to grow the bilayer configuration consisting of 15 nm LCO as the bottom layer and 5 nm LSMO as the top layer on (001) STO at T_S = 700 °C with P_{O2} = 0.4 and 0.2 mbar, respectively. After deposition, the samples are annealed in oxygen at 600 mbar for 30 min. The evolution of epitaxy in these bilayer systems and their structural quality was probed using a Philips X'pert PRO MRD x-ray diffractometer with Cu-K$_\alpha$ radiation of λ = 1.54 Å. The surface growth mechanism, roughness, and morphology of the bilayer systems are studied by means of an atomic force microscope (AFM) from INNOVA Bruker in tapping mode. The electronic structure and chemical composition of the bilayer heterostructures were probed using x-ray photo-electron spectroscopy (XPS). For this, we used a Kratos analytical spectrometer (model: AXIS Supra+) configured with a dual monochromatic x-ray source Al Kα/Ag Lα (2984.2 eV) with a spatial resolution less than 1 μm. Furthermore, a SQUID based magnetometer was used to study the temperature (10 K $\leq$ T $\leq$ 375 K) and field (0 Oe $\leq$ H $\leq$ 10 kOe) dependence of magnetization M (T and H). All the magnetization measurements are performed in the in-plane configuration (H $\perp$ [001]), and the experimentally obtained magnetization values are normalized by the unit cell volume of the total system. Consequently, the magnetization is expressed in Bohr magneton (μ_B) per total number of pseudo-cubic unit cells. The ferromagnetic resonance spectra were recorded using VersaLab (Quantum Design) at 300 K. Below we discuss the main results pertaining to the crystal structure involving the discussion of X-ray reflectivity and the corresponding reciprocal space maps, electronic structure using X-ray photoelectron spectroscopy, surface characterization using AFM and ferromagnetic resonance of the BLs followed by a detailed magnetic characterization.

3.3 Results and Analysis:

Structural analysis: X-ray diffraction line scans (θ–2θ) reveal that all BLs grown on the substrate are composed of high-quality single phase epitaxial thin films as shown in Fig.3.1. The θ–2θ line scans are used to probe the out-of-plane orientation of bilayers from 15° to 55°, which results in the out-of-plane (c) lattice parameters of LSMO and LCO as 3.86 and 3.79 Å, respectively, for both the bilayers [ICSD Nos. LSMO (56 630), STO (23 076), and LCO (17 668)] [117]. The bulk pseudocubic lattice constants of LSMO (3.87 Å) and LCO (3.81 Å) are lower than that of the STO substrate (3.905 Å). Such lattice parameters of LSMO and LCO induce an in-plane tensile strain in the present bilayers. The lattice mismatch between the film and substrate can be estimated through the following relation: $(a_s - a_b)/a_s$, where, a_s and a_b correspond to the pseudocubic lattice constant of the substrate and bulk sample. The mismatch of STO/LSMO and STO/LCO is found to be 0.9% and 2.4%, respectively. Moreover, the in-plane strain triggered by the

distortion of the film is calculated by using the following relation: $\varepsilon_{xx} = [-2\nu/(1-\nu)]\varepsilon_{zz}$, where ε_{zz} is the out-of-plane strain and ν is Poisson's ratio of the film.

The in-plane strain of the film is estimated as 0.2% and 0.62% for STO/LSMO and STO/LCO, respectively. Here, we have considered the values of ε_{zz} as −0.2% (−0.5%) and ν as 0.35 (0.38) for LSMO (LCO) samples. Hence, a considerable in-plane tensile strain induced in STO/LCO is found, which is larger than that of STO/LSMO, even though the lattice mismatch between the LSMO and LCO layers is almost similar in both the altered stacks of heterostructures. Furthermore, by considering in-plane and out-of-plane lattice parameters, the tetragonal distortion of LCO is estimated from the relation $t = 2(a-c)/(a+c)$ is ~0.03. All these results proclaim that the elastic deformation in STO/LCO is due to the considerable change in the substrate induced strain than STO/LSMO. On the other hand, the substrate-induced strain is expected to carry forward to the remaining layers as well (as the stacking sequence-developed strain) and influences the physical properties of the overall system. Although the magnitude of strain due to the stacking sequence is significantly less as compared to the substrate induced strain, it does enforce some changes in the anisotropic properties of the overall system.

High-resolution x-ray reciprocal space mapping (RSM) in the vicinity of (103) reflection [Figs. 3.1(b) and 3.1(c)] shows that the LSMO and LCO epitaxial layers of the BLs on STO are strained coherently to the substrate lattice, i.e., the in-plane lattice parameters of LSMO and LCO are the same with an in-plane parameter of the substrate (3.905 Å). Reciprocal space mapping is a technique to extract more information like microstructure, deviation ideal structure etc., from X-ray diffraction by surveying the reciprocal space is termed as reciprocal space mapping (RSM). Low-resolution reciprocal space mapping is the convenient

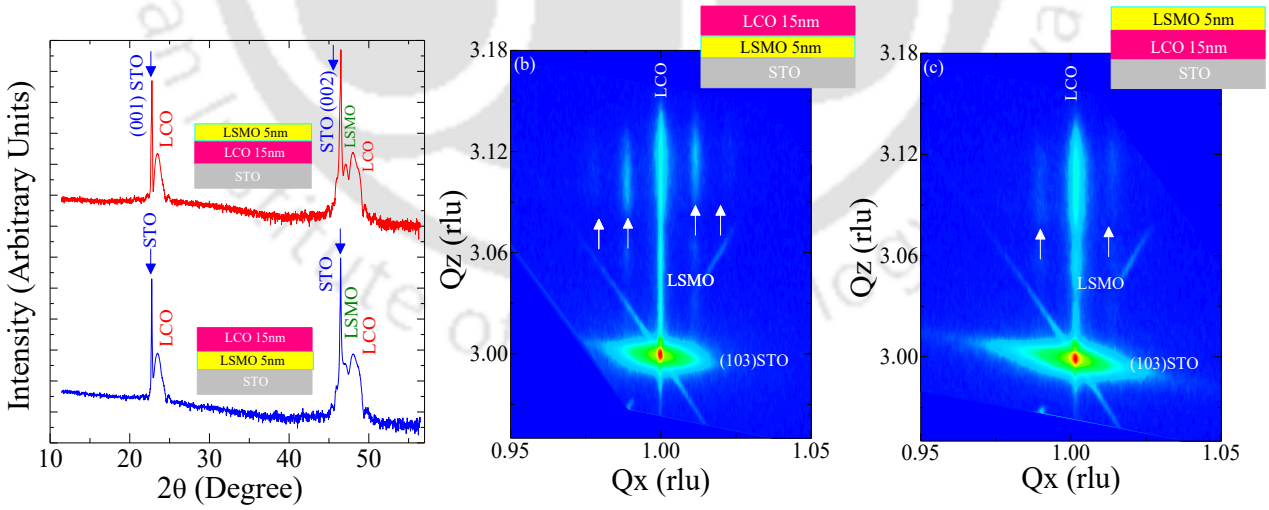

Fig. 3.1. (a) High-resolution θ–2θ x-ray scans around the (002) reflection of BL1 (blue) and BL2 (red) grown on $SrTiO_3$ (001) substrates. The LSMO and LCO peak positions are shown by arrow marks. The reciprocal space maps around the (103) reflection of (b) BL1 and (c) BL2. Both bilayers are coherently strained on the substrates. BL1 has stronger satellites along the in-plane direction [white arrows in (b) and (c)] than the BL2 configuration, which corresponds to the ordering of striped domains with a periodicity of 50 nm.

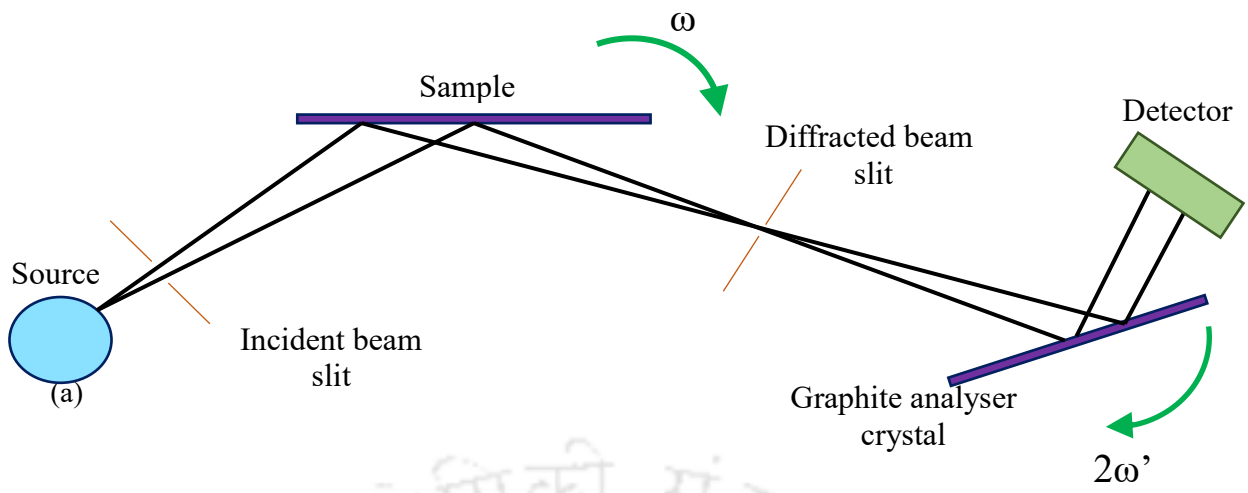

Fig. 3.2. A diffractometer for obtaining low-angular resolution reciprocal space maps.

technique for thin films with the data being collected digitally with a single detector. The basic geometry of low resolution slit-based RSM measurement is described in Fig. 3.2. In this case, the beam is probed by the slits instead of sample crystals giving an angular precision. The broadening arises from the spectral distribution of the source and the distribution of incident angles across the sampled region. The peak positions are less reliable because sample centring, or effective centring due to absorption, on the diffractometer axes displaces the apparent scattering direction. Low-resolution reciprocal space mapping has the advantage due to the increased intensity for probing weakly diffracting samples, whereas the large instrumental smearing effects acts as its disadvantage.

Thus, the coherently grown BLs of LSMO and LCO are under tensile strain (+0.9% for LSMO and +2.4% for LCO), referring to the bulk lattice parameters of 3.87 and 3.81 Å for LSMO and LCO, respectively. Hence, these magnitudes of in-plane and out-of-plane lattice parameters reveal that the strain tate of LSMO and LCO in the BL1 type sample is similar to that of the BL2 sample. In the RSM images, we also observed the side/lateral lobe diffraction (satellite) peaks along the in-plane direction [marked by arrows in Figs. 3.1(b) and 3.1(c)] in both BLs. The satellite peaks along the in-plane direction indicate that the periodic arrangement of the striped/barred domain along the in-plane direction with the lateral periodicity of the domain is ~50 nm. Such a periodic domain structure forms due to the competition between the elastic energy (as LSMO and LCO layers are under tensile strain on the STO substrate), the magnetostatic energy from the built-in magnetic field, and the crystallographic anisotropy energy, which conspire together to create the domains beyond a different layer sequence. The above results unambiguously indicate that the interface between LSMO and LCO is different in BL1 than in BL2. Hence, it is expected to have different physical behaviours of the bilayers. Interestingly, the periodic domain structure observed in BL1 is much more ordered than in BL2, and hence, one can expect additional strain developed as a consequence of the alteration of layer stacking sequences.

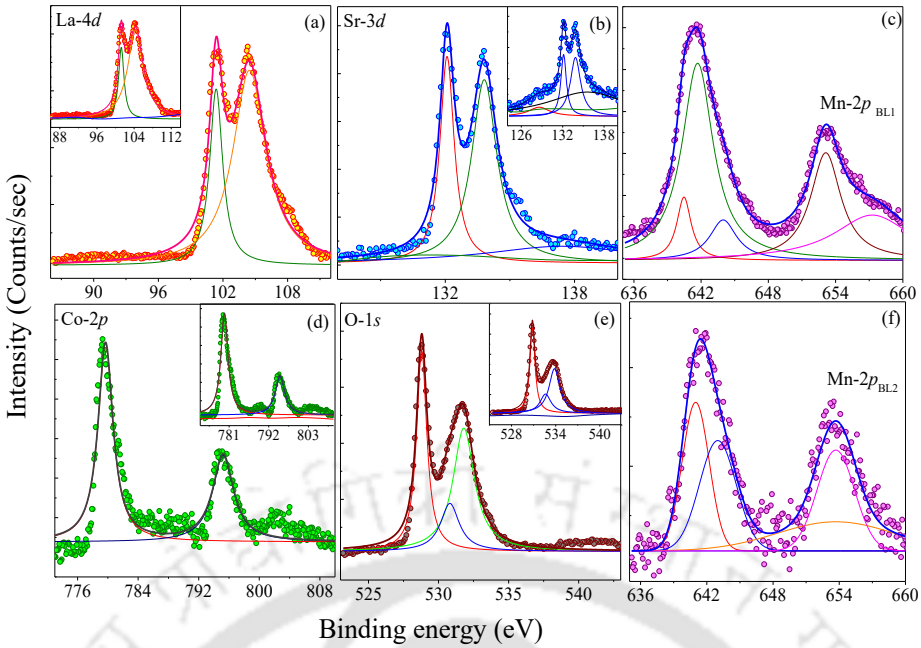

Fig. 3.3. X-ray photoelectron spectra of the bilayer systems: (a) La-4d (the inset shows the same for BL2), (b) Sr-3d (the inset shows the same for BL2), (c) Mn-2p for BL1, (f) Mn-2p for BL2, (d) Co-2p (the inset shows the same for BL2), and (e) O-1s (the inset shows the same for BL2) recorded at room temperature.

Electronic analysis: In order to understand the local atomic environment of the bilayers, we performed detailed x-ray photoelectron spectroscopy (XPS) measurements. Figures 3.3(a) – 3.3(f) illustrate the typical XPS spectrum in which the photoelectron intensity is plotted against the core-level binding energy of all the cations in the investigated system [BL1: La-4*d* (a), Sr-3*d* (b), Mn-2*p* (c) and (f), Co-2*p* (d), and O-1*s* (e)]. Insets of the corresponding figures depict the spectra for the BL2 system. All these core-level spectra of bilayer samples are measured under the standard calibration of the C-1*s* core level at 284.6 eV. In order to identify the accurate peak position of the core-level spectra for all these elements, we have analysed the measured core-level spectrum of each of the elements based on the peak fitting procedure initially by considering the Shirley baseline correction [118] The core-level spectrum of the La-4d orbital displays two major peaks centred at 101.2 and 104.4 eV with the peak separation of $\Delta E \sim 3.2$ eV surface stoichiometry [119,120]. The doublet of 4*d* orbitals corresponds to $4d_{3/2}$ and $4d_{5/2}$ electronic states originating from the spin–orbit splitting (ΔE_L). Needless to say, that the identified peaks of $4d_{3/2}$ and $4d_{5/2}$ are almost equally separated for both the bilayers. Moreover, the core level spectrum of the Sr-3*d* orbital reveals clear features of the doublet (like in La-4*d* core level spectra) with highly intensive cusps of $3d_{3/2}$ and $3d_{5/2}$ positioned at 132.1 and 133.8 eV, respectively. Here, the spectrum of Sr-3*d* possesses a low intensive feature around 137.6 and 140.4 eV shown in Fig. 3.3(b). In addition, the photoelectron spectra of the Mn-2p core level shown in Figs. 3.3(c) and 3.3(f) possess two major peaks attributed to $2p_{3/2}$ and $2p_{1/2}$ states located at 642.3 and 654.5 eV, respectively, with the separation of 12.2 eV (BL1).

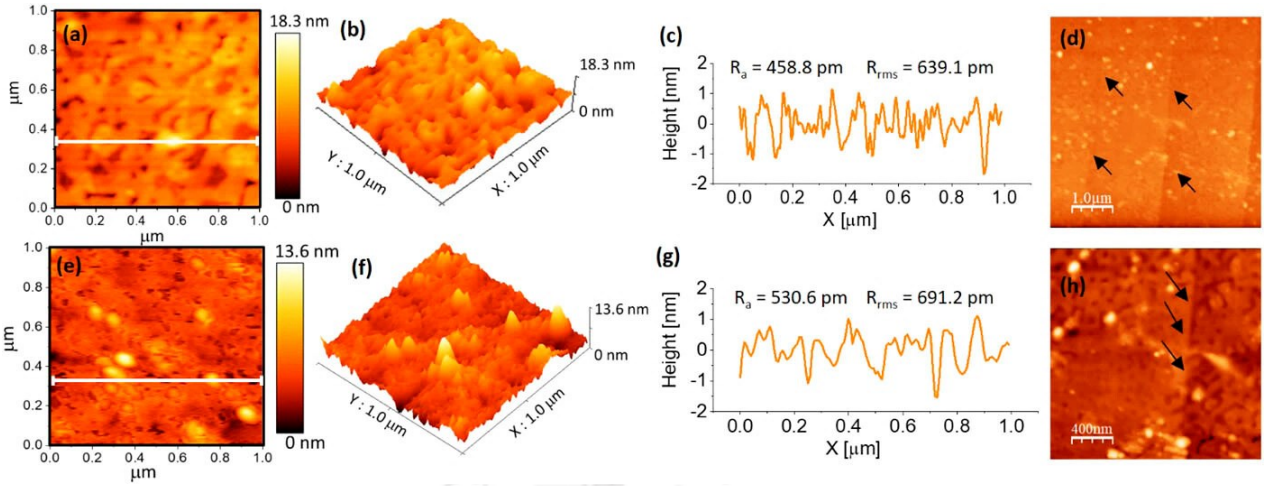

Fig. 3.4. Two-dimensional (2D) and three-dimensional (3D) atomic force microscopy (AFM) surface topology images of BL1 and BL2. The line profile plots of Bl1 and Bl2 are shown in (c) and (g), respectively. (d) and (h) 2D images with the striped-domain pattern of AFM for BL1.

The Mn-2$p_{3/2}$ satellite hump (645.7 eV) represents the contribution from the mixed (3+/4+) valence features at binding energies of ~640.2 and 642.2 eV [121]. The location of these deconvoluted peaks of the Mn-2*p* core level (640.1, 642.3, 650.3, and 654.5 eV) depends strongly on the oxidation states of (Mn^{3+}/Mn^{4+}) and on the covalence of the Mn–O bond [121]. Nevertheless, we have evaluated the dominant contribution of these two valences with the help of the relative intensity ratio (RIR) of Mn^{3+}/Mn^{4+}; it is expected that such a RIR of the two valence states modifies the relative electron hopping in the LSMO layer when we alter the stacking pattern of both the bilayers. The core-level spectra [Fig. 3.3(d)] of Co-2*p* resolved into two peaks with the states of 2$p_{3/2}$ and 2$p_{1/2}$ where those two states are to be found at 780.0 and 795.1 eV (with the binding energy separation of 15 eV for both the systems) [122]. Unlike in the valence states of Mn ions, the valence states of Co ions are more complex due to the concomitant three local spin arrangements in trivalent Co ions. Thus, the electron transfer across the interface of the bilayers is more difficult to identify with respect to the trivalent Co as they are influenced by the crystal field of oxygen ions. This is well known from the abundant literature available on the physical properties of the LCO_{δ} compound that exhibits higher oxygen deficiency (δ) than the LSMO system [123]. Finally, the core level spectra of O-1*s* [Fig. 3.3(e)] exhibit two main peaks at 528.6 and 532.2 eV, signifying the lattice oxygen and the hydroxyl group in which the deconvolution treatment allows two main peaks in consonance with the above and a minor hump. Nonetheless, the oxygen valence states are almost identical in both the bilayers, and we can believe that any noticeable change in the physical properties is not driven by the "δ" of oxygen.

Morphological analysis: To understand the surface topology and the growth mechanism, we performed the atomic force microscopic (AFM) measurements. Figures 3.4(a) and 3.4(e) show the two-dimensional (2D) and Figs. 3.4(b) and 3.4(f) the three-dimensional (3D) AFM surface morphology images of BL1 and BL2 systems, which show uniform and homogeneous grains with the striped-domain pattern prevalent in both the systems on large scales [Figs. 3.4(g) and 3.4(h)]. Globally, the line profile plots [Figs.

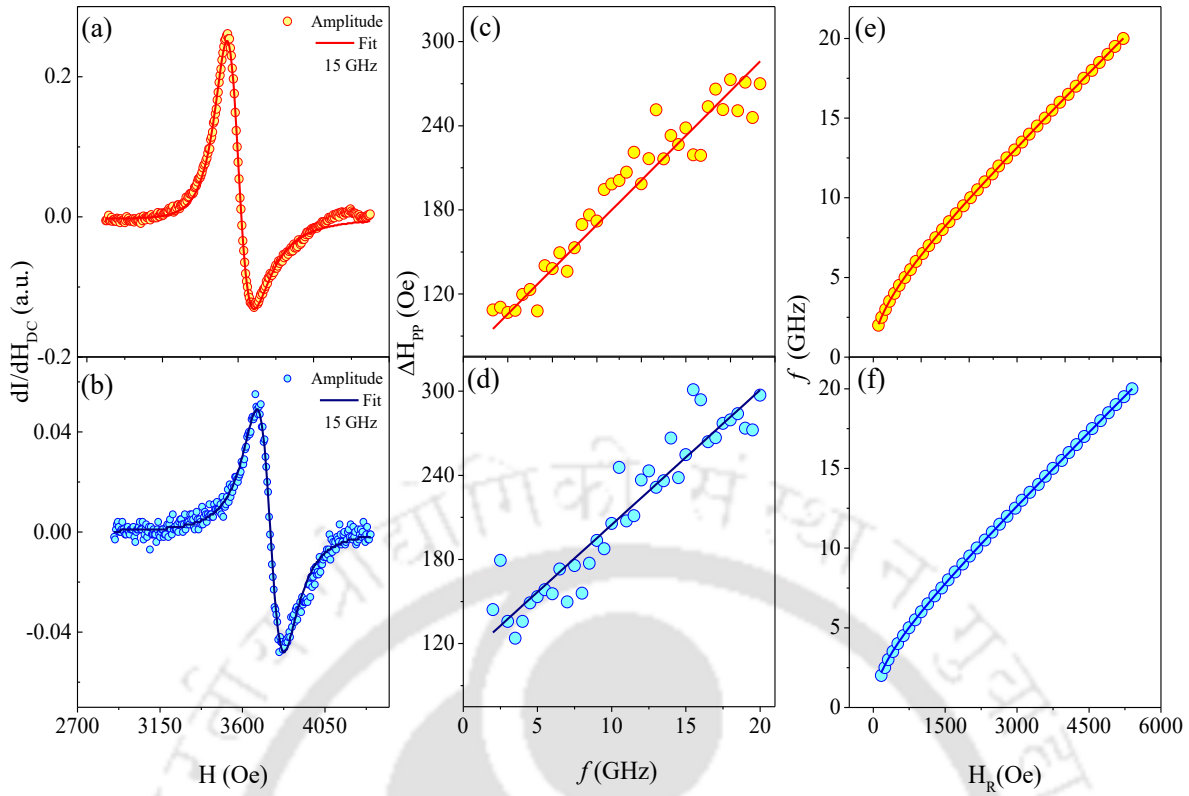

Fig. 3.5. Room temperature FMR spectra recorded at 15 GHz for (a) BL1 and (b) BL2 along with the Lorentzian fit (solid line), frequency dependence of the linewidth (ΔH_{PP}) for (c) BL1 and (d) BL2, and resonance field (H_R) dependence of the frequency at room temperature for (e) BL1 and (f) BL2.

3.4(d) and 3.4(h)] reveal very low root mean square (rms) roughness (939 pm and 1.23 nm) for both the systems representing the high quality of the thin films.

Ferromagnetic resonance analysis: In order to understand magnetization dynamics in the both BL systems and to estimate the anisotropy, we measured the ferromagnetic resonance (FMR) spectra at various frequencies (5 – 20 GHz) of the bilayers at 300 K. Figures 3.5(a) and 3.5(b) show the first derivative of the FMR absorption signal (of intensity dP/dH_{DC}) recorded for 15 GHz by sweeping the dc-magnetic field (H_{DC}) for BL-1 (a) and BL-2 (b) systems. The recorded spectra were fitted using the first derivative of Lorentzian symmetric and antisymmetric components to estimate the corresponding parameters: resonance field (H_R) and peak-to-peak linewidth (ΔH_{PP}) plotted as a function frequency [Figs. 3.5(c) and 3.5(d)]. Here, the solid curve represents the typical fit to the Lorentzian line shape consisting of both symmetric and antisymmetric contributions. We employed the below microwave dispersion relation that describes the absorption spectrum linking both the magnetic field and frequency in the in-plane configuration [124],

$$f_{FMR} = \gamma/2\pi \sqrt{H_R(H_R + H_{eff})}, \quad (3.1)$$

where f_{FMR} refers to the FMR frequency, γ is the gyromagnetic ratio, H_R is the resonant field, and H_{eff} is the effective magnetic field developed by the magnetic contribution of saturation magnetization ($4\pi M_S$) and anisotropy field (H_K). Accordingly, the FMR dispersion data are fitted with the above equation and estimated

the magnitude of H_{eff} ~ 3127 and 3770 Oe for BL1 and BL2, respectively. A systematic correlation between H_{eff} and $4\pi M_S$ (=3103 Oe) and H_K is established using the relation $H_{eff} = 4\pi M_S - H_K$, which yields the magnitude of H_K ~ 2185 Oe (corresponding anisotropy constant $K_U \sim 0.82 \times 10^5$ erg/cc) and 2326 Oe ($K_U \sim 1.33 \times 10^5$ erg/cc) for BL1 and BL2, respectively. These values are consistent with the anisotropy parameters obtained from the magnetic hysteresis measurements, which will be discussed below. Furthermore, from the fitting, the gyromagnetic ratio $\gamma/2\pi$ values are estimated as 29.48 GHz/T (29.22 GHz/T) for the respective bilayers BL1 (BL2). $\Delta H_{PP}(f)$ and $H_R(f)$ plots provide important information about the magneto-dynamic properties, such as the magnitude of the damping parameter (α) and inhomogeneous linewidth broadening (ΔH_0), according to the following expression [125,126]:

$$\Delta H_{PP} = 4\pi\alpha f/\gamma + \Delta H_0, \tag{3.2}$$

From the linear fits of the experimental data with Eq. 3.2, the magnitudes of the damping parameter and ΔH_0 are estimated as $\alpha = 0.0141$ (0.0143) and $\Delta H_0 = 108.8$ Oe (85.16 Oe) for BL1 (BL2), respectively. These magnitudes are quite higher than the typical damping parameter (2×10^{-3}) for the LSMO layer of thickness ~20 nm [124] and comparable with those of the LSMO/LNO heterostructure [127].

Magnetic analysis: Figures 3.6(a) and 3.6(b) show the temperature dependence of in-plane ($\mu_0 H \parallel$ [100]) magnetization M(T) of the bilayers [(a) BL1 and (b) BL2] measured under the field-cooled-warming (FCW) condition with H = 1 kOe from 10 to 383 K. The right-hand-side-scale in Fig. 3.6 represents the temperature variation of the differential magnetization (dM/dT vs T). The BL1 system shows two distinct

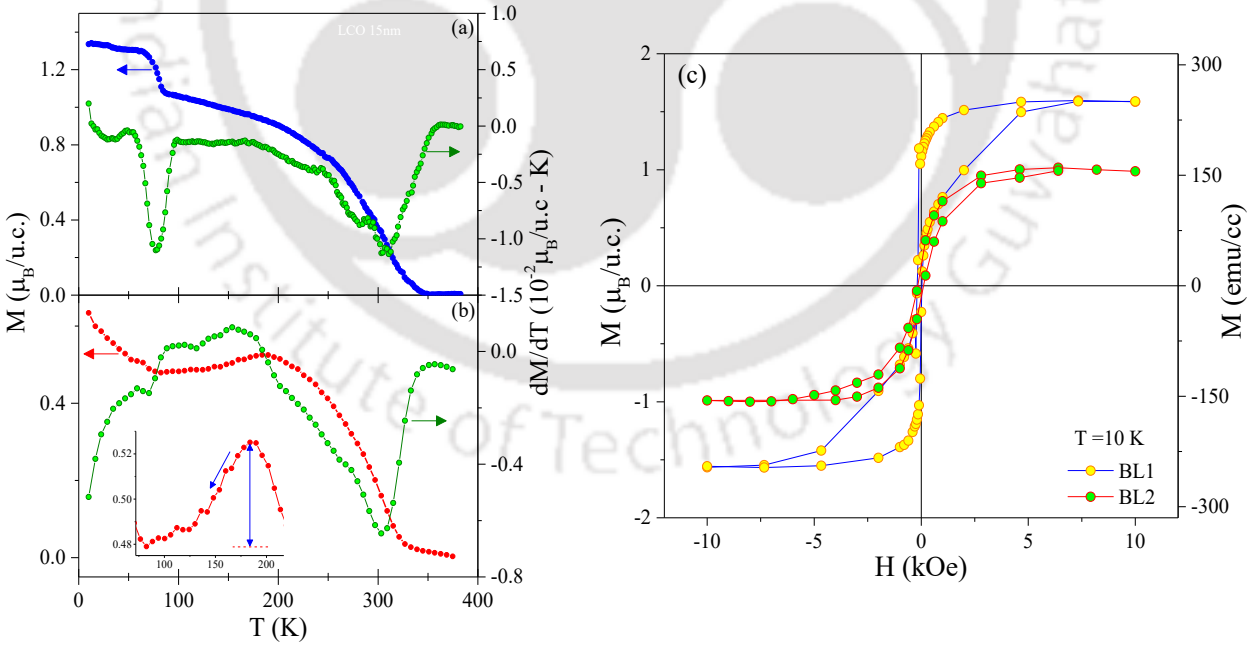

Fig. 3.6. Temperature dependence of magnetization M(T) of the bilayers (a) BL1 and (b) BL2 measured under the field-cooled-warming (FCW) condition with H = 1 kOe from T = 10–383 K. The right-hand-side-scale represents the corresponding temperature variation of the differential magnetization plots (dM/dT vs T). The inset in (b) shows the enlarged view of M vs T of BL2 between T = 72 and 217 K, which clearly depicts the drop-in magnetization until 72 K. (c) Magnetization vs field M(H) hysteresis loops of both the bilayers BL1 and BL2 recorded at T = 10 K under the field (H = 1 kOe) cooled condition.

transitions: a paramagnetic to ferromagnetic transition (T_C of LSMO) first takes place at ≈320 K and a second T_C around 77 K. In order to obtain the exact transition temperatures, we calculated dM/dT and plotted against T, which yields $T_C \approx 310$ and 77.23 K corresponding to LSMO and LCO, respectively, for the BL1 system. The reduced value of T_C measured in these bilayers as compared to that measured in bulk LSMO (T_C = 370 K) is due to the biaxial tensile strain (0.75%) experienced by coherently grown LSMO films on STO (001) and the finite-size/surface effect experienced by films of a few unit cells in thickness [128,129]. These figures clearly represent the dominant ferromagnetic nature of LCO and LSMO in BL1 as compared to BL2 whose ordering temperatures are significantly lower by 5–10 K. Nevertheless, at low temperatures, the BL2 configuration shows completely different magnetic characteristics in that a significant drop in the magnetization [inset of Fig. 3.6(b)] is noticed below 184 K down to 82 K, which provides the evidence for the weak antiferromagnetic pinned state (+ve dM/dT) across the interface of LSMO and LCO.

One of the strain sources in oxide thin films is from in-plane biaxial strain induced by the substrate. The biaxial strain manifests the reduced Curie temperature of manganite thin films in accordance with the Millis model. According to the model, the biaxial strain dependent Curie temperature of manganite thin films is related as $T_C(\varepsilon_B, \varepsilon^*) = T_C(0, 0)[1 - \alpha\varepsilon_B - \beta\varepsilon^{*2}]$. The values of α and β are considered as 1.55 and 1460, respectively[129]. Here, ε_B is the bulk compression, which is $(1/3)(2\varepsilon_{xx} + \varepsilon_{zz})$, and the biaxial distortion is $(1/2)(\varepsilon_{zz} - \varepsilon_{xx})$. The reduced Curie temperature of LSMO on STO is estimated to be at 349 K due to the biaxial strain of the STO substrate. This suggests that there is a significant contribution of substrate induced strain on the LSMO layer. This can clearly distinguish the contribution of substrate induced strain from the stacking sequence developed strain.

However, below 82 K, the ferromagnetic ordering of LCO dominates the overall magnetization of the BL2 system due to the superexchange between the trivalent Co high- and low-spin configurations in LCO[109]. The interfacial driven FM coupling strength is highly sensitive to the layer sequence and ordering; in the present case, it is significantly reduced in BL1 [Fig. 3.6(a)]. Negligible coercivity ($H_C \rightarrow 0$) in the field (H = 1 kOe)-cooled M–H (±10 kOe) hysteresis loops measured at 10 K provides further evidence to this to the AFM character in BL2 [Fig. 3.6(c)]. For all the fields, BL1 exhibits higher (60% higher in BL1 than in BL2 at 10 K for 10 kOe) magnetization as compared to BL2, signifying the fact that the layer sequence plays a key role in the overall magnetic structure of these layers. The remanence magnetization (M_R) at 10 K is ≈1.05 and 0.411 μ_B/u.c for both the BL1 and BL2 layers, respectively. It is possible that the Mn–O–Co superexchange path/bonds can mediate the AFM coupling along with the LSMO/LCO interface and influences the magnetic order of the LSMO layer upon altering the layer sequence. Previous studies revealed that the growth and alignment of the barred domain structure is strongly dependent on the thickness of the ferromagnetic LCO layer (t_{LCO}) because the rhombohedral distortions across the LCO/LSMO interface increases progressively with increasing "t_{LCO}," which, in turn, affects the magnetic properties. Moreover, the barred domain structure and t_{LCO} together influence the anisotropy of the bilayer configuration. Thus, motivated by these facts, we studied the role of magneto-crystalline anisotropy in both these systems using isothermal magnetization curves at low temperatures below the T_C value of LCO for different magnitudes

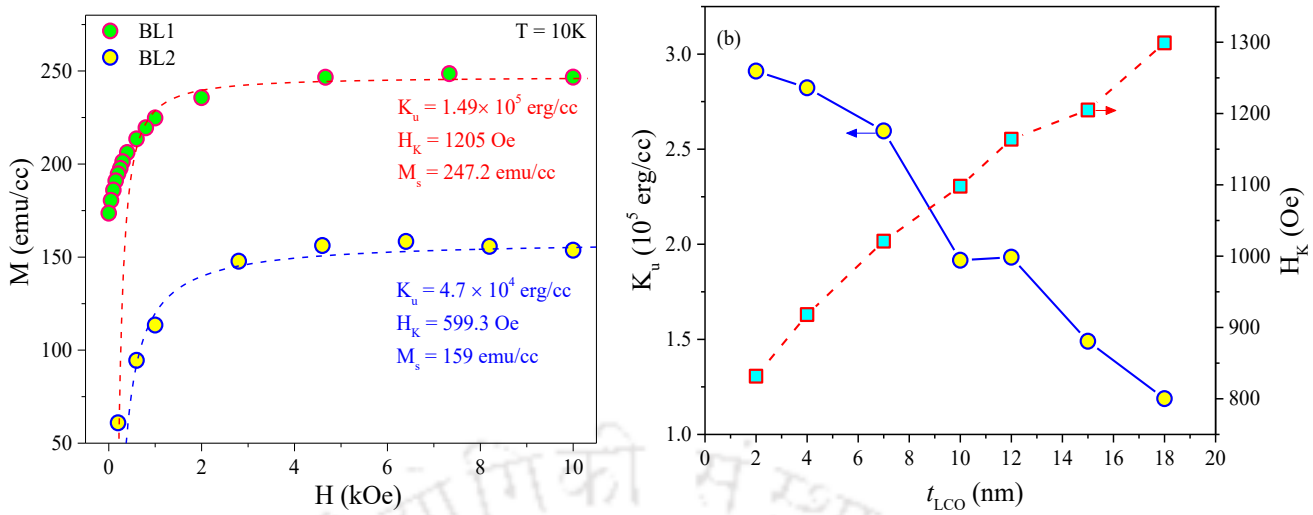

Fig. 3.7. (a) Isothermal magnetization curves (M–H) of both the bilayers BL1 and BL2 recorded at T = 10 K under the field (H = 1 kOe) cooled condition. (b) LCO thickness variation of the anisotropy constant K_u (t_{LCO}) and anisotropy field H_K (t_{LCO}) of the bilayer configuration BL1 for constant (5 nm) LSMO thickness and variable LCO thickness.

of t_{LCO} using the law-of-approach to saturation (LAS) technique. According to the LAS, the total magnetization $M = M_S(1\text{-}a/H\text{-}b/H^2) + \chi_{hf}H$, where the term $\chi_{hf}H$ represents the high-field susceptibility resulting from the increase in the spontaneous magnetization due to the external field (H). However, the first term a/H is associated with the presence of structural defects and nonmagnetic entities. The term b/H^2 is ascribed to the magneto-crystalline anisotropy. In the case of cubic systems with ferromagnetic features, the coefficient b is given by $b = 8/105\ (K_1^2)/(\mu_0^2 M_S^2)$ [131,132].

Following this analysis, the dotted lines in Fig. 3.7(a) represent the best fits to the experimental data points (scattered symbols) recorded at 10 K obtained using the LAS equation. The resultant parameters obtained from the best fits yield anisotropy field $H_K \approx 1205$ Oe (599.3 Oe), anisotropy constant $K_u \approx 1.49 \times 10^5$ erg/cc (4.7×10^4 erg/cc), and $M_S \approx 247.2$ emu/cc (159 emu/cc) for BL1 (BL2) systems, respectively. LSMO nanoparticles have anisotropy constant (K) value of 2.12×10^5 erg/cm^3 at 3K though we could not find any reported anisotropy value of bulk $LaCoO_3$. It is interesting to note that BL2 exhibits one order low magnetocrystalline anisotropy as compared to BL1 due to the antiferromagnetically pinned moments. This feature corroborates with the pseudo-AFM behaviour observed in BL2 that exhibits negligible coercivity, signifying the key role of the stacking sequence in the structural and magnetic behaviours of the investigated system [133]. A detailed LCO thickness (t_{LCO}) dependent study on the BL1 system by fixing the 5 nm LSMO layer thickness reveals anomalies in H_K (t_{LCO}) across $t_{LCO} \approx 10$ nm (1098 Oe) and 16 nm (1205 Oe). Beyond, $t_{LCO} = 18$ nm, both K_u and H_K decrease monotonically ($K_u \approx 1.18 \times 10^5$ erg/cc and $H_K \approx 1299$ Oe for 5 nm LSMO/18 nm LCO), and BL1 exhibits maximum in K_u (2.9×10^5 erg/cc) for an extremely lower thickness ($t_{LCO} \approx 2$ nm) of LCO layers shown in Fig 3.7(b). These magnitudes are in line with the previously reported values on highly epitaxial LSMO/STO (001) thin films of a few unit cells in thickness grown by pulsed laser deposition (PLD) using angle dependent ferromagnetic resonance spectroscopy measurements [134].

Interestingly, both BL1 and BL2 systems exhibit one order higher magnitude of anisotropy values as compared to the single crystalline manganites using torque magnetometry $K_1 = 1.8 \times 10^4$ erg/cc along the (100) plane] [135], inferring the highly epitaxial nature of the current investigated bilayers. On the other hand, in the present case, we have estimated the nearest-neighbour effective exchange constant J_{eff} for both the systems LSMO and LCO in the BL2 configuration using the below expression that has a molecular-field basis. Here, $J_{eff}/k_B = (3T_C)/(2S(S + 1)Z_{eff})$, where Z_{eff} (=6) is the number of the nearest-neighbour exchange coupled spins with S = 3/2 and 3/2 for LSMO and LCO, respectively, and T_C is the Curie temperature of LSMO and LCO. Accordingly, we estimated J_{eff} for both LCO and LSMO in the BL1 configuration as a function of LCO thickness (t). For all the thicknesses, the exchange interaction corresponding to LSMO dominates over LCO owing to the fact that the volume fraction of the former is higher as compared to the latter. As the thickness approaches very smaller values, J_{eff}/k_B reaches its maximum magnitudes of 5.47 and 21.93 K for LCO and LSMO, respectively.

These values closely match with $J_{eff}/k_B \approx 20 \pm 2$ K of highly epitaxial LSMO single layers grown on TiO_2-terminated STO (100) substrates using the PLD technique. The nature of $J_{eff}(t)$ is consistent with the variation of the effective number of spins available per unit volume ($N_V = M_S/\mu A$) each with the average magnetic moment "μA" in BL1 as a function of LCO thickness. Here, we considered $\mu A = 0.738\ \mu_B$ average between μ_{LSMO} and μ_{LCO}, where $\mu_{LSMO} = 4.591\ \mu_B$ for g = 2 and considered $\mu_{Mn^{3+}} = 4.9\ \mu_B$ (S = 2) and $\mu_{Mn^{4+}} = 3.87\ \mu_B$ (S = 3/2) and $\mu_{LCO} = 0.88\ \mu_B$. In this case, N_V reaches the maximum value of 1.023×10^{23} cm^{-3} as $t_{LCO} \rightarrow 0$, and for larger LCO thickness (18 nm) in the BL2 configuration, the effective number of spins available for the long-range ordering approaches 0.26×10^{22} cm^{-3}.

In what follows we provide a brief description of summary and conclusions of our work presented in this chapter.

3.4 Summary:

In this work, we demonstrated that the stacking sequence of LSMO/LCO epitaxial bilayers coherently grown on STO (001) substrates plays a vital role in the overall magnetic properties of the system. The biaxial tensile strain experienced by these layers along with the finite-size/surface effect collectively drives the ordering temperatures to lower values as compared to the bulk counterpart in both the bilayers. Interestingly, the bilayer sequence (15 nm) LCO/(5 nm) LSMO (BL2) exhibits a significant drop in the magnetization between T = 184 and 82 K, suggesting weak antiferromagnetic coupling across the interface of the two ferromagnetic constituents, resulting in a partial compensation of the overall magnetic moment. However, below 82 K, the ferromagnetic features of LCO dominate the overall magnetization of the BL2 configuration due to the dominant superexchange between the trivalent Co high and low-spin state configurations in LCO. On the other hand, the stacking sequence (5 nm) LSMO/(15 nm) LCO exhibits a strong ferromagnetic character with two distinct transitions at 320 and 77 K corresponding to the T_C value of LSMO and LCO, respectively. These results are consistent with the higher magnitude of anisotropy constant K_u ($\approx 1.49 \times 10^5$ erg/cc) in the BL1 configuration than $K_u \approx 4.7 \times 10^4$ erg/cc for the stacking

sequence (5 nm) LSMO/(15 nm) LCO. The frequency dependence of the FMR linewidth $\Delta H_{PP}(f)$ reveals the greater in-plane anisotropy in BL2, suggesting the existence of extrinsic mechanisms alongside the Gilbert intrinsic contribution. In addition, the other dynamic characteristics, such as gyromagnetic field ($\gamma/2\pi$), demagnetization fields ($4\pi M_{eff}$), and effective damping constant (α) of bilayers, are enhanced as compared to individual layers. Moreover, the nearest-neighbour effective exchange constant J_{eff} evaluated from the experimental magnetization data and molecular-field theory follows the linear variation with the increasing thickness (t_{LCO}) of LCO from 2 to 18 nm. As the thickness approaches their unit cell dimension, J_{eff}/k_B reaches its maximum magnitude of ≈5.47 and 21.93 K for LCO and LSMO, respectively, which is comparable with the previously reported value of $J_{eff}/k_B \approx 20 \pm 2$ K in highly epitaxial LSMO single layers. Nevertheless, the nature of $J_{eff}(t)$ is consistent with the variation of the effective number of spins available per unit volume (N_V), which varies between 1.02×10^{23} and 2×10^{22} cm^{-3} as $t_{LCO} \rightarrow 0$ and t_{LCO} approaches a maximum magnitude of 18 nm.

Chapter 4
Texture reliant properties of $La_{0.7}Sr_{0.3}MnO_3/LaNiO_3$ superlattices

In this chapter we mainly focus our studies on the orientation/texture dependent growth characteristics and various properties of $[La_{0.7}Sr_{0.3}MnO_3/LaNiO_3]_{10}$ superlattices (SLs) coherently grown on (001/011/111)-$SrTiO_3$ substrates by the PLD technique. In particular, a comprehensive study on the epitaxial nature, electronic structure, magnetic and magneto-transport properties, and Raman spectroscopy across the atomically flat interfaces of the above specified systems will be presented. We begin with a brief introduction to the systems under investigation and outline the details of experimental methods employed in line with the chapter 2 and discuss the key results. Final section of this chapter focuses on the summary of important findings.

4.1 Introduction:

Since the discovery of the colossal magnetoresistance (CMR) in 1994, the quest for materials that exhibit CMR including some novel magnetic properties are in demand for spintronics devices [136-143]. Specifically, the family of manganites with transition-metal elements as dopants are thoroughly investigated in the literature focusing on their remarkable magnetic and electronic properties, and this topic is still an active research field to date [144]. The unique combination of hole-doped manganites (e.g., $LaSrMnO_3$) and rare earth nikeletes (e.g., $LaNiO_3$, LNO) are very much in demand considering their unique temperature dependence of electrical and magnetic properties, such as high temperature superconductivity, large negative magnetoresistance, exchange bias coupling, and tunable metal-to-insulator transitions [143–145]. Such combinations of two distinct families of perovskite systems like half-metallic ferromagnet $La_{0.7}Sr_{0.3}MnO_3$ with metallic paramagnetic $LaNiO_3$ in the form of epitaxial thin-film heterostructures or superlattices (SLs) are considered excellent candidates for magneto-electronic devices, especially in magnetic recording and logic devices [79,146–148]. Moreover, it is well known that the bulk $LaNiO_3$ system exhibits distinctly different magnetic and electrical transport properties as compared to its 2D thin-film nanostructures as this system is unable to acquire stable magnetic ground state in its bulk lattice form [149,150].

The superlattice structures of the above described systems provide a unique playground to probe the effects of the interface, electronic structure modulation by local symmetry breaking, layer sequence dependent change of physical properties, proximity effects, exchange bias, strain driven polarity discontinuities, *etc.* [79]. In the present case, we have selected three different substrate orientations, (001), (011), and (111), of the $SrTiO_3$ (STO) single crystal because the growth dynamics in these orientations considerably affects the physical properties of the investigated systems as the rotations and distortions of oxygen octahedra in the perovskite structure alter with the substrate orientations and the chemical identity of the constituent elements [151–156]. Moreover, the octahedral structure across the interface is usually

different between the (111) and (001) orientations with altered symmetry rotation axes. Thus, one can expect uneven charge transfer between the interfaces of each sublayer, which provides a unique opportunity to control the spatial distribution of the spin density [152]. The $LaSrMnO_3$ thin films grown on (001) oriented $SrTiO_3$ exhibits enhanced coercive field, twinning, tunable electronic transport properties, and magnetic anisotropy [157–160]. On the contrary, the (111)-surface of $LaSrMnO_3$ induces considerably different epitaxial strains as compared to the (001) facet with hexagonal symmetry of an S_6 inversion-axis and provides a unique opportunity to realize Goldstone-like structural modes, topologically protected states, and unique geometries/structural-symmetries like buckled honeycomb lattice, Kagome lattice, triangular lattice, etc [161–168]. These differences between the interfaces grown on different crystallographic orientations and unique characteristics of the perovskite oxides motivated us to choose (001), (011), and (111) oriented $SrTiO_3$ substrates because such superlattice structures play an important role in the design and development of novel oxide electronic devices.

Also, commercially available pseudo-cubic single crystalline anisotropic [either (100) or (111)] substrates such as $LaAlO_3$ and $SrTiO_3$ provide good epitaxial interfaces across $La_{0.7}Sr_{0.3}MnO_3$ and/or $LaNiO_3$ layers, and, hence, such a multilayer geometry makes perfect platform for the characterization [169]. Consequently, the first work on the $[La_{0.7}Sr_{0.3}MnO_3/LaNiO_3]_3$ superlattice system reported low-field giant magnetoresistance and in-plane magneto-transport measurements of the dc-sputtered multilayers [170]. This system also exhibits large substrate-induced in-plane uniaxial anisotropy, which prefers the magnetization vector direction along the [010] orientation, despite its high cubic magneto-crystalline anisotropy with ⟨110⟩ easy axes in which the magnetic layers couple ferromagnetically through very thin (< 2 nm) $LaNiO_3$ spacer layer thickness. Beyond 2 nm of $LaNiO_3$ spacer layer thickness, the coupling strength decreases in an oscillating way similar to Ruderman–Kittel–Kasuya–Yosida (RKKY) interaction [171], whereas other studies reported weak antiferromagnetic coupling with exchange bias (2 kOe) in the ultrathin (2–5 unit cells) superlattices of $[LaNiO_3/SrTiO_3/La_{0.7}Sr_{0.3}MnO_3]_{10}$ [172]. Moreover, the first-principles based calculations by Ghosh *et al.* reported insulating ferroelectric-like behaviour with a tunable bandgap in the superlattices of $(La_{0.7}Sr_{0.3}MnO_3)_m/(LaNiO_3)_n$ for the ratio m/n = 1/1, 2/2, and 3/1 [173]. These authors also reported that the polar metallic phase can undergo a metal to insulator transition due to a small disproportionation of the oxidation state on the Ni sites; such a behaviour is highly sensitive to the concentration of delocalized holes in the system. These studies provide hope to the experimentalists to explore a new family of tunable polar metals by choosing appropriate intermixing of cation constituents across the interfaces of $La_{0.75}Sr_{0.25}MnO_3$ (LSMO) and $LaNiO_3$ layers [174]. Another study by Zhou *et al.* reported antiferromagnetic behaviour with significant robust exchange bias (H_{eb} ~ 750 Oe) and coercivity (~1865 Oe) in field-cooled hysteresis of pulsed laser deposited $[(La_{0.75}Sr_{0.25}MnO_3)_5/(LaNiO_3)_n]_{12}$ superlattices on (001) oriented $SrTiO_3$ single crystal substrates [174]. Interestingly, these authors also reported the emergence of metal to insulator transition for a lower $LaNiO_3$ thickness of superlattice configuration $(5/n = 2)_{12}$ in which localized moments are induced by the charge transfer between Mn and Ni ions across the interface [150,173]. The same research group also reported superconductivity across 3.7 K

in superlattices of two-unit cell thick $La_{0.75}Sr_{0.25}MnO_3$/three-unit cell thick $LaNiO_3$ by the pulsed laser deposition (PLD) technique [150]. However, the PLD grown bilayer configuration of 25 nm−$La_{0.75}Sr_{0.25}MnO_3$/35 nm− $LaNiO_3$ exhibits interfacial spin-glass behaviour and weak exchange bias [145].

Similar results are reported by Bhatt *et al.* in the PLD grown heterostructures of [$LaNiO_3$/$La_{0.75}Sr_{0.25}MnO_3$] and [$La_{0.75}Sr_{0.25}MnO_3$/6–9 unit cell thick $LaNiO_3$/$La_{0.75}Sr_{0.25}MnO_3$] on MgO (001) substrates using spin dependent polarized neutron reflectometry measurements with average local magnetization of ~ 80 emu/cc in which the interlayer exchange interaction depends on the stacking sequence [175]. On the other hand, Bhatt *et al*. reported spin mixed conductance without any exchange bias in the PLD grown trilayers heterostructures of $La_{0.75}Sr_{0.25}MnO_3$/$LaNiO_3$/$SrRuO_3$ with a spin diffusion length of ~ 3.2 nm in $LaNiO_3$ [176]. Apart from physical deposition techniques, the chemical solution based thin-film deposition method also yields high quality multilayers of [$LaNiO_3$/$La_{0.75}Sr_{0.25}MnO_3$] configuration [177]. Wang *et al.* reported the role of $LaNiO_3$ buffer layer on the structures and properties of ferromagnetic $La_{0.75}Sr_{0.25}MnO_3$ thin films using the chemical solution deposition technique on Si (100) substrates with $LaNiO_3$ as a buffer layer, which shows a significant increase of the metal to insulator transition temperature along with superior magnetoresistance behaviour [177]. Comparable results are reported in the case of $La_{0.75}Sr_{0.25}MnO_3$ thin films (15 nm) grown on the (001) $LaAlO_3$ substrate with $LaNiO_3$ as the buffer layer using the PLD technique in which in-plane anisotropy drives the system to exhibit an enhanced magnetic moment of ~ 3.10 μ_B/Mn and reduced coercivity as compared to the pristine $La_{0.75}Sr_{0.25}MnO_3$ without a buffer layer [178]. All the above results motivated us to reinvestigate this interesting superlattice system focusing on the anisotropic/orientational dependent changes occurring on the growth/morphology, local atomic environment, and other physical characteristics, such as magnetic transport, electronic transport, and Raman spectroscopy. In our previous study [179], we reported the structural and magnetic properties of a slightly different superlattice configuration $[La_{0.75}Sr_{0.25}MnO_3/LaNiO_3]_{10}$ coherently grown on $SrTiO_3$ (STO)-(001) and (111) with varying thickness of paramagnetic $LaNiO_3$ (t_{LNO} = 1.5, 3, and 5 nm) by fixing the $La_{0.75}Sr_{0.25}MnO_3$ thickness to 3.3 nm. However, here in the present work, we focus on the ten times repeated stacks of $La_{0.75}Sr_{0.25}MnO_3$/$LaNiO_3$ superlattice configuration grown on (001), (011), and (111) oriented $SrTiO_3$ substrates aiming to understand the directional dependence of the physical properties, which are discussed in Secs. 4.2-4.4.

4.2 Experimental Details:

The superlattices of [$La_{0.75}Sr_{0.25}MnO_3$ (LSMO)/$LaNiO_3$ (LNO)]$_n$ were fabricated by the PLD technique using a KrF laser of wavelength 248 nm as a source (n being the stacking periodicity). First, the LSMO bottom layer was grown on the $SrTiO_3$ (STO) single crystal substrate of different orientations (001), (011), and (111) with thickness t_{LSMO} (~ 4.2 – 4 nm). Upon the LSMO layer, the LNO top layer of thickness t_{LNO} ~ 3 - 2.6 nm was grown coherently with n = 10, and we label the three superlattices under

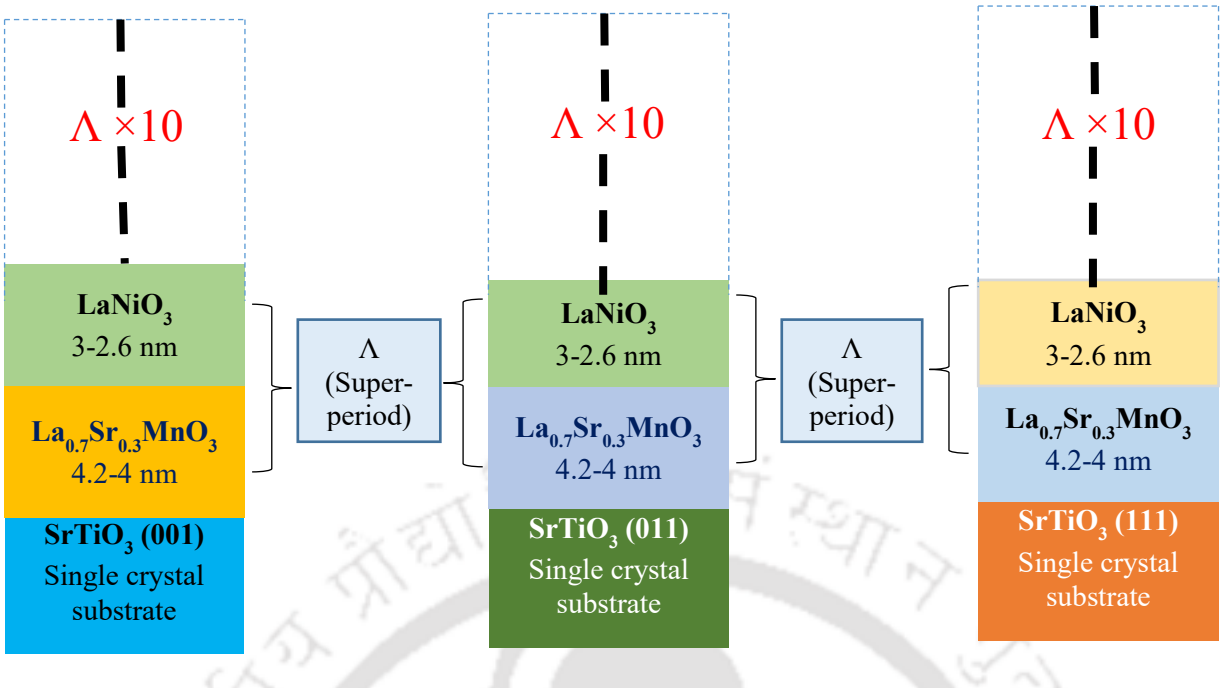

Fig. 4.1. The schematic structure of the SL-001, SL0-011 and SL-111 on the single crystal $SrTiO_3$ in the respective directional orientation.

investigation as SL-001, SL-011, and SL-111, corresponding to $[LSMO/LNO]_n$/(001)STO, $[LSMO/LNO]_n$/(011)STO, and $[LSMO/LNO]_n$/(111)STO, respectively (as illustrated in Fig. 4.1). During the deposition, the oxygen partial pressure of ~ 0.2 mbar was maintained dynamically. The energy fluence of the laser was kept constant at 2 J/cm^2 with a fixed substrate temperature of ~ 700°C followed by moderate post-annealing treatment in the presence of oxygen at ~ 400 mbar. These superlattice configurations are different as compared to the previous report by Lee *et al.* where LSMO/LNO $(4.5\text{ nm}/1.5\text{ nm})_{10}$ superlattices are fabricated on the (001) oriented STO single crystal by the radio frequency magnetron sputtering method [91]. The x-ray powder diffraction method was employed to study the crystallinity, phase-purity, and structure of the grown superlattices using a Phillips X'pert MRD based x-ray diffractometer with a working wavelength of 1.5405 Å. The surface morphology of the superlattices was captured using an atomic force microscope (AFM) from Oxford (Model-Cypher) at room temperature. A HORIBA Jobin Yvon Raman spectrometer was used to obtain the Raman spectra of the superlattice samples using backscattering geometry at room temperature with the laser source of wavelength ~ 488 nm. To probe the temperature and field dependence of dc-magnetization characteristics of the samples, we employed a SQUID magnetometer and PPMS-VSM instruments from Quantum Design. Typical protocols, such as the zero-field-cooling (ZFC) and field-cooling (FC) modes, were implemented to probe the magnetic behaviour of the system. The local atomic environment and the electronic/chemical structure of the foresaid superlattices were studied by the X-ray photoelectron spectroscopy (XPS) technique. For this, we employed an XPS instrument from Thermo Fisher Scientific 250Xi, which is capable of attaining ultrahigh vacuum (~ 10^{-7} mbar). The calibrated binding energy of the XPS spectrometer was fixed at 284.8 eV with a carbon 1s peak. The electron transport

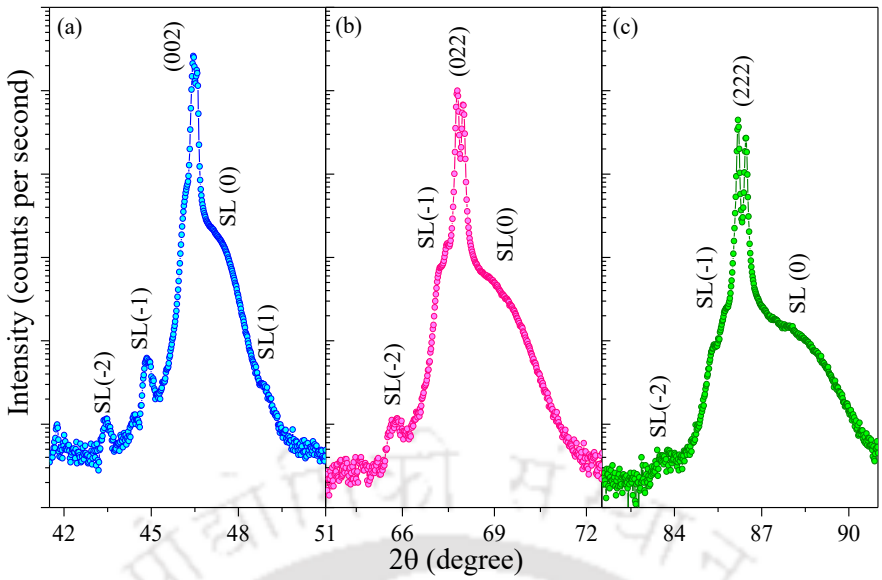

Fig. 4.2. X-ray diffraction pattern (measured under the θ–2θ scan configuration) of $[La_{0.7}Sr_{0.3}MnO_3/LaNiO_3]_{10}$ superlattices (SLs) deposited on $SrTiO_3$ substrates of different orientations: (a) (001), (b) (011), and (c) (111). SL(0) represents the reflection pertaining to the mean *c* axis parameter of the SL. One can clearly notice the satellite peaks (SL) on either side of the main reflections (002), (002), and (222) of the superlattices defined as SL-001, SL-011, and SL-111.

measurements were carried out using a homemade four-probe resistivity setup assembled with the liquid He based low-temperature accessory. All the measurements were performed in the longitudinal geometry where the current was sent along the film plane and the magnetic field was applied parallel to the current direction. The resistivity data as a function of temperature were recorded while warming the sample platform between temperatures T = 5 and 300 K. In the following sub-sections first, we provide the results and analysis of experiments performed on $[La_{0.7}Sr_{0.3}MnO_3/LaNiO_3]_{10}$ superlattices.

4.3 Results and Discussion:

4.3.1 Low-angle X-ray reflectivity and texture:

Figure 4.2 illustrates the θ–2θ x-ray diffraction patterns of $[La_{0.7}Sr_{0.3}MnO_3/LaNiO_3]_{10}$ superlattices deposited on STO with three different orientations, which are distinguished as SL-001, SL-011, and SL-111. From the diffraction pattern, one can clearly notice the presence of satellite-reflections labelled by SL(±1) on either side of the main peak SL(0) of (002) reflection; however, due to the broadening, these satellite-reflections are difficult to notice very clearly across (022) and (222) reflections at high angles of SL-011 and SL-111, respectively. Nevertheless, these satellite-reflections indicate the periodic structure of the layer stacks in the superlattices. The peak positions of LSMO and LNO are almost identical and they are closely spaced with each other in the intensity–2θ plane, and the average out-of-plane pseudo-cubic lattice parameter is ~ 3.765, 3.763, and 3.768 Å for SL-001, SL-011, and SL-111, respectively.

Cubic crystal lattice structure suggests the lattice parameters *a*, *b*, and *c* to be equal and the angles, α, β, and γ to be equal to 90°. $CaTiO_3$, and $SrTiO_3$ are two well-known examples of cubic oxide perovskites

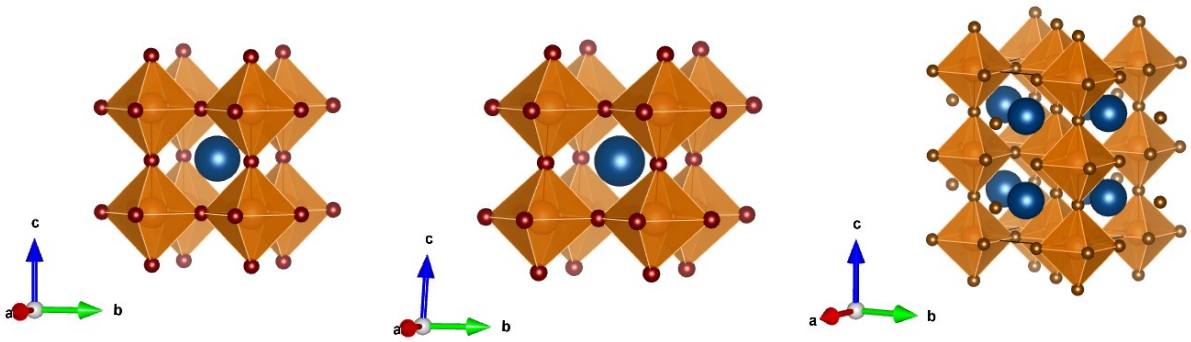

Fig. 4.3. Schematic crystal lattice representing the cubic, pseudo-cubic and tetragonal structures varying according to their lattice parameters.

with lattice parameters 3.8967 Å and 3.905 Å with space group $Pm\bar{3}m$ [180, 181]. The deviation of one of the lattice parameters from its' cubic symmetry i.e. $a = b \neq c$ makes it tetragonal phase and further change from tetragonal to $a \neq b \neq c$ makes it an orthorhombic structure. But during the structural phase transition from cubic to tetragonal, the systems adhere to stay in the cubic itself and resist the phase transformation and sometimes fail to fetch the perfect cubic symmetry with equal lattice parameters. In such case the resulting phase consists of lattice parameters $a \approx b \approx c$ and the angles α ≈ β ≈ γ which says the lattice parameters are nearly equal but not in an explicit manner. This resultant phase is known as Pseudo-cubic. It neither completely tetragonal nor cubic with the parameters look like almost same shown in Fig. 4.3.

In Fig. 4.4 given below, the substrate is a perovskite material with lattice parameter 3.8900 Å and pertaining to the cubic symmetry with space group $Pm\bar{3}m$. On the top of this single crystal substrate, a material (M) with cubic symmetry but different lattice parameter 3.6900 Å is grown to one-unit cell thickness. The interface explicitly shows that the lattice parameter of the material has to adjust itself in order to match with the lattice parameter of the substrate in order to be stable. In this process, the material will

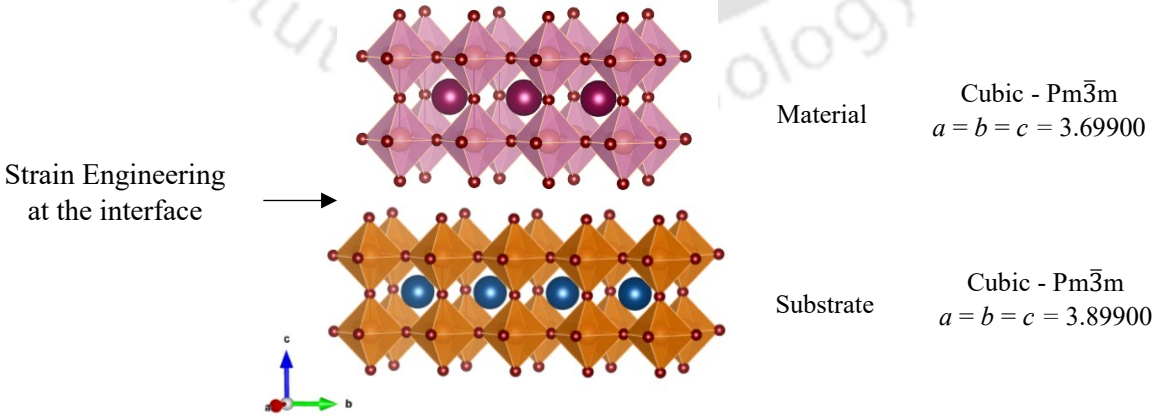

Fig. 4.4. Schematic representation of strain that appears in the in-plane lattice parameters of the material due to its' mismatch with the in-plane lattice parameters of the substrate which results in a pseudo-cubic structure in material.

change its' lattice parameters *a* and *b* at the interface while *c* remains almost same. The difference in the lattice constants of the substrate and the material is also very less which signifies the grown material will have the lattice parameters almost cubic but not perfectly cubic as it has in its' bulk form. This nearly cubic symmetry with small differences in their lattice parameters is referred as Pseudo Cubic crystal structure. This kind of structural phases arises due to the temperature conditions that is maintained during the grown of thin film as well. This phenomenon is very often appearing in the thin films, heterostructures, and superlattice multilayers.

Both LSMO (3.87 Å) and LNO (3.83 Å) encounter a tensile strain on the 001-$SrTiO_3$ (3.905 Å) substrate when these compounds are transformed into a thin-film form. Moreover, the lattice mismatch between the LSMO and STO is 0.9% and the value is around 1.9% for LNO. Thus, the LSMO grown on the bare STO substrate carries the same lattice mismatch between LNO on LSMO/STO. Such lattice strain between the LSMO and LNO is estimated to be around 1.03%. In contrast, the lattice strain of LSMO on 011-STO (2.76 Å) and 111-STO (2.25 Å) is estimated to be around 0.7% and 0.8%, respectively. Here, it is important to note that the LSMO films grown on (011) and (111) substrates are anticipated to experience similar lattice strain on the (001) substrate. Hence, in the present case, the overall repetitive superlattice structure is cumulatively contributing to the strain instead of the substrate contribution alone. The doublet feature in the substrate peaks [Figs. 4.2(b) and 4.2(c)] is more prominent at higher angles indicating the role of both $K_{\alpha1}$ = 1.54056 and $K_{\alpha2}$ = 1.54439 Å of the *x* rays. Figure 4.5 shows X-ray reflectivity (XRR) patterns of $[LSMO/LNO]_{10}$ superlattice for (001) and (111) orientations. The Kiessig fringe pattern of the

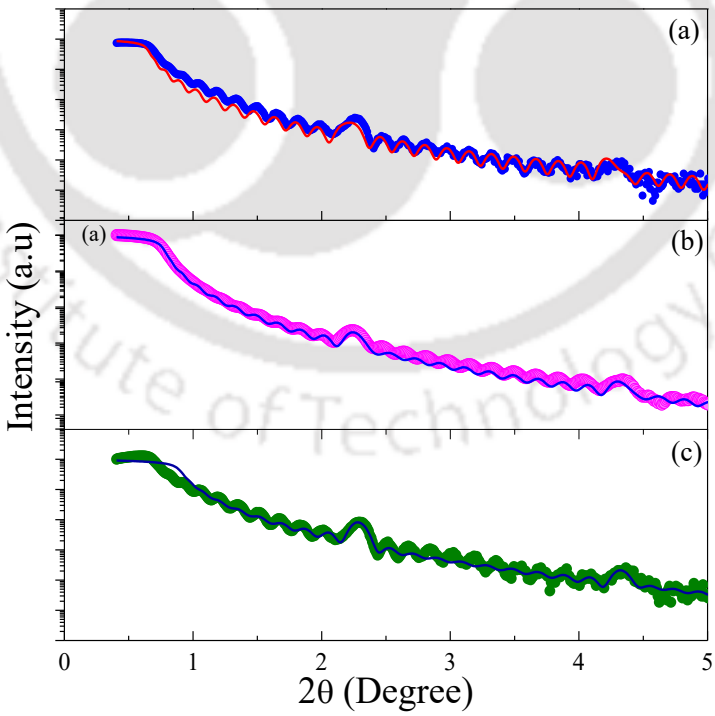

Fig. 4.5. X-ray reflectivity measurement of $[(LSMO)/(LNO)]_{10}$ SL grown on (a) STO (001), (b) STO (011), and (c) STO (111). The solid line represents the simulated pattern, and the scattered symbols represent the experimentally obtained data.

investigated system reveals the uniformity of the layer surfaces and the sharp interfaces of the superlattice with perfect periodicity of stacks which are free from any atomic layer diffusion. Also, from the analysis of XRR data, the thicknesses of individual LSMO and LNO layers are estimated, which are consistent with the deposited parameters. The thickness and the roughness of each superlattice are determined by the XRR data fitted by using GenX software. The estimated thickness and roughness of LSMO/LNO are found to be 3.97/2.84 and 0.9/0.24 nm for the (001) orientation, 4.2/3.0 and 1.3/0.22 nm for the (011) orientation, and 4.02/2.79 and 0.76/0.29 nm for the (111) orientation. In the present case, the average mass densities of LNO and LSMO are found to be ~7.01 and 6.2 g/cc, respectively. These are almost comparable to the mass density of bulk LNO of ~7.2 g/cc and bulk LSMO of ~6.5 g/cc.

4.3.2 Surface topology using Atomic force microscopy:

To understand the surface topology and the probable growth mechanism, we performed atomic force microscopic (AFM) measurements. Figure 4.6 characterizes the two-dimensional (2D) [(a)–(c)] and three-dimensional (3D) [(d)–(f)] AFM surface topology images together with the line profiles [(g)–(i)] for SL-001, SL-011, and SL-111, respectively. All the three systems display a uniform growth pattern. One can clearly distinguish the grain growth between these three systems, particularly the SL-111 system exhibits a quite different morphology as compared to the other two SL-001 and SL-011 systems. Upon close examination, one can clearly notice tiny islands along with the layer growth. Nevertheless, from 3D mapping, the overall surfaces of these two systems achieved a granularly packed structure with varying peak valley heights (3D) and coalescence of adsorbate islands. On the other hand, 3D images of SL-111 display uniform peak heights in which the growth mechanism is quite different with a higher degree of strain and chemical

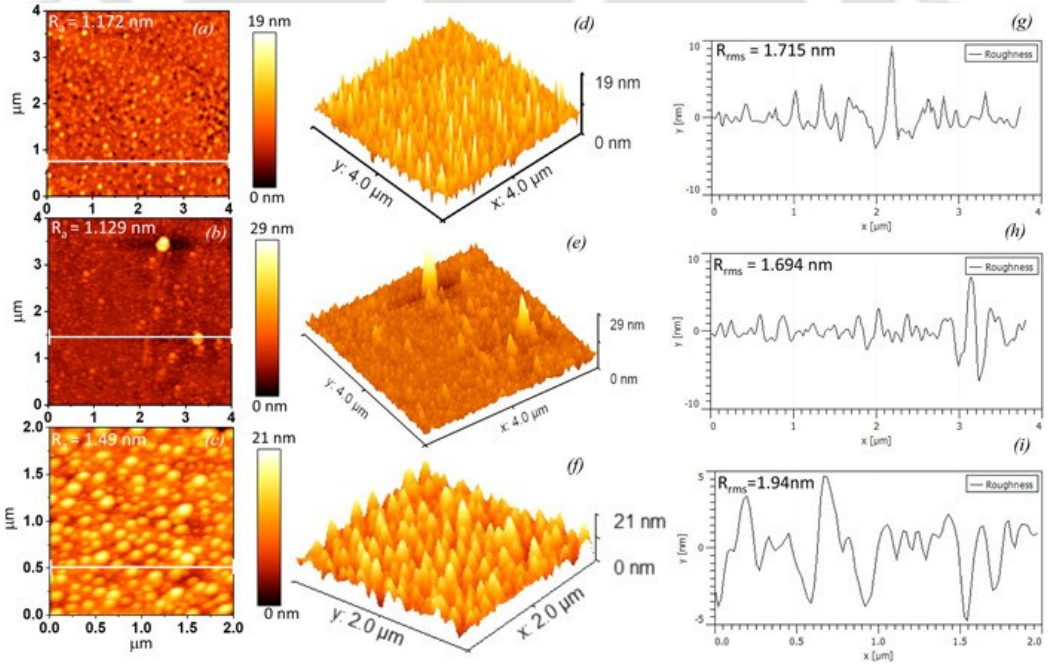

Fig. 4.6. The atomic force microscope (AFM) two-dimensional (2D) [(a)–(c)] and three-dimensional (3D) [(d)–(f)] surface topology images of $[La_{0.7}Sr_{0.3}MnO_3/LaNiO_3]_{10}$ superlattices grown on $SrTiO_3$ (STO) substrates of different orientations: (001) SL-001, (011) SL-011, and (111) SL-111. (g)–(i) represent the corresponding line profiles.

potential in comparison to the topology of the remaining systems discussed above. These results provide the evidence for more sharp interfaces with layer-by-layer continuous growth process with uniform nucleation. Figures (g), (h), and (i) represent the line profiles corresponding to the SL-001, SL-011, and SL-111 systems, respectively, where R_{rms} (1.694 – 1.94 nm) represents the root mean square average of height deviation taken from the mean image data plane and R_a (1.129–1.49 nm) is the arithmetic average of the absolute values of the surface height deviations measured from the mean plane. These magnitudes represent the fact that the investigated superlattice system is having a smooth surface and good quality of the uppermost layer.

To probe the electronic structure and local environment, we performed XPS measurements. Figure 4.7 shows the XPS spectral intensity vs core-level binding energy of various elements present in the SL-001, SL-011, and SL-111 systems: Sr-3*d* [(i), (v), and (ix)], O-1*s* [(ii), (vi), and (x)], Mn-2*p* [(iii), (vii), and (xi)], and La-3*d* [(iv), (viii), and (xii)]. Here, the binding energy of the carbon C-1*s* orbital (~284.8 eV) was used for the calibration of all the core-level spectra. In order to categorize the precise peak position of the core-level spectra for all the elements present in the superlattices, we have examined the measured core-level spectrum of each of the elements based on the peak fitting procedure of the Shirley baseline correction method. All fitting parameters of the experimental data are listed in Table 4.1.

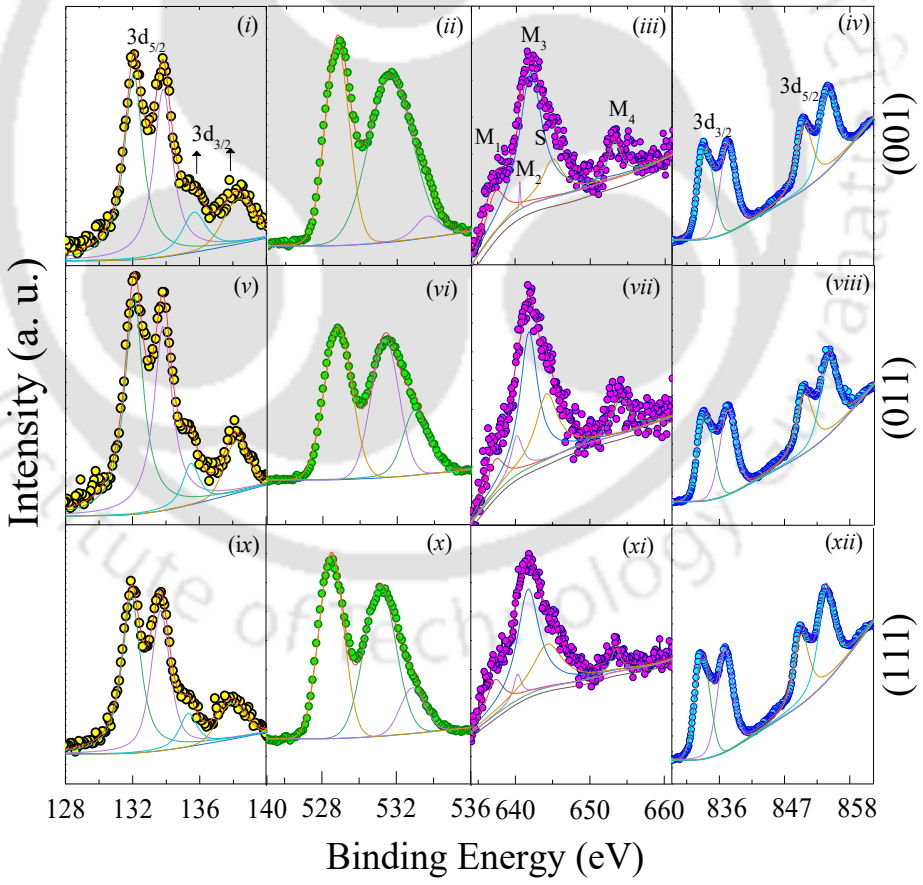

Fig. 4.7. X-ray photoelectron spectra (XPS) of Sr-3*d* [(i), (v), and (ix)], O-1*s* [(ii), (vi), and (x)], Mn-2*p* [(iii), (vii), and (xi)], and La-3*d* [(iv), (viii), and (xii)] of superlattices $[La_{0.7}Sr_{0.3}MnO_3/LaNiO_3]_{10}$ grown on $SrTiO_3$-(001) [(i)–(iv)], $SrTiO_3$-(011) [(v)–(viii)], and [(ix)–(xii)] grown on $SrTiO_3$-(111). Here, S represents the satellite peak.

4.3.3 Probing the electronic structure using XPS:

The binding energy of core-level spectra of Sr-3*d* shows two pairs of peaks with high and low intensities. The first pair of peak positioned at 131.7 and 133.4 eV is attributed to the core-level spectrum of the Sr-3$d_{5/2}$ electronic state with a separation of 1.74 + 0.02 eV, while the other pair of peaks is originating from the Sr-3$d_{3/2}$ electronic state situated at a higher binding energy (137.49 eV) with higher intensity of the first doublet as compared to the second one confirming the divalent oxidation state of Sr [182]. On the other hand, the core-level spectrum of Mn-2*p* shows three main peaks in the binding energy range of 640 – 655 eV, in which the high intensity peak is surrounded by two low intensity cusps on either side. It is well known that the XPS measurements are sensitive only to the top layers of the superlattice and the core-level spectra associated with the interiors layers is not very intense, for example, the Mn spectra have significantly more noise than the others since they correspond to a buried layer. The deconvolution of a Mn-2*p* core-level spectrum required a minimum of five peaks: four main peaks at 637.7 eV(M11), 641.68 eV(M22), 647.79 eV(M33), and 653.5 eV(M44) and one broad satellite peak at 644.9 eV(S). The observed values of spin–orbit splitting $\Delta(M_3{-}M_1) \sim 10.09$ eV and $\Delta(M_4{-}M_2) \sim 11.82$ eV suggest the mixed oxidation state of "Mn" (3+ and 4+) as expected for perovskites [121]. From the fitting, specifically, the peak positions centred at 640.15, 641.15, and 642.6 eV are identified for the valence states of Mn as 2+, 3+, and 4+, respectively [183,184]. The transition pertaining to divalent Mn is more dominant in the SL-001 superlattice as compared to the other systems, while the contribution of other two valence states of Mn (3+ and 4+) gradually enhances with a change in the orientation of substrates from (001) to (111) and (011). The cusp corresponding to these valence states shifts toward the higher binding energy regions signifying the dominance of trivalent and tetravalent Mn in SL-011 and SL-111 systems. Here, it is worth mentioning that the electrons in the e_g electronic state of Mn is able to hop to the nearest valence states of like or unlike ions in the superlattices. Consequently, one can anticipate the electronic charge transfer and recognize the presence of different valence states of Mn in LSMO. In order to find out such an increment of the valence states in Mn, we further iterated the calculations of valence state ratios (Mn^{2+}/Mn^{3+} and Mn^{3+}/Mn^{4+}) by considering the areas under intensive peak of Mn in all three superlattice systems. The relative intensity ratio (RIR) of Mn^{2+}/Mn^{3+} for all the three systems is approximately 0.25, whereas the RIR of Mn^{3+}/Mn^{4+} ratio is equivalent to 0.3, 0.4, and 0.4 for SL-001, SL-011, and SL-111, respectively. Such an increment in the RIR values of Mn^{3+}/Mn^{4+} in SL-011 and SL-111 confirms that the valence states of Mn actively participate in the charge transfer process to other transition-metal elements. A previous study by Wu *et al.* reported the evidence for the divalent Mn ions in the ultrathin films of $LaMnO_3$ from x-ray absorption spectroscopy (Mn L-edge spectra) in the form of a distinct shoulder across 640 ± 2 eV [185]. Similarly, in the present case, we cannot rule out the existence of such a feeble divalent character possibly arising due to the electronic reconstruction across the interfaces or due to the oxygen vacancies [186,187].

Table 4.1. The XPS fitting parameters corresponding to all the three superlattice systems (SL-001, Sl-011 and Sl-111) measured at 300 K.

Mn-2p

Sample	P1			P2			P3			P4			P5		
	BE (eV)	Area	FWHM	BE (eV)	Area	FWHM	BE (eV)	Area	FWHM	BE (eV)	Area	FWHM	BE (eV)	Area	FWHM
SL-001	653.0	6210	5.91	644.9	6621	3.79	641.7	14570	3.80	640.5	168	0.20	637.1	5739	3.81
SL-011	653.5	4880	3.78	643.1	9404	3.75	640.9	14158	3.77	640.2	2027	1.90	637.7	4067	3.79
SL-111	652.9	5152	4.92	643.9	7861	3.82	641.2	18592	3.76	640.3	1349	1.32	637.2	6016	3.74

Ni-2p

Sample	P1			P2			P3			P4			P5		
	BE (eV)	Area	FWHM	BE (eV)	Area	FWHM	BE (eV)	Area	FWHM	BE (eV)	Area	FWHM	BE (eV)	Area	FWHM
SL-001	879.2	137934	14.48	865.0	68165	7.0	861.1	37975	6.87	854.4	10608	2.78	850.4	68468	2.82
SL-011	879.3	35626	6.77	872.2	45156	5.6	862.6	136648	9.84	854.3	99990	2.85	850.2	62786	2.84
SL-111	879.5	54164	7.42	872.2	65151	6.3	861.8	20326	10.78	854.0	96676	2.80	850.1	82015	2.86

Ni-3p

Sample	P1			P2		
	BE (eV)	Area	FWHM	BE (eV)	Area	FWHM
SL-001	68.0	35884	5.15	71.80	658551	--
SL-011	67.7	422496	4.62	71.31	2.09E8	--
SL-111	67.45	45612	4.69	71.01	33093	6.97

On the other hand, the valence states of Ni 2*p*-core levels are situated closely to the core level of the La-3*d* orbital. Moreover, the binding energies of La doublet, i.e., peaks identified at 833.5 and 854.4 eV, originated from the spin–orbit splitting (Δ) of La-3$d_{3/2}$ and La-3$d_{5/2}$ core-level spectra. Separation of these two peaks is approximately estimated as Δ ~ 20.8 eV, which is comparable to the spin–orbit splitting of La [188]. From such mixed intensities of La and Ni core-level spectra, it is difficult to find out the accurate binding energy of Ni-2*p* core-level. Nevertheless, in the present superlattice systems, there is another Ni 2$p_{1/2}$ feature with a low intensive peak identified nearby mixed peaks of La and Ni. Such a feature refers to the different valence states of Ni, while the intensity and the broadness of the peak are increased with a change in the orientation of substrates. Here, the increment in the peak intensity of Ni 2$p_{1/2}$ spectrum with the orientation (SL-001, SL-011, and SL-111) unambiguously indicates the strong interaction/hybridization between Ni-3*d* and O-2*p* [189]. In the case of Ni-3$p_{3/2}$ orbitals, the dominated peak intensity around ~ 68 eV refers to the divalent Ni state (Fig. 4.8). In this case, the peak intensity gradually decreases while the binding energy increases. Moreover, the trivalent Ni state contribution is also evident in the spectrum with significant broadening as seen Fig. 4.8. Therefore, in the present case, for all the superlattices, the Ni-3$p_{3/2}$ state is associated with both valence states Ni^{2+}-3$p_{3/2}$ and Ni^{3+}-3$p_{3/2}$. From the mathematical fits (solid lines in Fig. 4.8), we have estimated the ratio of $Ni^{3+/2+}$ as 0.11, 0.3, and 0.12 for SL001, SL011, and SL111, respectively. These values are almost comparable to the $Ni^{3+/2+}$ ratio of the previous reports [190–193].

Here, the increment of divalent Ni states is consistent with an increase in the valence states of tetravalent Mn ions. Thus, the change in valence states of Ni and Mn unambiguously signifies the charge transfer occurring across the interfaces of the superlattices. Furthermore, depending on the hybridization strength of

Ni-3*d*–O-2*p* bonds, the O-1*s* spectrum is deconvoluted into three Gaussian–Lorentzian peaks centered at 528.82, 531.33, and 532.9 eV, which are associated with the metal–oxygen (M–O) bonding, surface oxygen, and excess oxygen at the surface of superlattices, respectively. Particularly, the core-level XPS spectra centered at 528 and 531 eV reveal that oxygen exists in more than one species with a slightly distorted rhombohedral structure, which provides evidence that the chemical bonding of Ni–O is purely covalent instead of ionic nature [193]. Usually, the alternating stack of polar layers measures the formal charges on the sublayers of each perovskite unit cell. Such polar layers are the important driving force for charge transfer across interfaces of three distinctly oriented superlattice systems studied in this work. The above results reveal a complex local atomic environment across the interfaces, in that the mixed valent $Ni^{2+/3+}$ and $Mn^{3+/4+}$ electronic states prevail at the core level with enhanced relative intensity ratio of the cations in the superlattices grown on (111) oriented STO substrates as compared to those grown on (001) and (011) STO. It is anticipated that the interfacial charge transfer between the polar layers plays a key role on other physical properties of the investigated system.

4.3.4 Electronic transport and magnetic properties

Figure 4.9 illustrates temperature dependence of electrical resistivity ρ(T) of all three superlattice systems, SL-001, SL-011, and SL-111, of different orientations displaying an insulating behaviour all over the temperature scale. The magnitude of resistivity is increased progressively with the change in orientation from SL-001 to SL-111 where both of individual layers, i.e., LSMO and LNO, exhibits a metallic character [194–202].

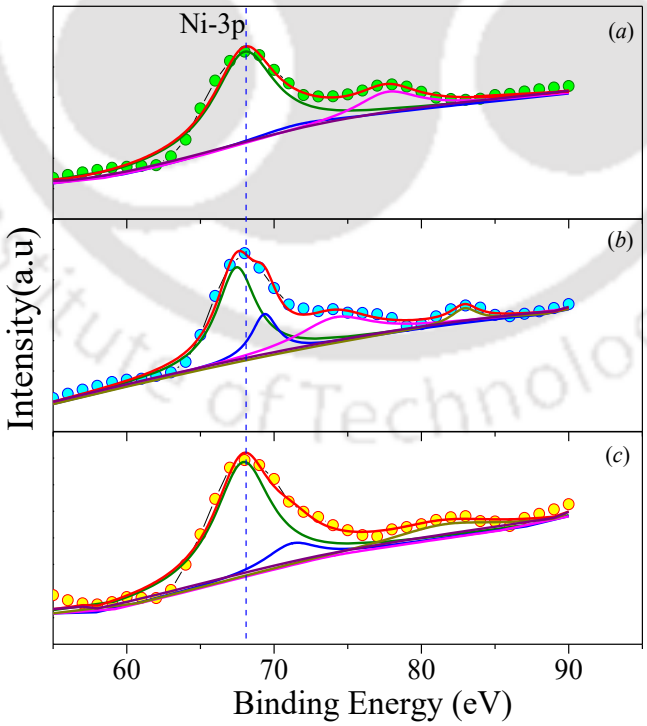

Fig. 4.8. Ni 3*p* core-level x-ray photoelectron spectra (XPS) corresponding to the $[La_{0.7}Sr_{0.3}MnO_3/LaNiO_3]_{10}$ superlattices grown on (a) $SrTiO_3$-(001) (SL-001), (b) $SrTiO_3$-(011) (SL-011), and (c) $SrTiO_3$-(111) (SL-111).

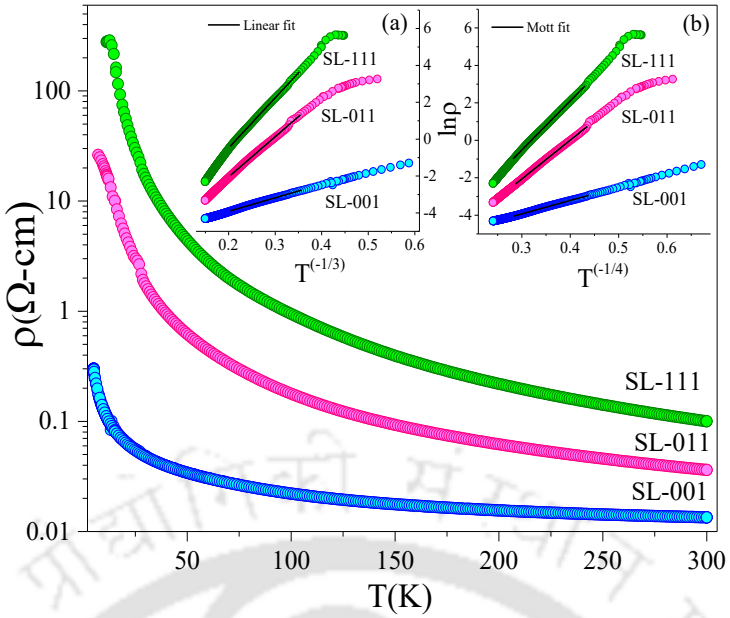

Fig. 4.9. Temperature variation of electrical resistivity ρ(T)ρ(T) of $[La_{0.7}Sr_{0.3}MnO_3/LaNiO_3]_{10}$ superlattices on three different orientations of the STO substrate (SL-001, SL-011, and SL-111). Insets (a) and (b) represent logarithmic variation of ρ(T) plotted against $T^{-1/3}$ and $T^{-1/4}$, respectively, corresponding to the 2D-variable range hopping (VRH) and 3D-VRH models.

In the present case, we expect that the insulating behaviour is driven by the charge transferring electronic states across the interfaces [203,204]. It is well known that the interface between the two layers plays a key role and/or one can anticipate the possibility of a dimensional crossover of charge transport phenomena [204–206]. Such an increasing trend in ρ(T) is accompanied with the localized electron dynamics within the insulating layers, which is analysed by considering the variable range hopping (VRH) model,

$$\rho = \rho_0 \exp(T_0/T)^m \quad (4.1)$$

Here, ρ_0 corresponds to the residual resistivity and T_0 represents the localized temperature. The value of the exponent term in the equation is considered as m = 1/3 and 1/4 for 2D and 3D VRH models, respectively. The fitting of the experimental data with the above described mathematical expression for these two models is provided in the insets of Fig. 4.9, which are referred to as a linear fit to the 2D model (22.4 – 119 K) and a Mott fit for the 3D model (27.2 – 158 K) [195]. The resulting fitted parameters are listed in Table 4.2. Also, the hopping energy ($\epsilon_h = (1/3)k_B T^{2/3}(T_0^{1/3})$) of three superlattice systems for the 2D model and the hopping energy ($\epsilon_h' = (1/4)k_B T^{3/4}(T_0^{1/4})$) for the 3D model are estimated at T = 300 K from the fitting parameters and these values are tabulated in Table 4.2. We noticed a large magnitude of hopping energy (34.56 and 40.33 meV for 2D and 3D cases, respectively) for the SL-111 system, which is due to the high energy gap developed by the accumulation of disorderness in the individual constituents of polar layers [194]. Furthermore, the density of states $N(E_F)$ of the superlattice was calculated for 2D using the relation $T_0 = 13.8/[k_B N(E_F)\alpha^2]$, where α is the localization length and its magnitude is considered to be ~2 Å, which is approximately of the order of the Ni–O bond distance in all three superlattice systems. The order of

Table 4.2. The list of fitted parameters of temperature dependent resistivity values with the 2D- and 3D-VRH models for all the superlattices SL-001, SL-011, and SL-111.

System	ε_h (2D) (meV)	ε'_h (3D) (meV)	N(E_F) (2D) (eV^{-1} cm^{-2})	N′(E_F) (3D) (eV^{-1} cm^{-3})	R_{hp}
SL-001	9.37	11.13	1.0×10^{18}	9.8×10^{24}	0.72
SL-011	27.8	32.16	3.8×10^{16}	1.4×10^{23}	2.15
SL-111	34.56	40.66	2.0×10^{16}	5.5×10^{21}	2.67

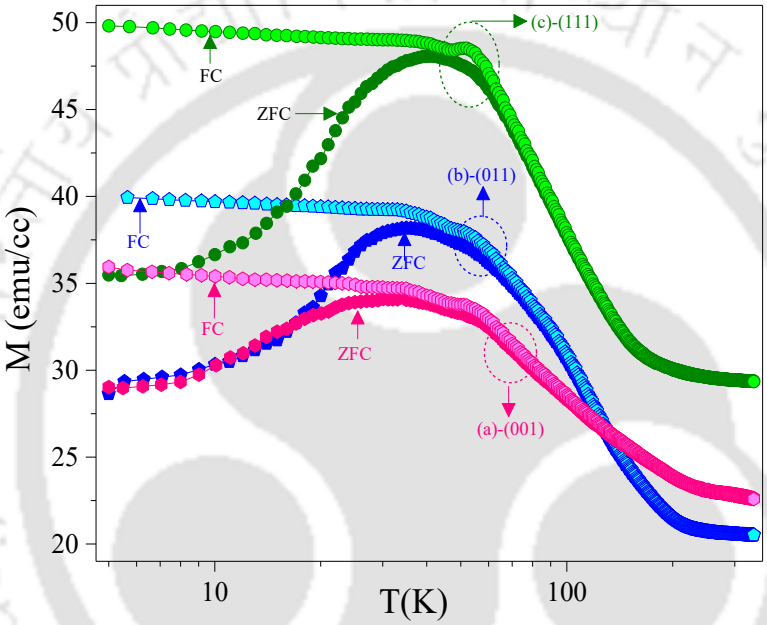

Fig. 4.10. Temperature dependence of magnetization M(T) measured under zero-field-cooled (ZFC) and field-cooled (FC) conditions for the superlattices $[La_{0.7}Sr_{0.3}MnO_3/LaNiO_3]_{10}$ grown on (a) (001), (b) (011), and (c) (111) oriented $SrTiO_3$ substrates. Here, the external magnetic field H_{DC} = 1000 Oe.

magnitudes of N(E_F) is higher in the case of SL-(001) by a factor of two as compared to the other two superlattice systems, and these rough approximations are comparable with the previous results reported in the literature [194].

Furthermore, the ratio of mean hopping distance (R_{hp}) and localized length (α), i.e., $R_{hp}/\alpha > 1$, signifies the validity of the 2D VRH model within the measured temperature range for the superlattices grown on 011 and 111 orientations. Here, R_{hp} is estimated from the relation $R_{hp} = (1/3)\alpha(T_0/T)^{1/3}$ at T = 300 K [195]. However, the R_{hp}/α ratio for the SL-001 system is lower than unity, which suggests that the deviation of resistivity data from the 2D model is due to the low magnitude of resistivity. On the other hand, the analysis pertaining to the 3D-VRH model for m = 1/4 with the localized temperature $T_0 = 5.7/[k_B N'(E_F)\alpha^3]$ is

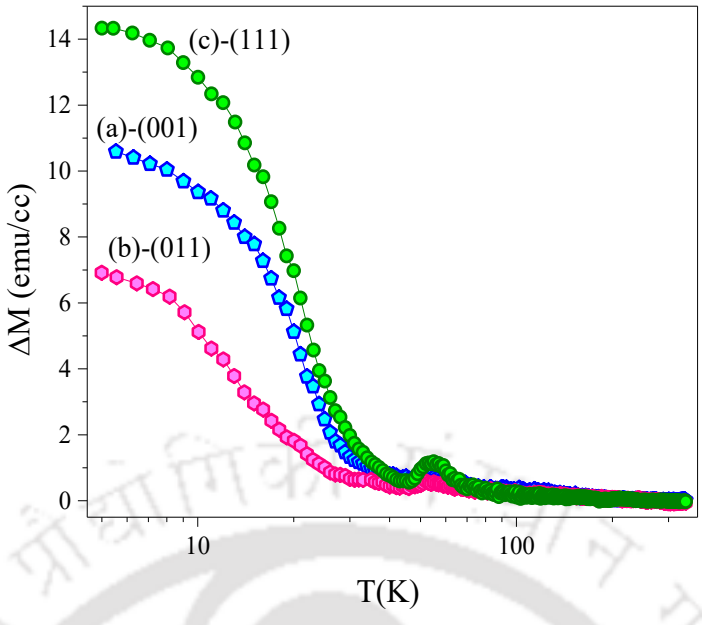

Fig. 4.11. The difference between FC and ZFC magnetization (ΔM) plotted with respect to the temperature for the $[La_{0.7}Sr_{0.3}MnO_3/LaNiO_3]_{10}$ superlattices grown on (a) (001), (b) (011), and (c) (111) oriented $SrTiO_3$.

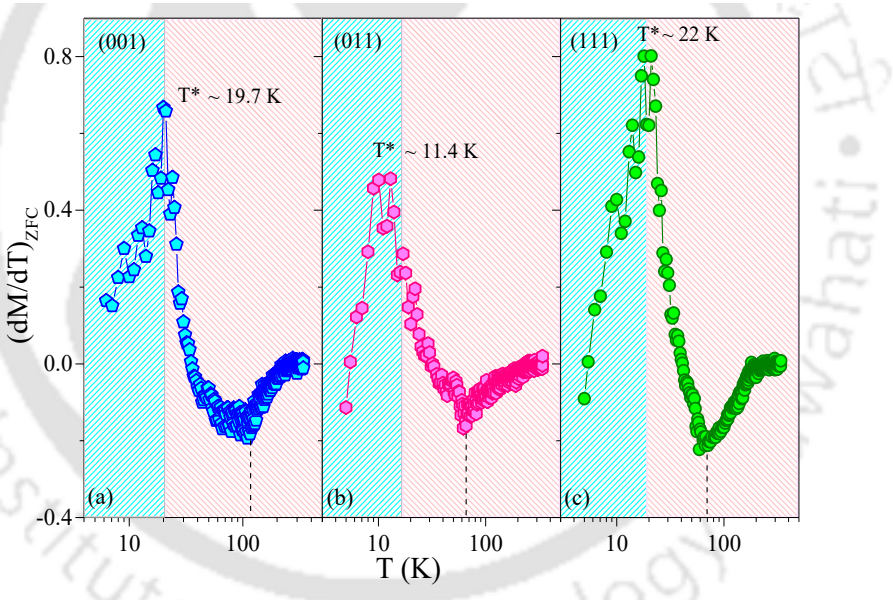

Fig. 4.12. The temperature dependence of differential magnetization plots (dM/dT) calculated form the ZFC magnetization data for the superlattices $[La_{0.7}Sr_{0.3}MnO_3/LaNiO_3]_{10}$ grown on (001), (011), and (111) oriented $SrTiO_3$ substrates (which are labelled as SL-001, SL-011, and SL-111).

quite different as compared to the previous model. In this case, the density of states for the 3D model [$N'(E_F)$] of all three samples is estimated to be nearly two orders higher in magnitude for SL-001 as compared to the other two configurations.

Such an increment in the density of states indicates the substrate orientation dependence of crossover behaviour that might cause a reduction in the electronic charge transferring process across the interface in the SL-001 system. Consequently, there is a chance of substrate orientation induced dimensional crossover that is driven by the strain modification across the individual stacks of the superlattice structure, where

charge hopping is almost negligible across the interface. Nevertheless, the role of interface and orientation is very significant in magnetic properties of the superlattices.

Figure 4.10 shows the temperature dependence of magnetization [M(T)] measured under zero-field-cooled (ZFC) and field-cooled (FC) conditions for the superlattices SL-001, SL-011, and SL-111. Here, the data are recorded with an increase in the temperature after the ZFC/FC protocols in the presence of an external magnetic field H_{DC} = 1000 Oe. We considered the total volume of the superlattice in normalizing the magnetization data to reflect the interface effects also. One can clearly notice large bifurcation between the M_{ZFC} and M_{FC} curves ($\delta \sim$ 14.33emu/cc for SL-111) due to the inherent magneto-crystalline anisotropy and/or finite size effects driven by small thicknesses of the samples. However, the overall magnetization drops significantly at higher temperatures T > 250 K as evident from the temperature dependence of difference magnetization (ΔM) plots obtained from the M_{ZFC} and M_{FC} values (Fig. 4.11). For a precise understanding of the ordering temperatures, we calculated the differential magnetization dM/dT and plotted against the temperature as shown in Fig. 4.12. The ferromagnetic Curie temperature T_C is clearly distinguishable from the minimum of dM/dT vs T plots ($T_C \sim$ 110, 67, and 72 K for SL-001, SL-011, and SL-111, respectively). This T_C is significantly lower in its magnitude as compared to the pristine LSMO compound, which exhibits T_C around 369 K in bulk grain size samples. The magnitude of T_C obtained in the present case is still lower as compared to the monolayer LSMO system, which exhibits $T_C \sim$ 220 and 200 K for $[LSMO/LNO]_x$ superlattices reported previously [195]. However, at low temperatures, dM/dT exhibits maximum (peak T^*), which clearly indicates a completely different magnetic behaviour at low temperatures either due to a weak interlayer/interface driven antiferromagnetic coupling or a spin-glass (SG) (loosely bound spins across interface) state. Among the three superlattice systems, SL-111 exhibits higher $T^* \sim$ 22 K as compared to the other two systems at 19.7 and 11.4 K for SL-001 and SL-011, respectively. Also, the interface will affect the magnetic order significantly at very low-dimensions $t_{LSMO} \leq$ 5 unit cells and the degree of interdiffusion will affect magnetic ordering leading to the reduced magnetic ordering temperatures [207–209].

In order to gain more insight into such a weak AFM/SG behaviour, we performed hysteresis loop measurements at T = 5 K in the FC ($H_{DC} \sim$ 70 kOe) protocol under in-plane geometry. It is well known that the magnetic response of the superlattices grown on STO (011) and (111) oriented substrates exhibits a slightly different behaviour because the in-plane directions are quite different. For example, for STO (011) oriented substrates, the Miller indices of directions are [100] and $[0\bar{1}1]$, and for STO (111) oriented substrates, the Miller indices of in-plane directions are $[1\bar{1}0]$ and $[\bar{1}\bar{1}2]$, while for standard STO (001) oriented systems, the substrate edges are typically cut to align along the [010] and [100] substrate directions. Thus, with a fourfold symmetry, measurements performed along either direction should essentially yield the same magnetic response. Figure 4.13 shows the magnetic field dependence of magnetization (M–H) hysteresis plots for all three superlattice systems, which show negligible asymmetry in the loops from the origin indicating the negligible exchange bias ($H_{EB} \sim$ 110 and 75 Oe for SL-111 and SL-011, respectively). However, SL-111 and SL-001 superlattices exhibit high coercivity $H_C \sim$ 2 and 1.9 kOe, indicating the

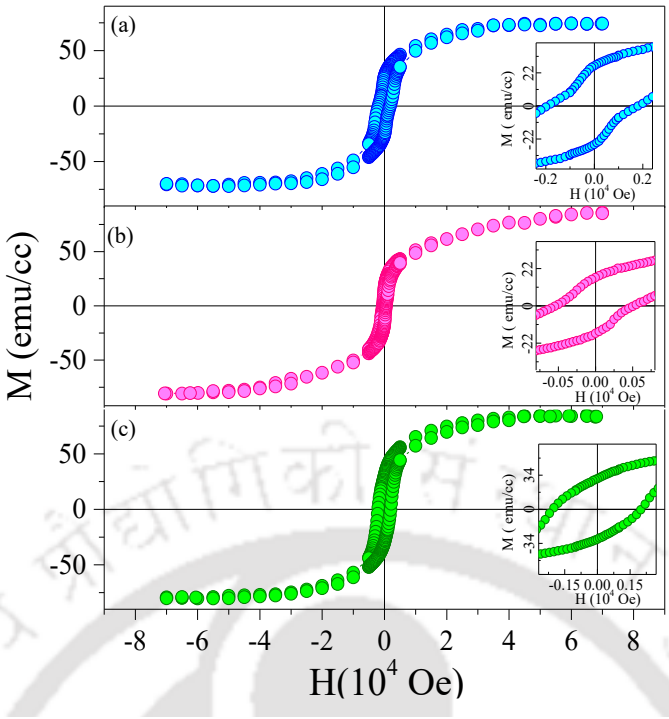

Fig. 4.13. Magnetic hysteresis (M-H) loops recorded at temperature (T = 5 K) for the $[La_{0.7}Sr_{0.3}MnO_3/LaNiO_3]_{10}$ superlattices grown on (a) (001) (blue), (b) (011) (pink) and (c) (111) (green) oriented $SrTiO_3$. The insets are picturized to show the coercive field (H_C) and remanance magnetization (M_R) at low-fields.

predominance of large magneto-crystalline anisotropy present in the system. From this analysis, we conclude that the artificial AFM coupling arising from the interlayer/interface coupling is very weak at lower temperatures; moreover, a feeble exchange bias indicates the charge transfer across the interface of the LSMO/LNO.

On the contrary, the saturation magnetization (M_S) values at high fields show a different trend, in which SL-011 exhibits higher M_S as compared to the SL-001 and SL-111 systems (Table 4.3). The corresponding average ground state-spin (S_{AVG}) configurations are estimated from the expression $M_S = N_A g \mu_B S_{AVG}$, where N_A, g, and μ_B are the Avogadro number (6.023×10^{23}), Landé splitting factor, and Bohr magneton (9.27×10^{-24} JT^{-1}), respectively. Consequently, S^{AVG} turns out to be maximum (0.63) for SL-011, 0.54 (close to 1/2) for SL-111, and 0.46 for SL-001. We have estimated the magnitude of the effective exchange interaction J_{eff} [$= 3T_C k_B/2ZS(S+1)$] in the investigated superlattice systems following the molecular field theory concept with the number of exchange-coupled nearest neighbours Z = 6 with the standard ground state-spin configuration S = 3/2. This analysis yields J_{eff} = 0.63, 0.385, and 0.41 meV for the superlattices SL-001, SL-011, and SL-111, respectively, which is lower as compared to the bulk single crystal values J_{eff} = 2.07 meV. However, the magnitude of J_{eff} evaluated from the S_{AVG} obtained from the current M–H measurements shows significant enhancement of J_{eff} (= 3.52 meV for SL-001, 1.4 meV for SL-011, and 1.86 meV for SL-111). In order to determine the magnetic anisotropy present in the LSMO/LNO

superlattices, we employed the Law of Approach to Saturation, the LAS method, and fitted the experimentally obtained M–H data with the below equation: [210,211]

$$M = M_S\,(1 - a/H - b/H^2) + \chi H \tag{4.2}$$

In the above equation, the last term χH represents the field-induced enhancement of the spontaneous magnetization of the domains (commonly known as forced magnetization); this term is typically small for T < T_C, which is essentially negligible.

While the term a/H is normally inferred due to microstresses/structural defects, the term b/H^2 is due to crystal anisotropy of the material [212]. The solid lines in Fig 4.14 represent the best fits [of the Eq. 4.2] to the experimental data points (represented by symbols). Consequently, we have evaluated the cubic magnetic anisotropy constant K_1 from the expression

$$b = \frac{8}{105}\frac{K_{\text{eff}}^2}{\mu_0^2 M_S^2} \tag{4.3}$$

In the above expression, μ_0 represents the permeability of free space. The magnitudes of a and b are governed by the lower field limit chosen for the fitting of LAS expression.

The origin of the 1/H term and the corresponding parameter a is generally interpreted due to the presence of crystal imperfections such as dislocations, nonmagnetic inclusions/dilution effect, and trapped domain walls [212]. Usually, the 1/H term predominates in the intermediate field range, whereas the term b arises due to crystal anisotropy of the material and the $1/H^2$ term prevails for very large fields (H = $4\pi M_S$). Nonetheless, there are a few complications while applying this equation both from experimental and theoretical points of view. In particular, choosing the lower field limit is quite tricky and depends on the compound and its properties; however, it should be chosen high enough so that the motion of domain walls and rotation of magnetization should be completed on approaching the limited field.

Nevertheless, the changes in magnetization with field at high field regimes are very critical in this case and are considered negligibly small excluding in the vicinity of T_C, which are difficult to probe precisely. For SL-011 superlattices, the magnitudes of K_1 are considerably larger (~ 9.25×10^3 J/m^3) than other superlattices (4.1×10^3 and 1.6×10^3J/m^3 for SL-001 and SL-111, respectively) consistent with the ferromagnetic behaviour of the superlattices. The equivalent fitting parameters evaluated using the above analysis are listed in Table 4.3. Additionally, we evaluated the anisotropy field H_K along (001) using the relation $H_K = 2K_{eff}/\mu_0 M_S$. Among all the systems, SL-011 superlattices exhibit very high values of H_K (~18.2 kOe) (Table 4.3), whereas for the other systems, the magnitude of H_K is significantly low, which lies in the range of 3.67–1.6 kOe due to the decrease of the magnetic exchange interactions [185]. These results are in line with the previous reports both from magnetization as well as using angle dependent torque measurements: quantitatively, the magnitude of K_{eff} ~ 7.2×10^3 and 4×10^3 J/m^3 (H_K ~ 5 kOe) for PLD grown LSMO/(001)-STO thin films of thickness 7.6 and 250 nm STO substrate, respectively [213,214]. In

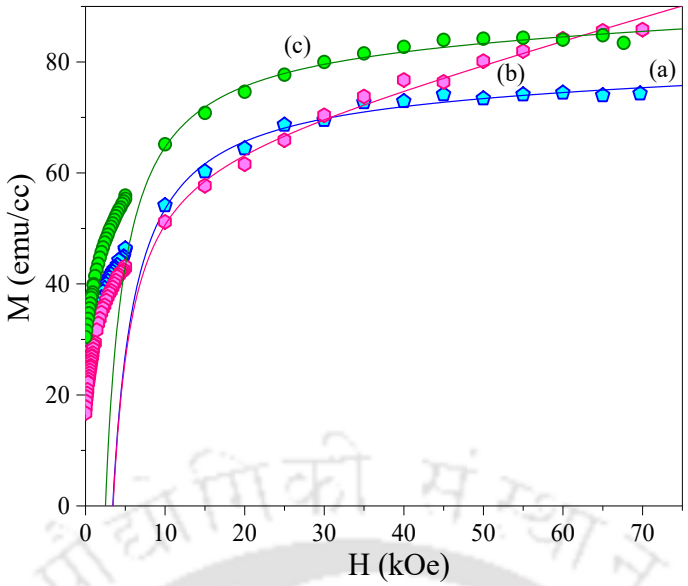

Fig. 4.14. The MH isotherms recorded at 300 K in the first quadrant where the data are fitted with the LAS Eq. 4.2 for SL-001 (a), SL-011 (b), and SL-111 (c).

these studies, no perpendicular uniaxial anisotropy was noticed in which the symmetry axis normal to the plane of the film is expected. Also, previous studies on the angle dependent magneto-optical Kerr magnetometry studies on $La_{0.67}Sr_{0.33}MnO_3$ thin films grown on (001) oriented $SrTiO_3$ substrates reveal large anisotropy features induced by the defects in the crystal structure rather than the magnetoelastic effects [215]. The magnitude of K_{eff} obtained in the present case is one order smaller than that of LSMO-18 nm/$LaCoO_3$-3 nm thin films (220×10^3 J/m^3) grown on (001) oriented $SrTiO_3$ substrates [213, 217]. Similarly, a huge enhancement (5.6×10^5 J/m^3) in the anisotropy energy density was reported in the case of ⟨011⟩ oriented LSMO nanostripes [132]. It is well known that in the case of the bulk single crystals of LSMO, the easy axis lies diagonal to the (111) Miller indices of planes due to the rhombohedral distortion, which is linked to the magnetocrystalline anisotropy of the system [213,218–221]. However, the LSMO (001) sample has an out-of-plane component of magnetization in the bulk with [111] as the easy axis anisotropy, and the magnetization at the surface changes from [111] to [110] direction. Such a predisposition of magnetic moments at the surface essentially decreases the density of surface magnetic charge but pins the bulk magnetic domains intact. From the anisotropy energy point of view, such a tendency is preferable since the Miller indices of the [110] direction makes the minimum angle with the [111] direction as long as the surface spins are bound to the surface plane [213,219,221]. It is expected that the biaxial strain induced by the substrate plays a significant role on the Mn–O–Mn bond distances and bond angles, which, in turn, modifies the degree of the Jahn–Teller splitting of the e_g energy levels causing alteration in the effective spin exchange energy [207,222]. On the contrary, the extent of the Jahn–Teller splitting of the e_g energy levels is negligible in the case of SL-111 superlattices, which essentially causes a drastic change in the anisotropy of the systems and exchange coupling [223,224].

Table 4.3. M-H hysteresis loop parameters for all the superlattices SL-001, SL-011 and SL-111 measured at 5K under field (70kOe) cooled conditions.

System	M_S (emu/cc)	M_R (emu/cc)	H_c (Oe) $(H_+-H_-)/2$	K_1 ($\times 10^3 J/m^3$)	H_K (kOe)
SL-001	74.3	27	-1900	4.1	10.8
SL-011	87	17	-525	9.25	18.2
SL-111	84	30	-2000	1.6	3.67

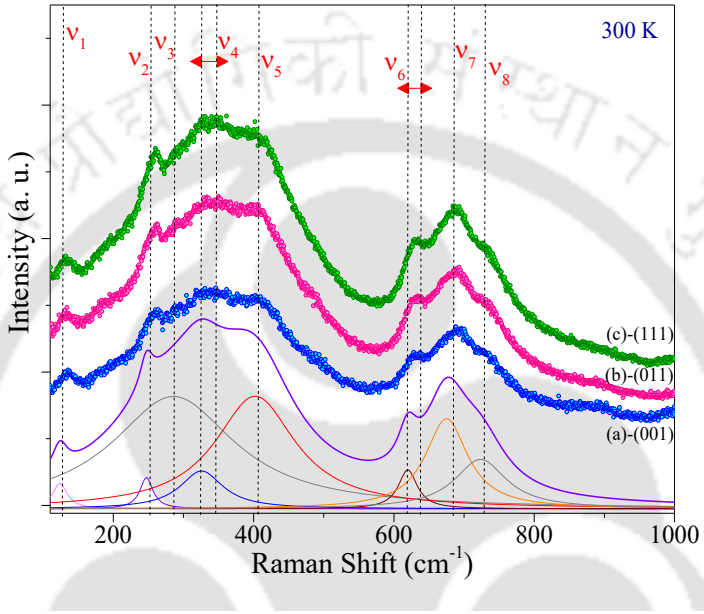

Fig. 4.15. The Raman spectra of the superlattices $[La_{0.7}Sr_{0.3}MnO_3/LaNiO_3]_{10}$ grown on $SrTiO_3$-(001) (a), (011) (b), and (111) (c), respectively, from top. The solid lines represent the corresponding Gaussian fits of each individual modes.

4.3.5 Orientation dependence analysis of Raman spectra:

Since the influence of epitaxial nature and substrate orientation is significant on the resistivity and magnetic properties of the superlattices, we also probed the vibrational modes and symmetry properties using the Raman spectroscopy measurements. Figure 4.15 depicts Raman spectra [Raman shift (cm^{-1}) vs intensity] recorded at room temperature for the three systems SL-001, SL-011, and SL-111 along with the individual Lorentzian peak fittings. In total, seven active Raman modes are discerned at 123 (ν_1), 245 (ν_2), 284 (ν_3), 326 (ν_4), 395 (ν_5), 620 (ν_6), 680 (ν_7), and 728 cm^{-1} (ν_8) in the frequency range of 100 – 1000 cm^{-1}. Substrate to sample individual comparative results are depicted in Figs. 4.16, 4.17 and 4.18 for (001), (011), and (111), respectively, on the same scale in which the solid and dotted lines represent fits to the sample and substrate, respectively, for each mode. Usually, the bulk LSMO stabilizes in the orthorhombic D_{2h}^{16} crystal structure with *Pnma* space group, though the crystal structure changes with the extent of substitution level and with different elements [225,226]. Previous experimental studies on single crystals of this system reported a distorted orthorhombic structure (*Pbnm*) when the Sr substitution is less than 0.175 (x) and transforms to a

Table 4.4. The assignment and the corresponding residing positions of the Raman modes observed in the superlattice systems (SL-001, Sl-011 and Sl-111).

System	Mode 1 (v_1) (cm^{-1})	Mode 2 (v_2) (cm^{-1})	Mode 3 (v_3) (cm^{-1})	Mode 4 (v_4) (cm^{-1})	Mode 5 (v_5) (cm^{-1})	Mode 6 (v_6) (cm^{-1})	Mode 7 (v_7) (cm^{-1})	Mode 8 (v_8) (cm^{-1})
	A_{1g}	$A_g(2) \rightarrow A_g(7)$	A_g (4)	B_{3g}	E_g or A_g / B_{2g}	B_{2g}	-	-
SL-001	121.2-129.4	250	284.2	307.5-351.9	397	619.4	688.1	723.7
SL-011	113.5- 125.1	253.8	284	325.1-347.4	395.5	619.4	680.3	723.7
SL-111	120.9-136.4	251	288.4	319.7-353.2	394.5	620.2	678.2	730.2

rhombohedral structure of the *R-3c* space group for $(x) \geq 0.175$. A similar type of structural deformation occurs in case of thin films of $LaMnO_3$ depending on the oxygen stoichiometry [227]. However, in the present case, we interpreted the Raman spectra based on the *Pnma* symmetry (D_{2h}^{16}) following the previously reported data on the superlattices of $La_{0.7}Sr_{0.3}MnO_3/SrRuO_3$ [225]. In the case of SL-001 superlattices, majority of the spectra closely matches with the (001) oriented bare STO substrate, reflecting the fact that these modes are tightly coupled with the substrate. However, the SL-111 system shows markedly different mode locations in comparison to the bare substrate of (111) orientation. All these changes are listed in Table 4.4.

In general, the rare earth perovskites with orthorhombic *Pnma* symmetry (D_{2h}^{16}) exhibit 24 Raman-active phonon modes corresponding to the factor group analysis: $7A_g^{RS} + 5B_{1g}^{RS} + 7B_{2g}^{RS} + 5B_{3g}^{RS} + 8A_v + 9B_{1U}^{IRA} + 7B_{2U}^{IRA} + 9B_{3U}^{IRA}$ [Raman scattering (RS), vibrational (V), and infrared active (IRA) modes]. These Raman-active modes can be classified into two symmetric and four antisymmetric stretching modes, four bending modes, and six rotation and tilt modes of the octahedra [228,229]. For SL-001, ν_1 modes are assigned to A_{1g} phonon modes; in the present case, a slight shift of these modes is noticed as compared to the standard mode location due the epitaxial stress [230]. ν_2 and ν_3 modes originate due to $A_g(2) \rightarrow A_g(7)$ and $A_g(4)$, respectively, corresponding to the MnO_6 octahedra rotation in the yy direction of $O_1(x)$ atom in the former case giving rise to a small distortion corresponding to the La/Sr (rare earth element R) atomic shift along the [010] direction [218]. The third weak intensity mode ν_3 is associated with the rotation of MnO_6 octahedra in the out-of-phase x direction giving rise to a distortion along the [101] direction [218]. Usually, in the low frequency regime (100 – 200 cm^{-1}), all modes are dominated by the La–O bond vibrations in accordance to the A_g and B_{2g} symmetry or B_{1g} and B_{3g} modes, where the vibrations of La and O1 are either within the xz plane or in the y axis [231].

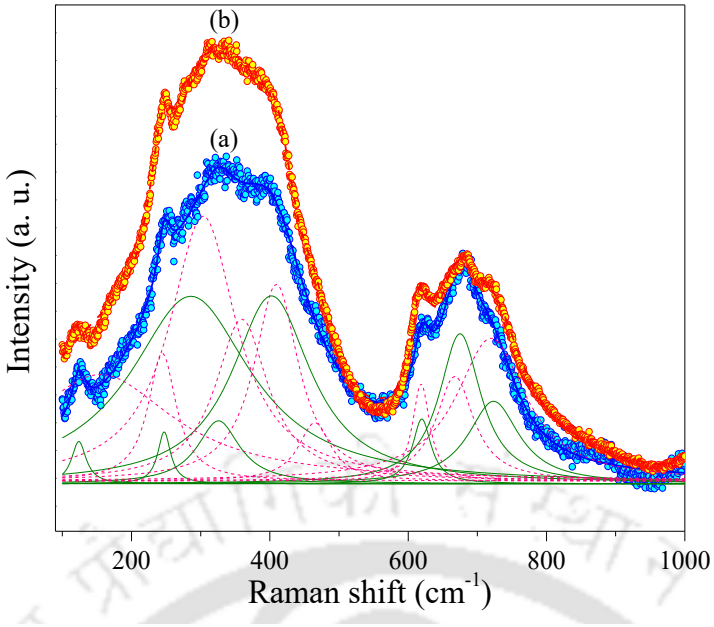

Fig. 4.16. The comparative Raman spectra between the (a) investigated system SL-001 and (b) bare substrate STO-001 recorded at room temperature. The dotted and solid lines represent the Gaussian fits for the sample and the substrate, respectively, of each mode.

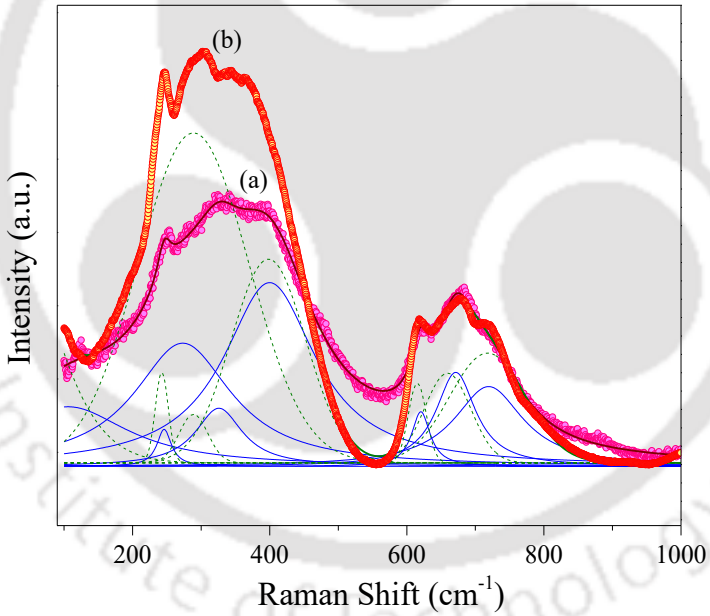

Fig. 4.17. The comparative Raman spectra between the (a) SL-011 system and (b) bare substrate STO-011 recorded at room temperature. The dotted and solid lines represent the corresponding Gaussian fits for sample and substrate, respectively, of each individual mode.

For the low and intermediate frequency region ($200 - 300 cm^{-1}$), the Raman modes are expected to appear due to the tilt of octahedral accompanying the rotations in the x- or y axis [232]. The vibrational modes across 198 and 249 cm^{-1} in the orthorhombic symmetry of LSMO can be assigned to the Ag mode, and the modes between 308 and $620 cm^{-1}$ are associated with the B_{2g} mode [232,233]. The A_g and B_{2g} modes are associated to the bending/rotation of octahedral apical oxygen and stretching of the Mn–O bond, respectively [233,234]. In all the three investigated systems, the transition across 245 cm^{-1}

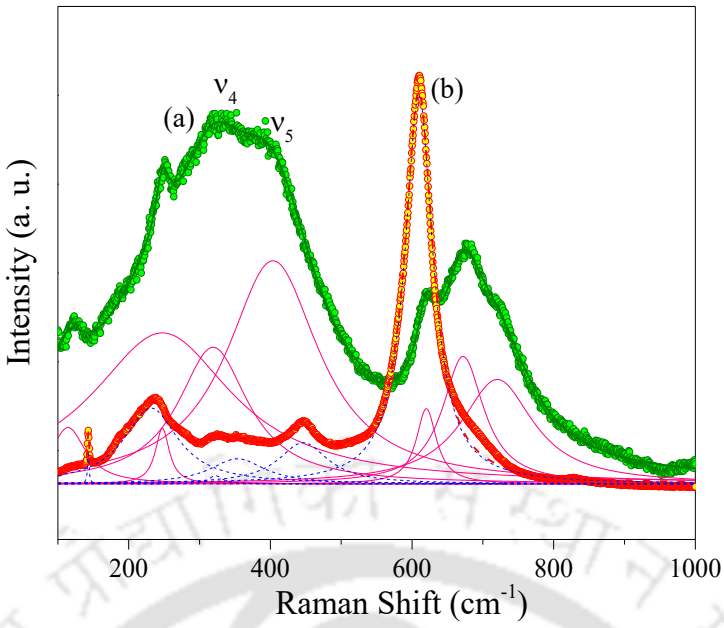

Fig. 4.18. The Raman spectra of the (a) SL-111 system and (b) bare substrate STO-111 recorded at room temperature. The dotted and solid lines represent the corresponding Gaussian fits for the sample and the substrate, respectively.

is associated with the $A_g(2)$ mode in accordance with the results of lattice dynamical calculations reported by El-Aziem *et al* [232]. Interestingly, this mode is shifted toward the higher wavenumber side in the case of the SL-011 system as compared to SL-001 and SL-111 indicating the role of anisotropy.

It is well known that in the case of perfectly oriented single crystals, the macroscopic electric field effect accompanying the longitudinal optic vibrational modes (LOM) lifts the energy degeneracy across the zone centre and causes the emergence of polar optical modes. Due to such effects, LOM usually appear at a slightly higher energy side than the transverse optic modes (TOM) derived from the same triply degenerate acoustic F_{1u} modes [235,236]. Since in the present case no LOMs are noticed, we rule out of the role of the substrate-induced macroscopic electric field (except the strain field) on the global Raman/vibrational characteristics of the investigated system. The transitions between 307.52 and 353.2 cm^{-1} pertaining to the ν_4-mode are arising due to the (100) and (111) STO single crystal substrates (combination of transverse acoustic modes, TAMs, and TOMs: $TOM_2 \pm TAM$, $TOM_2 \pm TOM_1$, and $2TOM_1$) [235]. In the cubic phase of STO, neither the F_{1u} nor the triply degenerate optical modes F_{2u} are Raman active; hence, no first-order Raman lines are traceable at room temperature. On the other hand, the band of ν_5 phonon modes is highly sensitive to the substitution of A-site cations in the perovskite structure, ABO_3 (as the mass of A changes), assigned to the vibrational modes of the oxygen cage/Apical-O in the E_g symmetry of LNO [227,237], [238]. A significant change in the location of ν_5 is noticed in the present superlattices 397 (for SL-111), 395.5 (for SL-111), and 394.5 cm^{-1} (for SL-111). These results are in line with the previous reports where high frequency modes in LNO/Si are noticed between 399 and 451 cm^{-1} [237]. The vibrational modes ν_6 and ν_7 appearing within the bands 618−620 and 678 − 688 cm^{-1} are linked with the MnO_6 octahedral stretching with symmetric and antisymmetric vibrations and characteristic peak [230].

A drastic change of the location of the ν_6 vibrational mode with the orientation of substrates [from 723.7 (SL-001) to 730.2 cm^{-1} (SL-111)] is the main eye-catching spectral signature in which a weak second order two-phonon interaction driven by the local distortion induced in the crystal is very significant, which occurs primarily because of the presence of a polarons. Such transitions usually occur as a consequence of the violation/relaxation of the spectroscopic selection rules due to the crystal symmetry breaking, which, in the present case, may take place across the interfaces of the superlattices [238]. Overall, it is quite evident that all modes closely resemble the substrate characteristics influencing much of the growth pattern and pointing toward the highly oriented epitaxial growth except the ν_4 and ν_8 modes that slightly differ in the case of SL-111 superlattices.

4.4 Summary:

To sum up, we have successfully explored the changes occurring in the physical properties of $[La_{0.7}Sr_{0.3}MnO_3/LaNiO_3]_{10}$ superlattices' (SL) grown on the $SrTiO_3$ substrate with three distinct surface termination (001/011/111) orientations by the PLD technique. From the x-ray reflectivity data, we demonstrated that these superlattice stacks possess well-defined even interfaces between the individual constituent layers of $LaNiO_3$ and $La_{0.7}Sr_{0.3}MnO_3$. AFM mapping reveals the atomically sharp growth characteristics. XPS analysis revealed the presence of mixed valence states of Ni in LNO layers and Mn in the LSMO layer and confirms that charge transferable interfaces are present across the layers. The temperature dependence of the electrical resistivity data validates the 3D VRH model with a large magnitude of hopping energies of the charges ($\geq$ 40 meV) for the SL-111 system. Such a behaviour is associated with the high energy gap developed by the accumulation of disorderness in the individual polar layers. Moreover, the entire superlattice systems exhibit reduced ferromagnetic ordering temperatures ($67 \leq T_C \leq 110$ K) with altered ground state-spin (S_{AVG}) configuration from S=3/2 due to which a substantial enhancement in the effective exchange interaction ($J_{eff} \sim 3.52$ meV) was noticed in these superlattices as compared to the pristine LSMO/LNO systems.

The differential magnetization plots reveal pseudo-antiferromagnetic coupling below 22 K, which is ascribed to the weak interlayer/interface coupling between the layers. Also, the SL-011 system exhibits bulk anisotropy field $H_K \sim 18$ kOe and cubic anisotropy constant $K_1 \sim 9.3 \times 10^3$ J/m^3 in comparison to the other two orientations. The Raman spectroscopy data demonstrate the dominant directional dependent features in the investigated system; in particular, the second order two-phonon interaction caused by the local polaronic distortion leads to major changes in the location of vibrational excitations. This work demonstrated a great potential of exploring directional dependent changes in complex magnetic layers and their tunability for the magneto-electronic applications, which may provide more emergent physical phenomena across the interfaces.

Chapter 5
Magnetic ordering and phonon instabilities in $Dy_{1-x}Ce_xCrO_3$

In this chapter we primarily give emphasis to the changes occurring in magnetic, structural and phonon spectra of $Dy_{1-x}Ce_xCrO_3$. A systematic study of various compositions of Ce substitution on the perovskite lattice of dysprosium chromate ($DyCrO_3$) which exhibits quite unique magnetic behaviour at low-temperatures such as spin-reorientation transitions exchange bias etc. We start this chapter by providing a detailed background of the parent compound followed by the experimental techniques and their results. Analysis of the results and their comparative discussions with similar family of compounds are illustrated in the third section. Finally, we provide a brief summary of the important results obtained in this family of perovskite system.

5.1 Background Literature:

The rare earth perovskites (REPs) which exhibit local orthorhombic lattice distortion have been the subject of intense research activity since last few decades because of their unique electronic and magnetic properties [239–242]. Some of the characteristics, such as, metal-to-insulator transitions, giant/colossal magnetoresistance, charge-ordering, multiferroicity, exchange-bias, magnetic compensation and piezo/pyroelectricity noticed in these compounds make them important candidates to use as switching devices and other magnetoelectronic devices [243–252]. Among the REP oxides, chromite systems mainly $DyCrO_3$, $YCrO_3$, $SmCrO_3$, $EuCrO_3$ and $CeCrO_3$ are the interesting compounds not only from the view point of their novel magnetic and electronic properties but also owing to their excellent gas sensing and photocatalytic characteristics [251–258]. There are few studies on such systems that report field-induced polarization, switching characteristics, and strong magnetoelectric effects, which open up a constructive approach in designing novel switching devices apart from their gas-sensing applications [259]. Among these chromites, $DyCrO_3$ is quite an interesting system because it exhibits antiferromagnetic (AFM) behaviour below the Néel temperature ($T_{N_1} \sim 140$ K) and also develops ferroelectric domains due to off-centre displacement of the Cr^{3+} (d^3) ion leading to a strong magnetoelectric coupling [260,261]. At room temperature $DyCrO_3$ exhibits an orthorhombic structure with space group *Pbnm* or *Pnma* and displays *G*-type AFM characteristics below T_{N_1} with feeble canted ferromagnetic (FM) signatures. Depending on the ionic radius of the rare-earth (RE) ion, the AFM ordering may vary from 110 K to 230 K [262,263]. Apart from all these, the temperature dependence of the magnetization, $M(T)$ of $DyCrO_3$ and its sister compounds $ErCrO_3$/$YbCrO_3$ are fairly comparable to that of $HoCrO_3$ (10.4 μ_B) in which the $M(T)$ data provides clear signatures of spin-reorientation transition temperature ($\sim$ 24.8 K in case of $DyCrO_3$) along with the weak FM character [264]. Nevertheless, such weak FM character has been understood based on the Dzyaloshinskii–Moriya (DM) type antisymmetric exchange interaction [265]. Although the dominant interaction below 50 K is essentially due to the ordered spin system of trivalent Cr ions ($S = 3/2$), the polarized electrons in the lowest-lying Kramers' doublet of the individual trivalent RE ions play a key role

in the low-temperature magnetic properties where strong magnetoelectric coupling is expected for trivalent Ising Dy spins which orders antiferromagnetically below 3.8 K for example [264]. Experimental studies by Yin *et al* provided the evidence for such predictions in which induced electric dipoles in $DyCrO_3$ are formed due to the displacement of trivalent Cr, thus, voiding the d^0 rule [260].

Last few decades have witnessed an unprecedented growth in the studies on $DyCrO_3$ due to the advancements in state-of-art technology. Initial studies by Yamaguchi *et al* reported that the $DyCrO_3$ undergoes stepwise magnetization process in comparison to the one-step magnetization process noticed in $DyAlO_3$ which does not possess any transition-metal ion [262]. Such indirect interaction between trivalent Ising Dy spins induced by the Cr^{3+} – Dy^{3+} exchange interaction, together with the superexchange interaction between Dy^{3+} spins collectively causes the stepwise change in the magnetization. Experimental studies by McDannald *et al.* reported reduction in T_{N_1} (145 K → 140 K) and lowest asymmetric (1.9 K)/symmetric (9.35 K) magnetic exchange interactions in Er substituted $DyCrO_3$ polycrystals [261]. While the Nd substituted $DyCrO_3$ polycrystals exhibit a large negative exchange bias ($H_{eb} \sim -2212$ Oe) between the AFM ordering temperature and spin-reorientation transitions within the canted $\Gamma_{7,Cr}$ phase where a progressively increasing trend has been noticed in the H_{eb} with increase in the Nd substitution at Dy sites [265,266]. It is interesting to note that the mixed perovskites such as orthochromite–orthoferrite $RFe_{0.5}Cr_{0.5}O_3$ (R = Tb, Dy, Ho, Er) exhibits metamagnetic like transitions across 7 kOe along with spin reorientation transitions [267]. Whereas, Sm substitution at the Dy site results in the suppression of the spin reorientation and prominent alteration in the vertical shift in the residual magnetization. Further this substitution yields exchange bias effect under both zero-field-cooled (ZFC) and field-cooled (FC) protocols of *M–H* measurements signifying the important role of trivalent Dy and Sm interaction as compared to the weak FM Cr^{3+} sublattice [268]. On the other hand, the higher magnetic moment of the Dy^{3+} ions (10.65 μ_B) which orders at 216 K is also a potential candidate for the magnetocaloric applications with large magnetic entropy change with relative cooling powers of ~10.85 J kg^{-1} K^{-1} and 256 J kg^{-1}, respectively for a field change of 40 kOe at 5 K. These particular features motivated us to carry out the present work comprising Ce substitution at Dy sites in $DyCrO_3$ system for the first time [269]. Moreover, the other end compound $CeCrO_3$ and its derivatives are equally important systems among the family of rare earth chromates [65]. Regardless of having some synthesis hurdles in preparing the monophasic $CeCrO_3$, it exhibits some remarkable properties such as relaxor-like behaviour in dielectric permittivity, (frequency dispersion in ε_r with peak maximum at 372 K) and AFM behaviour with T_{N_1} as high as 260 K comparable to $LaCrO_3$ which significantly reduces to 178 K along with the unit-cell volume with the incorporation of Eu [270–272].

Despite numerous reports available on these interesting systems, a comprehensive study on the Ce substituted $DyCrO_3$ system has not been done until now in the literature. Therefore, in this work an attempt has been made to synthesize the single phase $Dy_{1-x}Ce_xCrO_3$ with wide composition range $0.1 \leqslant x \leqslant 0.5$ and to study the changes occurring in the crystal structure and the associated variations in the magnetic ordering

and phonon Raman spectra. Our main objective is to probe the changes occurring in the physical properties by tuning the mean cation radius with systematic site dependent substitution of Ce in $DyCrO_3$ which is the key aspect in tailoring the properties of the perovskite system [273].

The following sections has been organized as follows: in experimental section we provide details pertaining to the materials synthesis and characterization. It is followed by the key results and their analysis related to the crystal structure, magnetic ordering and phonon spectra for various levels of Ce substitution in $DyCrO_3$ system. Finally, we provide summary of important results of the investigated system.

5.2 Experimental Details:

In this section we provide a brief description of experimental methodology utilized to characterize various compositions of polycrystalline $DyCrO_3$ perovskite compound synthesized using the conventional solid-state reaction method. For more details, please refer to chapter 2. In brief we used the high purity binary oxides such as dysprosium (III) oxide (Dy_2O_3), chromium (III) oxide (Cr_2O_3) and cerium dioxide (CeO_2) as precursors. Stoichiometric proportions of these oxides were mixed for 5 h in air using the agate mortar with pestle to obtain the homogeneous mixture followed by calcination at 1273 K for 12 h in air. These raw calcined powders were regrinded for 2 h and pelletized by applying 60 kN pressure using a hydraulic press. These pellets were finally sintered for 36 h at 1823 K in air and the cooling procedure was driven by the natural and free cooling in the oxygen atmosphere (rate ~ 2.8° min^{-1}) to the room temperature. This entire process yielded the desired hard dense dark green colour perovskite ceramics of composition $Dy_{1-x}Ce_xCrO_3$. In order to check the phase purity and the compositional variation in the crystal structure, we employed x-

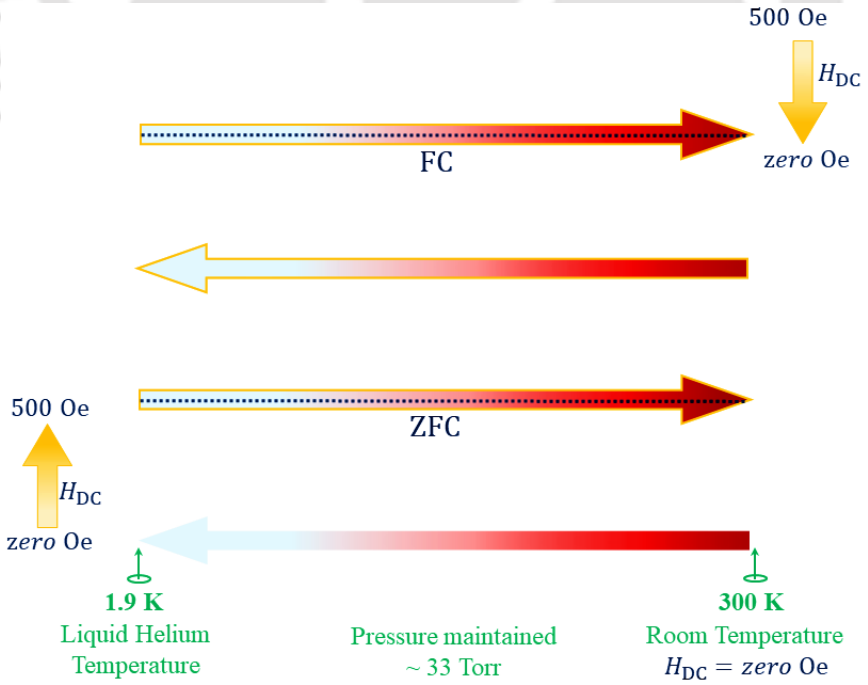

Fig. 5.1. Layout represents the protocol of temperature dependent magnetic measurements performed. High temperatures (red), Low temperature (cyan blue), external magnetic field (orange), and data points (dotted lines).

ray powder diffractometer from Rigaku model: TTRAX III using CuKα_1 radiation (λ = 1.540 56 Å) as source at room temperature. These measurements were performed between the Bragg angles 10° $\leqslant 2\theta \leqslant$ 90° with slow scan speeds (2-degree min^{-1}) at an interval of ~0.02°. These X-ray diffraction patterns (XRD) were refined using Rietveld method by means of FullProf suite and the corresponding crystallographic parameters were extracted for all the compositions. To probe the electronic structure and for the elemental analysis, we employed x-ray photoelectron spectroscope from Kratos Analytical Ltd (model: AXIS Supra+) having Al Kα/Ag Lα (2984.2 eV) lab source. The core-level X-ray photoelectron spectra (XPS) were fitted with the Lorentzian–Gaussian distribution after calibrating with C-1*s* binding energy 282.6 eV and subtracting the background by using Tougaard method.

All the magnetic properties were examined by means of temperature and magnetic field dependence of the magnetization measurements performed with a vibrating sample magnetometer (VSM) equipped with physical property measurement system (PPMS) from Quantum Design (Model: Dynacool) with the field sweep capacity of ±90 kOe and reaching low temperatures upto 1.9 K from 300 K. These measurements were performed under both ZFC-warming and FC-warming protocols (Fig. 5.1). These experiments were complemented by the specific heat measurements performed using PPMS Quantum design by the heat-pulse calorimetry technique. To perform the low temperature measurements, we have maintained a pressure of the order ~33 Torr. To visualize the shift in phonon modes and to characterize the vibrational excitation, we employed Raman spectrometer from HORIBA Jobin Yvon operating under backscattering geometry. In the micro-Raman mode, the exciting laser sources used for the measurement were 632.8 nm (He–Ne laser). In the following we present our results related to structural and magnetic behaviour of $DyCrO_3$.

5.3 Results and Discussion:

5.3.1 Phase evaluation and electronic structure:

Figure 5.2 shows the XRD pattern of the bulk polycrystals of $Dy_{1-x}Ce_xCrO_3$ obtained after sintering for various compositions x between 0.1 and 0.5 along with their corresponding Rietveld refinement data. All these patterns show monophasic nature (perovskite with space group: *Pbnm* with z = 4) of the synthesized samples except for higher compositions $x^* \geqslant 0.6$ where nonmagnetic CeO_2 (*Fm-3m*) emerges as secondary phase. However, our attempts to prepare compositions with x = 0.9 did not yield perovskite structure, thus, we optimized the synthesis parameters including the heat treatment conditions of all the compounds identical with the sample having the lower and intermediate composition range x = 0.1–0.5 only.

Since the trivalent Ce possesses larger ionic radius 1.07 Å more than that of Dy^{3+}(0.912 Å), one can expect significant increase in the unit-cell volume and the cause of difficulty in the formation of single perovskite phase beyond x^*. All the calculated crystallographic parameters are listed in Table 1. It is well known that the REPs with structure (RE)BO_3 (where RE = rare earth material, B = transition metals) usually exhibit distortion in the BO_6 octahedra associated with the tilt in REO_{12} polyhedra which in turn leads to

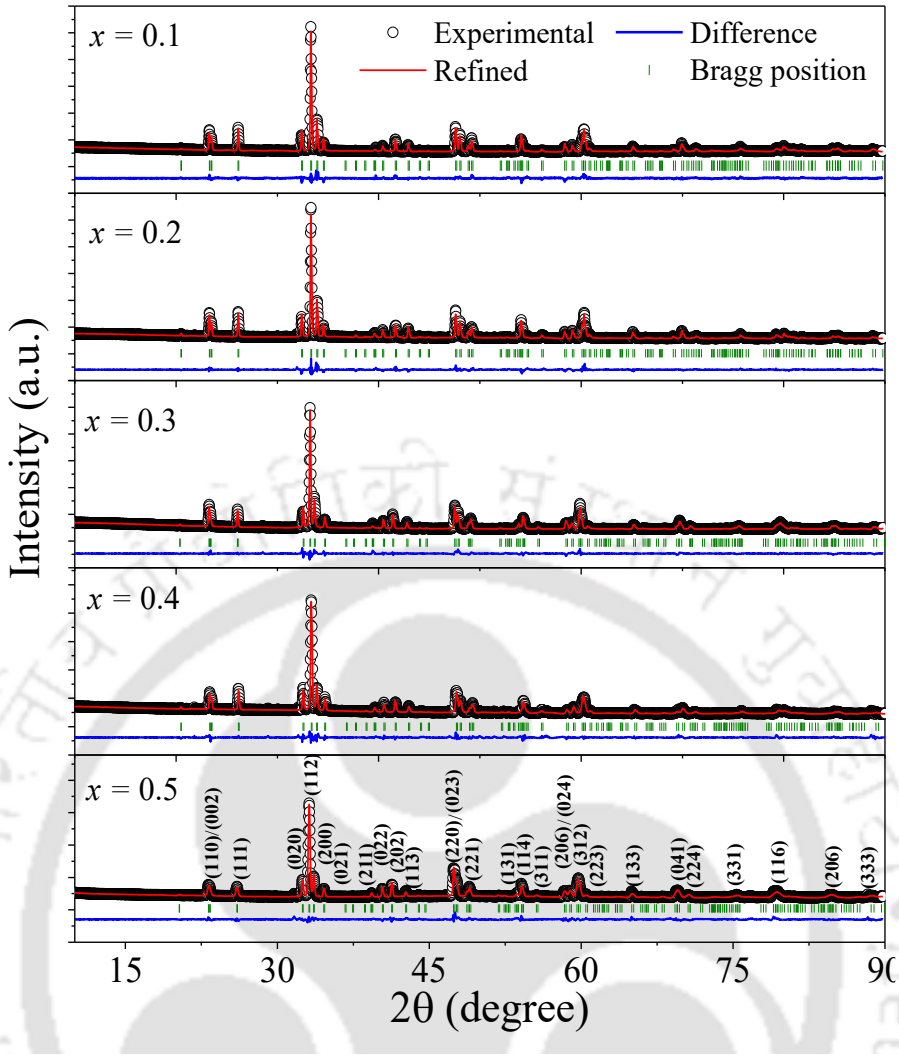

Fig. 5.2. Rietveld refinement of the XRD patterns obtained at room temperature for different compositions of the $Dy_{1-x}Ce_xCrO_3$ ($0.1 \leqslant x \leqslant 0.5$). All the peaks are indexed according to the orthorhombic *Pbnm* space group of perovskite structure wherein the experimental data are shown in the black colour line, while, the refinement data are shown in the red colour line. The difference between them is represented by blue colour line. Here the Bragg positions are displayed by the olive colour vertical lines.

departure from its perfect cubic structure (of space group: *Pm3m*). Similar trend has been observed in the present case as well [274,275].

Here we have considered the cell dimensions of the investigated system as $a \approx b \approx \sqrt{2}a_p$ and the longer symmetry axis $c \approx 2a_p$, where a_p is the pseudocubic cell parameter of the *Pbnm* structure [276]. These primitive cell parameters match well with both the end compounds $CeCrO_3$ and $DyCrO_3$ [65,261]. Now, the variation of the lattice parameters has been visualised with respect to the A-site cationic radius (Dy and Ce) as it is more convenient and better way to represent the structure. The mean radius (R_{Mean}) has been calculated by using the following expression [275]

$$R_{Mean} = \sqrt{\left[(1-x) \times R^2_{Dy^{3+}}\right] + \left[x \times R^2_{Ce^{3+}}\right]} \quad (5.1)$$

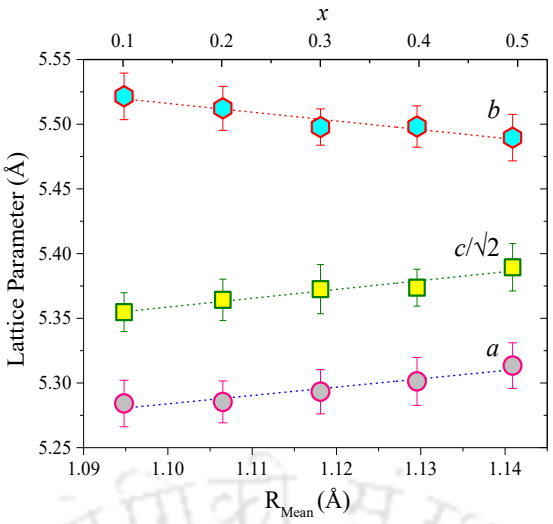

Fig. 5.3. The variation of the primitive cell lattice parameters (*a*, *b* and *c*) with respect to the mean cationic radius (R_{Mean}) of A-site ions in the $Dy_{1-x}Ce_xCrO_3$ lattice. Here *x* varies from 0.1 to 0.5. The data points representing square, circle and hexagon are corresponding to *a*, $c/\sqrt{2}$, and *b* respectively. The lattice parameter exhibits increasing behaviour along the *a* and *b* axis upon increase in R_{Mean} while it shows decreasing trend along *b* axis upon increase in R_{Mean}. The top axis represents the doping concentration of Ce.

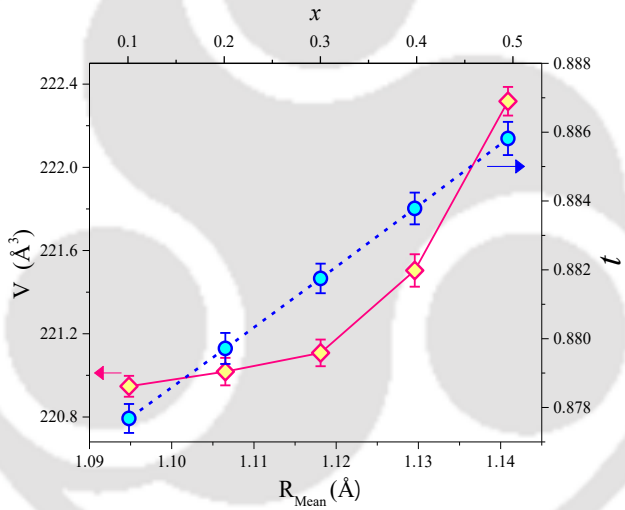

Fig. 5.4. The variation of the unit cell volume (V) and tolerance factor (*t*) of the Ce doped $DyCrO_3$ systems with respect to their mean A-site cationic radius (R_{Mean}). The top axis represents the doping concentration of Ce.

Here, radius of $R_{Dy^{3+}}$ = 1.083 Å with IX coordination number and that of$R_{Ce^{3+}}$ = 1.196 Å with same coordination number and the magnitude of R_{Mean} for the intermediate compositions lies between the pristine ($DyCrO_3$) and the end compounds ($CeCrO_3$). All the compounds with different compositions stabilize in orthorhombic crystal structure *Pbnm* (no. 62) with slightly distorted structure that closely resemble with the pristine system $DyCrO_3$.

In Fig. 5.3 we represent the variation of all the three lattice parameters ('*a*', '*b*' and '*c*') as a function of R_{Mean} in which one can clearly notice a progressively increasing trend of unit cell volume, *V* (Fig. 5.4) with the increment of R_{Mean} in which both *a* and *c* follows the Vegard's law. However, *b* shows an opposite

trend. These magnitudes are falling in between the standard lattice constants of the two end compounds: a = 5.276(5.485) Å, b = 5.529(5.479) Å and c = 7.565(7.735) Å [65,261,273,277]. Nearly 0.62% increment in the magnitude of V has been observed for the investigated system for 4.21% increment in the R_{Mean} as shown in the Fig 5.4 in which the variation of tolerance factor (t) as function of R_{Mean} has also been represented on the right-hand side scale which was calculated using the standard expression given below [275].

$$t = \frac{(1-x)\times R^2_{Dy^{3+}} + \left(x \times R^2_{Ce^{3+}}\right) + R_{O^{2-}}}{\sqrt{R_{Cr^{3+}} + R_{O^{2-}}}} \tag{5.2}$$

In the above expression the $R_{Dy^{3+}}$, $R_{Ce^{3+}}$, $R_{Cr^{3+}}$, and $R_{O^{2-}}$ represent the ionic radii of the individual ions Dy, Ce, Cr, and O, respectively. The linear variation of the $t(R_{Mean})$ is in consonance with the $V(R_{Mean})$ both of which provide evidence for the incorporation of higher radius Ce diffused into the perovskite lattice of $DyCrO_3$ causing slight distortion to the orthorhombic crystal structure. The scale of the deviation (d_{Cell}) from the ideal cubic structure *Pm3m* has been estimated with the help of the following equation which is plotted in Fig. 5.5 along with the magnitude of octahedral distortion as given in Eq. 5.3.

$$d_{Cell} = \frac{10^2}{3a_p^2}\left[\left(\frac{a}{\sqrt{2}} - a_p\right)^2 + \left(\frac{b}{\sqrt{2}} - a_p\right)^2 + \left(\frac{c}{2} - a_p\right)^2\right]^2 \tag{5.3}$$

In the above expression, a_p being the pseudocubic primitive cell parameter considered as the average $\frac{1}{3}\left(\frac{a}{\sqrt{2}} + \frac{b}{\sqrt{2}} + \frac{c}{2}\right)$ [276]. Here the magnitude of d_{Cell} (in ppm) diminishes from 341.45 ppm (for x = 0.1) to 178.74 ppm (for x = 0.5) which indicates the relaxation of the cell distortion with increasing the Ce^{3+} (large size) substitution at the D y^{3+} sites. This result is consistent with the fact that the higher end compound

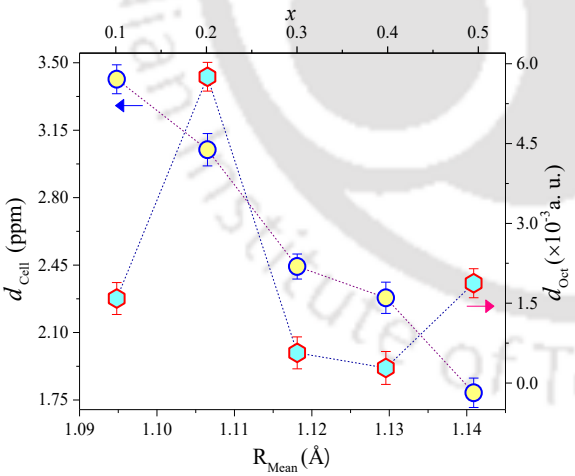

Fig. 5.5. The cell distortion factor (d_{Cell}) of $Dy_{1-x}Ce_xCrO_3$ (with $0.1 \leqslant x \leqslant 0.5$) plotted as a function of mean cationic radius (R_{Mean}) which is calculated using the Eq (5.3) from the refinement data. While the octahedral distortion (d_{Oct}) factor plotted along the right-hand side scale with respect to R_{Mean} is calculated using the Eq (5.4). The top axis represents the doping concentration of Ce.

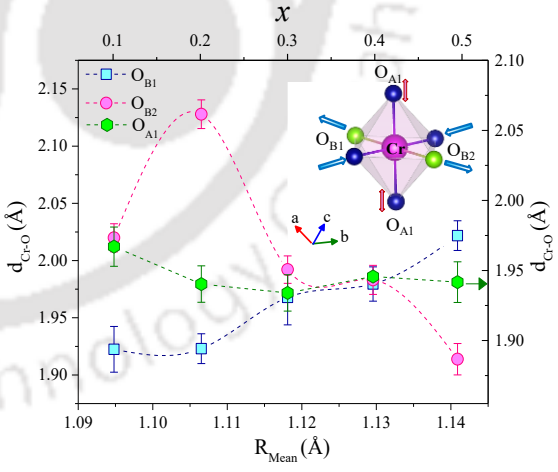

Fig. 5.6. The Cr–O bond length (d_{Cr-O}) variation plotted as a function of the mean cationic radius (R_{Mean} for $0.1 \leqslant x \leqslant 0.5$) at A-site of the perovskite structure which has been calculated from the Rietveld refinement. The dotted lines are the visual guides and the inset depicts the schematic of the octahedral distortion. The top axis represents the doping concentration of Ce.

$CeCrO_3$ exhibits nearly perfect cubic structure with lattice parameter a = 3.89 Å [278]. In order to probe the exact octahedral distortion occurring in the present system we calculated the octahedral distortion (d_{Oct}) factor using the below expression [271,279].

$$d_{\mathrm{Oct}} = \frac{1}{6}\sum_{i=1}^{6}\left[\frac{d_{(\mathrm{Cr-O})i} - d_{\mathrm{avg}}}{d_{\mathrm{avg}}}\right]^2 \quad \text{where}$$

$$d_{\mathrm{avg}} = \frac{1}{6}\sum_{i=1}^{6} d_{(\mathrm{Cr-O})i} \tag{5.4}$$

The variation of d_{Oct} with R_{Mean} (as shown in the *right-hand scale* of Fig. 5.6) exhibits cusp like anomaly which increases between x = 0.1 and 0.3 with a maximum at x_p = 0.2 consistent with the previous studies in which the averaged bond distances between IX coordinated Cr alters along with the basal and the apical oxygen atoms [279]. This distortion across x_p is also associated with the weak FM characteristics observed in the magnetic measurements of the present system, which will be discussed in detailed in the latter sections. It is well known that the distortion factors are related to the octahedral tilt angles θ and ϕ in the pseudo-cubical planar rotation of the [101] and [010] axes which are calculated both from the lattice parameters and atomic positions, these magnitudes are listed in the Table 1. The tilt angles calculated from the atomic position using the relations are $\theta = \tan^{-1}\frac{\sqrt{2w_{O1}^2 + 2u_{O1}^2}}{c}$ and $\phi = \tan^{-1}\frac{\sqrt{2w_{O2}^2 + 2u_{O2}^2}}{\sqrt{a^2+b^2}}$. Following the notation of O'Keeffe and Hyde, the distortions in the perovskite structure can essentially be described by only one tilt angle Φ about the 'three-fold axes' of the regular octahedra. This Φ can be estimated from the following

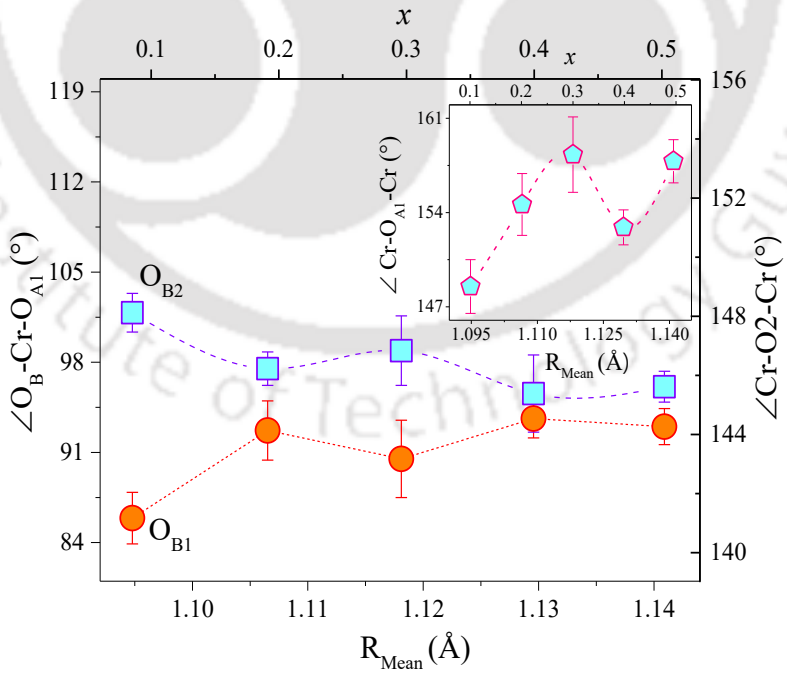

Fig. 5.7. The variation of the bond angle $\angle O_{B1}$–Cr–O_{A1} and $\angle O_{B2}$–Cr–O_{A1} derived from the Rietveld refinement with respect to mean cationic radius, R_{Mean}. The inset represents bond-angle $\angle$Cr–O_{A1}–Cr variation with R_{Mean} for the composition range $0.1 \leqslant x \leqslant 0.5$. The top axis represents the doping concentration of Ce.

expressions (from lattice parameters): $\Phi = \cos^{-1}\frac{\sqrt{2}a^2}{bc}$, $\theta = \cos^{-1}\frac{\sqrt{2}a}{b}$, and $\phi = \cos^{-1}\frac{a}{b}$, and the corresponding relation between θ, ϕ and Φ is given by $\cos\Phi = \cos\theta\cos\phi$ [218,280]. Usually, the value of θ estimated from atomic positions of O atoms along the [101] pseudo axes varying from 10.36° (for x = 0.1) to 12.25° (for x = 0.5). Whereas, θ is estimated from the lattice parameters of the primitive cell shows an opposite trend with an increase of 3.41% as x varies between x = 0.1(9.32°) and x = 0.5(14.56°). However, the tilt angle related to [010] axes shows nearly 14% change between the two compositions. These results induce the tilting angle Φ shift from the 'three-fold-axes' which reduces from 19.20° to 17.39° upon increasing Ce content from x = 0.1 to x = 0.5. Overall our results demonstrate that the anomalous reduction of the tilt angles is associated with the relaxed CrO_6 octahedral distortion with increasing the Ce substitution and these results are consistent with the previous reports [275,280].

From the Fig 5.6, we can clearly visualize the change in the interatomic separation between the oxygen and the transition metal Cr ($d_{Cr–O}$) in basal plane (O_{B1}, O_{B2}) and apical oxygen atoms (O_{A1}). The O_{A1} atoms residing along the longer c-axis are quite rigid and they do not vary much as compared to the oxygen atoms residing on the a–b basal plane (O_{B1} and O_{B2}) which change their position freely with respect to the Cr-atoms. As the Ce substitution increases from x = 0.1 to 0.5 a significant elongation of $d_{Cr-O_{B1}}$ is noticed within the a–b plane. On the other hand, $d_{Cr-O_{B2}}$ shrinks to 1.914 Å which can be easily visualized from the inset of Fig. 5.6. The bond lengths $d_{Cr-O_{B1}(\downarrow)}$ and $d_{Cr-O_{B2}(\uparrow)}$ show opposite trend below a certain composition x = 0.3 and become comparable between R_{Mean} = 1.12 Å and 1.13 Å, and deviates beyond x = 0.4. The maximum up-rise in $d_{Cr-O_{B2}}$(2.125 Å) occurs at x = 0.2 which is in-line with the compositional variation of octahedral distortion discussed above. The elongation and the contraction of the bond lengths of the Cr-basal oxygen atoms are actually responsible for the distortion in CrO_6 octahedra. While the stretching of the $d_{Cr-O_{B1}}$ can be understood on the basis of the competition between diagonally distorted CrO_6 octahedra, whereas, the $d_{Cr-O_{A1}}$ bond remains almost unaltered in terms of distortion [279].

Both the basal oxygen atoms vary their positions symmetrically with respect to each other by increasing the Ce composition, while the apical oxygen atoms position deviate from the c-axis with a marginal skew angle ~11° confirming the bending of the CrO_6 octahedra along c-axis. The bond angle $\angle O_{B2}–Cr–O_{A1}$ between the basal and apical oxygen atoms exhibits a maximum skewness of around 17° for R_{Mean} = 1.09 Å and 1.14 Å corresponding to the compositions x = 0.1 and 0.5 (see Fig. 5.7) and reduces to 2.5° when the mean radius is maximum depicting the minimum tilt of the octahedra in the a–c or b–c plane [271]. As the Ce substitution increases beyond x = 0.3 the system eventually moves towards more stabilized region with significant reduction of the distortion (inset of Fig. 5.7). The apical oxygen and the rare earth Dy/Ce change their positions in random fashion inside the primitive cell. The absence of linearity in their position with respect to composition do not have any direct correlation with the changes occurring in the position of CrO_6 octahedra. Such changes in the bond angles and bond lengths play a very important role on the magnetic exchange interactions and decide the global magnetic ordering of the system which will be discussed in the later sections.

Table 1. The calculated parameters obtained from the refinement of the powder X-Ray diffraction results of $Dy_{0.9}$ $Ce_{0.1}CrO_3$ (DCO1), $Dy_{0.8}$ $Ce_{0.2}CrO_3$ (DCO2), $Dy_{0.7}$ $Ce_{0.3}CrO_3$ (DCO3), $Dy_{0.6}$ $Ce_{0.4}CrO_3$ (DCO4) and $Dy_{0.5}$ $Ce_{0.5}CrO_3$ (DCO5).

Parameters	DCO1	DCO2	DCO3	DCO4	DCO5
a (Å)	5.284	5.285	5.293	5.301	5.313
b (Å)	5.522	5.512	5.498	5.498	5.490
c (Å)	7.573	7.586	7.598	7.599	7.6212
V($Å^3$)	220.96(5)	221.02(6)	221.11(6)	221.51(7)	222.32(6)
R_{Mean} (Å)	1.095	1.107	1.118	1.129	1.141
t	0.878 (4)	0.880(5)	0.882(4)	0.884(5)	0.886(5)
θ From atomic positions	10.36	11.94	12.094	12.144	12.254
θ From Lattice Parameters	9.314	9.838	9.855	9.42	9.632
ϕ From atomic positions	18.814	17.36	17.28	16.48	15.87
ϕ From Lattice Parameters	16.862	16.497	15.678	15.384	14.56
Φ	19.198	19.138	18.452	17.979	17.396
R_{wp}	15.9	15.1	14.2	16.7	15.8
R_p	21.4	20.4	18.2	21.9	21.8
$Cr–O_{A1}$ (Å)	1.967	1.940	1.934	1.946	1.9417
$Cr–O_{B1}$ (Å)	1.922	1.923	1.968	1.980	2.022
$Cr–O_{B2}$ (Å)	2.020	2.128	1.992	1.983	1.914
$Cr–O_{A1}–Cr$ (º)	148.51	154.6	158.3	152.902	157.81
d_{Cell}	341.5	304.9	244.28	228.04	178.7

Figures 5.8(a)–(d) show the core-level XPS spectra of all the elements present in the perovskite system for the Ce composition $x = 0.3$. The core level spectra of all the elements were calibrated with the C-1*s* binding energy 284.8 eV. The binding energy dependence of the ejected photoelectron intensity is probed for each of the element separately. The Dy-4*d* core level spectra are deconvoluted into three peaks located at 151.4 eV (not fitted), 153.3 eV, and 156.2 eV. Among these core level transitions, the peaks are residing at 153.3 eV and 156.2 eV with an extra hump at 151.4 eV. The peak at 153.3 eV is generated due to the Dy–Cr bond associated

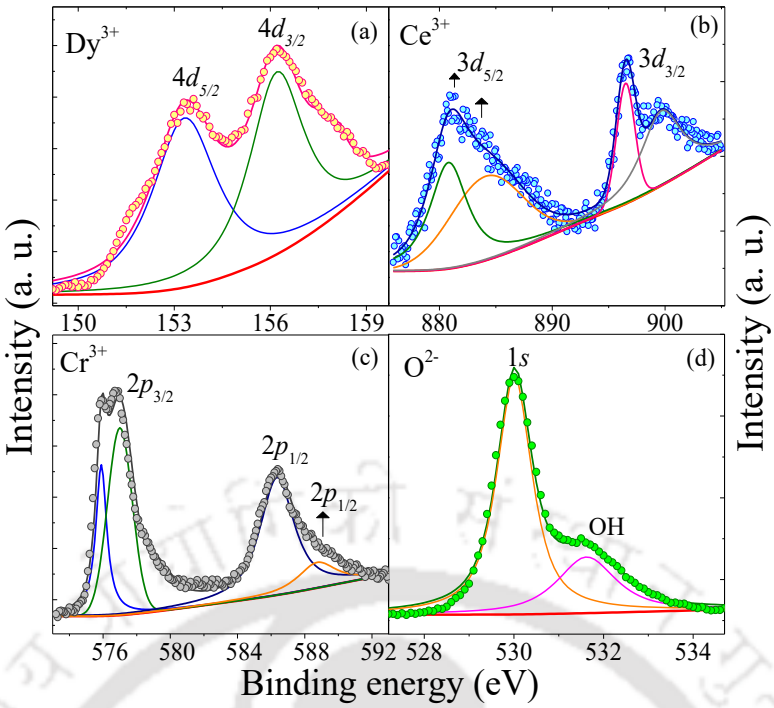

Fig. 5.8. The core level x-ray photoemission spectra corresponding to the individual constituents of $Dy_{0.7}Ce_{0.3}CrO_3$ bulk polycrystalline sample: (a) Dy-4*d* (b) Ce-3*d* (c) Cr-2*p*, and (d) O-2s core levels. Here the scattered symbols represent the experimentally obtained data points while the solid lines represent the peak fitting data.

with $4d_{3/2}$ and the one at 156.2 eV is due to Dy–O bond associated with the $4d_{5/2}$ orbitals present in the system [281]. However, the shoulder across the binding energy 151.4 eV is due to metallic Dy^0 with $4d_{5/2}$ core levels [282]. These two peaks are separated by the difference in the binding-energy, $\Delta \sim 2$ eV are commonly characterized as the spin–orbit coupling strength and its magnitude confirms the trivalent oxidation state of Dy in each composition. On the other hand, the deconvolution of Ce-3*d* core-level spectra require four independent peaks located at 880.8, 884.5, 896.4, and 899.3 eV corresponding to the doublets at $3d_{5/2}$ and $3d_{3/2}$ in-line with the previous studies cited in the reference [283]. The core level of Ce with xenon like configuration with filled *s* orbital and *d* orbital validating the trivalent oxidation state [283]. While the transition metal Cr-2*p* core-level spectra consist of four peaks located at 575.2, 576.9, 586.3 and 588.7 eV in which the peaks centred at 586.3 eV and 588.7 eV are originating from the doublet of $2p_{1/2}$ electronic state. The other two cusps are linked to the $2p_{3/2}$ states with no signature of any satellite peaks. Finally, the oxygen O-1*s* core-level spectra exhibit a highly intense peak across 529.4 eV originating due to O^{2-} ions along with a hump at ~531.5 eV due to the surface absorbed oxygen species from hydroxide (O–H) metal oxygen bond [281]. After discussing the detailed electronic structure, we now move our focus towards the magnetic properties of the Ce substituted $DyCrO_3$.

5.3.2 Magnetic characteristics:

Systematic investigation of the magnetic properties of the discussed system has been performed under traditional measurement protocols such as ZFC and FC at different temperatures (1.9K $\leqslant T \leqslant$ 300 K)

and fields (−90 kOe ⩽ H ⩽ 90 kOe). Figure 5.9 shows the temperature dependence of magnetization $M(T)$ measured under both ZFC and FC conditions in the presence of constant magnetic field (H = 500 Oe). Here the data is collected under warming conditions for both the cases (ZFC and FC). These plots reveal three different transitions in which the main transition from disordered paramagnetic state to low-temperature G-type AFM ordering across T_{N_1} = 151.8 K (for x = 0.1) which shifts to higher temperatures (161 K) upon increasing the Ce content till x = 0.5 (Table 5.2). Below this transition, both $M_{ZFC}(T)$ and $M_{FC}(T)$ monotonously increases and exhibits bifurcation below the irreversibility temperature (T_{IRR} ~ 45.5 K) for x = 0.5 where, T_{IRR} decreases to 31 K as x is decreased to x = 0.2 and finally vanishes.

Here an interesting feature was observed in the lower temperature transitions. The mildly diluted samples of compositions x = 0.1, 0.2, and 0.3 exhibit another prominent spin reorientation transition (T_{SR}) at very low temperatures 3.5 K for x = 0.1 and approaches to zero for the other two compositions (x = 0.4 and x = 0.5). On the contrary, the samples with higher Ce compositions show another transition (T_{PC}) in the intermediate temperature region close to T_{IRR} = 31–45.5 K, for x = 0.2–0.5. However, for very dilute compositions x ⩽ 0.1 this transition cannot be traced from the M–T plots. It is interesting to note that previous studies by Yin *et al* reported two spin-reorientation transitions across T_{SR_1} = 39.2 K and T_{SR_2} = 24.8 K along the x and z axes, respectively, in the $DyCrO_3$ single crystals [263]. This particular feature may be attributed to the rotation of the trivalent Cr moment in the a–c plane [263]. Across the T_{PC}, the trivalent Cr spins undergoes phase transition from $\Gamma_4(Gx, Ay, Fz)$ canted AFM state to a mixed phase Γ_2, where the FM

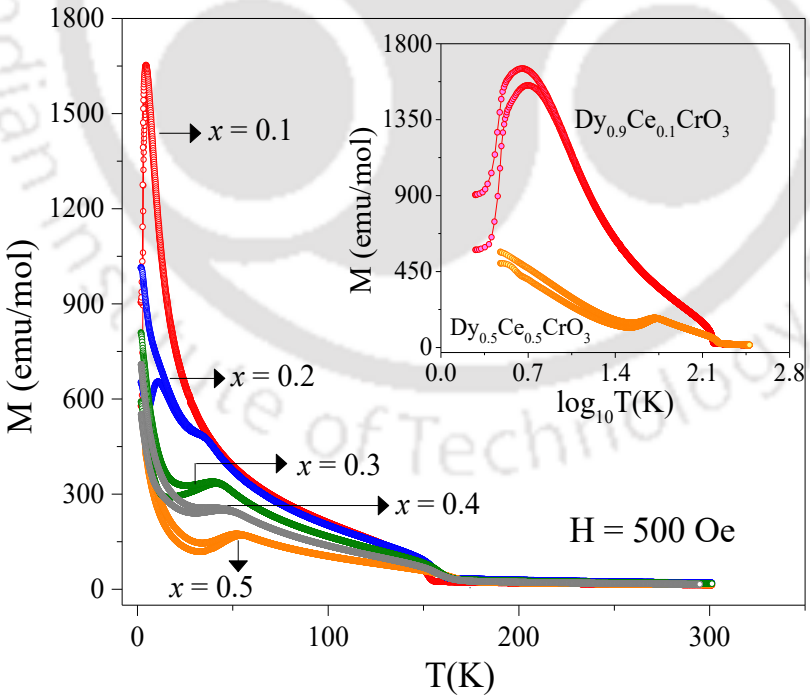

Fig. 5.9. Thermal dependence of magnetization $M(T)$ data for various compositions of the $Dy_{1-x}Ce_xCrO_3$ (0.1 ⩽ x ⩽ 0.5) system measured under ZFC (solid colour) and FC (faded colour) conditions. Here data are recorded while warming the sample from low temperatures 1.9 K to 300 K under the application of external field H = 500 Oe. The inset figure represents comparison of M–T (ZFC and FC) between the compositions x = 0.1 and 0.5.

Table 5.2. The Neel temperature (T_{N_1}), Phase transition temperature (T_{PC}) and the Spin-reorientation temperature (T_{SR}) of all the samples.

Sample Name	T_{N_1} (K)	T_{PC} (K)	T_{SR}(K)
$Dy_{0.9}Ce_{0.1}CrO_3$	151.8	-	3.5
$Dy_{0.8}Ce_{0.2}CrO_3$	154.7	31	8
$Dy_{0.7}Ce_{0.3}CrO_3$	156.4	33.5	16.8
$Dy_{0.6}Ce_{0.4}CrO_3$	157	39.9	-
$Dy_{0.5}Ce_{0.5}CrO_3$	161	45.5	-

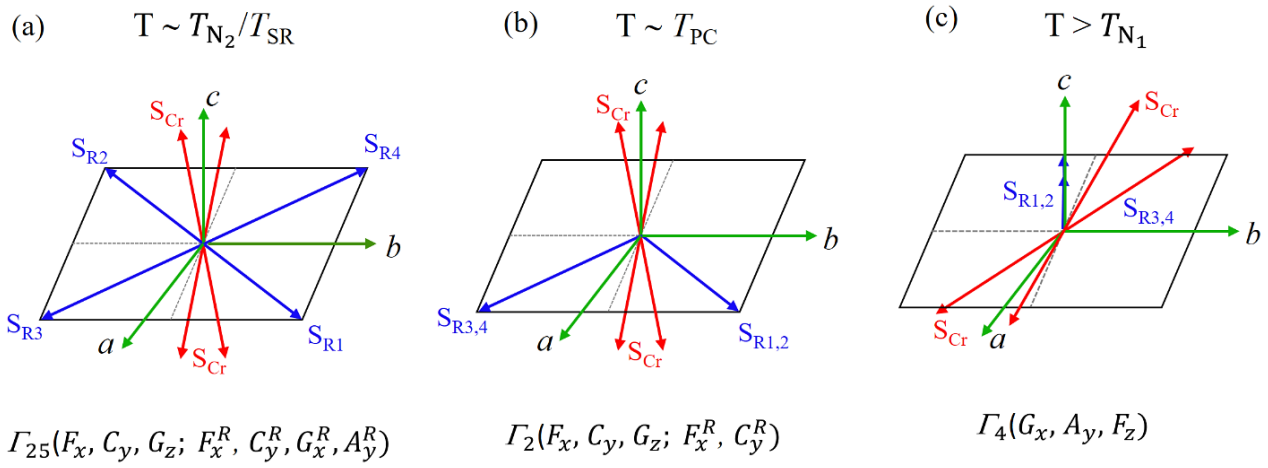

Fig. 5.10. Schematic representation of the temperature evolution of spin arrangements of the rare-earth elements-Dy/Ce (S_{R1}, S_{R2}, S_{R3}, S_{R4} in *blue* arrows) and Cr (S_{Cr} in *red* arrow) in the temperature regions at (a) $T = T_{SR}$, (b) $T = T_{PC}$, and (c) $T > T_{N_1}$ respectively.

component rotates from x to z axis and the spins get aligned towards the trivalent Ce spins partially as a consequence of which the moment decreases below the transition temperature (note that $T = 31$ K for $x = 0.2$ while for $x = 0.5$, $T = 45.5$ K). Similar type of phase transitions often termed as Morin phase which is expected to be of first order in nature linked to the spin-reorientation transition is noticed in the other rare-earth systems such as $DyFeO_3$ (35 K), $ErCrO_3$ (22 K), and $TbCrO_3$ (22 K) [259].

The sublattice spins of trivalent Dy and Cr in $DyCrO_3$ mainly favor two types of spin configurations namely $\Gamma_2\,(F_x,\ C_y, G_z;\ F_x^R, C_y^R)$ and $\Gamma_5(G_x^R, A_y^R)$, although these two configurations are not compatible with each other [284,285]. In the present case we anticipate the Landau's second-order phase transition occurring at T_{PC} is mainly originating due to the change in the free energy. The induced local effective field (H_L) due to the trivalent Cr and coupling between the trivalent spins of the rare-earth ions (Ce and Dy)

belonging to the Γ_2 configuration is illustrated in Fig 5.10. In the present case we also find that the magnetic symmetry group belongs to the $D_{2h}(C_{2h})$ $m'm'm$ [286]. In addition, we noticed that the single-ion anisotropy of highly magnetic Dy^{3+} ions (~10.65 μ_B) is large enough and the spins of Dy^{3+} are usually confined to their easy axes such that the net moment of these ions polarize along the H_L (x-axis). This particular feature yields the configuration of the Dy^{3+} spins as $\Gamma_2\ (F_x,\ C_y, G_z)$ [285,286].

Now we shift our focus towards investigating the effect of temperature on the magnetic properties of $DyCrO_3$. We find that upon decreasing the temperature, the trivalent Dy spins exhibit ordering and influence all transitions below T_{SR} (T_{N_2}). Such ordering of Dy spins corresponding to the onset of weak FM nature arising from the alignment of Dy^{3+} spins along Cr^{3+} spins. This leads to a significant increase of the magnetic moment below T_{SR} having the magnetic structure as $\Gamma_{25}\ (F_x,\ C_y, G_z;\ F_x^R, C_y^R, G_x^R, A_y^R)$ in the absence of external field [287]. So overall, we find that the coupling between the trivalent Dy and Cr spins is mainly responsible for the low temperature spin reorientation which is similar to the case of several other compounds of RE perovskite family which shows weak-FM like behaviour. Here the rare earth spins start reordering themselves due to the influence of magnetic interaction between the rare earth ions [66,261,273,287–290]. The magnitudes of T_{SR} in case of Ce substituted systems (~3.5 K, 8 K and 16.8 K for x = 0.1, 0.2 and 0.3, respectively) are quite high as compared to the second critical temperature T_{N_2}(~2 K) of pristine $DyCrO_3$ single crystals initially reported by Tsushima *et al.* [287]. Such enhancement of the T_{SR} in the

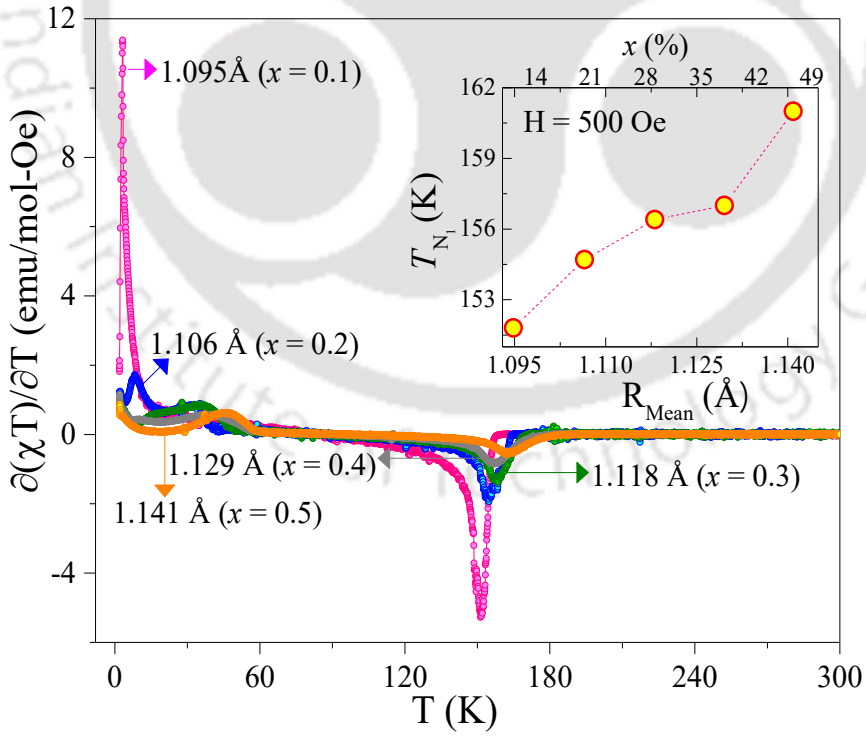

Fig. 5.11. The temperature dependence of the differential dc-magnetic susceptibility $\partial(\chi T)/\partial T$ of various compositions of DCCO systems. The inset represents variation of the AFM transition temperature (T_{N_1}) as a function of composition, x, and mean cationic radius, R_{Mean}.

present case indicates the presence of competing exchange interaction between the trivalent Dy and Ce ions. It is well known that dysprosium ion is a typical example of the Ising- type spin configuration, which is usually confined in the orthorhombic *a*–*b* plane, aligned ±27° from the *b*-axis of the unit cell. Moreover, they exhibit two-step discontinuous magnetization transitions in the *M*–*H* plane across 3.5 kOe and 14.3 kOe when measured along the *a*-axis [286,287]. Each discontinuity in the magnetization results in a change of magnetic moment (~2.2 μ_B) which is associated with the flip of a Dy spin from +27° to −27° or vice versa measured in the *a*–*b* plane. This signifies the cell doubled state (of magnetic unit cell) in comparison to the crystallographic unit cell when $H \parallel a$-axis [284,285,287]. However, a different scenario emerges in case of $DyAlO_3$ system (T_{N_2} ~ 3.52 K) in which only single discontinuity has been reported with slightly larger flip angle ±33° [286]. On the other hand, in case of the end compound $CeCrO_3$ the T_{SR} occurs across 15 K due to the ordering of the trivalent Cr and Ce spins [270,291]. Usually, the Cr spins in orthorhombic rare earth chromites are ordered in the *G* mode in which the rare-earth ordering strongly couples to the Cr-spins for temperature lower than 282 K except for the case of terbium [292].

In order to accurately determine the magnetic ordering temperatures, we calculated the differential magnetic susceptibility ($\partial(\chi T)/\partial T, \chi = (M/H)$) for ZFC case. In Fig. 5.11 we show the temperature dependence of $\partial(\chi T)/\partial T$ for different compositions. It is quite evident from the plot that with increasing the composition from x = 0.1 to 0.5 leads to the enhancement of T_{N_1} (negative maximum) from 151.8 K to 161 K, respectively. The position of these ordering temperatures is slightly lower as compared to those obtained from the $\chi(T)$ data by few percent. This phenomenon is expected since the singular behaviour occurs at the inflection points just below the peak position in χ–T plots as the variation of $\partial(\chi T)/\partial T$ versus T is closely related to the temperature dependence of the specific-heat $C_P(T) \sim A\frac{\partial(\chi T)}{\partial T}$. The location of positive

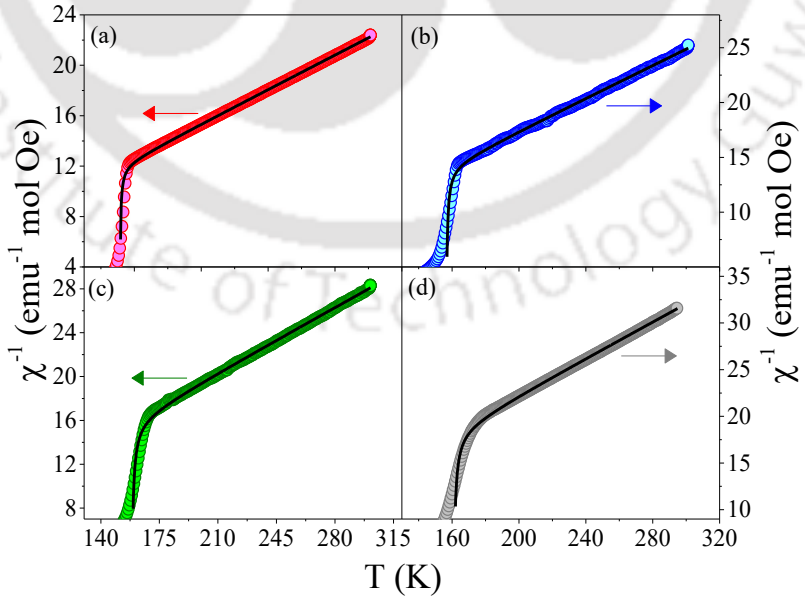

Fig. 5.12. The temperature dependence of inverse dc-magnetic susceptibility, χ^{-1}, for different compositions: (a) x = 0.1, (b) x = 0.2, (b) x = 0.3 and (d) x = 0.4 of the $Dy_{1-x}Ce_xCrO_3$ systems. The solid lines represent the mathematical fits corresponding to the DM interaction (Eq (5.5)) discussed in the text

maximum as shown in the inset of Fig. 5.11 is close to T_{PC} = 31 K, 33.5 K, 39.9 K, 45.5 K for x = 0.2, 0.3, 0.4 and 0.5, respectively. Moreover, the external field has significant impact on the ordering temperatures as noticed from the $M_{ZFC}(T)$ (for x = 0.1) measured between H = 300 Oe and 50 kOe. The field variation of the AFM ordering temperature $T_{N_1}(H)$ obtained from the above plots reveals progressive increase of T_{N_1} from 149.17 K to 154.59 K with increase in the field from the 300 Oe to 50 kOe accompanied by the broadening of transition as expected for any typical AFM system. Interestingly, we find that the spin-reorientation transition also increases with the measuring field and disappears at high fields. In order to understand such changes, we quantitatively probe the exchange interactions in this system through mathematical fitting of the experimental data of $\chi(T)$ with the DM interaction term as displayed in Fig. 5.12 and evaluated all the relevant parameters [261]. Majority of the rare-earth based canted AFM perovskite systems above T_N follows the DM antisymmetric exchange interaction in their susceptibility data instead of the Curie–Weiss (CW) law $\chi = \frac{C}{(T-\theta)}$ often used to determine the effective magnetic moment in the paramagnetic regime [257]. Usually, the DM interaction accounts for the susceptibility perpendicular to the easy axis distinct from the CW law, which relates to the susceptibility parallel to the easy axis of the system [293]. Henceforth, we employed the below expression (Eq 5.5) related to the DM interaction to understand the temperature dependence of inverse paramagnetic susceptibility ($\chi^{-1}(T)$) as it is difficult to determine the parallel and perpendicular susceptibilities independently [265].

$$\chi = \frac{C}{(T-\theta)} \frac{(T-T_0)}{(T-T_N)} \tag{5.5}$$

Here, C is the Curie constant, θ is the Weiss temperature, T_N is the Néel temperature of the system and T_0 is a fitted parameter. The inverse susceptibility $\chi^{-1}(T)$ plots of different compositions of the investigated system

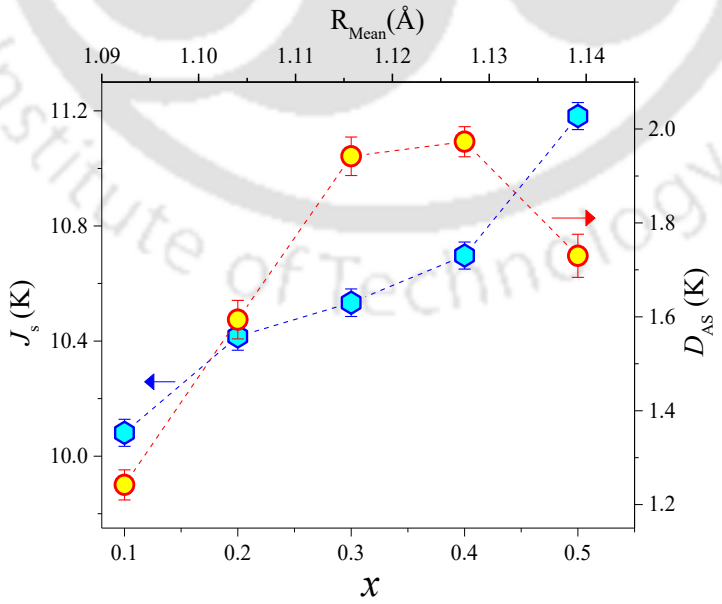

Fig. 5.13. The composition dependence of magnetic exchange interactions (both symmetric and asymmetric components J_S and D_{AS}) evaluated from the DM interaction method for the bulk poly crystals of $Dy_{1-x}Ce_xCrO_3$ with top axis representing R_{Mean}..

are fitted (as represented by the solid lines) to the above expression as depicted in Fig. 5.12. The corresponding parameters evaluated from the best fits are listed in Table 5.3. It is interesting to notice that the magnitude of compositional variation of the AFM ordering temperature is consistent with the composition dependence of the exchange interactions. It is quite evident that both the terms in the above expression $(T - T_0)/(T - T_N)$ play a significant role in the vicinity of T_{N_1} which results in a sharp falloff in the magnitude of χ^{-1} since the variance between AFM ordering temperature and T_0 is less than 3 K. Performing a similar analysis proposed by Moriya [265] we estimated the nearest-neighbour dominant exchange interactions between both symmetric J_S and antisymmetric super-exchange interaction D_{AS} using the following relations. The equation relates the order parameter T_N with Boltzmann constant k_B, spin S, coordination number z and fitting parameter T_0 (acquired from the $\chi^{-1}(T)$ and DM fits) [265]

$$T_0 = \frac{2ZJ_S S(S+1)}{3k_B} \tag{5.6}$$

$$T_N = \frac{2ZJ_S S(S+1)}{3k_B}\left[1 + \left(\frac{D_{AS}}{J_S}\right)^2\right]^{1/2} \tag{5.7}$$

Usually, from the modified CW law one can obtain the information about the J_S between Cr^{3+} ions, while, from the DM method the other exchange interactions D_{AS} (such as the Dy^{3+}–Cr^{3+}, Ce^{3+}–Ce^{3+} and Dy^{3+}–Dy^{3+} interactions) can be extracted. Accordingly, using Eq 5.6 and the values of T_0, z (=6) and S (=3/2) we quantitatively estimated the magnitude of J_S which lies between 10.08–11.18 K for x = 0.1–0.5. Whereas, the magnitudes of T_{N_1} and D_{AS} (1.24–1.73 K) are estimated using the Eq. 5.7 which are one order of magnitude less than that of symmetric case as expected for trivalent Dy/Cr, Dy/Ce, Ce/Ce and Dy/Dy ions. The above results are consistent with the previous reports on $Dy_{0.7}Y_{0.3}CrO_3$ (J_S = 9.47 ± 0.006 and D_{AS} = 1.9 ± 0.1), $Dy_{0.7}Er_{0.3}CrO_3$ (J_S = 9.351 ± 0.005 and D_{AS} = 1.9 ± 0.1) and $Dy_{0.7}Ho_{0.3}CrO_3$ (J_S = 9.542 ± 0.007 and D_{AS} = 2.0 ± 0.1) [260]. These magnitudes are nearly 5.4 times smaller than those obtained from the molecular field approximation $\left(J = \left(\frac{3k_B T_{N_1}}{2S(S+1)}\right)\right)$. Figure 5.13 illustrates the detailed composition dependence of the exchange interactions J_S and D_{AS} present in the investigated system. Both the quantities J_S and D_{AS} increase progressively with increase in the Ce content. However, D_{AS} starts decreasing beyond x = 0.4 as it is expected that the average separation between the Ce atoms decreases upon increasing the composition leading to an enhancement in the exchange interactions.

Fig. 5.14 shows the variation of μ_{eff} obtained from CW law, modified CW law with χ_0 obtained from both theoretical Hartree–Fock (HF) and experimental paramagnetic temperature (HT) region for $Dy_{0.9}Ce_{0.1}CrO_3$. The effective magnetic moment, μ_{eff} evaluated from the CW law shows a decreasing trend (μ_{eff} ~ 10.84–8.46 μ_B/f.u.) with increasing Ce composition (x ~ 0.1–0.5). For an accurate determination of the magnetic

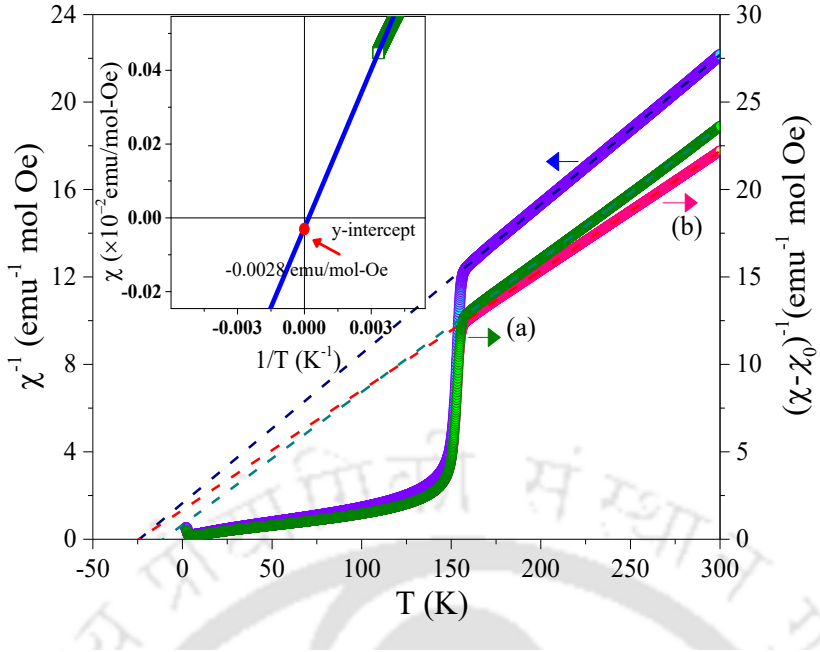

Fig. 5.14. Thermal dependence of inverse paramagnetic susceptibility $\chi^{-1}(T)$. With and without subtraction of the diamagnetic contribution (χ_o). The inset shows the $\chi(T^{-1})$ plot where the intersect shows the estimation of χ_0 in the high temperature limit.

moment we have plotted the temperature dependence of the inverse magnetic susceptibility ($1/\chi$), and evaluated the temperature independent term χ_0 (in the HT limit obtained from the χ versus $1/T$) along with the detailed calculations performed using non-relativistic HF method [294]. Usually, the residual susceptibility, χ_0 at higher temperature could be either positive (Van Vleck susceptibility) or negative (diamagnetic contribution) depending on the nature of the magnetic system[56]. The overall magnitude of χ_0 obtained from the HF is approximately -1.30×10^{-4} (-1.35×10^{-4}) emu mol^{-1} Oe^{-1} for $x = 0.1(0.5)$. While, the experimentally obtained values are of the magnitude -2.8×10^{-4} (-1.3×10^{-4}) emu mol^{-1} Oe^{-1} for $x = 0.1(0.5)$, respectively.

The magnitudes of μ_{eff} ($10.807_{HF}(10.717)_{HT}$ μ_B/f.u. − $8.428_{HF}(8.427)_{HT}$ μ_B/f.u.) obtained from the linear fits of modified CW-law after subtracting the χ_0 in paramagnetic zone $\chi - \chi_0 = \frac{C}{(T-\theta)}$ are consistent with those obtained from the *ab initio* density functional theory based calculations and the standard spin-only values calculated with the theoretical expression $\mu_{eff} = \sqrt{(1-x)\mu_{Dy}^2 + x\mu_{Ce}^2 + \mu_{Cr}^2}$ [260]. A detailed comparison of all these values along with the finite orbital contribution to the Cr atoms is listed in Table 5.3.

In the forthcoming section, we discuss the role of external magnetic field in the overall magnetization of the $Dy_{1-x}Ce_xCrO_3$ system. Figure 5.15 shows the typical five cycle field dependent magnetization hysteresis loops measured at 1.9 K between −90 kOe to +90 kOe field measured under ZFC condition with sweep mode. Clear saturated loops with negligible coercive fields and increasing magnetic moment are evident from these plots for all the compositions. Also, negligible exchange bias field was noticed in the 90 kOe

field cooled *M–H* measurements for all the samples. The first quadrant *M–H* isotherms (inset of Fig 5.15) are fitting well to the law of approach to saturation (LAS) expression given below through which we obtain the cubic anisotropy field constant and saturation magnetization [295]

$$M = M_S\left(1 - \frac{a}{H} - \frac{b}{H^2}\right) + \chi_h H \tag{5.8}$$

In the above Eq. 5.8, the last term (χ_hH) represents the field-induced enhancement of the spontaneous magnetization of the domains, commonly known as forced magnetization. This term is typically small for $T < T_C$. The origin of the $1/H$ term and the corresponding parameter a is generally attributed to the presence of crystal imperfections such as dislocations, nonmagnetic inclusions/dilution effect, and trapped domain walls [57,296]. The $1/H$ term predominates in the intermediate field range, whereas, the term b arises due to crystal anisotropy of the material and the $1/H^2$ term prevails for very large fields ($H \gg 4\pi M_S$) [57]. Nonetheless, there are some complications to apply this equation for both experiment and theoretical analysis. In particular, choosing the lower field limit is quite tricky and solely depends on the compound and its properties. However, it should be chosen high enough so that the motion of domain walls and rotation of magnetization should be complete on approaching the limited field.

The solid lines in the inset of Fig. 5.16 represent the best fits to the Eq. 5.8 of the experimental data obtained from the *M–H* isotherms. Consequently, we have evaluated the cubic magnetic anisotropy

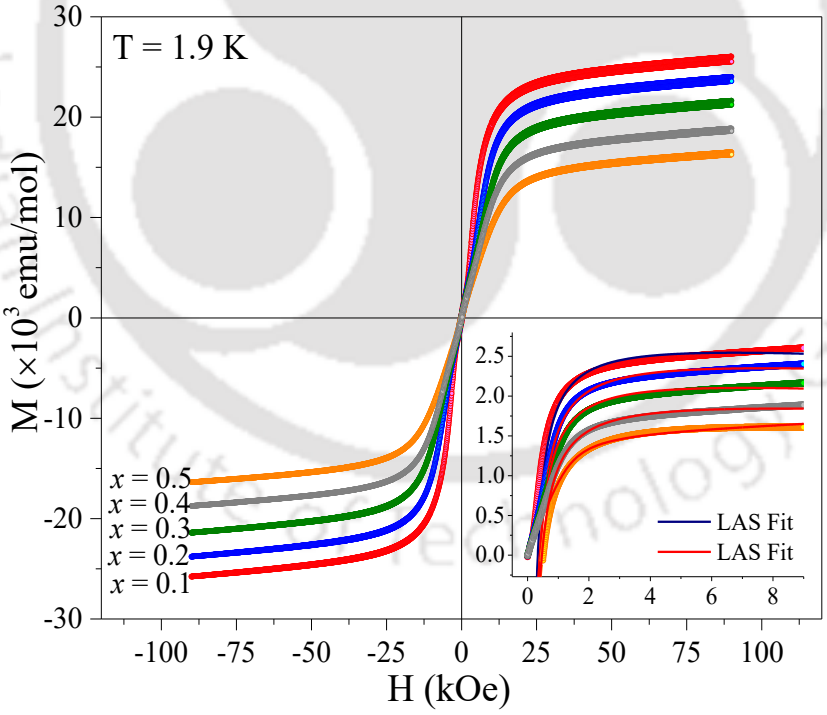

Fig. 5.15. The magnetic field dependent magnetization (*M–H*) hysteresis loops measured at 1.9 K between −90 kOe to +90 kOe for various compositions (x = 0.1–0.5) of $Dy_{1-x}Ce_xCrO_3$ system. The inset shows isothermal magnetization curves at T = 1.9 K measured under ZFC mode. The solid lines represent the mathematical fitting based on the LAS to the experimental data recorded for different compositions.

constant K_1 from the below relation:

$$b = \frac{8}{105}\frac{K_1^2}{\mu_0^2 M_S^2} \tag{5.9}$$

Here μ_0 represents the permeability of free space, while the magnitudes of a and b are governed by the lower field limit chosen for the fitting of LAS expression. The changes in magnetization with field in high field regimes are very critical in this case and are considered as negligibly small excluding in the vicinity of transition temperature (across the long-range ordered state to disordered paramagnetic state) which are difficult to probe precisely. From the analysis based on the best fits of the experimental data we have evaluated all the parameters M_S (28 219 emu mol^{-1} → 18 318.6 emu mol^{-1}) and K_1 (36.47 J m^{-3} → 18.97 J m^{-3}) which decrease linearly with increasing the Ce composition (x = 0.1–0.5) as shown in the main panel of the Fig. 5.16. Such drastic reduction in these quantities is the consequence of the antiferromagnetically coupled trivalent Cr and Ce sublattices unlike the trivalent Dy and Cr sublattices together with strong antiparallel alignment between the trivalent Cr-spins. Additionally, we have evaluated the anisotropy field H_K for all the compositions using the relation: $H_K = \frac{2K_1}{\mu_0 M_S}$ which also follows the same trend (25 847 Oe|$x_{=0.1}$ → 20 707.1 Oe|$x_{=0.5}$) as shown in the right hand scale of Fig. 5.16. The magnitudes of the M_S values obtained from the M–H experimental results are consistent with theoretical ($M_S = N_A\, g_{Avg}\, S\mu_B$) counterpart by considering the 3/2 ground state spin configuration of all the magnetic species with average Landé g-factor g_{Avg} ~ 1.8604 following the individual contribution $1/g_{Avg} = (1/g_{Dy}^{3+} + 1/g_{Cr}^{3+} + 1/g_{Ce}^{3+})$. We extended the field dependence (up to 50 kOe) studies further for the lowest composition x = 0.1

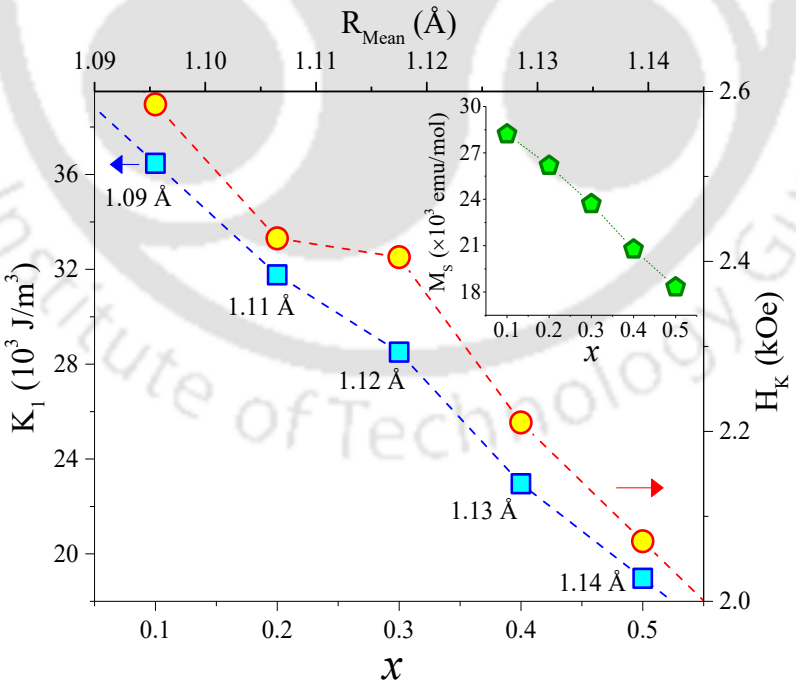

Fig. 5.16. The composition (x = 0.1–0.5) dependence of anisotropy field (H_K—right hand scale) and anisotropy constant (K_1—left hand scale) obtained from the LAS fitting of the M–H virgin isotherm curves recorded at 1.9 K. Here the solid lines represent the linear fits to the experimental data with top axis representing R_{Mean}. The inset shows composition dependent variation of the saturation magnetization ($M_S(x)$) for $Dy_{1-x}Ce_xCrO_3$ system.

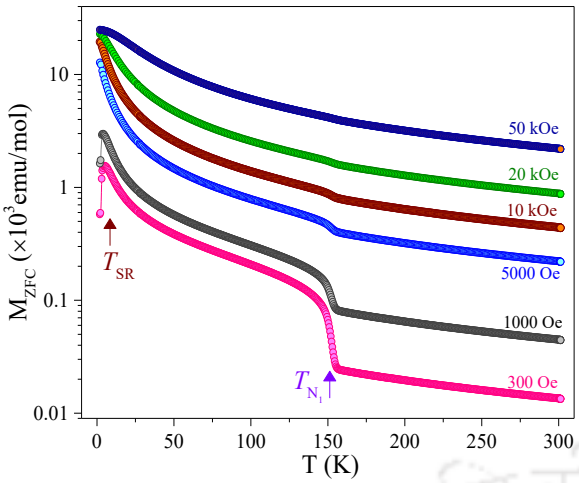

Fig. 5.17. The temperature dependence of the magnetization $M_{ZFC}(T)$ measured at different magnitudes of the external magnetic field (varying from 300 Oe to 50 kOe) of the composition $Dy_{0.9}Ce_{0.1}CrO_3$.

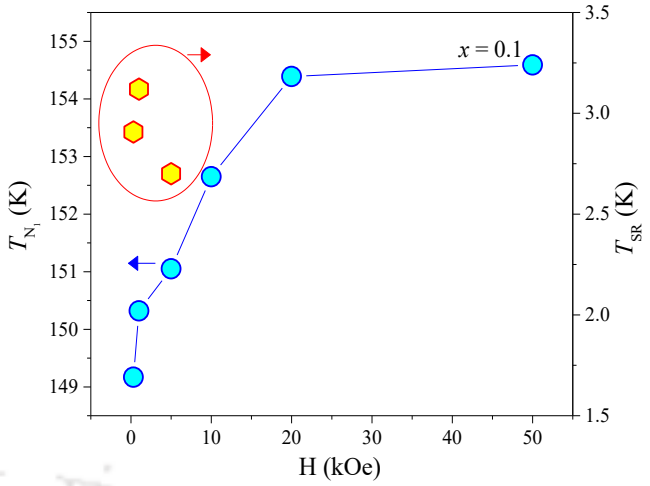

Fig. 5.18. The field variation of the Néel temperature ($T_{N1}(H)$) and spin reorientation ($T_{SR}(H)$) for the $Dy_{0.9}Ce_{0.1}CrO_3$ system obtained from the $M_{ZFC}(T)$.

($Dy_{0.9}Cr_{0.1}O_3$) as shown in the Fig. 5.17 where the temperature dependence of the ZFC magnetization is shown for different measuring fields. It is interesting to note that both the transition temperatures T_{SR}/T_{N_2} and T_{N_1} (the spin reorientation transition and main AFM ordering temperature) disappear upon increasing the field, instead a much-broadened variation is evident (typical behaviour of any AFM system under high fields). Figure 5.18 shows the field variation of T_{N_1} for the $Dy_{0.9}Cr_{0.1}O_3$ system in which T_{N_1} increases progressively with the field. The T_{SR} for x = 0.1, 0.2, and 0.3 does not exhibit any field variation except it collapses beyond a critical field ($H^* \geqslant$ 1kOe). The temperature (3 K to 130 K) variation

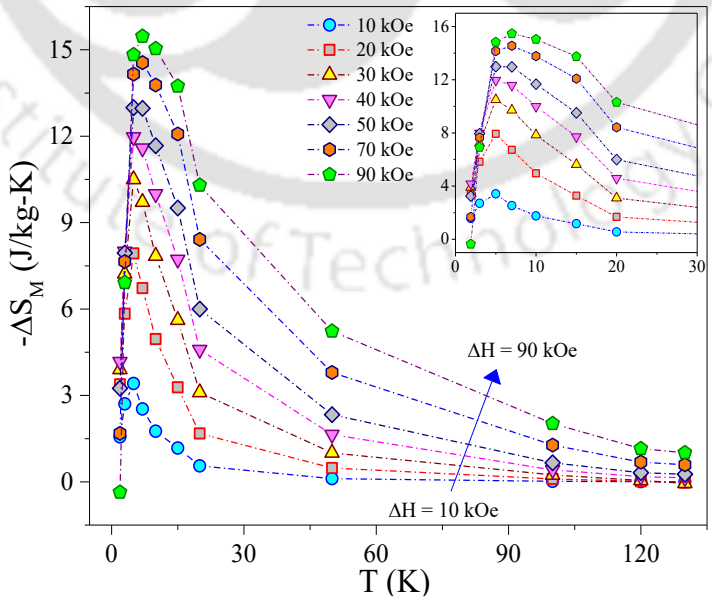

Fig. 5.19. The temperature variation of the magnetic entropy change ($-\Delta S_M(T)$) for a different field change (10 kOe ≤ ΔH ≤ 90 kOe) of $Dy_{0.9}Ce_{0.1}CrO_3$ system estimated using the Maxwell's thermodynamic relations applied to the experimentally obtained M-H isotherms.

Table 5.3. The comparative tabulation of the derived parameters from the magnetic study.

Sample Name	DCO1	DCO2	DCO3	DCO4	DCO5
T_{N_1} (K) (from d(χT)/dT)	151.8	154.7	156.4	157	161
μ_{eff} (μ_B/f.u.) (DFT-Theoretical)	10.824	10.29	9.73	9.13	8.49
μ_{eff} (μ_B/f.u.) (Spin only)	10.833	10.311	9.761	9.178	8.555
μ_{eff} (μ_B/f.u.) (Spin and orbital)	10.849	10.344	9.814	9.253	8.655
μ_{eff} (μ_B/f.u.) (C-W law)	10.839	10.259	9.633	8.989	8.464
μ_{eff} (μ_B/f.u.) (C-W_{HF} law)	10.807	9.442	9.605	8.962	8.428
μ_{eff} (μ_B/f.u.) (C-W_{HT} law)	10.717	9.476	9.684	8.962	8.427
M_S (emu/mol) (from M-H)	28219	26178	23706	20773	18319
M_S (emu/mol) (M-T Cr spins)	16738	16738	16738	16738	16738
M_S (emu/mol) (M-T Cr Dy spins)	33062	29049	29383	27415	25780
M_S (emu/mol) (M-T Cr, Dy , Ce spins	26995	23583	23991	22384	21049
T_{N_1} (K) (from D.M)	151.5	156.7	158.7	161.16	168.3
$\theta_{D.M}$ (K)	-25.15	-33.9	-32. 2	-31.1	-30.1
$C_{D.M}$ (emu K/mol-Oe)	14.6	13.4	11.8	10.3	9.1
T_0 (K)	151.2	156.7	158	160.5	167.7
J_S (K)	10.08(4)	10.42 (5)	10.54(5)	10.70 (4)	11.20 (4)
D_{AS} (K)	1.24 (3)	1.59 (4)	1.94 (4)	1.97 (3)	1.73 (4)
H_C (Oe)	325	247	224	206	204
M_R (emu/mol-K)	570	357	304	249	219
M_{EB} (emu/mol-K)	45.92	4.15	6.40	19.33	5.59

of the magnetic entropy change ($-\Delta S_M(T)$) is shown in Fig. 5.19 for a field change (ΔH) between 10 kOe and 90 kOe of $Dy_{0.9}Ce_{0.1}CrO_3$ system estimated using the experimentally obtained *M–H* isotherms. We employ the Maxwell's thermodynamic relations to calculate the entropy change, where the maximum entropy change (~16 J kg^{-1} K^{-1} for $\Delta H \sim$ 90 kOe) occurs at low-temperatures especially across the T_{SR} and its magnitude decreases monotonically with increasing the temperature. These values are larger than the Ce free $DyCrO_3$ system ($-\Delta S_M$ = 10.92 J kg^{-1} K^{-1} at 4 T) and Er substituted $DyCrO_3$ system reported previously [256]. Moreover, the relative cooling power

$$RCP = \left|\Delta S_{M,Max}\right| \times \delta T_{FWHM} \tag{5.10}$$

calculated from the $\Delta S_M(T)$ plots (~269–767.3 J kg^{-1} for ΔH = 30–70 kOe) for Ce substituted $DyCrO_3$ systems are much better as compared to the previous reports [65], [266]. After discussing the effect of temperature and external field on the magnetic properties of Ce substituted $DyCrO_3$ we now present the specific heat analysis in the following section.

5.3.3 Specific Heat analysis:

In order to understand the nature of phase transitions occurring in the investigated systems we performed a detailed temperature dependence of specific heat C_P(T) measurements for two cases (i) H = 0 and (ii) in the presence of H = 90 kOe. In Fig 5.20 we show the variation of specific heat C_P at zero and finite field. We find that all the transitions noticed in the $M(T)$ (*right hand scale*) are in congruence with the C_P/T data. Especially the λ-like anomaly from AFM to paramagnetic transition around 149 K (T_{N_1}) which happens due to the ordering of trivalent Cr spins and associated with the magnetic transition temperature to $\Gamma_2\ (F_x,\ C_y, G_z)$ phase [297]. Almost no significant difference has been noticed between the C_P(T) data measured in the presence of field and zero-field case except across the T_{SR}.

Furthermore, we have extracted the individual contributions of the lattice [$C_{P\text{-}Lattice}(T)$] and magnetic [$C_{P\text{-}Magnetic}(T)$] specific heats from the total specific heat $C_{P\text{-}Total}(T)$ using the Debye's model [288]. In general, the contribution of $C_{P\text{-}Lattice}$ is a sum of both electronic $C_{P\text{-}electron}$ and phonon $C_{P\text{-}Phonon}$ parts, however, the electronic contribution is significant only at very low temperatures, the influence of phonon part can be easily extracted using the following expression [288]:

$$C_{P-Phonon} = Nf_D\left(\frac{\Theta_D}{T}\right)$$

$$= 9NR\left(\frac{T}{\Theta_D}\right)^3 \int_0^{\Theta_D/T} \frac{x^4 e^x}{(e^x-1)^2} dx \tag{5.11}$$

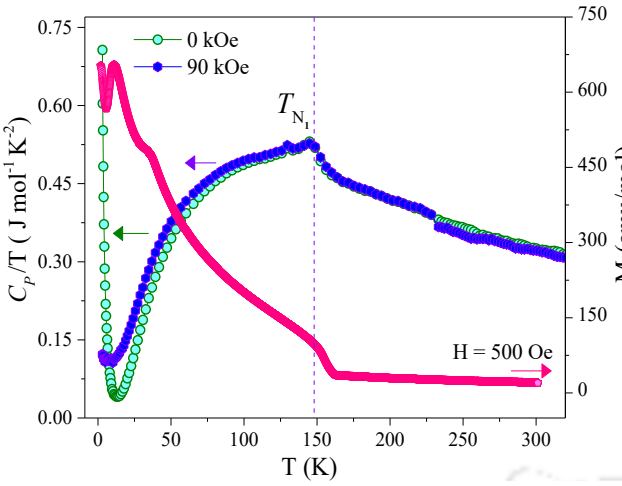

Fig. 5.20. The temperature dependence of the heat-capacity ($C_P\,T^{-1}(T)$ of bulk polycrystalline $Dy_{0.5}Ce_{0.5}CrO_3$ system recorded under both zero-field and finite field $H = 90$ kOe field. The *right-hand scale* represents the temperature variation of the magnetization data ($M(T)$) for the same composition for comparison.

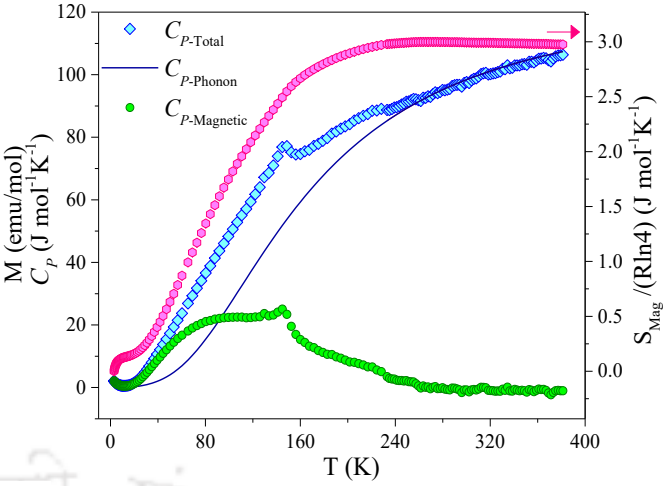

Fig. 5.21. Thermal variation of total specific heat $C_{P\text{-Total}}$ data measured for $H = 0$ condition for the bulk $Dy_{0.5}Ce_{0.5}CrO_3$ system. Along with the $C_{P\text{-Total}}(T)$ the individual contribution of magnetic ($C_{P\text{-Magnetic}}$) and phonon ($C_{P\text{-Phonon}}$) parts and their temperature variation is also plotted on the LHS which are estimated from the Debye model of specific heat. The RHS represents the temperature dependence of the magnetic entropy $S_{Mag}(T)$ calculated using the numerical integration of the $C_{P\text{-Magnetic}}\,T^{-1}$.

The left-hand side scale of Fig. 5.21 shows the temperature dependence of the individual contributions of $C_{P\text{-Lattice}}(T)$ and $C_{P\text{-Magnetic}}(T)$ specific heats of bulk polycrystalline system $Dy_{0.8}Ce_{0.2}CrO_3$. In the above expression, the quantity $f_D(\Theta_D/T)$ represents Debye function ($= 9R(T/\Theta_D)^3 \int_0^{\Theta_D/T} \frac{x^4 e^x}{(e^x-1)^2} dx$), where N is the number of atoms per formula unit, R is the universal gas constant (8.314 J mol^{-1} K^{-1}), and Θ_D is the Debye temperature. To estimate the contribution of $C_{P\text{-Phonon}}$ and Θ_D, we have fitted the experimentally obtained high temperature $C_{P\text{-Total}}$ data with the above expression (fitted curve is shown by the solid line in Fig. 5.21). Here the effect of magnetic contribution ($C_{P\text{-Magnetic}} = C_{P\text{-Total}} - C_{P\text{-Lattice}}$) is nearly four times smaller than the $C_{P\text{-Total}}$ and is very negligible for $T > T_{N_1}$. The fitting analysis yields $\Theta_D = 390$ K for $Dy_{0.8}Ce_{0.2}CrO_3$ bulk system which matches with the previously reported rare-earth chromate systems [298–300]. These results are consistent with the analysis of $C_{P\text{-Total}} = \gamma T + \beta T^3 + \delta T^{3/2}$ with $\gamma =$ 0.551 J K^{-2} mol^{-1}, $\beta =$ 4.0 × 10^{-6} J K^{-4} mol^{-1} and $\delta =$ 0.445 J K$^{-3/2}$ mol^{-1} respectively for zero measuring field obtained from the non-linear fits of the temperature dependence of $C_{P\text{-Total}}/T$ data as illustrated in Fig. 5.22 [300-303].

Moreover, from the numerical integration of $C_{P\text{-Magnetic}}\,T^{-1}$ data in the temperature range of 3 K to 380 K, the magnetic entropy (S_{Mag}) has been calculated which is represented by in the LHS panel of Fig. 5.21. Across T_{N_1} the magnetic entropy is about 33.4 J mol^{-1} K^{-1} and is larger than the expected theoretical value of ~11.526 J mol^{-1} K^{-1}, obtained using R ln(2S + 1) for $S = 3/2$ ground state spin. It is quite intriguing to notice that the saturation of the magnetic entropy occurs at a temperature 100 K higher than the long-range ordering temperatures with a further residual magnetic gain to a total of 33.4 J mol^{-1} K^{-1} at 380 K. Such a

large magnitude of entropy beyond the ordering temperature indicates the contribution of the spin entropy beyond the ground state of the magnetic entropy for trivalent rare-earth ions and transition metal ions which is present in the investigated system. In the following we discuss the results obtained from the Raman spectroscopy that mainly provide us the information related to different vibrational excitations in this interesting system as a function of Ce content.

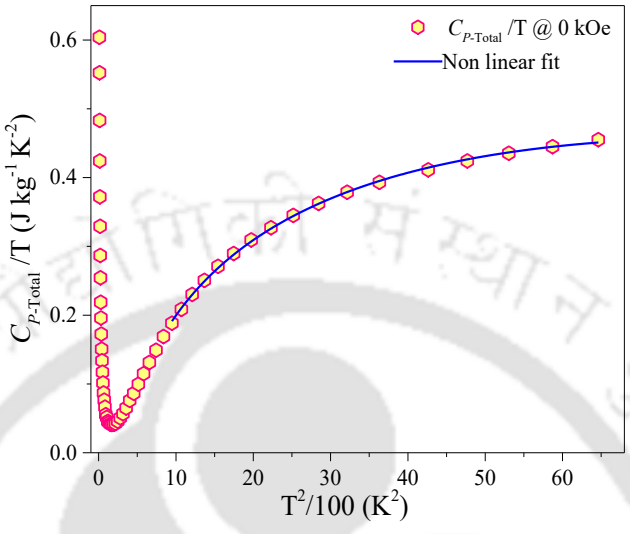

Fig. 5.22. The temperature ($T^2/100$) variation of the $C_{P\text{-Total}}T^{-1}$ plots for H = 0 for $Dy_{0.5}Ce_{0.5}CrO_3$ system along with the nonlinear curve fitting (shown by solid curve) based on the mathematical expression $C_P = \gamma T + \beta T^3 + \delta T^{3/2}$.

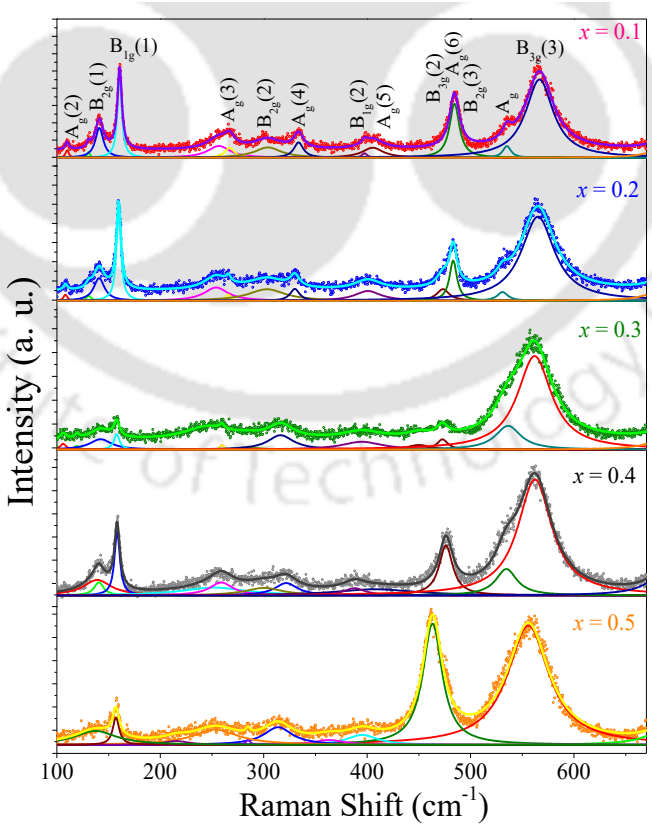

Fig. 5.23. Raman spectra of various compositions of $Dy_{1-x}Ce_xCrO_3$ (x = 0.1–0.5) system measured at room temperature. The solid lines represent the corresponding Lorentzian fits.

5.3.4 Raman spectroscopy and analysis:

In this section, we discuss a detailed compositional dependence of the Raman spectra of $Dy_{1-x}Ce_xCrO_3$ measured at room temperature along with the individual Lorentzian fits shown by the continuous solid lines (as depicted in Fig. 5.23). Usually, the $RCrO_3$ family exhibits in total 60 Γ point phonon modes including 24 Raman active, 25 infrared active, eight silent and three acoustic modes corresponding to the distorted orthorhombic *Pbnm* structure in which the mirror plane is vertically set to the *c*-axis or in the *Pnma* symmetry where the mirror plane is vertical to the *b*-axis. Here the distortion from the ideal cubic *Pm3m* structure is a result of the tilting of the CrO_6 octahedra [275,304]. Accordingly, we noticed four very prominent intensity Raman peaks at 561, 486, 160, 140 cm^{-1} associated with the spectroscopic term symbols $B_{3g}(3)$, a mixed mode ($B_{3g}(2)/A_g(6)/B_{2g}(3)$), $B_{2g}(1)$ and $A_g(2)$, respectively.

Here we first discuss the Raman active modes according to the point-group analysis: $7A_g+ 7B_{1g}+ 5B_{2g}+ 5B_{3g}$ modes for *Pbnm* structure with the Raman tensors along *xx*, *yy*, *zz* axes ascribed to the A_g mode whereas the *xy* axis is associated with the B_{1g}, *xz* axis for B_{2g} and B_{3g} with *yz*. While the same spectral features are occasionally interpreted in terms of the *Pnma* symmetry and consist of the modes $7A_g + 5B_{1g} + 7B_{2g} + 5B_{3g}$. Here, the interchange of the B_{1g} with B_{2g} corresponds to the non-vanishing *xz* component, referred to as B_{2g} in *Pbnm* and B_{1g} along *xy* for *Pnma* [275]. In the present case, we followed the spectral term symbols corresponding to the lattice symmetry *Pbnm* and analysed the data. It is well known that the reduced space group is simply the outcome of three different kinds of alteration in the crystal structure such as (a) distortion of the CrO_6 octahedra, (b) Jahn–Teller (J–T) distortion and (c) displacement of the A-site cation based on which we have labelled all the modes in the present case [66,275,304]. Thus, we can rule out the possibility of the J–T distortion in [Ar]$3d^3$ for Cr^{3+} (unlike d^4 for Cr^{2+}) which leads to Cr–O bond rigidity [275]. The location of these models is systematically tabulated in Table 4 and grouped out all modes

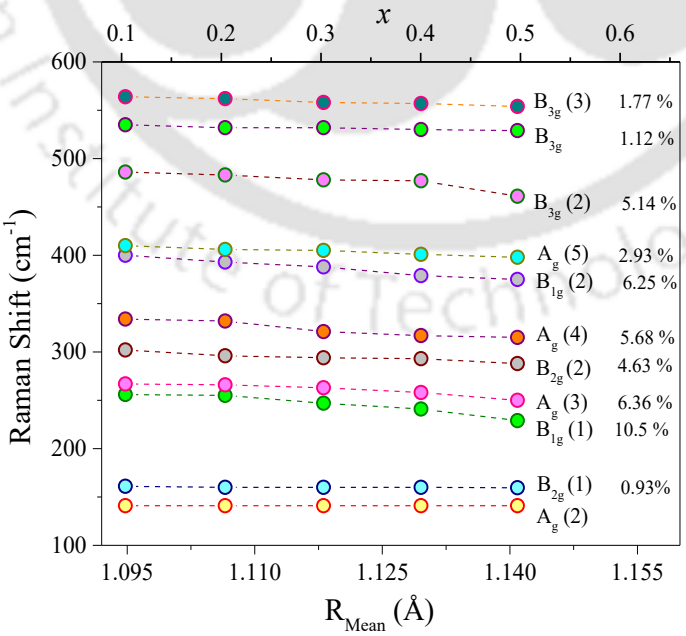

Fig. 5.24. The change in Raman shift of $Dy_{1-x}Ce_xCrO_3$ (x = 0.1–0.5) system represented as a function of the mean cationic radius (R_{Mean}) of different modes.

on the basis of three kind of distortions discussed above. Firstly, the rare earth cation or A-site cation displacement generates the active modes, like, $3A_g+ 1B_{1g}+ 3B_{2g}+ 1B_{3g}$. Secondly the octahedral tilt (and/J–T) leads to the emergence of the modes $2A_g+ 2B_{1g}+ 1B_{2g}+ 1B_{3g}$. Finally, the modes $2A_g$, $4B_{1g}$, B_{2g} and $3B_{3g}$ appear as a consequence of one symmetric and one bending of the CrO_6 octahedra, two bending and two stretching of the CrO_6 octahedra, symmetric stretching of the CrO_6 octahedra, and two antisymmetric plus one bending mode of the CrO_6 octahedra, respectively [261,275]. Out of the 24 phonon modes, we noticed $6A_g$, $2B_{3g}$, $3B_{1g}$, $2B_{2g}$ modes and others are having very low intensity, which we were not be able to detect [261,275,305]. Usually, the rare earth orthochromites are subtle towards any change of the A-site cation radius as well as the mass of rare-earth cation. The intensified Raman mode $B_{3g}(3)$ quantifies the relevant distortions together with the efficient absorption of the incident energy of the photons.

Figure 5.24 shows the relative shift of the Raman modes obtained from the fitting of the peaks with Lorentzian function with the increase of Ce substitution. As noticed from the lower wavenumbers the first two intense modes noticed at 141 cm^{-1} and 161 cm^{-1} are mainly due to the displacements of rare-earth cations (Dy/Ce) along the *x*-direction as such modes vary in their positions according to the relation $\omega = \sqrt{\frac{k}{\mu}}$, where ω is angular frequency, k is the force constant and μ is the reduced mass of the system. Therefore, the heavier atoms shift towards lower frequency region. Although the cationic radius in the investigated system vary significantly from ~1.095 Å ($x = 0.1$) to 1.141 Å ($x = 0.5$), we did not notice any prominent shift in the two modes $A_g(2)$ and $B_{2g}(1)$. In the present case, $A_g(2)$ is almost pinned at 141 cm^{-1} while the $B_{2g}(1)$ decreases slightly (0.7%) with increasing the Ce content. On the other hand, the $A_g(4)$ mode located around

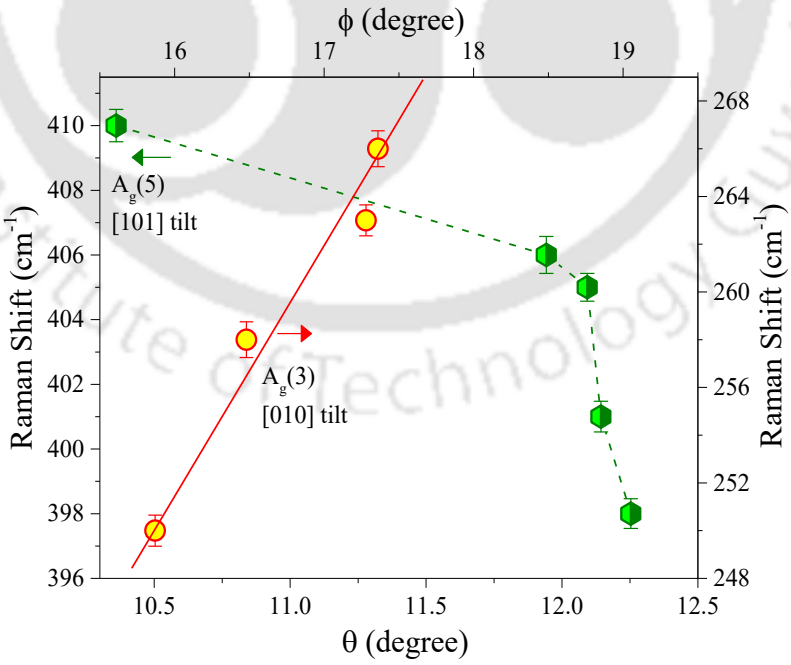

Fig. 5.25. The Raman shifts plotted as a function of the octahedral tilt angles (θ for (010) and ϕ for (101) planes) for the $A_g(5)$ and $A_g(3)$ modes for $Dy_{1-x}Ce_xCrO_3$ ($x = 0.1$–0.5). The solid line represents linear fit corresponding to the slope 23.1 cm^{-1} $degree^{-1}$.

Table 5.4. The Lorentzian fitted Raman bands of $Dy_{1-x}Ce_xCrO_3$ (x = 0.1(DCO1) - 0.5 (DCO5)) with corresponding symmetry operations. The peak positions of pure $DyCrO_3$ have been taken from reference.

Symmetry	DCO[275]	DCO1	DCO2	DCO3	DCO4	DCO5
A_g (2)	141	141.0(5)	141.0(3)	141.0(4)	14.01(5)	141.0(6)
B_{2g} (1)	160.5	161.0(7)	160.0(5)	160.0(3)	160.5(4)	159.5(5)
B_{1g}(1)	260.5	256.0(5)	255.0(4)	247.0(6)	241.0(5)	229.0(5)
A_g (3)	270.2	267.0(6)	266.0(7)	263.0(6)	258.0(7)	250.0(6)
B_{2g} (2)	305.5	302.0(8)	296.0(5)	294.0(5)	293.0(5)	288.0(5)
A_g (4)	335.6	334.0(5)	332.0(4)	321.0(4)	317.0(6)	315.0(5)
B_{1g} (2)	397.2	400.0(5)	393.0(6)	388.0(6)	379.0(5)	375.0(4)
A_g (5)	409.5	410.0(5)	406.0(6)	405.0(4)	401.0(5)	398.0(4)
B_{3g} (2)/A_g (6) /B_{2g} (3)	482-491	484.0-486.0 (8)	473.0-483.0 (8)	460.0-478.0 (7)	470.0-477.0 (5)	456.0-461.0 (6)
B_{3g} (3)	560	564.0(5)	562.0(6)	558.0 (6)	557.0(5)	554.0(7)

334 cm^{-1} is greatly affected by the A-site cation (Dy/Ce move along ($-x$) direction) mass as it shifts from 315 cm^{-1} to 334 cm^{-1} with the reduction of the Ce from x = 0.5 to 0.1. Whereas, the B_{2g}(2) mode located at 302 cm^{-1} shifts towards lower wave number side with increasing the Ce substitution which is linked to the translation motion of the A-site cation along the z-direction. In addition, we find that the B_{1g}(2) symmetry mode is susceptible to the A-site cation shifting along z-direction and this mode overlaps with the A_g(5) mode giving sharp and intense peak which diminishes for lower Ce content and lower cationic radius systems. The next prominent mode observed at 267 cm^{-1} is referred to the A_g(3) mode and it is greatly altered with the varying size of cations and this mode is generated due to the in-phase rotation of the CrO_6 octahedra around [010] axes [275]. Similarly, the weak shoulder across 410 cm^{-1} (A_g(5) mode) arising from the out-of-phase rotation of the CrO_6 octahedra along x-axis and this region of the spectrum has special importance among the $RCrO_3$ family of compounds because it exhibits substantial change in its position due to the rotation around [101] pseudocubic axes [275].

From the discussion up to this point it is clear that the octahedral tilting/bending of O–Cr–O bond leads to phenomenal distortions along with pseudocubic rotation axes of Miller indices [101] and [010]. Consequently, in Fig. 5.25 we illustrate the A_g(5) Raman spectra in consonance with the tilt angle obtained from the crystal structure analysis discussed in section 5.3.1. With increasing the [101] tilt angle ($\theta \rightarrow$ 10.36° to 12.25°) the A_g(5) mode gradually shifts from 410 cm^{-1} to 398 cm^{-1} and this behaviour is quite opposite to the case of A_g(3) soft mode and its variation with the [010] tilt angle (φ). This result is quite contrasting to the previously reported systems such as in orthochromites and orthomanganites in which both the tilt angles

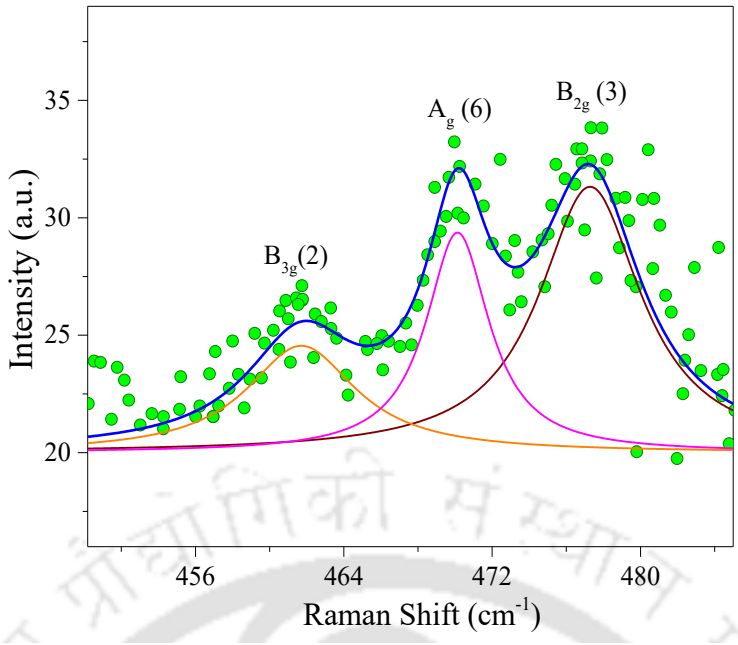

Fig. 5.26. The deconvolution of the three different Phonon modes namely $B_{2g}(3)$, $A_g(6)$ and $B_{3g}(2)$ appearing in the region between 460 cm^{-1} and 478 cm^{-1} for the composition $Dy_{0.7}Ce_{0.3}CrO_3$. Here the scattered symbols are the experimental data points while the solid lines correspond to the peak fits.

exhibits similar trend falling under the same linear slope with increasing Raman shift [288]. In the present case the linear variation (slope ~ 23.1 cm^{-1} $degree^{-1}$) of the Raman shift continues up to $\varphi \sim 17.36°$ and departs thereafter. An opposite trend in the Raman shift has been observed with θ increasing from 10.36° to 11.94° beyond which a sudden fall to 398 cm^{-1} is evident for highly substituted Ce in $DyCrO_3$ [275,306].

For the higher compositions ($x \geqslant 0.3$) a relatively broad and very high intensity mode ($A_g(6)$) is emerging which is essentially deconvoluted into three different modes (461, 470 and 477 cm^{-1} for $x = 0.3$ shown in Fig. 5.26). This mode becomes sharper and shows very high intensity for $x > 0.3$. However, for lower Ce compositions this region (482.2–490.6 cm^{-1} for 10% Ce doped $DyCrO_3$) is quite complex with superposition of three different modes namely $A_g(6)$, $B_{2g}(3)$ and $B_{3g}(2)$ in which the spectral bands are crossing each other. This whole band substantially shifts towards the higher energy/lower frequency region (from 485 cm^{-1} to 460 cm^{-1}) with increasing Ce doping. Previous studies on the single $DyCrO_3$ crystals reveals that the $A_g(6)$ mode is the most reliable in the entire spectrum to account any lattice distortion present in the system and it is mainly driven by the bending and stretching of the CrO_6 octahedra [307].

5.4 Summary:

Monophasic polycrystalline bulk $Dy_{1-x}Ce_xCrO_3$ perovskite oxides of compositions $x = 0.1$–0.5 have been successfully investigated using various characterization techniques. Firstly, the crystal structure analysis performed by means of Rietveld refinement of the XRD data reveals that all the compounds exhibit orthorhombic structure (of space group *Pbnm*) with moderate lattice distortion and enhanced tolerance factor with the substitution of higher ionic radius trivalent Ce (1.07 Å) at the Dy^{3+} (0.912 Å) sites. These results

demonstrate that the octahedral distortion is associated with the elongation and compression of the bond lengths of basal O_{B1} and O_{B2} respectively. While the optical O_{A1} is more rigid, pertaining to the Cr atoms in the CrO_6 octahedra. The increase in the tolerance factor leads to the stabilization of Ce diffusion inside the $DyCrO_3$ matrix as well as the decrease of d_{Cell} parameter by 47.6% in the same range to form cubic structure and reducing the tilt angles. It has been noticed that the bond lengths corresponding to the Cr-apical oxygen are rigid in comparison with that of Cr-basal oxygen. For the pristine compound $DyCrO_3$, the Néel temperature, T_{N_1} was found to be around 145 K, however, with Ce substitution T_{N_1} increases to ~260 K. For $DyCrO_3$, the low temperature phase transition occurs at 2 K (Γ_{25}) whereas with the inclusion of Ce, we observed another transition between 31 K and 45.5 K with Γ_2 (F_x, C_y, G_z) configuration. The magnitudes of exchange parameters, J_S and D_{AS} in Ce substituted compounds increase by one order compared to the parent system $DyCrO_3$. Further, we also noticed a significant enhancement in the overall magnetic entropy change (ΔS_M) with improved RCP (~360 J kg^{-1}) for 10% Ce substituted $DyCrO_3$ system measured at T = 5 K (for ΔH = 40 kOe), whereas, the previous studies on $DyCrO_3$ reported 256 J kg^{-1} under same conditions [66, 287]. Moreover, all the compositions exhibit G-type AFM character with $\Gamma_4(Gx, Ay, Fz)$ spin-configuration and undergoes a phase-transition across T_{PC} ($< T_{N_1}$) with Γ_2 (F_x, C_y, G_z) spin configuration through a mechanism involving the variation in total free energy change which is associated with the induced local effective field caused by strong coupling between the trivalent Cr and rare-earth ions Ce/Dy. The low-temperature spin-reorientation transition T_{SR} (3.5 K–16.8 K) was significantly suppressed for $x \geqslant 0.4$ and a weak FM character (of Γ_2 configuration) emerges due to the Dy spins. On the other hand, the AFM character in these perovskites are interpreted in terms of antisymmetric (DM) exchange interaction between the trivalent cations which increases progressively with the extent of Ce substitution. These magnetic characteristics probed by the dc-magnetization studies are complemented by the temperature and field dependence of heat-capacity data C_P(T) which yields the Debye temperature (Θ_D) to be ~390 K, perfectly matching with literature. Finally, the phonon modes $A_g(5)$ and $A_g(3)$ exhibit opposite trend in their position (~3.09 ± 3 cm^{-1}) with increasing the Ce content corresponding to the CrO_6 octahedral tilt angles (θ, ϕ) around pseudocubic Miller axes [101] and [010] which is quite different in comparison to the other perovskites. The phonon spectra are quite complex in region between 470 cm^{-1} and 490 cm^{-1} which essentially consists of the three modes $A_g(6)$, $B_{2g}(3)$, and $B_{3g}(2)$, all of which collapse into a single phonon mode $A_g(6)$ for $x \geqslant 0.4$.

Chapter 6

Effect of Sm substitution on the structural, electronic and magnetic behaviour of rare earth Perovskite $GdCrO_3$

In this chapter we present a comprehensive investigation of the effect of different substitution of Sm on the structure, magnetic structure, specific heat, and phonon spectroscopy of the rare earth perovskite $GdCrO_3$, where, Gd was substituted with Sm. In particular, we will present a comprehensive analysis pertaining to the substitution of 10%, 50%, and 90% of Sm substitution in the A site of $GdCrO_3$ which exhibits presence of interesting coexistence of magnetic phases, negative magnetization, multiple compensation temperature, etc. We start with a brief introduction of the rare earth perovskite $GdCrO_3$ and related systems and outline the details of experimental methods used to synthesize and characterize the samples which great details have already been provided in the chapter 1 and chapter 2. It is followed by the key results findings pertaining to the effect of the Sm substitution on the crystal, electronic, structural distortion, different magnetic phases and magnetic structure of $GdCrO_3$. We end the chapter with main summary of the key findings and conclusions.

6.1 Introduction:

The rare earth orthochromites ($RCrO_3$, where R being rare-earth element) have been examined vigorously over the past few decades using various diverse characterization techniques such as neutron diffraction, heat capacity, Mossbauer analysis, magneto-dielectric and optical-absorption spectroscopy [259], [292], [308]. These techniques have been widely used to probe the ferroelectricity driven by the co-existence of local non-central symmetry and multiple magnetic ordering (antiferromagnetic and ferromagnetic behaviour) in $RCrO_3$. Along with these properties phenomena such as exchange bias, spin reorientation transitions, negative magnetization and its reversal, spin glass state etc., have been the extensively studied in $RCrO_3$ related systems [292,308–311]. Magnetization reversal phenomenon noticed in these types of compounds is quite intriguing and attaining the huge scientific attention owing to different temperature dependence of magnetic moments between the cations of constituent sublattices. Here the net magnetization experiences change in the polarity from positive to negative value after a particular temperature popularly termed as compensation temperature (T_{Comp}) which is the key feature of $RCrO_3$ related systems [53]. It is well known that the phenomena of magnetization reversal rely on the presence of two distinct states of the magnetization making the materials perfectly accessible for switchable devices such as volatile magnetic memory storage, thermo-magnetic switches, high speed read/write magnetic memories, thermally assisted magnetic random-access memory, etc. [312,313]. In general, most of the materials exhibit T_{Comp} far below the room temperatures limiting their potential applications in magneto-electronic devices. Therefore, it is pertinent from the research point of view to have a better understanding of tenability of T_{Comp} at high temperature for the above applications. The induced internal field by the transition metal oxide sublattice (Cr^{3+}, Mn^{3+}, etc.) play a major role in magnetization reversal of $RCrO_3$ related systems, in

which rare earth elements (Gd^{3+} and/or Ce^{3+}) couples antiferromagnetically with transition metal ions which polarizes them to get aligned in the opposite direction (with respect to applied field) causing reversal in the magnetization [314]. Most of the $RCrO_3$ materials (e.g. $PrCrO_3$, $YbCrO_3$, $HoCrO_3$) display the magnetization reversal under field cooled warming (FCW) protocol. However, the first end compound $GdCrO_3$ exhibits the negative magnetization only under field-cooled cooling (FCC) mode indicating the interesting measurement protocol/history dependent features [315].

On the other hand, the second end compound $SmCrO_3$ is another intriguing system which shows negative magnetization under zero field cooled warming (ZFCW) protocol [316]. Interestingly, this newly emerging compound displays multiferroicity and temperature dependent rapid spin reorientation phase transition. The short-range abrupt spin reorientation character can be of tremendous useful for application in thermomagnetic power generation, magnetic refrigeration and in spin switching devices [317,318]. The formation of metastable glass arises due to the inequality between the free energies where the metastable state persists with fluctuating energy below which the low temperature ordered phase begins by overcoming the energy barrier [319,320]. The thermomagnetic history dependent kinetic arrest similarly signifies the viscous retardation of the AFM phase growth against the FM phase. Recent studies found this exceptional feature in $Ce(Fe_{0.96}Ru_{0.04})_2$ [321], $La_{0.5}Ca_{0.5}MnO_3$ [319], $Fe_{0.955}Ni_{0.045}Rh$ [320], Gd_5Ge_4 [321] and $SmCrO_3$ [323]. Some recent studies also suggest low-temperature spin-glass like features in $SmCrO_3$ and related compounds [323]. Here both the end compounds $GdCrO_3$ and $SmCrO_3$ crystallize in orthorhombic structure (*Pbnm* space group) with AFM ordering temperature at 171 K and 192 K with Γ_4 (G_x, A_y, Fz; F_R) spin configuration and go through spin reorientation at 7 K and 37 K respectively with Γ_2 (F_x, C_y, G_z; F_x^R, C_y^R) spin alignment. While the $GdCrO_3$ attains a high isothermal entropy change of 36.9 J kg^{-1} K^{-1} with adiabatic temperature change ΔT of ~ 19 K (with relative cooling capacity of 542 J kg^{-1} (for ΔH~ 7 T)) which is quite useful for the magnetic refrigeration [67]. On the other hand, $SmCrO_3$ shows the conventional field-cooled negative exchange bias field as high as 4709 Oe at 10 K. Moreover, below the spin reorientation temperature (~33 K) spin glass like features have been noticed in this system where the high temperature Γ_4 state coexist with Γ_2 state [324].

Hence, we have chosen the parent compounds $GdCrO_3$ and $SmCrO_3$ for their distinguished behaviour of magnetization reversal in FCC and ZFCW cases respectively by keeping 10% Sm in $GdCrO_3$ (GSO1) and 10% of Gd in $SmCrO_3$ (GSO9) and both Gd and Sm with 50% ratio expecting promising magnetization reversal under both FCC and ZFCW protocols. Here, in this work, we report a comprehensive study on the structural, magnetic, and Phonon spectroscopy of both the end compounds $GdCrO_3$ and $SmCrO_3$ with few intermediate compositions prepared by standard solid-state reaction method. Here Sm is substituted at Gd sites of $GdCrO_3$ system. In particular, we considered the following three compositions 10%, 50% and 90% of Sm at the A-site of $GdCrO_3$ that exhibits complex Cr^{3+}-Cr^{3+} and R^{3+} (Gd^{3+}, Sm^{3+})-Cr^{3+} interactions which is responsible for the multiple T_{Comp} over a wide temperature interval. To the best of our knowledge an extensive dependent Raman spectroscopy study is lacking in the literature and our results fulfils such gaps

in the literature with a detailed temperature dependent study. The high T_{Comp} ~ 195 K noticed under ZFCW protocol and large negative magnetization (~17 emu/mol) within the narrow temperature region make the investigated system attractive for the applications in magneto-electronics. In the following section we provide the experimental details and discuss these results in the light of already reported data on the similar type of systems along with a comparative analysis of all the results. Finally, we correlated all the different results and provide concluding remarks and future outlook.

6.2 Experimental Details:

The polycrystalline $Gd_{1-x}Sm_xCrO_3$ (GSO) perovskites with compositions x = 0.1 (GSO1), 0.5 (GSO5) and 0.9 (GSO9) were prepared using the standard solid-state reaction method at high sintering temperatures and atmospheric pressure. The primary materials being: Gadolinium (III) oxide (Gd_2O_3), Samarium (III) oxide (Sm_2O_3) and Chromium (III) oxide (Cr_2O_3) with 99.9 % purity. These binary oxides were mixed according to the proper stoichiometric proportions for 5 h in air using the agate mortar and pestle in order to obtain a homogeneous mixture. This product was calcined in alumina crucible at 1000ºC for 12 h in air followed by regrinding of 2 h and pelletized by applying 60 kN pressure using a hydraulic press. These pellets were sintered at 1200º C for 36 h in air and slowly cooled in air to room temperature. This process leads to grain growth and attains high density without any pores inside the pellet. The X-ray powder diffraction (XRD) measurements of the samples were carried out to using X-ray powder diffractometer of model: Rigaku; TTRAX III equipped with Cu-$K\alpha_1$ radiation (λ = 1.54056 Å) as laser source. The diffraction angle (2θ) variation was kept between 10º and 90º with slow scan speed of 2 degrees/minute with step size ~ 0.02. These studies confirm the monophasic nature of the samples. Moreover, the crystallographic parameters and other relevant data has been extracted by means of Rietveld Refinement method using FullProf suite software. X-ray photoelectron spectroscope (XPS) was used to probe the electronic structure and oxidation state of the constituent elements (Gd, Sm, Cr, O) to complement the phase purity. These measured were performed using a high-resolution PHI 5000VVersaProbe III Scanning XPS with microprobe Al Kα (544 eV). The core-level X-ray photoelectron spectra were calibrated with C-1*s* binding energy 282.6 eV. In order to characterize the vibrational excitations a detailed Raman spectrum were recorded using a HR Raman spectrometer (model: LabRam HR) from Horiba Jobin Yvon using monochromatic radiation of wavelength λ ~ 632.8 nm He-Ne laser (20mW laser power) operating under backscattering geometry. Temperature dependent Raman study has been performed down to the liquid-nitrogen temperatures 80 K from 300 K using the THMS600 module. For a precise understanding of magnetic structure of GSO we performed the DC magnetization measurements using a physical property measurement system (PPMS) from Quantum Design (Model: Dynacool) assembled with a vibrating sample magnetometer (VSM) accessory. The magnetization data has been recorded between the temperatures 1.9 K and 300 K for different magnetic fields (H ~ ± 90 kOe). Various measurements protocols have been employed to measure the magnetization, few of them are zero-field-cooled-warming (ZFCW), field-cooled-warming (FCW) and field-cooled-cooling (FCC) protocols. In the following section we present the results and analysis pertaining to the above experiments.

6.3 Results and Discussion:

6.3.1 Crystal structural analysis:

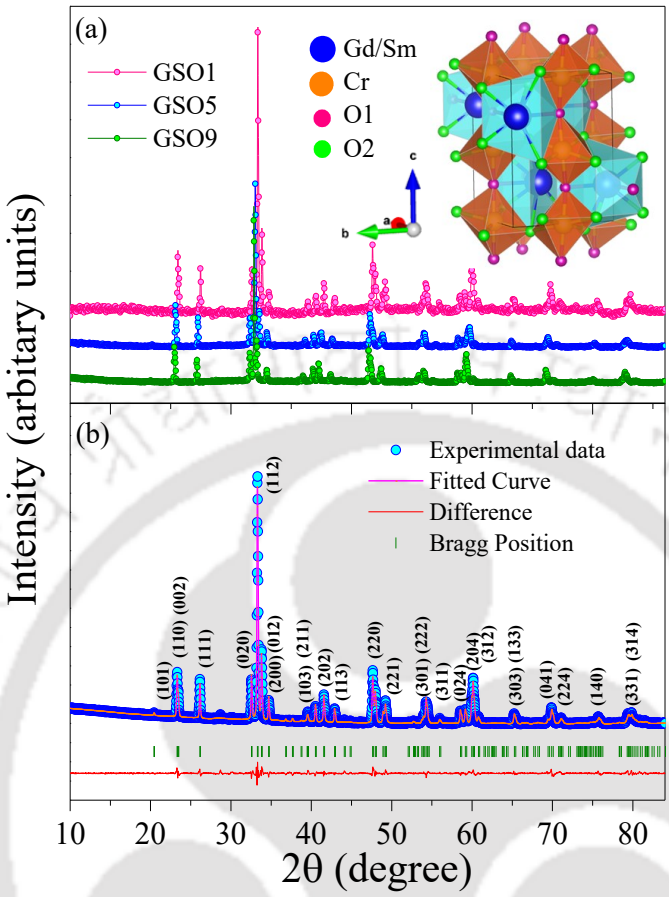

Fig. 6.1. (a) The room temperature XRD of $Gd_{0.9}Sm_{0.1}CrO_3$ (GSO1), $Gd_{0.5}Sm_{0.5}CrO_3$ (GSO5) and $Gd_{0.1}Sm_{0.9}CrO_3$ (GSO9) represented as pink, blue and green lines respectively. (b) The XRD of GSO5 along with Rietveld refinement considering Pbnm space group of distorted orthorhombic systems. The pink spheres represent the experimental data, black, blue and green lines refer to the fitted curve, difference and Bragg positions respectively. The inset shows the unit cell structure of Gd0.5Sm0.5CrO3 where blue, white, yellow, pink, and green spheres symbolize Gd, Sm, Cr, apical and basal oxygen, respectively. The refinement shows the phase purity of all the three compositions.

We begin our analysis with the crystal structure for different compositions of the investigated system. The associated crystallographic cell parameters are calculated and analysed by means of powder XRD for all the three compositions of GSO with x = 0.1, 0.5 and 0.9. Fig. 6.1(a) shows the XRD patterns of GSO1, GSO5 and GSO9 along with the Rietveld refinement data of GSO5 (Fig. 6.1(b)) which conforms the perovskite structure and the phase purity with goodness of the fit χ^2 = 2.67 for GSO5. The unit cell structure obtained from VESTA after refinement for the same sample is displayed in the inset of Fig. 6.1(b). Here the blue spheres represent A-site cation (Gd^{3+}/Sm^{3+}) and yellow spheres show the B-site Cr^{3+} ions. While the apical and basal equilateral oxygen have been represented with pink and green smaller spheres. The A-site cations move in opposite direction with respect to each other in CrO_6 octahedra in both in-phase and out-phase tilting with respect to [001] and [110] axes. All the Bragg peaks are indexed using *Pbnm* space group (no. 62) with

distorted orthorhombic perovskite structure where the absence of any extra peak signals devoid of any secondary phase present in the system.

Table 6.1 The refined crystallographic parameters obtained from XRD of $Gd_{1-x}Sm_xCrO_3$ (x = 0.1 (GSO1), 0.5 (GSO5), 0.9 (GSO9)).

Structural Parameters		GSO1	GSO5	GSO9
a (Å)		5.299 (7)	5.300 (1)	5.329 (5)
b (Å)		5.497 (8)	5.475 (16)	5.465 (9)
c (Å)		7.581 (10)	7.572 (20)	7.606 (8)
V (Å^3)		220.846 (25)	219.751 (37)	221.549 (22)
R_{Avg} (Å)		1.056	1.066	1.0764
θ [110]		8.95	5.4	9.427
φ [001]		14.613	16.218	10.474
t		0.676	0.677	0.677
Gd (4*c*)	*x*	0.9866 (4)	1.0121(4)	0.9937 (6)
	y	0.0571 (16)	0.0551 (2)	0.0344 (3)
	z	0.2500	0.2500	0.2500
	Ocs	0.5	0.5	0.5
Cr (4*b*)	*x*	0.0000	0.0000	0.0000
	y	0.5000	0.5000	0.5000
	z	0.0000	0.0000	0.0000
	Ocs	0.5	0.5	0.5
O1 (4*c*)	*x*	0.0490 (1)	-0.029(3)	0.0216 (2)
	y	0.4736 (13)	0.4835 (1)	0.5538 (1)
	z	0.2500	0.2500	0.2500
	Ocs	0.5	0.5	0.5
O2(8*d*)	*x*	0.8122 (1)	0.7029(9)	0.7307 (7)
	y	0.2116 (13)	0.2865 (2)	0.2965 (3)
	z	-0.0507 (9)	0.0624 (3)	0.0440 (4)
	Ocs	1.0	1.0	1.0
Cr-O1		1.918(6)	1.901(13)	1.927(1)
Cr-O21		2.059(5)	2.017(4)	2.062(1)
Cr-O22		1.911(7)	1.960(3)	1.846(2)
<Cr-O2>		1.985	1.988	1.954
<Cr-O>		1.963	1.959	1.945
θ_1 (Cr-O1-Cr)		162.1(3)	169.2(9)	161.1462(2)
θ_2 (Cr-O2-Cr)		148.2(4)	146.70(11)	155.2013(7)
Δ (10^{-4})		12.026	5.7909	20.876

The refined lattice parameters are listed in Table 6.1. The hole doped GSO with Sm substitution at some of the Gd cations shows increment in the cell parameter *a* while reduction in *b* and *c* due to the due to the larger cationic radius of Sm^{3+} (~1.079 Å with VIII coordination no.) than that of Gd^{3+} (~1.053 Å with VIII coordination no.) [68,314,325]. The occupancy of two A-site cations (Sm and Gd) at same crystallographic site induces the disorder in the unit cell which has been characterized using the average radius of A-site cations as calculated by:

$$R_{Avg} = \sqrt{(1-x) \times R_{Gd^{3+}}^2 + x \times R_{Sm^{3+}}^2} \tag{6.1}$$

Where $R_{Gd^{3+}}$ and $R_{Sm^{3+}}$ are the radii of the Gd and Sm cations, respectively. From the Table 6.1. it can be seen that a distinct anomaly in volume and lattice parameter *c* occurs for $x = 0.5$ and changes thereafter for further increase of *x*. In order to understand and validate the above scenario the other cell parameters are systematically evaluated. Here the tolerance factor is calculated by Goldschmidt's formula as given below.

$$t = \frac{((1-x) \times R_{Gd^{3+}} + x \times R_{Sm^{3+}}) + R_{O^{2-}})}{\sqrt{(R_{Cr^{3+}} + R_{O^{2-}})}} \tag{6.2}$$

The magnitude increases with increasing the Sm substitution at the Gd sites indicating the stabilization of the unit cell towards *Pm3m* ideal cubic space group. Here two types of oxygen atoms are denoted by apical oxygen-O1 and basal equilateral oxygen O21 and O22. The sudden reduction in the octahedral distortion (Δ) by one

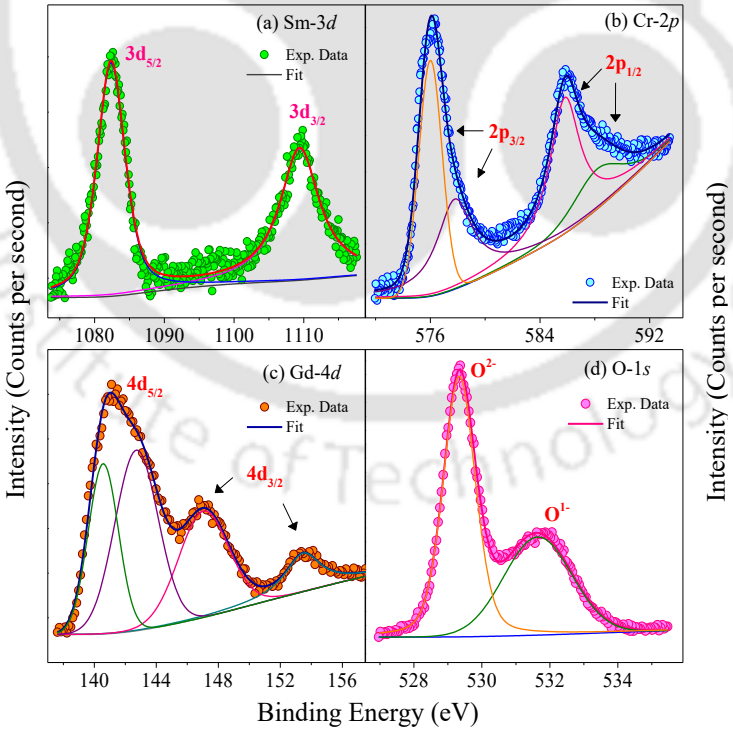

Fig. 6.2. The X-ray photoemission spectra of the individual elements of GSO5 bulk polycrystalline sample: (a) Sm-3*d* (green), (b) Cr-2*p* (blue), (c) Gd-4*d* (orange) and (d) O-1*s* (pink) core levels. Here the spheres represent the experimentally obtained data points while the solid lines represent the peak fitting data. The phase purity confirms the presence of proper oxidation states of the constituent elements.

factor for GSO5 can be attributed to the drop of *b* axis length by 0.4% which increases rapidly with increasing the Sm substation from *x* =0.5 to 0.9. Further, the averaged bond distances $d_{(Cr-O)}$ between IX coordinated Cr and all the basal and the apical oxygen atoms for N = 6 has been calculated by considering the magnitude of Δ as reported in the Ref. [326]. The average Cr-O21 bond length changes exactly in the reverse way as that of with Cr-O22 with Sm^{3+} substitution which indicates the shrinking of one Basal-Oxygen-Cr bond with elongation of the another keeping the whole trend constant overall inside CrO_6 octahedra. Similar anomaly bond length has been noticed for GSO5 system as well. The in-phase (θ) and out-phase (φ) tilting with respect to [110] and [001] axes have been calculated using $\theta = 180 - [Cr - O_1 - Cr]/2$ and φ = $cos^{-1}[\cos\frac{[180-[Cr-O2-Cr]]}{2}/\sqrt{cos\theta}$] which are listed in Table 6.1. We noticed a prominent change in GSO5 pointing towards the minimum and maximum bending of the CrO_6 octahedra which is in line with the bond length variation as well. The large rare earth cation size shares bond angles between both the apical and basal oxygen that increases from 2.356 Å to 2.749 Å and 2.341 Å to 2.544 Å for the compositions GSO1 - GSO9, respectively confirming the high sensitivity of oxygen affinity of the rare earth. Inside the CrO_6 octahedra, the bond angles between Cr-O1-Cr and Cr-O2-Cr shows similar trend (Table 6.1.) in-line with the previously specified parameters. Concurrently, the prominent anomaly and the continuous deviation of the tilting angles and the octahedral distortion with Sm/Gd substitution may have a strong influence on the magnetic properties and Raman spectra as well which will be discussed below.

6.3.2 Electronic structure and X-ray photoelectron spectroscopy:

In order to probe the electronic structure of the synthesized perovskites we performed XPS studies through one can confirm the oxidation states of the constituent elements to validate the phase purity of the system. Figure 6.2 shows the XPS spectra of GSO5 system. Using these spectra, the surface level electronic structure of the elements is studied. All the core level spectra have been calibrated with the C-1*s* binding energy peak located at 285 eV. The Tougaard algorithm for background correction and all the chemically different states are determined with the help of least square fitting of the experimental data. The binding energy dependence of the ejected photoelectron intensity is probed for each of the elements separately: a) Sm-3*d* b) Cr-2*p* c) Gd-4*d* and d) O-1*s*. Here the Sm-3*d* core level spectra (Fig. 6.2(a)) are deconvoluted into two peaks cantered at 1082.2 eV and 1109.4 eV. Among these the lower binding energy peak is associated with the $3d_{5/2}$ and the peak at higher energy is originating due to $3d_{3/2}$ state. These two peaks separated by the large binding-energy Δ ~ 27 eV are generally characterized as the spin-orbit coupling which confirms the trivalent oxidation state of Sm [327]. The deconvolution of Gd-4*d* core-level spectra (Fig. 6.2(c)) requires four individual spectra lines which consists of 2 doublets associated with the $4d_{5/2}$ and $4d_{3/2}$ core levels. The peaks at 140.7, 142.7, 146.8 and 153.2 eV are indexed on the basis of the listed experimental data available in the literature. Here Gd with Xenon like configuration with filled *s* orbital and singly occupied *f* and *d* orbitals get oxidised to Gd^{3+} indicates the presence of trivalent state of Gd. The splitting of the 4*d* orbitals due to spin-orbit coupling in $4d_{5/2}$ (146 and 153 eV) and $4d_{3/2}$ core levels (140 and 142 eV). We did not observe any additional transitions pertaining to the electronic state of constituent elements studied in this

case which confirms the purity of the sample. On the other hand, the Cr-2*p* spectra (Fig. 2(b)) consists of 4 peaks at: 575.8 and 577.9, 585.5 and 588.3 eV which are consistent with the range given in the standard XPS database of NIST [328]. The peaks at 585 and 588 are originating due to the doublet of $2p_{1/2}$ electronic state and the other two peaks are ascribed to the $2p_{3/2}$ state with no signatures of any satellite peaks. In this case the spin-orbit splitting is ~ 9.7 eV and 10.4 eV validates the existence of the trivalent state of Cr ion. Finally, the O-1s core-level spectra exhibit asymmetrical behaviour which is quite evident from the two-peak behaviour as a result of surface absorbed oxygen species. These O-1s peaks are situated at 529.3 and 531.7 eV in which the former one is due to the saturated O^{2-} ions confirming the O1s state. While the shoulder like second peak locating at 531 eV can be attributed to the surface originated excess oxygen in the form of hydroxide (O-H) [51], [329]. Notice that the peak values are little higher as compared to the ideal cases. Nevertheless, the transition energy of the electrons from 1*s* to 2*p* unfilled orbital is ascribed to the binding energy of the O. The increment of the binding energy is related to the 2*p* orbital hybridization with 1*s*. We did not find any signatures of oxygen-metal bonds associated with metal oxidation on the surface [330,331].

6.3.3 Raman spectroscopy analysis:

Now we move our focus to analyse distinct structural deviation of orthorhombic *Pbnm* structure from ideal cubic *Pm-3m* structure in terms of the Raman active modes. Generally, the *Pbnm* space group follows the Glazer's notation $a^-b^+a^-$ tilt which shows the mirror symmetry along the [010] plane and has three tilts having two of them with equal magnitude [332]. Figure 6.3 shows the Raman spectra recorded at room temperature in the wavenumber range 100-1000 cm^{-1} for three different systems GSO1, GSO5 and GSO9. For each spectrum, the Lorentzian functions are used to evaluate the exact peak position and the respective linewidths. Based on the *Pbnm* crystal symmetry, 24 Γ modes are generated in primitive cell at the Brillouin zone centre as given below.

$$\Gamma = 7A_{1g} + 7B_{1g} + 5B_{2g} + 5B_{3g} \tag{6.3}$$

here A_{1g} and B_{1g} are the symmetric modes, two B_{2g} and two B_{3g} represent antisymmetric modes, one A_{1g}, two B_{2g} and three B_{3g} corresponds to bending modes, two A_{1g}, one B_{1g}, two B_{2g}, one B_{3g} rotational mode and three A_{1g}, three B_{1g}, one B_{2g} and one B_{3g} are arising due to the A-site cation displacement. j of the appearance of the Raman active modes breaking the perfect cubic symmetry are: (*i*) displacement of the A-site cation in the *Pm3m* cubic structure (*ii*) distortion of the transition metal oxide octahedral, and (*iii*) Jahn- of the Raman activation as Cr^{3+} is JT inactive because the transition metal Cr in its stable ionized state Cr^{3+} with [Ar]$3d^3$ configuration fail to show JT phenomenon unlike Cr^{2+} with d^4 electrons exhibiting JT effect in both high and low spin state. Among the above indexed 36 modes few are optical and acoustic which are Raman inactive [334]. Overall, depending on the composition, we find total 10-11 modes detected exhibit blue and red shift for the respective modes. While the rest of the probable Teller (JT) distortion [333]. In the present

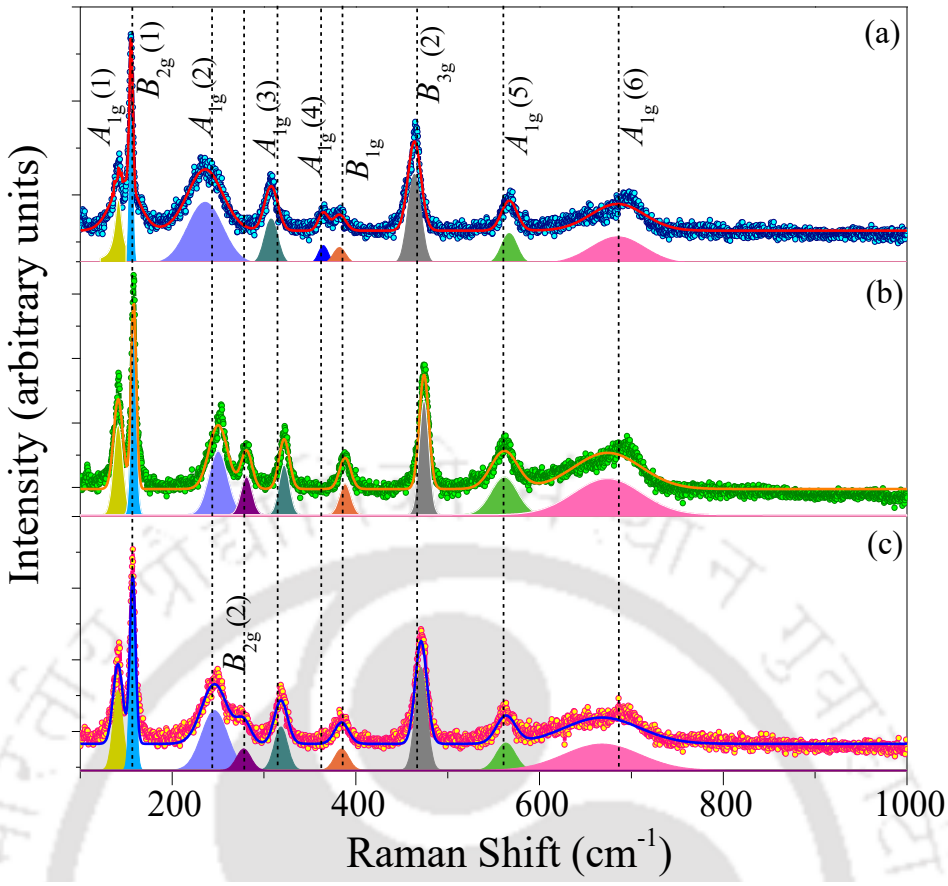

Fig. 6.3. The Raman spectra measured at room temperature (300 K) of (a) GSO9-blue (b) GSO5- green and (c) GSO9-pink within the range of 100 cm^{-1} – 1000 cm^{-1} along with the Lorentzian fittings corresponding to each spectrum. The nomenclatures of the individual modes are indexed. All the relevant phonon modes of the characteristic vibration present in the constituent molecules can be seen.

modes are not visible due to their low intensity [335–338]. All the modes are indexed respectively and matches well with the previously available literature and compared our results appropriately and these modes are listed in Table 6.2. The Raman mode shift is directly proportional to $\frac{1}{\sqrt{d}}$ with d as bond length of the atoms, which are included and compared with the data given in Table 6.1. The fluctuation occurring in each mode positions move towards the higher wavenumbers upon decreasing the bond length. However, the modes at the lower wavenumber (within the range of 160 cm^{-1}) arise mainly due to the displacement of the A-site cation (Sm and Gd) in the perovskite lattice. The $A_{1g}(1)$ mode appears due to the movement of magnetic Gd^{3+} and Sm^{3+} cations along the z direction out of plane, whereas, the $B_{2g}(1)$ phonon mode emerges due to the movement of cations at A-site lying in the x-direction. A shoulder like anomaly is found near 137 cm^{-1} for GSO1 and disappears for the rest of the two compositions. The same scenario was noticed in case of $B_{3g}(1)$ mode, which comes out as a result of the translation symmetry along y-direction corresponding to the Gd^{3+} and Sm^{3+} cations. Now, this peak is very prominent for $GdCrO_3$ pristine compound but after doping Sm of higher cationic radius the translation symmetry might have been diluted and hence it is not visible for higher Sm concentration compositions GSO5 and GSO9. [275]. The angular frequency (ω) is linked with the vibration of the atoms as $\omega \propto \sqrt{\frac{k}{m}}$, in which k being the force constant and m is the reduced mass of the constituent atoms [337].

Table 6.2 The calculated positions of individual Raman modes from Lorentzian fits at room temperature spectra for GSO1, GSO5 and GSO9 along with the pristine $GdCrO_3$ and $SmCrO_3$ values taken from reported data. (The data for undoped $GdCrO_3$ and $SmCrO_3$ are taken from previous reports).

Modes	$GdCrO^{333}$ cm^{-1}	GSO1 cm^{-1}	GSO5 cm^{-1}	GSO9 cm^{-1}	$SmCrO_3^{333}$ cm^{-1}
$A_{1g}(1)$	142.2	140.15	141.71	143.27	140.8
$A_{1g}(2)$	255.5	239.15	250.45	235.73	231.5
$A_{1g}(3)$	324.9	318.54	318.22	309.10	309.1
$A_{1g}(4)$	392.4	384.68	387.96	365.85	365.7
$A_{1g}(5)$	561.2	562.29	563.23	565.76	-
$A_{1g}(6)$	-	663.16	675.67	686.48	-
B_{1g}	388.7	384.68	387.96	383.29	382.4
$B_{2g}(1)$	159.3	157.9	158.21	155.41	155.2
$B_{2g}(2)$	284.5	274.6	280.87	-	252.7
$B_{3g}(1)$	137.1	shoulder	-	-	-
$B_{3g}(2)$	473.6	471.47	473.88	466.16	454.7

The substitution of lighter Sm (atomic mass: 150.36 u) at the Gd site (atomic mass: 157.25 u) shows a little change in the mode positions, especially $A_{1g}(1)$ mode which changes about 2.2% in its position as they tend to shift a little towards the lower wavenumber. This kind of displacement arises due to the vibrations which show little effect on the CrO_6 octahedra distortion. The next spectrum observed at 235 cm^{-1} arises due to the in-phase rotation of the CrO_6 octahedra along *y*-direction and termed as $A_{1g}(2)$ vibrational mode which shift ~ 11 cm^{-1} for GSO5 as compared to the other two compositions. The $B_{2g}(2)$ mode around 275 cm^{-1} are related to the Gd/Sm cation displacement in the Gd/Sm-O_{12} polyhedra along the *z*-direction. As the larger size Sm (r_{Sm} = 1.079 Å) substitutes the Gd position (r_{Gd} = 1.053 Å) orthorhombicity get reduced resulting the diminution of the mode intensity of GSO9 [338]. The $A_{1g}(3)$ mode of GSO9 occurring at ~ 318 cm^{-1} shows a huge shift of 9.44 cm^{-1} as a result of change in Gd/Sm-O bond length in the opposite directions of *x* axis of Gd/Sm-O_{12} polyhedra. The mode across 384 cm^{-1} is designated as an allowed symmetry crossover of $A_{1g}(4)$ and B_{1g} modes originating from out of phase rotation of CrO_6 octahedra in the *x*-direction. While the Gd/Sm-O stretching and anti-stretching movement takes place along the *z*-direction. In case of GSO9 system the evolution of the two prominent peaks finally merges slowly and shows similar spectrum as that of GSO5 and GSO1 (with increasing the R-site cationic radius). The $B_{3g}(2)$ mode at ~ 470 cm^{-1} is insensitive towards the orthorhombic distortion which occurs due to the out of phase bending or stretching of the CrO_6 octahedra [338]. This mode maintains a sharp intensity with a little shift in position (1.2 %). The prominent and broad peak fixed at ~ 563 cm^{-1} is labelled as $A_{1g}(5)$ arising from the antisymmetric stretching of the CrO_6 octahedra [336]. In the present case a broad phonon-mode within the range of 660 - 690 cm^{-1} can also be noticed for the Sm substituted systems contrary to the pristine compositions $GdCrO_3$ and $SmCrO_3$ [337]. This particular feature indicates the complex mixture of atomic distortion and defects caused by the two cations at A site

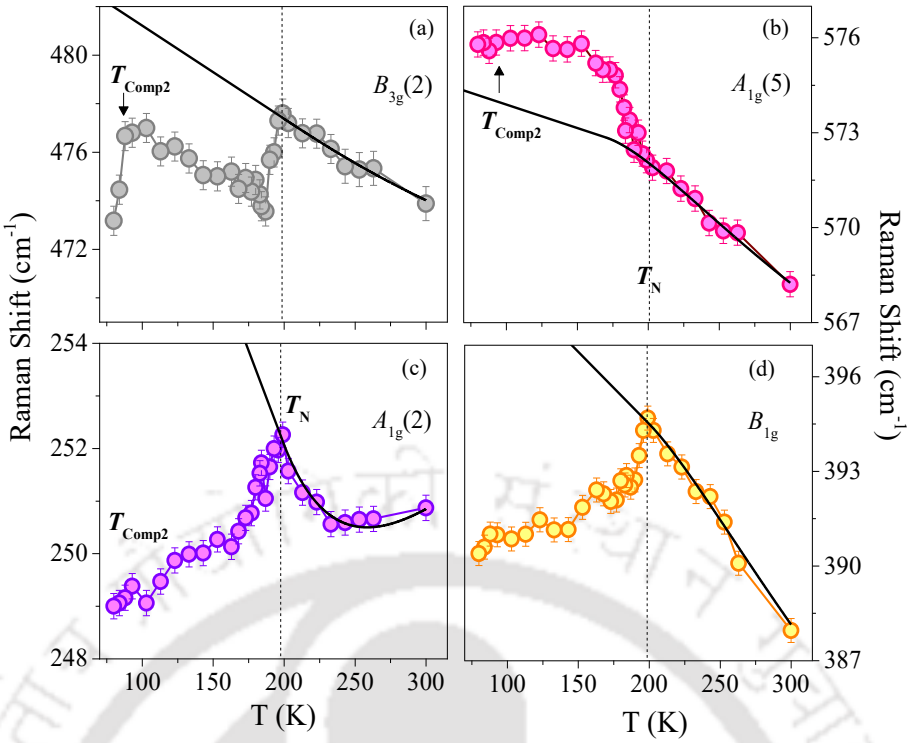

Fig. 6.4. The thermal evolution of the Raman shifts of GSO5 for some of the selected Raman modes: (a) B_{3g} (2), (b) A_{1g}(5), (c) A_{1g}(2), and (d) B_{1g} in the temperature region 80 K- 300 K in scattered spheres with frequency error bars. The solid black lines represent the fitted curves of frequency dependence of anharmonic phonon-phonon scattering according to Eq. 5. The dashed lines are guide to eyes for T_N. Presence of modes attributed to the anharmonic nature can be seen at lower temperature.

which is denoted by A_{1g}(6) mode. Following the previous studies such mode deviation can be attributed to the local breathing mode of oxygen that solely arises from the charge transfer between the unpaired *d* and *f* orbitals of rare earth cations and the unfilled *p* orbitals of the neighbouring oxygen ions [339]. Interestingly, the addition of Sm^{3+} at the Gd^{3+} site reflects the change in the intensity and sharpness (FWHM) of the Raman spectrum which clearly refers to the structural deformation (tolerance factor) of the system.

6.3.3.1 Temperature dependent Raman analysis:

In order to correlate the origin of Raman active modes with the magnetic transitions we performed a detailed temperature dependent Raman measurement were carried out in the temperature range 80 K - 300 K within 100 – 800 cm^{-1} wavenumber range. The prominent observations as a result of anharmonicity of the primitive cell lattice dynamics are realised by means of: (*a*) The lower wavenumber modes got intensified when the measurement temperature approaches towards T_N (~196 K) and starts getting diminished as the temperature reaches 113 K, thereafter, maintains the similar intensity variation at low-temperatures. (*b*) The sharpness of the modes of higher wavenumber decreases significantly (FWHM increases) while the lower wavenumber modes become sharper as the temperature approaches T_N and starts getting broader for $T < T_N$. No structural phase transition was observed in the investigated temperature and wavenumber range. To precisely obtain the Raman peak position, FWHM and intensity, the deconvoluted spectrum using Lorentzian

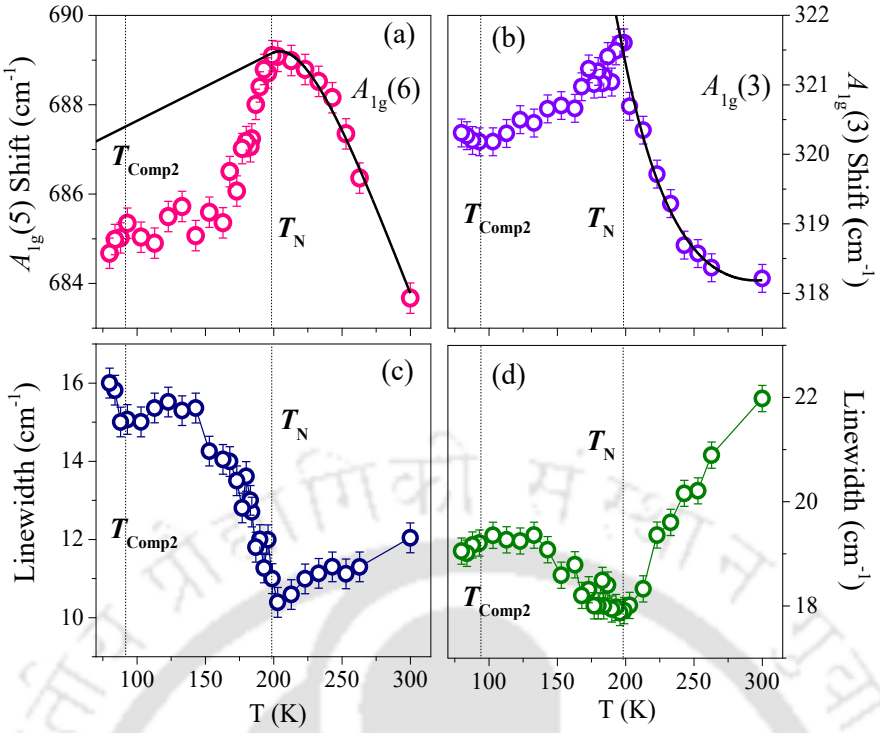

Fig. 6.5. The temperature dependence of the specific modes (a) A_{1g} (6) and (b) A_{1g} (3) within the temperature range of 80 K-300 K in the top panel. The corresponding linewidths are plotted in in the bottom panel. The scattered symbols are the data points along with frequency error bars. The solid black line is the fitted curve with equation (5). The dotted lines are the guides to the eye representing the T_N and T_{Comp2}. The spin-phonon coupling can be confirmed as the origin of the. deviation of the specific modes from anharmonicity.

profiles at each and every individual temperature we executed Granado *et al.* mathematical relation as given below [340]:

$$\omega(T) = \omega_0(T) + \Delta\,\omega_{lat} + \Delta\,\omega_{s-ph} + \Delta\,\omega_{el-ph} + \Delta\,\omega_{anh} \tag{6.4}$$

In the above expression $\omega_0(T)$ is the frequency of the corresponding mode at absolute temperature in the harmonic approximation. The second term corresponds to the frequency of the lattice expansion/contraction driven by the changes occurring in the ionic binding energy which is generally applicable for the isotopically expanded systems. The $\Delta\,\omega_{s-ph}$ represents the deviation of phonon frequency of spin-lattice coupling as a result of the phonon modulation of the spin-exchange integral. The fourth term elucidates the effect of a renormalization of the electronic states of the constituent elements and can be neglected for low carrier concentration. The last term signifies the change in the intrinsic anharmonic frequency at constant volume which is formulated as follows [340].

$$\omega_{anh}\,(T) = \omega_0 + A\left[1 + \frac{2}{e^{\frac{\hbar\omega_0}{2k_BT}}-1}\right] + B\left[1 + \frac{3}{e^{\frac{\hbar\omega_0}{3k_BT}}-1} + \frac{3}{(e^{\frac{\hbar\omega_0}{3k_BT}}-1)^2}\right] \tag{6.5}$$

Here A and B are the anharmonic coefficients obtained from the Raman data fitting above T_N. The detailed thermal response of some of the specified phonon modes namely: B_{3g} (2), A_{1g} (5), A_{1g} (2) and B_{1g} are depicted

in Figs. 6.4(a) – 6.4(d) respectively within the temperature range 80 K - 300 K. All the modes show gradual softening or hardening with fixed anomaly at T_N. However, the mode B_{3g} (2) exhibits a hardening nature below T_N similar to the previous reports on $YCrO_3$ polycrystalline sample which are related to the relaxing of the CrO_6 octahedra [341]. The out-of-phase rotation of the octahedra associated with B_{1g} fitted with Eq. 6.2 shows a prominent softening at low temperature with the deviation from the anharmonicity indicating the presence of another factor possibly direct spin-phonon coupling. The hardening of antisymmetric stretching mode A_{1g} (5) can be understood as a result of exchange-striction effect and the presence of Cr^{3+}-Cr^{3+} AFM coupling. In $GdCrO_3$ this mode hardening is consistent along with the cell volume reduction indicating a strong spin-phonon coupling of Gd^{3+}-Cr^{3+} interaction [336]. The softening of in-phase rotation of the CrO_6 octahedra driven in A_{1g} (2) below the transition temperature is consistent with the previous results [342]. Such softening can be ascribed to the quasi-harmonic effect and thus could be related to the change in the tilt angles (θ_1 and θ_2) arising due to the Gd^{3+}-Cr^{3+} exchange interaction [342]. Figure 6.5 demonstrates the thermal evolution of A_{1g} (6) and A_{1g} (3) modes. The softening of A_{1g} (6) mode by ~ 0.5 % towards liquid nitrogen temperature happens as a consequence of Cr^{3+} ordering because of magnetostriction effect. However, it should be noted that the FWHM is related to the phonon life-time which usually alters with measurement temperature. From Fig. 6.5(c), it is clear that the inconsistency around the same temperature precluded the magnetostriction effect present in the system implying the existence of direct spin-phonon coupling. Previously reports by Sarkar *et al.* reported higher (>3) oxidation state of Cr as the origin of this particular mode but the XPS analysis of the Cr-cation

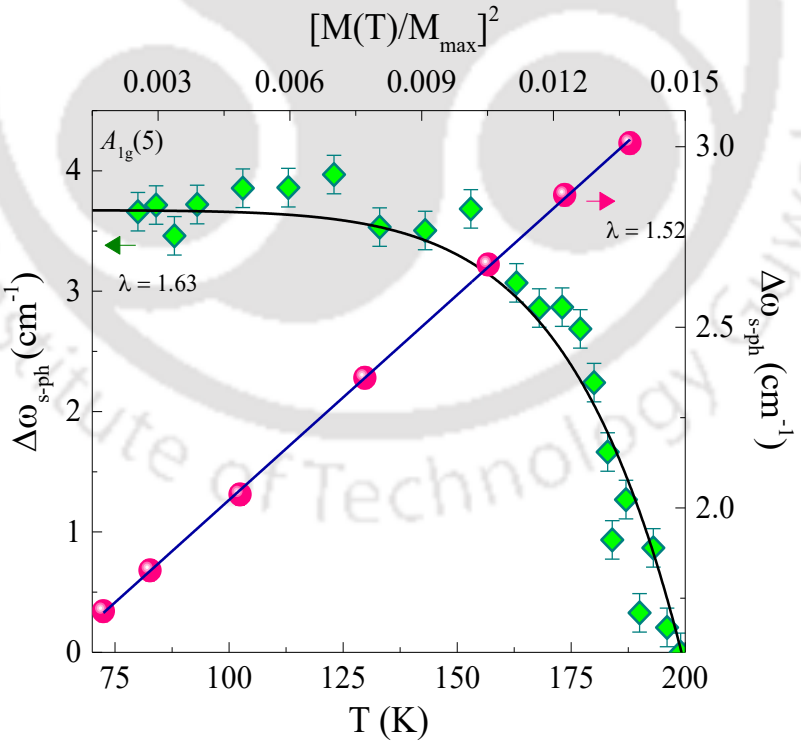

Fig. 6.6. The thermal dependence of the $\Delta\omega_{s\text{-}ph}$ of the A_{1g} (5) mode in the *left-hand side* scale (green squares) with the black curve fitted with Eq. 6.8(a). The *right-hand scale* represents the variation of $\Delta\omega_{s\text{-}ph}$ with respect to $[M(T)/M_{max}]^2$ (pink spheres) and the black straight-line is the curve fitted with Eq. 6.8(b). The direct correlation between phonon instability and magnetic characteristics with the help of chosen mode A_{1g} (5) can be established.

oxidation state ruled out that possibility [337]. The intense softening of the $A_{1g}(3)$ mode down to transition shows similar anomaly in the linewidth as well (Fig. 6.5(d)) which refers to the influence of Gd^{3+}-Cr^{3+} spin-phonon coupling on the A-site cation (Gd/Sm) movement in the Gd/Sm-O_{12} polyhedra [336]. The atypical characteristics of the Raman spectrum of deviation of the particular frequency from its intrinsic nature is related to the renormalization of the phonon modes due to the corresponding magnetic transition. This shift can be written in the form as:

$$\Delta\omega_{s-ph} = \omega(T) - \omega_0 = \lambda < S_i . S_j > \tag{6.6}$$

where $\omega(T)$ symboligies the renormalized phonon frequency at a particular temperature, λ represents the spin-phonon coupling constant which depends on the change in the bond length and bond angle between the atoms concerning Oxygen atoms. The spin-spin correlation function $< S_i . S_j >$ is denotes the average of the nearest neighbour i^{th} and j^{th} site spin interaction [340]. Now, from the molecular field theory approximation the spin-spin correlation function can be written as:

$$< S_i . S_j > \approx 4 \left[\frac{M(T)}{4\,\mu_B}\right]^2 \tag{6.7}$$

with $M(T)$ is the magnetization of the Ferromagnetic contribution coming from the transition metal ions. So, finally inserting Eq. 6.7 into Eq. 6.6, thermal dependence of the frequency mode arising due to the spin-phonon coupling can be simplifies into:

$$\Delta\omega_{s-ph} \approx \lambda\, S^2\, [1 - (\frac{T}{T_N})^{\gamma}] \tag{6.8a}$$

$$\approx \lambda\, [\frac{M(T)}{M_{sat}}]^2 \tag{6.8b}$$

where S = 3/2 and M_{sat} is the saturation magnetization of the corresponding system [336]. Here, $A_{1g}(5)$ mode is analysed in particular as it shows prominent deviation from the ideal anharmonic nature and followed a particular trend as shown in Fig. 6.6. Here, thermal dependence (green sphere) along with the fitted curve (with Eq. 6.8(a) shown with the black line and right-hand side and top scale is the variation according to Eq. 6.8(b) (pink spheres represent experimental points while the black line shows the linear fit). Here, the co-existence of both positive and negative shifts is the result of the competitive interaction of canted AFM and FM correlations below Néel temperature. Following this, Eq. 6.6 can be written in the form of lattice vibration force constants k_1 and k_2 as:

$$\Delta\omega_{s-ph} \propto -k_1 < S_i . S_j > + k_2 < S_i . S_k > \tag{9}$$

assumption of k_1 and k_2 corresponding to the FM and canted AFM exchange interactions between the nearest spins $< S_i . S_j >$ and $< S_i . S_k >$, respectively which depends on the temperature. The magnitude of $(k_2 - k_1)$ indicates the polarity of the phonon mode shift [341]. In Fig. 6.6 the excellent fit of experimental data with the above expressions represent the domination of nearest neighbour Cr^{3+}-Cr^{3+} antisymmetric exchange interaction. The symmetric exchange coupling constant (J_e) is an order higher in magnitude than that of the

with the antisymmetric one (D) (see Table 6.2). The values of spin-phonon coupling constant from magnetization data using the equation 6.8b with M(T) and M_{Sat} values taken from the temperature dependent magnetization plots (λ ~ 1.52) matches well with that of obtained from the order parameter (λ ~ 1.63) and with the previous reported data [336]. These results corroborate the existence of strong magnetoelectric coupling present in the system, as evidenced by the dielectric measurement and the enhancement of polarization with magnetic field reported previously [336].

6.3.4 Magnetic structure:

6.3.4.1 Temperature dependence of magnetization:

In Fig. 6.7 we show the temperature dependence of the dc magnetization M(T) measured under conditions such as ZFCW, FCC and FCW protocols in the presence of external applied field of H_{DC} = 100 Oe for all the three investigated system. Here M(T) behaviour of GSO1 system depicted in Fig. 6.7(a) shows a robust anti-ferromagnetic ordering with Néel temperature T_N = 196 K. Upon further decrease of temperature, the magnetization increases for FCC. Beyond $T_{Bifurcation}$ = 157 K the magnetization decreases corresponding to the change of the slope (Fig. 6.7(a)) and the net magnetization M_{Net} becomes zero at T_{Comp1} = 116 K which finally exhibit large negative magnetization. After attaining the maximum negative magnetization (~ -293.9 emu/mol) at 19 K the magnetic moment increases (+ve M) further and around 6.7 K, a significant zero-crossover was evident in M_{FCC}, although M_{FCW} crosses the null point at slightly higher temperatures ~ 19 K, overall now we call this point as cross over point second compensation point (T_{Comp2} = 6.7 K). Interestingly, both M_{FCC} and M_{FCW} increases monotonously till 2 K. However, the M_{ZFCW}(T) shows the clear role of trivalent Gd spins which orders across 9.3 K commonly referred as spin-reorientation temperature (T_{SR} = 9.3 K), yet at higher temperatures M_{ZFCW} gradually decreases till 145 K where the system goes through the zero-crossover of magnetization and gradually decreases its value as the temperature approaches T_N. While for GSO9 (Fig. 6.7(c)) the M(T) variation shows entirely different trend in which the magnetization switches the polarity at 29.8 K (T_{Comp1}) upon heating from 2 K and reaches a maximum negative magnetization at 111 K and slowly increases the magnetization till 196.5 K (T_{Comp2}) and becomes the paramagnetic beyond T_N. Both FCC and FCW increases below T_N with significant hysteresis between them till 27 K and crosses the zero-magnetization axis at 18 K (T_{Comp1}). On the other hand, the M(T) of GSO5 exhibit similar trend as GSO1 with slight change in the ordering temperatures as evident from Fig. 6.7(b). Significant enhancement in the T_N (193.7 K) was noticed in this composition as compared to the other two systems GSO9 and GSO1 in which the polarity of magnetization changes nearly twice measured under all the three protocols. Here, the hysteresis between the FCC and FCW becomes smaller in both the temperature ranges and the magnetic moment with a crossover across 76 K (T_{Comp2}) and attains a maximum negative magnetization (-116.6 emu/mol at 30 K) for M_{FCC} shows a positive magnetization, cross over temperature after 9.7 K (T_{Cross}). The dc magnetization under ZFCW protocol shows a spin-flip at 29 K (T_{SF}) and slowly reaches to T_{Comp1} at 181.3 K followed by T_N. The arrows of pink, green and violet colours depict the spins of Cr^{3+}, Gd^{3+} and Sm^{3+}, respectively.

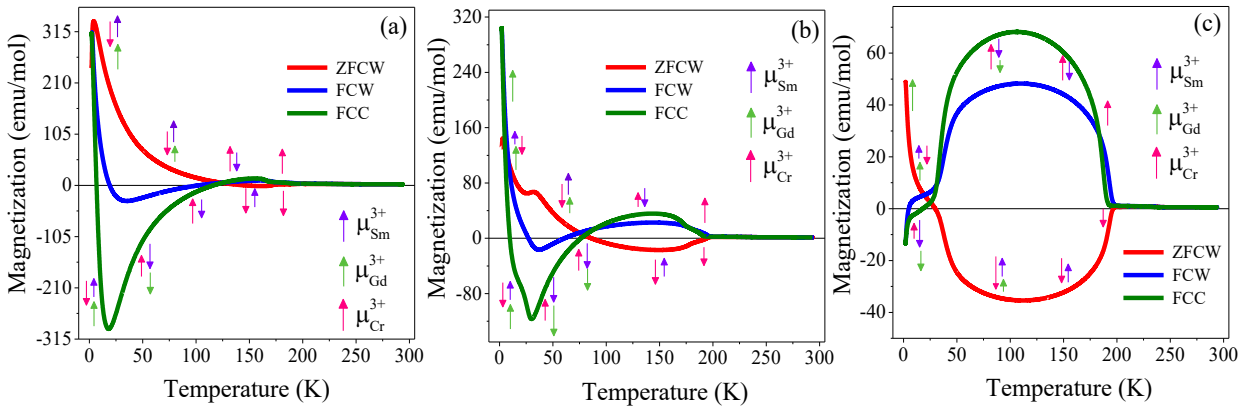

Fig. 6.7. The temperature dependence of three different magnetization protocols ZFC, FCC and FCW for (a) GSO1 (b) GSO5 and (c) GSO9 measured under an external field of H_{DC} = 100 Oe. The respective spins of Sm^{3+}, Gd^{3+} and Cr^{3+} are designated by purple, green and red colour respectively. The compensation temperature and multiple magnetic crossovers are present in all the three compositions in the high temperature regime.

After discussing different magnetic transitions and their trend/magnitudes, now we turn our focus on the role of different cations in deciding their global magnetic behaviour. In the present case the magnetic ordering is completely dominated by the co-existence of the competing multiple exchange interaction between the cations present in the system: Cr^{3+}-Cr^{3+}, Gd^{3+}-Gd^{3+} and Gd^{3+}-Cr^{3+}. The structural and magnetic unit cells are equivalent for rare earth orthochromite oxides ($RCrO_3$) with the Wyckoff positions 4*b* for Cr $(\frac{1}{2}, 0, 0)$, $(\frac{1}{2}, 0, \frac{1}{2})$, $(0, \frac{1}{2}, \frac{1}{2},)$ and $(0, \frac{1}{2}, 0)$. The first magnetic transition starting from room temperature is T_N which is attributed to the ordering of Cr^{3+} sublattice in *G*-type AFM configuration along with FM component which is explained on the basis of Dzyaloshinskii-Moriya exchange mechanism [342]. At T_N, the rare earth Sm^{3+} and Gd^{3+} moments are in disordered configuration. According to the Bertaut *et. al* the magnetic unit cell orders with the propagation vector $k = 0$ maintaining the Γ_4 (G_x, A_y, F_z) configuration intact [343]. The Γ_4 configuration carries an uncompensated FM component oriented parallel to *z* crystallographic axis with Cr spins oriented along the dc field for M_{FC} and opposite to it under M_{ZFC} condition. Upon lowering the temperature to 161 K (185 K) for GSO1 (GSO5), the FC and ZFCW curves start to deviate opposite to each other and has been nomenclature as $T_{Bifurcation}$. Structural or magnetic phase transitions are absent here, however only the Cr^{3+} spins start to get aligned and creates an internal field on the rare earth sublattices. The temperature range of this region is negligible for GSO9. Further, on decreasing the temperature the rare earth Sm^{3+} spins slowly start to polarize themselves antiferromagnetically with the internal field of Cr^{3+} sublattice aligning antiparallel to the Cr^{3+} spins. The GSO1 system experiences a fully compensated sublattice magnetization of competing Cr and Sm (and some of Gd) moments at T_{Comp1} ~ 145 K and the compensation shifts to lower temperatures for GSO5 (~ 75 K) as more Sm^{3+} moments persist to hold the uncompensated Cr^{3+} spins back to AFM configuration towards *x*-axis. For GSO9, the antiparallel contribution of Gd^{3+} spins along with Sm^{3+} followed by the change in slope at ~ 37 K assigned as T_{SR} accompanied by the maximum negative magnetization (T_{Min}). Previous studies by Gorodetsky *et al.* reported that the spin-reorientation

transition at T_{SR} could be a continuous process with second order in nature where the AFM Cr^{3+} spins rotate to align in Γ_2 (F_x, C_y, G_z) spin orientation [324]. But later in 2022 T. Sau et al. claimed the transition to be first order in nature by the help of Neutron diffraction [316]. This feature manages to persist in GSO5 at lower temperatures (28 K) as the smaller number of Sm^{3+} moments are not enough to rotate the Cr^{3+} spins from *z* to *x* crystallographic axis at higher temperatures. For Gd rich system (i.e. GSO1 in the present case), the anomaly at 9.3 K is due to the continuous rotation of uncompensated Gd spins from *z*- to *x*-axis driven by Gd^{3+}-Cr^{3+} anisotropic exchange interaction which is designated as T_{SR} or T_N^{Gd} that occurs at lower temperature (~5.8 K for GSO5). The sharp change in slope of M(T) around 28.3 K (labelled as T_{SF}) is noticeable in GSO1 and GSO5 in both M_{FCC} and M_{FCW} protocols. The flipping of the Cr^{3+} spins and both the rare earth spin moments can be explained using the Zeeman energy: $E_{Zeeman} = -\mu_0 M_{Net} H_{DC} \cos\theta$, where μ_0 is the permeability of free space, M_{Net} is the net resultant moment of Cr^{3+} and B site cation (Sm^{3+} and Gd^{3+}) of a primitive magnetic cell and θ is the angle between the M_{Net} and H_{DC}. Here the angle θ changes from $\theta = \Pi$ to $\theta = 0$ as E_{Zeeman} changes from positive to negative with lowering the temperature. In the case of M_{FCW}(T), the region becomes little broader than M_{FCC}(T) as flipping the spins from stabilized zone takes more thermal energy. Hereafter, the magnetization increases due to activation of high trivalent Gd spins (of ~7.94 μ_B) with lowering the temperature finally leading to a M_{Net} to be zero (at T_{Comp2}) ~ 7 K (9.7 K) for GSO1 (GSO5), respectively, where the combined magnetization of Cr^{3+} and antiferromagnetically ordered Gd^{3+}-Sm^{3+} along *x*-axis counterpoises each other. For Sm rich GSO9, the large hysteresis between the FCC and FCW starting from T_N to T~30 K is the indication of disordered mixed phase magnetic regions having glassy arrested spin states termed as magnetic glass (T_{MG}) [323]. Cooling the system through T_{SR} induces the arrested metastable state which is AFM insulating in nature and the onset of freezed kinetic motion becoming more pronounced across T_{MG}. This scenario continues till the temperature is cooled enough (super-cooled state) to activate the trivalent Sm and Gd spins completely to be navigated towards the internal induced field [344]. This extra magnetic ordering is due to the orientation of polar phase either to Γ_{26} $(C_x, G_y, C_x; C_x^R, A_y^R, F_z^R)$ or Γ_{27} $(F_x, C_y, G_z; F_x^R, C_y^R, G_z^R)$ [316].

Figures 6.8(a) and 6.8(b) depict the temperature dependence of the 1st derivative of (χT) for H_{DC} = 100 Oe. As the magnitude of the (χT) signifies the magnetic energy associated with the magnetic unit cell and the temperature derivative denotes the exact location of the AFM to PM phase transition region (T_N) and T_{SR}. Figure 6.8(a) shows the change in T_N from 193.8 K (GSO1) to 194 K (GSO9) which agrees well with the values obtained from M-T curves with the increment of magnetic moment of ~92.7% as discussed above. The other hump at lower temperatures ~ 171 K (GSO1) and 177.8 K (GSO5) is the signature of change in slope which follows the similar trend as T_N which shifts towards the higher temperature with increasing of Sm concentration. Interestingly, this feature is absent in GSO9. The calculated effective moment (μ_{eff}) of GSO5 is 6.845 μ_B $/f.u.$ and here the temperature independent diamagnetic susceptibility term (χ_0) has been subtracted from the current experimental values in which magnitude of χ_0 was obtained from the non-relativistic Hatree –Fock calculations performed by Mendelsohn and Biggs [294]. In order to estimate the μ_{eff} the inverse susceptibility data (for T > T_N) has been plotted and fitted with the Curie-Weiss(CW) Law:

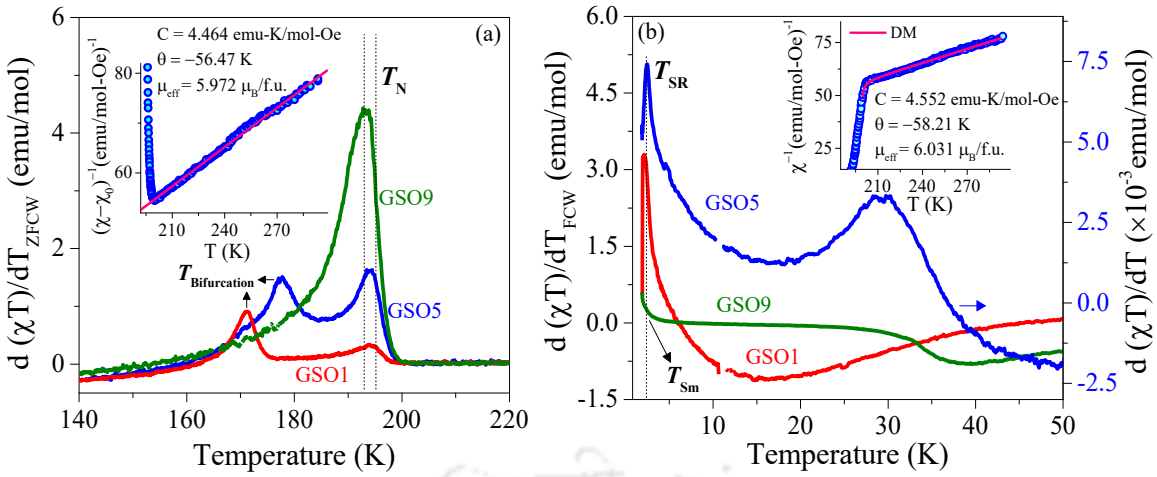

Fig. 6.8. The thermal dependence of temperature derivate of (χT) of GSO1 (red), GSO5 (blue) and GSO9 (green) under (a) ZFCW and (b) FCW protocol with the Curie-Weiss and modified Curie-Weiss fit considering the antisymmetric DM interactions in the insets of (a) and (b) respectively. The exact temperature corresponding to the different transitions have been indicated.

$\chi^{-1} = \frac{T-\theta}{C}$ as shown in the inset of Fig. 6.8(a). Here θ being the Weiss temperature, C is the Curie constant. This analysis yields μ_{eff}= 5.97 μ_B $/f.u.$ and the other parameters are tabulated in Table 6.3. Figure 6.8(b) describes the thermal variation of T_{SR} as it changes from 2.23 K (for GSO1) to 2.46 K (for GSO5). We employed the Dzyaloshinskii–Moriya (DM) interaction in the present case as the contribution of weak FM component along the *z*- crystallographic axis accounting for the DM exchange interaction, the average susceptibility data deviate from the linear behaviour in the vicinity of T_N [265]. Figure 6.8(b) inset shows the inverse susceptibility fitted with the DM modified CW law $\chi^{-1} = \frac{(T-\theta)\,(T-T_N)}{C\,(T-T_0)}$, where T_0 and T_N are the characteristic parameters extracted from the fits. Here we find that the perpendicular contribution is dominant for the average susceptibility $\chi_{Avg} = \frac{\chi_{||} + 2\,\chi_{\perp}}{3}$ for G_xF_z type canted AFM system. The symmetric (J_e) and antisymmetric (D) exchange interactions occupying Cr^{3+} moments can be evaluated using the semi-quantitative analysis reported in previous studies [52,329] and the evaluated parameters are tabulated in Table 6.3.

In the earlier section, we found that along with the dominating canted AFM of Cr^{3+} it has a passive weak FM component (M_{Cr}) inducing an internal field (H_{int}) on the rare earth cations. Hence, the rare earth cationic moments (M_{Sm} and M_{Gd}) start to aligned antiferromagnetically with the decrease in temperature below T_N from paramagnetic alignment. This causes into the negative magnetization of $|M_{Cr}| = |M_{Sm/Gd}|$. The magnitude and the polarity of the induced H_{int} have been obtained by fitting the phenomenological relation given by Cooke [265] under applied field of H_{app} within the range of 40 K to 150 K:

$$M = M_{Cr} + C_{Gd}\frac{(H_{int} + H_{app})}{(T-\theta)} \qquad (10)$$

Table 6.3. The calculated fundamental parameters of magnetization data for $Gd_{1-x}Sm_xCrO_3$ (x = 0.1 (GSO1), 0.5 (GSO5), 0.9 (GSO9)). From Hartree-Fock approximation, effective magnetic moment $\mu_{eff-H.F}$ (μ_B / $f.u.$). CW constant, CW temperature and effective magnetic moment C_{CW}(emu. K/mol. Oe), θ_{CW} (K), μ_{eff-CW} (μ_B /$f.u.$), respectively from CW Law. CW constant, CW temperature, effective magnetic moment, Neel temperature, fitting parameter, symmetric and anti-symmetric exchange constant, C_{DM}(emu. K/mol. Oe), $\theta_{DM}(K)$, $\mu_{eff-DM}(\mu_B/f.u.)$, T_N(K), T_0(K), J_e (K) and D (K), respectively, from DM Modified CW Law. Magnetic contribution from Cr-sublattice, CW temperature, and induced internal magnetic field, M_{Cr-FCC}, (emu/mol), θ_{NM-FCC} (K), and $H_{int-FCC}$ (Oe), respectively obtained from the NM fit Eq. 6.10 under FCC condition. Magnetic contribution from Cr-sublattice, CW temperature, and induced internal magnetic field, M_{Cr-FCW}, (emu/mol), θ_{NM-FCW} (K), and $H_{int-FCW}$ (Oe), respectively obtained from the NM fit Eq. 6.10 under FCW condition. Saturation magnetization, M_S (emu/mole), magneto-crystalline field, H_K (Oe), and magneto-crystalline anisotropy constant, K_1 (J/m^3) obtained from LAS fit.

Parameters	GSO1	GSO5	GSO9
$\mu_{eff-H.F.}$	8.47	6.84	4.68
C_{CW}	6.64	4.46	2.58
θ_{CW}	-19.7	-56.2	-227.5
μ_{eff-CW}	7.29	5.97	4.54
C_{DM}	6.62	4.55	2.68
θ_{DM}	-20.9	-58.2	-234.9
μ_{eff-DM}	7.28	6.03	4.63
T_N	197.4	199.2	201.9
T_0	197.27	199.06	201.25
$J_{e.}$	13.15	13.27	13.42
D	1.10	0.96	2.155
M_{Cr-FCC}	124.45	176.23	71.78
θ_{NM-FCC}	-16.39	-52.89	-237.67
$H_{int-FCC}$	-2123.06	-4245.18	-5320.54
M_{Cr-FCW}	34.01	52.966	-
θ_{NM-FCW}	-25	-52.14	-
$H_{int-FCW}$	-654.46	-1354.86	-
M_S	36852.36	20081.78	3823.27
H_K	1374.55	1247.52	2207.29
K_1	25.33	12.53	4.22

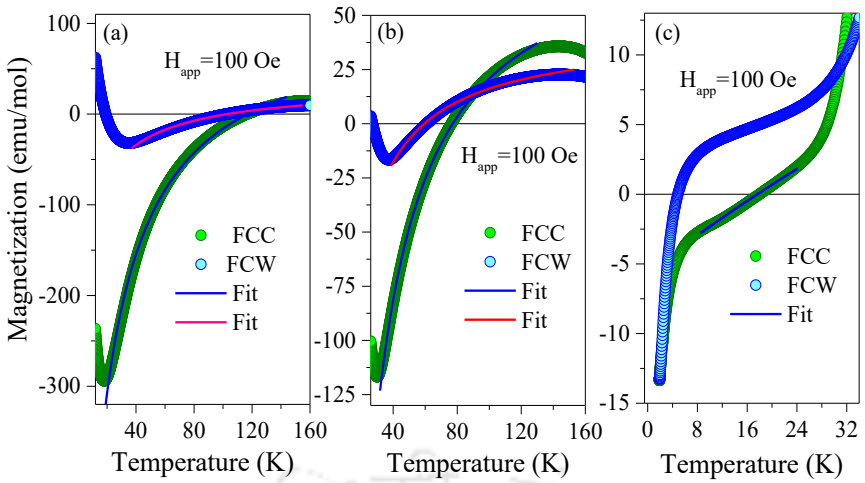

Fig. 6.9. The FCW (blue) and FCC (green) magnetization curves of GSO1, GSO5 and GSO9 respectively from left with the solid lines fitted with $M = M_{Cr,Sm} + C_{Gd}\frac{(H_{int}+H_{app})}{(T-\theta)}$. The H_{int} leads the occurrence of negative magnetization affecting the individual magnetization of rare earth sublattices.

where, C_{Gd} is the Curie Constant of Gd^{3+} ion. The C_{Gd} of ground state is 7.87 emu. K/Oe. mol obtained analytically [67], has been kept fixed during the fitting process. The fitted data is displayed in Fig. 6.9 with H_{app} of 100 Oe for both FCC and FCW curves and the obtained parameters are listed in Table 6.3. The fitting is done only for FCC case for GSO9 as the magnetization doesn't reach negative value for FCW. For The negative magnetization persists only for the H_{app} till 400 Oe for GSO1 and GSO5 (data not shown) and afterwards the field becomes strong enough to overcome the induced H_{int} of Cr^{3+} working together to increase the resultant M increases positively. The negative value of H_{int} indicates the antialignment of Cr spins with respect to the H_{app}. The magnetic moment M_{Cr} is found to increase rapidly both in FCC and FCW cases upon increasing the Sm content from GSO1 to GSO9, indicating dominant contribution of FM component of Cr^{3+} which align towards the rare earth cations. The value of H_{int} increases from -2123 Oe (GSO1) to -5321 Oe (GSO9) for FCC protocol indicating the requirement of higher field to polarize the rare earth moments by the H_{int} [345].

6.3.4.2 Disordered magnetic phases: Magnetic glasslike arrest of kinetics:

In general, the magnetic glasslike state appears in the presence of an external magnetic field, which is markedly different from the more well-known metastable state such as the spin-glass state. Usually, the glassy signature is profound in crystalline solids with non-equilibrium cluster of frozen ferromagnetic and antiferromagnetic spin structures driven by the thermomagnetic history [318]. The slowed down relaxation of the magnetic phase transition is the result of the retardation in the nucleation and growth of the super-cooled AFM phase. The huge divergence between the FCC and FCW magnetization curves of GSO9 indicates the thermomagnetic irreversibility which has a significant role in phase coexistence [318]. For FCC, the T_{SR} is assigned to Γ_4 to Γ_2 first order-phase transition based on the result reported by T. Sau *et al.* [316] and our magnetic measurements. But for the proper confirmation, neutron diffraction study is required where the

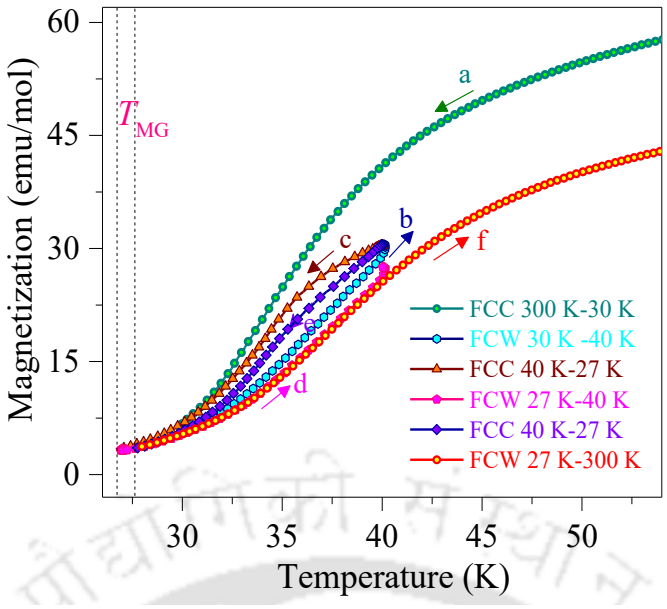

Fig. 6.10. The cycling loops within the magnetic glass like transition temperature where the sample is taken to room temperature with the presence of 100 Oe external field (FCW), then cooled to 30K (FCC), further warmed till 40 K(FCW), cooled to 27 K (FCC), warmed to 40 K (FCW), again cooled to 27 K (FCC) and finally warmed till room temperature (FCW). The very existence of the frozen magnetic glass like characteristics have been confirmed.

reverse (Γ_2 to Γ_4) occurs during g the FCW protocol as a result of the Sm^{3+}-Cr^{3+} exchange interaction as precluded in the previous section. The thermomagnetic irreversibility assists the higher volume fraction of the FM phase obtained in the FCC than that of the FCW in the range of 180 K to 30 K relates the higher magnetic moment of FCC than FCW. In other words, gradual thermal hysteresis within the range of 190 K to 25 K and multiple crossovers between the FCC and FCW occurs due to the kinetic arrest of the FM to AFM transition signifying magnetic glass behaviour. The scattered islands of the FM matrix in the AFM background (FCW) and vice versa under FCC in the vicinity of the T_{SR} hinders the phase transition leading to the non-equilibrium magnetic glass state [346]. In the vicinity of the spin reorientation transition, the induced field due to the anisotropic exchange interaction between Sm^{3+}-Cr^{3+} provides separately polarised positive and negative fields on up and down spins of Cr^{3+} which becomes stronger with reduction in the temperature as the rare earth Sm^{3+} moments (and Gd^{3+} at much lower temperatures) get activated [324]. On overcoming the crystalline barrier anisotropy, the effective field rotates the spins along the crystallographic axis *x* to parallel to *y* direction leading the spin reorientation [347]. Characteristic magnetic glass behaviour is thus investigated with the temperature sweeps under different cooling and warming protocols in the phase transition regime as shown in the Fig. 6.10. The limitation of cooling temperature is kept here with the applied field ~ 100 Oe. The investigated sample is cooled from room temperature 300 K to 30 K under the field bias of H_{DC} = 100 Oe followed by a hold time of 100 secs. Subsequently sample has been warmed till 40 K with the slow sweep rate and again cooled till 27 K followed by warming up to 40 K. Finally, cooled again till 27 K with the same sweep rate followed by gradual warming till 300 K. The FCC magnetization appears at higher in magnitude than that of the FCW. During the cooling protocol, the large anisotropy of the Cr^{3+} holds some of the FM

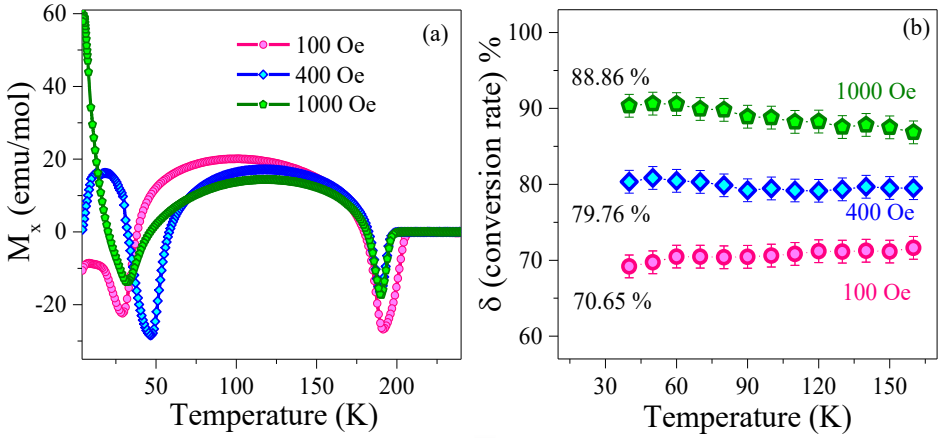

Fig. 6.11. (a) The transformation of M_X (= M_{FCC} - M_{FCW}) with respect to temperature of GSO9 under specified H_{DC} = 100 Oe (pink), 400 Oe (blue) and 1000 Oe (green). (b) The temperature dependence of conversion factor δ (δ = M_{FCW}/M_{FCC}) for the respective fields (100 Or, 400 Oe and 1000 Oe) within the temperature range of 40 K – 160 K. The frozen state can be realized with the help of phase fraction of FM clusters over AFM spins.

clusters contributing to the AFM dominant Γ_4 phase in the super-cooled condition in the vicinity of the T_{SR}. This mixed phase of both Γ_4 and Γ_2 is metastable and gives rise to the frozen glassy nature (T_{MG}). With further reduction in temperature below T_{MG} the energy involved with the Sm^{3+}-Cr^{3+} exchange interaction overcomes the anisotropy energy and the majority of the spins inherit Γ_2 configuration with higher energy values by slowly rotating throughout all the infinitesimal angles [347]. For the FCW protocol, during the transforming process a little number of spins with Γ_2 configuration stays like islands in the majority Γ_4 phase due to the relatively smaller Sm^{3+} / Gd^{3+} anisotropy. Hence, the system seeking equilibrium try to maintain the lower energy AFM phase lowering the magnetization in the warming protocol [346]. The magnetization difference between the FCW and FCC protocol i.e., M_{FCC}-M_{FCW}, defined as M_X is shown in Fig. 6.11(a) to understand the phase fraction of FM/AFM components. The increment of field from 100 Oe to 1000 Oe diminishes the divergence of the magnetization difference within the range of 60 K - 185 K. The maximum of the $M_X(T)$ can be observed at ~ 105 K for H_{DC} = 100 Oe and increases to 113 K for higher fields of 400 Oe and 1000 Oe. It is interesting to note that the glassy nature exists at 1000 Oe and it can be predictable that the higher field H_{DC} > 1000 Oe can slowly demolish the frozen state as the greater number of FM spins will be aligned in the FCW mode. Hence the difference between the heating and cooling curve get diminished [346]. It is previously reported that the thermomagnetic irreversibility depends strongly on the phase fraction, δ defined as the ratio of the AFM/FM phase in the FCW protocol and vice versa in the FCC magnetization is calculated by the fraction of M_{FCW} to M_{FCC}. Figure 6.11(b) shows the invariant nature of δ over the broad temperature region of 40 K to 160 K. The mean values of the phase fraction calculated is approximately 70.65%, 79.76% and 88.86% for H_{DC} = 100 Oe (pink), 400 Oe (blue) and 1000 Oe (green) respectively. Evidently, the above-mentioned values signify the comparative number of spins aligned to AFM phase during FCW protocol where some of the AFM phase restricts themselves while cooling under the same field and remaining fraction (1- δ) represents the FM clusters to the frozen AFM phase (by value 29.35 %, 20.24 % and 11.14 % respectively for 100 Oe, 400 Oe and 1000 Oe).

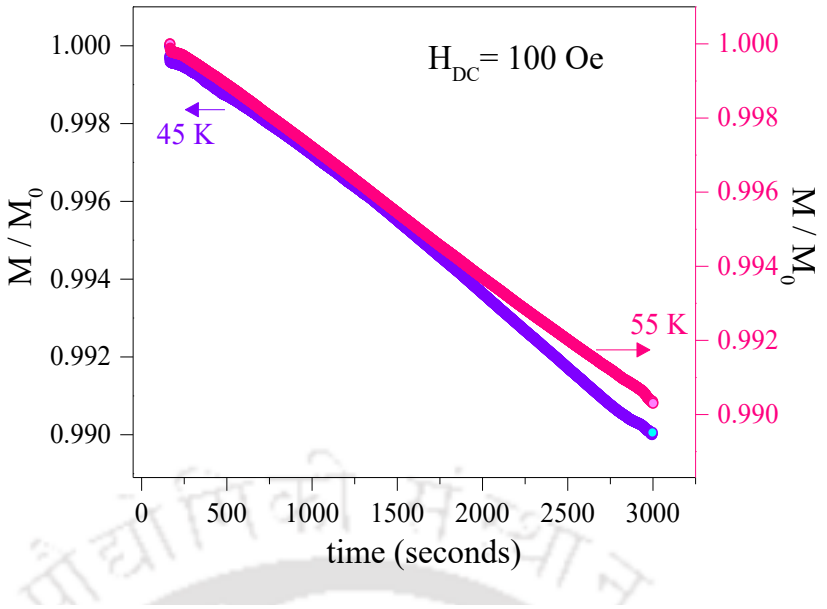

Fig. 6.12. The time dependence of normalized magnetization at chosen temperatures 45 K (left hand side) and 55 K (right hand side) of GSO9 under the FC condition with H_{DC} = 100 Oe. The relaxation behaviour of the GSO9 sample over time holds for both the temperature.

To further study the metastable glassy behaviour associated with GSO9, the time dependent magnetization is measured at 45 K and 55 K (shown in Fig. 6.12) and 6 K (not shown in figure). For each measurement, the investigated system is cooled from room temperature (300 K) to 6 K under the H_{DC} = 100 Oe; and kept for 10 minutes for homogenous spread of the temperature throughout the domains inside after which the field was reduced to zero and the system was warmed to the measured temperatures (i.e. to 45 K and 55 K) and the magnetization was recorded as a function of time for 60 minutes. The magnetization curve plotted in Fig. 6.12 is normalized with respect to the primary magnetization at t = 0. The strong relaxation in the magnetization behaviour can be observed in both the temperatures. The phase fraction AFM/FM clusters starts to get arrested on cooling from 300 K in the presence of field and stay intact with the removal of field. The normalized magnetization starts to decrease with time because, the local free energy of the remaining phase fraction gets utilized to convert the system to sustainable AFM phase. With the increase of temperature, the local free energy barrier increases sharply as the phase fraction is more at higher temperature, so the phase transition rate slows down a bit at higher temperatures [318].

6.3.4.3 Time dependence of magnetization:

With the aim of establishing the polarity change of the magnetization, the magnetic switching experiments are executed at appropriate temperatures under both FCC (70 K) and ZFCW (180 K) protocols for GSO5 as shown in Fig. 6.13. To understand the magnetization switching, the sample was cooled from paramagnetic temperature (T > T_N) to 180 K (near to T_N) and an external field (H_{DC}) of 100 Oe was applied and kept constant for 5 minutes. After this the field has been increased to 600 Oe which was fixed for 5 minutes. This cycle is repeated for a number of times in order to verify the reproducibility of the switching behaviour. Such identical reversible bipolar switching of magnetization was performed for FCC protocol as well at a

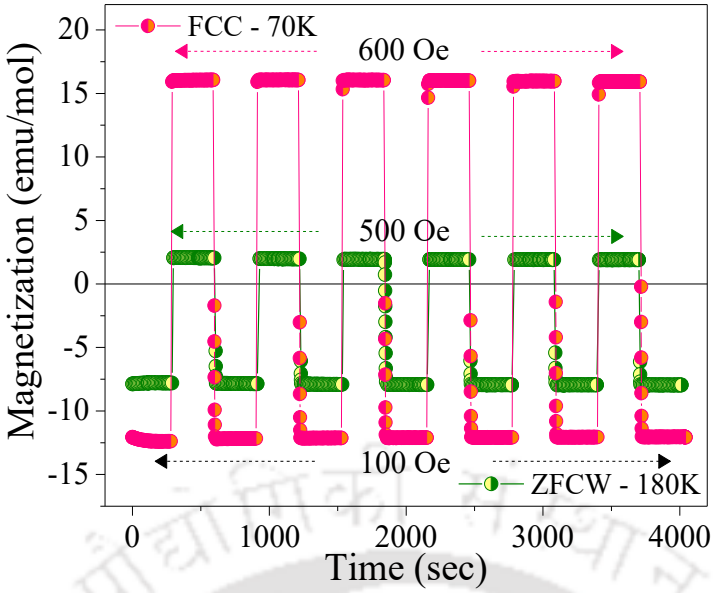

Fig. 6.13. The time dependence of magnetization at 180 K (ZFCW-green) and 70 K (FCC-pink) at fields varying between 100 Oe and 500 Oe and 100 Oe and 600 Oe respectively for GSO5. The switching of the polarity of magnetization with respect to field as a parameter stabilizes at each state for a time period of 5 minutes.

temperature (70 K) below T_{Comp1}. Here, the sample was cooled till 70 K from room temperature under H_{DC} = 100 Oe and the sequence was repeated several times (100 Oe→600 Oe→100 Oe) with a stability time of 5 minutes' duration between each field change. The stability after the removal of the external field corresponding to each state has been detected without any significant decay of magnetization. For 100 Oe field combined magnetization remains in the negative state with spins aligning antiferromagnetically to each other when the higher field (500 Oe and 600 Oe) flips the spins in the opposite direction causing the net magnetization to be positive. It is interesting to note that the magnetization can be switched from positive to negative by changing the H_{DC} to particular values in the same direction instead of switching the field direction as those in FM systems. The very existence of these two different polarity magnetization states varying with external actuator like magnetic field approves the application of this material in volatile magnetic memories including in magnetic switches and magnetic data storage devices [348].

The stability of the negative magnetization has been ascertained for the same sample by time dependent magnetization behaviour for both ZFCW and FCC cases keeping field and temperature as variable parameters as shown in Fig. 6.14(a) and 6.14(b). Here, the sample was cooled from 300 K to 150 K (50 K) under H_{DC} = 0 Oe (H_{DC} = 100 Oe) and was kept for a short duration of 2 minutes for homogeneity of the thermal alignment of the spins followed by the field variation of 50 Oe, 100 Oe, 500 Oe, 800 Oe, 1000 Oe (1100 Oe) and 2000 Oe (1500 Oe) with 5 minutes of hold time at each field for data recording with respect to time and plotted in Fig. 6.14(a). For Fig. 6.14(b) the sample was cooled from paramagnetic temperature region to 80 K with no external field applied and data was recorded for 5 minutes of duration before the temperature was changed to 90 K and further repetition of measurement to different temperatures (100 K,

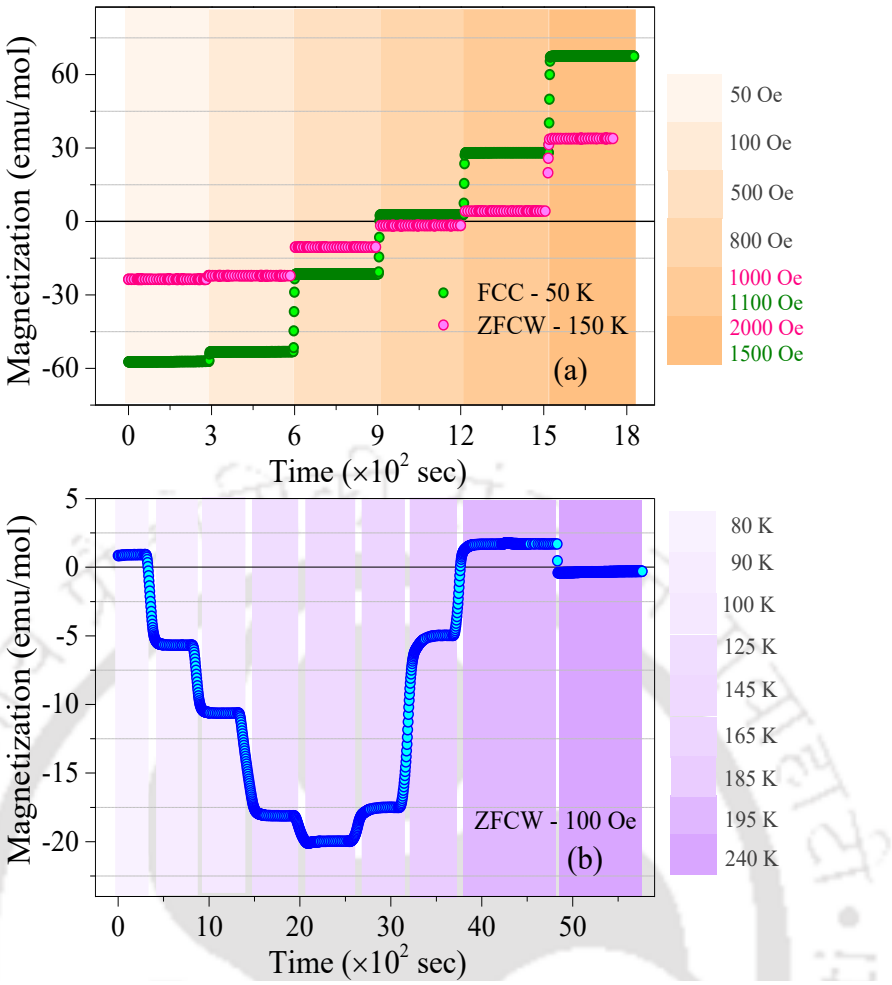

Fig. 6.14. (a) The magnetization variation at different fields at constant temperatures of 50 K (FCC-*orange*) and 150 K (ZFCW-*blue*) with respect to time. (b) The magnetization variation with respect to time at different temperatures under ZFCW protocol (at 100 Oe field). For data recording at each stable condition, 5 minutes of holding time is maintained. The tuning of different stable states in both positive and negative magnetization with respect to field and temperature is quite feasible for GSO5.

125K, 145 K, 165 K, 185 K, 195K and 240 K) for H_{DC} = 100 Oe. The accurate and stable negative magnitudes of magnetization can be noted for lower fields (~50 Oe) and spontaneous polarity switching for higher field (1000 Oe). The change in the magnetic field and temperature has been shown by the different shade of colour. The negative amplitudes for fixed field magnetization between the T_{Comp1} and T_N with maximum negative moment of ~ -19 emu/mol follows the MT data in which the negative moment of ~ -17 emu/mol (see Fig. 6.7). The time dependent magnetization data concludes the constancy of the polarity switching at different temperatures and fields making the investigated system applicable for switching devices in large scale for its multiple switching applications [313].

6.3.4.4 Field dependence of magnetization:

Figure 6.15 depicts the hysteresis loops of GSO1, GSO5 and GSO9 recorded within the field range of ± 90 kOe at 1.9 K under standard ZFC mode. The inset shows enlarged view of the respective plots at lower fields (± 60 kOe) showing the finite coercivity and remanance. As predicted, the magnetization value drops to

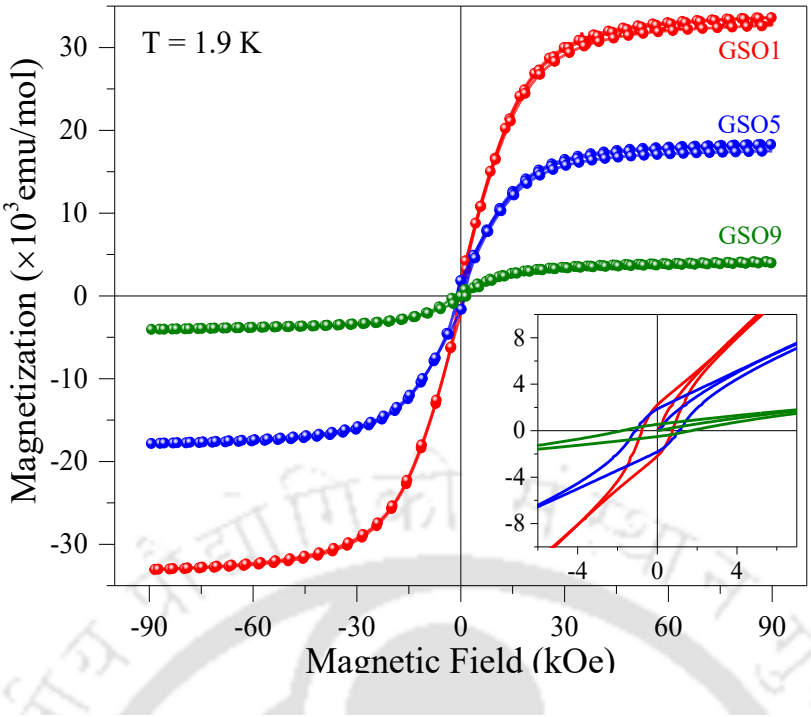

Fig. 6.15. The field dependence of magnetization (M-H) of 5 cycles hysteresis loops at 1.9 K within ± 90 kOe for GSO1 (red), GSO5 (blue) and GSO9 (green) under ZFCW protocol. The inset shows the enlarged view of the loops at the low magnetic field (± 60 kOe). The relative difference among the three compositions and saturation magnetization, coercivity and exchange bias prominently noticed.

~87.7% (at + 90 kOe) with increasing substitution of Sm (90%) at Gd side. The insertion of Sm^{3+} at A-site cationic position increases the AFM interaction and weakens the FM character in the system attained from Gd^{3+} as evident from the decreasing moment and coercivity with increasing Sm substitution (as shown in the inset of Fig. 6.15). The hysteresis has been scarcely observed for GSO9 so the negligible amount of the remanance field indicates the prevalence of the weak FM Γ_4 phase at the low temperature region. The remanance decreases to 548 emu/mol from 2194 emu/mol with the reduction of Sm substitution to 90% from 10% where the coercivity increases from 14 kOe (GSO1) 15.5 kOe (GSO9). The overall decrease of the magnetization is due to the lower moment of the Sm^{3+} (~0.84 μ_B) as compared to the Gd^{3+} (~7.94 μ_B). In order to explore the influence of different cations on magnetic anisotropy, the amplitudes of anisotropy constant (K_1), anisotropy field (H_K) and saturation magnetization (M_S) are calculated using the Law of approach to saturation, LAS [52]. The experimentally obtained 1st quadrant M-H virgin curves are fitted with the LAS expression and extracted the parameters given above which are listed in Table 6.3 for all the three compositions. From this analysis it is very clear that K_1 falls rapidly to 1/6th of the value of GSO1 to GSO9 due to the lower magneto-crystalline anisotropy and flexibility of rotation of the spins from easy axis. However, the magnitude of anisotropy does not show any systematic variation except it reaches to 2207.3 kOe (GSO9) from 1374.6 kOe (GSO1).

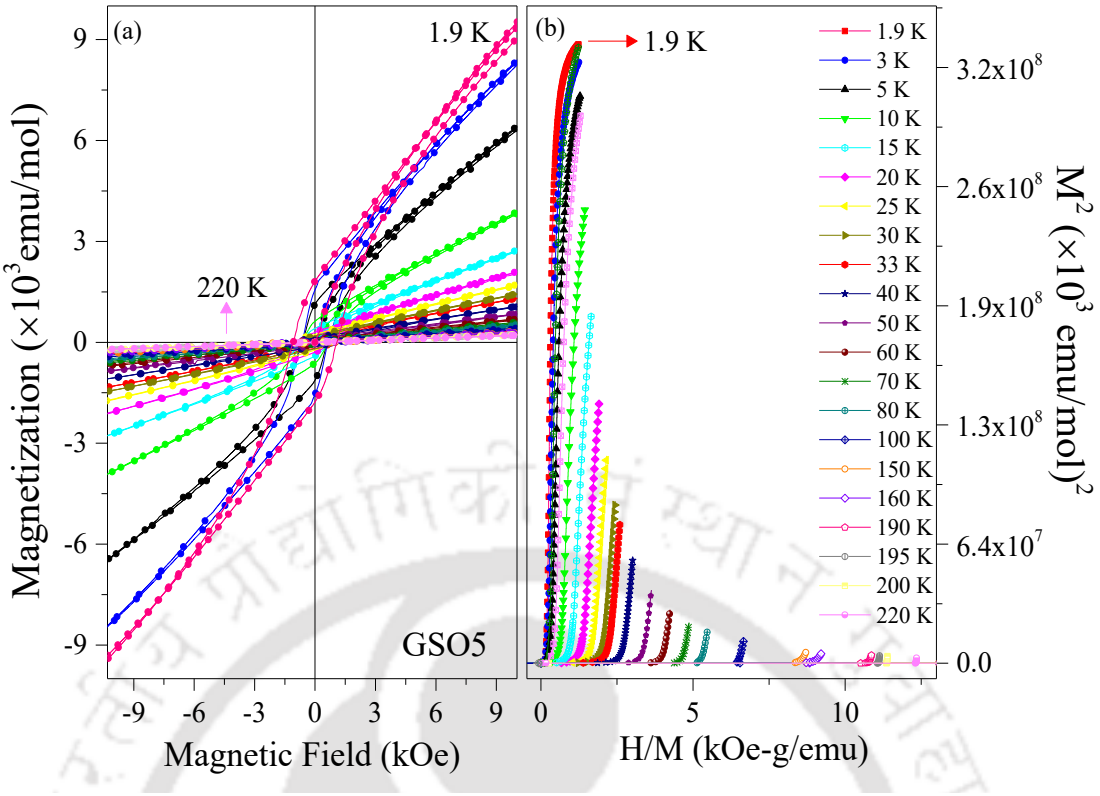

Fig. 6.16. (a) The field dependence of magnetization (M-H hysteresis loops) at different temperatures ranging from 1.9 K to 220 K GSO5 under ZFCW protocol for GSO5. (b) The Arrot plots (H/M vs. M^2) of the first quadrant isothermal magnetization of GSO5 within the temperature range 1.9 K to 220 K. The gradual dominance of AFM character of the sample while moving towards T_N and the confirmation of second order phase transition in GSO5 has been observed.

For a better understanding of the domain dynamics of GSO5, the detailed field dependent study at different temperatures has been performed. As described above typical five-cycle M-H loops (±90 kOe) were measured under ZFC mode at various temperatures between 1.9 K and 220 K (above T_N). Here the M-H data has been collected with a field sweep of 200 Oe/minute and before the commencement of each measurement the sample temperature has been upraised above T_N in order to attain a perfect randomization of the spin to bring virgin state. In Fig. 6.16(a) the recorded data at certain temperatures are plotted to depict that the moments of the constituent elements which are not able to attain saturation even up to 90 kOe external field. For T>160 K, the curves became almost straight-line signifying the strong AFM component dominated over FM component. On the other hand, Fig. 6.16(b) shows the Arrot plots (M^2 versus H/M) made from the M-H isotherms recorded at different temperatures which shows positive slopes near T_N signifying the second order phase transition from the disordered paramagnetic state to AFM phase in GSO5 which is in-line with the previous discussions. Nevertheless, all the M-H loops exhibit asymmetry in their position (H_{C1} and H_{C2}) on either side of the loop causing finite exchange bias field ($H_{EB} = (H_{C1}+H_{C2})/2$) even under ZFC condition. The temperature dependence of both H_{EB} and H_C ($=(H_{C1}-H_{C2})/2$) are shown in Fig. 6.17(a) and 6.17(b). The weak FM character induced by the anisotropic DM interaction in this AFM perovskite systems is the main origin of the loop asymmetry in which the equivalent AFM and FM components play a significant role in deciding the magnitude of the H_{EB}. Clear anomalies were visible in the plots of $H_{EB}(T)$ and H_C (T) at the characteristic

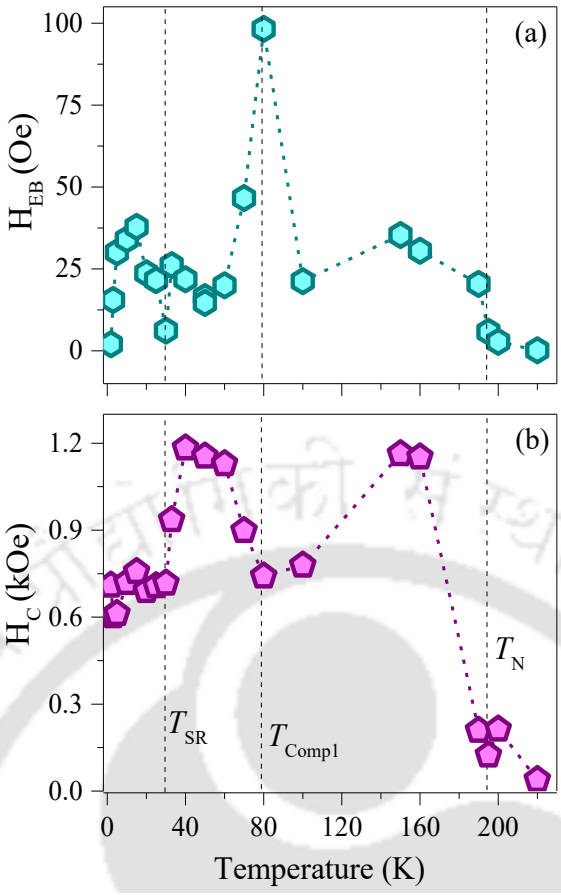

Fig. 6.17. The thermal variation of exchange bias (H_{EB}) coercive field (H_C) of GSO5 under ZFCW protocol in the temperature range of 1.9 K- 220 K. Presence of anomalies in H_{EB} and H_C corresponding to transition temperatures for GSO5 indicate the appearance of different magnetic spin structure.

temperatures T_{SR}, T_{Comp1} and T_N. Both these quantities increase slowly below T_N and show a divergence at T_{Comp1} with a sudden fall to 6.2 kOe and 717 kOe, respectively near T_{SR}. A prominent change in the slope of H_{EB}(T) and H_C (T) across 195 K indicates the onset of the spin alignment in the AFM, $\Gamma_4\,(G_x, A_y, F_z)$ phase. Moreover, a gradual increment in both H_{EB}(T) and H_C (T) was evident below T_N due to strong anisotropy of trivalent Cr ions which holds the spins along the easy axis direction of G-type AFM component usually orders along *x*-direction. These spins start rotating around *z*-axis and thus influences FM component which moves away from easy axis as T approaches T_{Comp1} (here ~ 80K) down to T_{SR} (here ~ 30 K) where the complete rotation is executed as precluded in the previous section.

6.3.4.5 Magnetic phase-diagram:

After gathering the important results obtained above pertaining to both magnetic and structural along with spectroscopic data of different compositions of the GSO systems now we are in a position to shed light on the global magnetic phase diagram of this interesting perovskite system. Figures 6.18 and 6.19 represents the variation of magnetic ordering temperatures plotted as a function of field (T-H) obtained from the time and field dependent magnetization data recorded under both ZFCW and FCC conditions, respectively for all the three investigated systems GSO1, GSO5 and GSO9. The solid orange spheres represent the magnitude of T_N while the striped region shown below designated as $\Gamma_4\,(G_x, A_y, F_z)$ AMM phase. On the other hand, the data

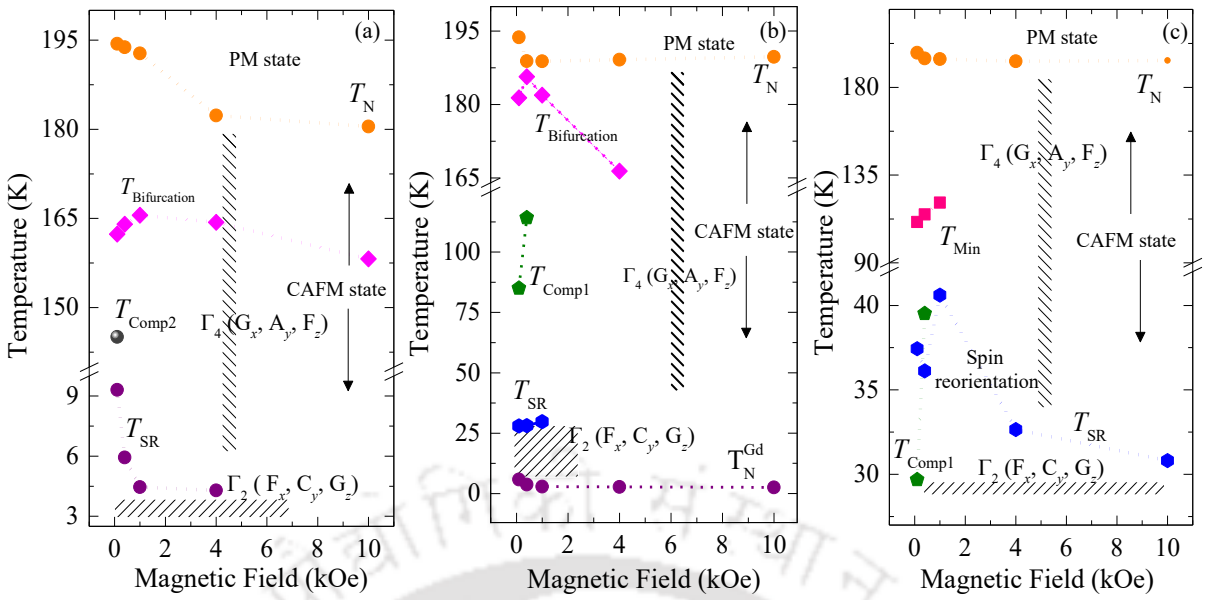

Fig. 6.18. Magnetically rich H-T phase diagrams of (a) $Gd_{0.9}Sm_{0.1}CrO_3$, (b) $Gd_{0.5}Sm_{0.5}CrO_3$, and (c) $Gd_{0.1}Sm_{0.9}CrO_3$ under the ZFC protocols. The solid symbols are the data points and the lines connecting them are the guide to the eyes. The shaded regions symbolize the particular magnetic phase of Γ_4, Γ_2 where the compensation temperatures (T_{Comp1}, T_{Comp2}), bifurcation temperature ($T_{Bifurcation}$), Maximum negative magnetization (T_{Min}) spin flip temperature (T_{SF}), spin reorientation temperature (T_{SR}), ordering temperature of Gd and Sm (T_N^{Gd}, T_N^{Sm} are denoted with the respective symbols. All the data points are taken under ZFCW protocol.

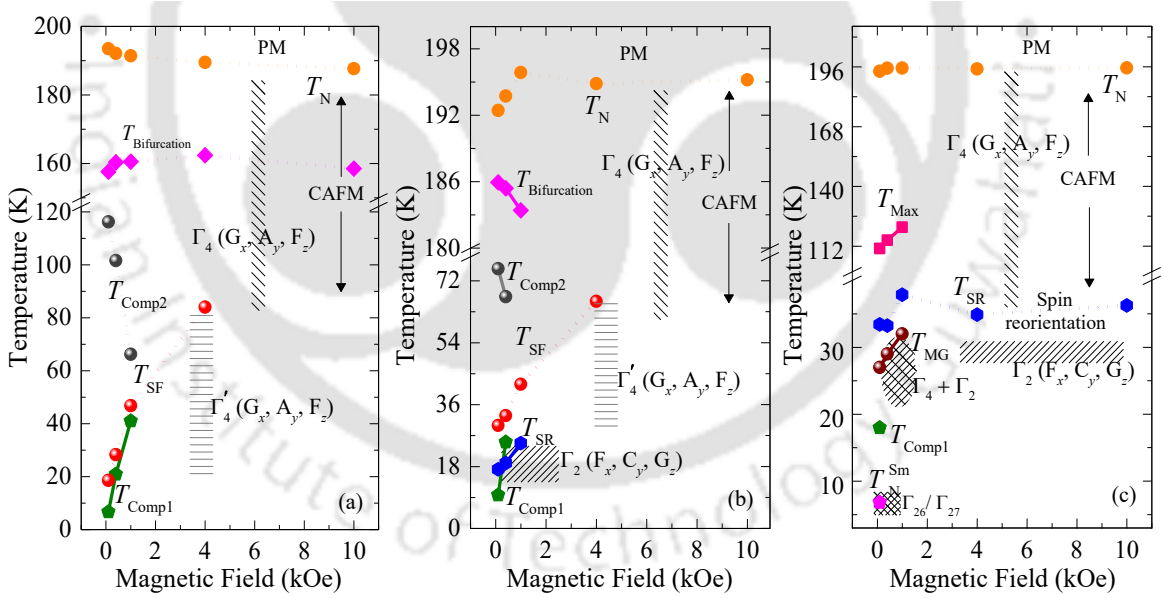

Fig. 6.19. Magnetically rich H-T phase diagrams of (a) $Gd_{0.9}Sm_{0.1}CrO_3$, (b) $Gd_{0.5}Sm_{0.5}CrO_3$, and (c) $Gd_{0.1}Sm_{0.9}CrO_3$ under FCC protocol. The solid symbols are the data points and the lines connecting them are the guide to the eyes. The shaded regions symbolize the particular magnetic phase of Γ_4, Γ_2, Γ_4', Γ_{26}/Γ_{27} where the compensation temperatures (T_{Comp1}, T_{Comp2}), bifurcation temperature ($T_{Bifurcation}$), Maximum positive magnetization (T_{Max}), Maximum negative magnetization (T_{Min}) spin flip temperature (T_{SF}), Magnetic glass temperature (T_{MG}) spin reorientation temperature (T_{SR}), ordering temperature of Gd and Sm (T_N^{Gd}, T_N^{Sm} are denoted with the respective symbols. The Γ_4' is the change in the spin directions keeping the magnetic phase intact. All the data points are taken under FCC protocol.

points represented by solid squares in magenta refers the $T_{Bifurcation}$ which diminishes at higher field (4000 Oe-ZFCW case) for the samples GSO5, however this variation completely vanishes for the composition GSO9. The phase remains as canted AFM Γ_4 as there is no change in the magnetic ordering was noticed. The crossing of zero net magnetization across T_{Comp2} shown in dark grey spheres (prominently noticed in FCC protocol) for 10% and 50 % Sm substituted systems for a certain magnetic field upon decreasing the temperature is very prominent in the phase diagram as the temperature is decreased with the rate 43% and 10.77%, respectively. While for the ZFCW case, the magnetic compensation not able to takes place except for GSO1 system at 100 Oe as the combined induced field including the magneto-crystalline anisotropy field of Cr^3 and rare earth cations are weaker than the applied external field. Another compensation, T_{Comp1} arises at lower temperature for all the samples (FCC) for a very specific span of temperature 7K-40 K due to the activity of the rare earth cations at lower temperature keeping the Γ_4 (G_x, A_y, F_z) magnetic structure intact (shown in green pentagon symbols of Fig 19(c)). Here the T_{SF} has been shown with red spheres below which the Γ_4' state is designated as horizontal lines. Upon lowering the temperature to 37 K (for GSO9) in ZFCW condition, the dominating AFM component orient along crystallographic z-axis making the anisotropy energy low enough to allow the spins to make a transition to different magnetic phase Γ_2 with dominant FM component towards easy axis. Such reorientation T_{SR} is recognizable in all the three compositions are shown by the blue colour hexagon and the slanted lines represents the associated Γ_2 phase. As it is very clear from this study that the contribution of Gd and Sm spins are very prominent at low-temperatures and we present their ordering temperatures T_N^{Gd} and T_N^{Sm} with purple and magenta symbols, respectively (Fig. 18 and Fig. 19). The spin reorientation temperature overlaps with the T_N^{Gd} for GSO1 making the phase transition below 9.3 K for ZFCW protocol and gradually decay to 4.3 K with the increasing field value of 4000 Oe. For GSO9, the Sm ordering induces the change in magnetic phase to either of Γ_{26} $(C_x, G_y, C_x; C_x^R, A_y^R, F_z^R)$ or Γ_{27} $(F_x, C_y, G_z; F_x^R, C_y^R, G_z^R)$ only at low field of 100 Oe under FCC case. The magnetic glass signature with mixed phase of Γ_4 and Γ_2 configuration in the form of frozen FM and AFM clusters in the narrow temperature range of 27 K-32 K are labelled as maroon spheres (Fig. 6.19). The frozen spins refuse to persist after a certain amount of applied field making the metastable phase more sensitive. Overall, we find that the investigation of the spin-dynamics using different external probes make this study more interesting.

6.4 Conclusions:

In summary, a strong correlation has been established between the structural crystallographic and magnetic properties of Sm substituted $GdCrO_3$ perovskite system using a comprehensive study of XRD, Raman and dc-magnetization. In general, the investigated system undergoes a G-type AFM phase transition at T_N = 197 K (GSO1) - 201 K (GSO9) with Cr^{3+} along with Gd^{3+} and Sm^{3+} ions aligned in Γ_4 (G_x, A_y, F_z) configuration. All the three compositions namely GSO1, GSO5 and GSO9 show multiple crossovers or polarity change in magnetization under ZFCW, FCC and (or) FCW protocols. At lower temperature below 40 K, the anisotropic exchange interaction between rare earth and Cr^{3+} rotates the AFM component along *z*-axis from the easy axis and the magnetic phase changes to Γ_2 (F_x, C_y, G_z) configuration. The Sm rich GSO9 shows

the interesting characteristics of magnetic field driven short range metastable frozen state of simultaneous existence of both Γ_2 (F_x, C_y, G_z) and Γ_4 (G_x, A_y, F_z) phases as the FM clusters in the AFM background matrix for FCW case which ceases to exist for higher magnetic field. Clear anomalies are detected in the Raman spectra across the magnetic ordering temperatures specifying the direct spin-phonon coupling present in the system. These studies also reveal gradual hardening of the $A_{1g}(5)$ mode at around 563 cm^{-1} with respect to temperature which assures the Cr^{3+}-Cr^{3+} AFM coupling interaction complemented by exchange-striction effect. The variation of the tilt angles as calculated from refined structural parameters of XRD engages in the quasi-harmonic effect due to Gd^{3+}-Cr^{3+} exchange interaction which soften he $A_{1g}(3)$ mode. Across the different substitution levels, the GSO shows multiple magnetic compensations under the ZFCW, FCC and FCW cases. Overall, the intriguing characteristics explored under the substitution of Sm^{3+} in the $GdCrO_3$ making it a potential candidate for the applications in the field of tunable thermo-magnetic switching devices, magnetic sensors and non-volatile magnetic memory storage devices.

Chapter 7
Conclusions and future work

This chapter summarize the important experimental results obtained in this work and describes an outlook for the possibility of future research work. In the thesis work we established a systematic study of epitaxial strain on the electronic and magnetic structure of thin-film superlattices and bulk grain sized perovskite oxides. Below we provide chapter wise key findings of all the important results presented in the previous chapters and wrap-up this section by discussing the possible future research work and outlook of novel perovskite family of compounds with main focus on their potential applications in spintronic devices.

7.1 Conclusions:

As we demonstrated in Chapter 3 the role of epitaxial strain on the atomically flat interfaces of LSMO/LCO bilayers becomes quite important entity for the spintronic devices, in what follows we illustrate the key results pertaining to the electronic and magnetic structure. Firstly, we observed that the bilayer sequence LCO (15 nm)/LSMO (5 nm) (BL2) exhibits large magneto-crystalline anisotropy ($K_u \approx 4.7 \times 10^4$ erg/cc) and weak anti-FM coupling across the interface of the two FM constituents. Secondly, the partial compensation of the magnetic moment within a specific temperature window ($\Delta T = 184 - 82$ K) reveals the dominant AFM coupling at low-temperatures. However, for T ≤ 82 K, the FM superexchange interaction between the trivalent Co high-spin and low-spin states governs the overall magnetic ordering in BL2. The magneto dynamic features probed by the frequency dependent FMR on this system yield the gyromagnetic ratio ($\gamma/2\pi \sim 29.22$ GHz/T), demagnetization fields ($4\pi M_{eff} \sim 3770$ Oe), and effective damping constant ($\alpha_{eff} \sim 0.0143$) for the BL2 configuration. Moreover, the strength of the nearest-neighbour exchange interaction J_{eff} in the BL2 configuration exhibits linear falloff with the increasing LCO layer thickness ($2 \text{ nm} \leq t_{LCO} \leq 18$ nm). This scenario is also consistent with the variation of the effective number of spins available per unit volume [$10 \text{ cm}^{-3} \leq N_V (\times 10^{22}) \leq 2 \text{ cm}^{-3}$] with increasing t_{LCO}. As t_{LCO} approaches negligibly small values (< 2 nm), the magnitude of J_{eff}/k_B reaches its maximum ~ 5.47 K (for LCO) and 21.93 K (for LSMO), which is in good agreement with $J_{eff}/k_B \sim 5 \pm 2$ K (20 ± 2 K) for highly epitaxial LCO (LSMO) single layers. These results demonstrate that the layer sequence control of magnetic coupling across the interfaces opens a constructive approach for exploring the novel electronic devices.

In Chapter 4 we examined the texture/orientation dependent growth characteristics along with the other physical properties including the electronic structure, magnetic and magneto-transport, and vibrational excitations in atomically flat interfaces of $[La_{0.7}Sr_{0.3}MnO_3/LaNiO_3]_{10}$ superlattices coherently grown on (001/011/111)-$SrTiO_3$ substrates by the PLD technique. Initial studies pertaining to the X-ray reflectometry confirms the periodic superlattice stacks from the Kiessig interference fringes and well-defined even interfaces between the nickelate and manganite layers. A complex local atomic environment across the interfaces was noticed, yet trivalent La, divalent Sr, and mixed valent $Ni^{2+/3+}$ and $Mn^{3+/4+}$ electronic states

prevail at the core level with enhanced relative intensity ratio of the Mn ions in the superlattices grown on (111) oriented $SrTiO_3$ substrates as compared to those grown on (001) and (011) oriented $SrTiO_3$. Our results on the temperature dependence of electrical resistivity $\rho(T)$ reveals the prevalence of 3D variable range hopping [$\rho(T) = \rho_0 \exp(T_0/T)^{1/4}$] mechanism of electronic transport with large magnitude of hopping energies (≥ 40 meV) for the SL-111 system. This SLs exhibits high energy gap between the localized states owing to the presence of inherent disorderness across the interfaces which contains the polar layers. Moreover, all SL systems exhibit reduced ferromagnetic ordering temperatures ($67 \leq T_C \leq 110$ K) with a low-temperature anomaly ($11.4 \leq T^* \leq 22$ K) and a substantial enhancement in the effective exchange interaction ($J_{eff} \sim 3.52$ meV) having altered ground state-spin configuration $S \sim 1/2$ different from S=3/2 of $La_{0.75}Sr_{0.25}MnO_3$. Nevertheless, the SL-011 system exhibits large anisotropy field $H_K \sim 18$ kOe and cubic anisotropy constant $K_1 \sim 9.3 \times 10^3$ J/m^3 in comparison to the other two orientations. Finally, the Raman spectroscopy results demonstrate the appearance of second order two-phonon interaction driven by the local polaronic distortion that causes a significant change in the vibrational excitations of the investigated system. Here most of the Raman modes follow the substrate-induced, highly oriented epitaxial growth pattern except for two modes ν_4 (326 cm^{-1}) and ν_8 (728 cm^{-1}), which slightly differ in the case of SL-111 superlattices.

Next, we extended our study to analyse the role of Ce substitution on the crystal structure, temperature and field dependence of magnetic characteristics and phonon instabilities of $DyCrO_3$ polycrystalline compounds in chapter 5. All the investigated compounds exhibit distorted orthorhombic crystal structure with a distortion factor of $d_{Oct}/d_{Cell} \sim 6 \times 10^{-3}$/3.5 ppm (for $x \sim 0.2$) for *Pbnm* space group that follows Vegard's law. The bonds between apical oxygen atoms (O_{A1}) and Cr atoms stand more rigidly in comparison with the basal oxygen atoms (O_{B1}/O_{B2}) resulting the octahedral distortion and thereby causing the changes in phonon modes. The CrO_6 octahedral tilt angle θ rotates with respect to the Miller pseudocubic axis [101] which varies from 10.36° ($x = 0.1$) to 12.25° ($x = 0.5$) and significantly influences the $A_g(5)$ phonon stability by 3% for a change in A-site mean radius from 1.095 Å to 1.141 Å for $x = 0.1$ and 0.5, respectively. From the magnetization measurements we find that these series of compositions exhibit canted antiferromagnetic (AFM) ordering with Néel temperature, T_{N_1} that increases from 151.8 K ($x = 0.1$) to 162 K ($x = 0.5$) which also manifests as a significant reduction in the magneto-crystalline anisotropy ($H_K \sim 2.58$ kOe → 2.07 kOe, $K_1 \sim 36.47$ J m^{-3} → 18.97 J m^{-3}) while maintaining the stable $\Gamma_4(G_x, A_y, F_z)$ AFM configuration. Both Dzyaloshinskii–Moriya interaction method and modified Curie–Weiss law are employed to analyse the inverse paramagnetic susceptibility, χ^{-1} ($T > T_{N_1}$). Further, we have evaluated the symmetric (J_S) and antisymmetric exchange (D_{AS}) constants, which show progressively increasing trend (J_S → 10.08 K to 11.18 K and D_{AS} → 1.24 K to 1.73 K) with the incorporation of Ce inside the perovskite lattice. Furthermore, the role of Ce substitution on the low-temperature spin reorientation transition ($T_{SR} \sim 3.5$ K → 16.8 K pertaining to the Γ_{25} phase configuration) and emergence of Γ_2 ($F_x, C_y, G_z; F_x^R, C_y^R$) weak-FM phase between 31 K and 45.5 K have been demonstrated in consonance with the phonon spectra.

Next, we have presented an extensive analysis of the effect of Sm substitution in the Gd site of the rare-earth perovskite $GdCrO_3$ on its structural, electronic, and magnetic structure. We have considered the three substituted configurations namely 10%, 50%, and 90% of Sm on the Gd site of $GdCrO_3$ which have been termed as GSO1, GSO5, and GSO9 respectively. Using different state-of-the-art tools and techniques, like, XRD, Raman and dc-magnetization, we have established a strong correlation between the structural crystallographic and magnetic properties of Sm substituted $GdCrO_3$ perovskite system. Using the room temperature Raman spectroscopy, we have obtained the presence of Sm induced structural distortion in the investigated compounds which becomes more prominent with the high concentration of the substitution. Further, we found that the system undergoes a G-type AFM phase transition across T_N = 197 K (GSO1) - 201 K (GSO9) with Cr^{3+} along with Gd^{3+} and Sm^{3+} ions aligned in $\Gamma_4\,(G_x, A_y, F_z)$ configuration. Under the ZFCW, FCC and FCW protocols all the three compositions GSO1, GSO5 and GSO9 display presence of multiple crossovers or polarity change in the magnetization. At low temperature (below 40 K), an interesting change of the magnetic phase into the $\Gamma_2\,(F_x, C_y, G_z)$ configuration was observed which can be attributed to the anisotropic exchange interaction between rare earth and rotation of the AFM component of Cr^{3+} along z-axis from the easy axis. Among the all the Sm substitution we find that the Sm rich compound GSO9 exhibits presence of magnetic field driven short range metastable frozen state characterized by the co-existence of both $\Gamma_2\,(F_x, C_y, G_z)$ and $\Gamma_4\,(G_x, A_y, F_z)$ phases as the FM clusters in the AFM background matrix (termed as magnetic glass) for FCW case which disappears at strong magnetic field. We have also demonstrated the presence of direct spin-phonon coupling by detecting clear anomalies in the Raman spectra across the magnetic ordering temperatures which indicate a slow hardening of the A_{1g} (5) mode at around 563 cm^{-1} upon changing the temperature assures the Cr^{3+}-Cr^{3+} AFM couplings that results the magneto-striction effect. We have obtained the softening of A_{1g} (3) mode due to the triggering of Gd^{3+}-Cr^{3+} exchange interaction as a result of harmonic effect obtained from Raman spectra. Overall, we have found that the GSO5 appears to be the excellent candidate for the tunable thermo-magnetic switching devices, magnetic sensors and non-volatile magnetic memory storage devices.

7.2 Prospective for Future Work:

In this thesis we have provided an extensive exploration of different interesting, structural, electronic, magnetic, heat capacity and phonon modes of some of the rare earth manganite and chromite systems keeping in mind their huge industrial applications. However, as the number of such materials are large in number and due to present limitation of state-of-art tools and techniques available to explore their basic physical analysis we could not cover many of the interesting features associated to these promising materials. In this section we provide a brief overview about the different experimental and theoretical exploration which will certainly provide a great roadmap for the future research by keeping our findings in thesis at the base of those studies.

1. In chapter 3, we have characterized the structural, electronic and magnetic properties of $[La_{0.7}Sr_{0.3}MnO_3/LaCoO_3]$ bilayers with exchange in the stacking sequence. However, it would be

interesting to extend our analysis to explore the ac-magnetic properties, resistivity, phonon modes with variable temperature, power and laser sources. The optical properties of the aforementioned bilayer with the help of UV-visible spectrum would be the other direction that can lead to tune the band gap which will be helpful to understand the overall transport properties of electron, magnons, etc. It would nice to extend the ab-initio calculations of the these superlattices which will helpful in making the structural and magnetic response of these superlattices more systematic.

2. In chapter 4, we have analysed the strain induced structural, magnetic and morphological changes in $[La_{0.7}Sr_{0.3}MnO_3/LaNiO_3]_{10}$ superlattices in particular orientation. It would be interesting to extend this for another orientation which will bring some universal picture of mechanical response of these class of superlattices. In other direction the detailed ac-magnetometry and temperature dependent Raman modes would be a good way to distinguish their optical properties at different range of temperatures.

3. In chapter 5, we have established an intimate connection between the structural, magnetic and phonon characteristics for compositional based $Dy_{1-x}Ce_xCrO_3$ polycrystalline compounds. However, we could not provide a detailed temperature dependent phonon stability along with resistivity measurements which can be another direction in which the work can be extended.

4. In chapter 6, we have found the coexistence of FM in the AFM background which have been associated with the presence of newly evolving field of magnetic glass nature due to the substitution of 90% Sm in $GdCrO_3$ resulting the $Gd_{0.1}Sm_{0.9}CrO_3$ polycrystal. In the present study we could not analyse the detailed dynamics of these magnetic phases, it would be interesting to analyse those aspects using the AC magnetic susceptibility. The most interesting composition namely, $Gd_{0.5}Sm_{0.5}CrO_3$ can be revisited using neutron diffraction to quantify the exact contributions of magnetic moments on overall magnetization as well as characterizing the magnetic structure like identifying the sublattices responsible for the history dependent magnetization. The origin of the magnetization reversal of these two above mentioned samples along with $Gd_{0.9}Sm_{0.1}CrO_3$ can be investigated thoroughly by the means of ac-magnetization and resistivity.

Bibliography

[1] J. He *et al.*, *Phys. Rev. Lett.* **105**, 227203 (2010).
[2] M. Imada, A. Fujimori, and Y. Tokura, *Rev. Mod. Phys.* **70**, 1039 (1998).
[3] I. Zutic´, J. Fabian, and S. Sarma, *Rev. Mod. Phys.* **76**, 323 (2004).
[4] F. Hellman *et al.*, *Rev. Mod. Phys.* **89**, 025006 (2017).
[5] R. Ramesh, and N. A. Spaldin, *Nature* **6**, 21 (2007).
[6] K. Yoshii, *Appl. Phys. Lett.* **99**, 142501 (2011).
[7] Y. Cao *et al.*, *Appl. Phys. Lett.* **104**, 232405 (2014).
[8] R. Waser, "Nanoelectronics and Information Technology," *Wiley-VCH, Berlin*, (2005).
[9] H. Y. Hwang *et al.*, *Nat. Mater.* **11**, 103 (2012).
[10] L. You *et al.*, *Adv. Mater.* **22**, 4964, (2010).
[11] J. Chakhalian *et al.*, *Nat. Phys.* **2**, 244, (2006).
[12] J. Chakhalian et. al., *Science* **318**, 1114 (2007).
[13] N. Reyren et. al., *Science* **317**, 1196 (1979).
[14] J. A. Alonso et. al., *Inorg. Chem.* **39**, 917 (2000).
[15] J. A. Alonso et. al., *J. Mater. Chem*. **7**, 2139 (1997).
[16] K. M. Parida, A. Nashim, and S. K. Mahanta, *Dalton trans.* **40**, 12839 (2011).
[17] H. B. Lal, R. D. Dwivedi and A. N. Gaur, *J. Mater. Sci. Mater.* **7**, 35 (1996).
[18] S. Yin *et al.*, *J. Appl. Phys.* **123**, 053904 (2018).
[19] L. H. Yin *et al.*, *Appl. Phys. Lett.,* **104**, 032904 (2014).
[20] A. Urushibara *et al.*, *Phys. Rev.B.* **51***,* 14103 (1995).
[21] G. Zhou *et al.*, *ACS Appl. Mater. Interfaces* **9**, 3156 (2017).
[22] J. Son *et al.*, *Appl. Phys. Lett.* **97**, 202109 (2010).
[23] B. Hildebrandt *et al.*, *Crit Rev Oncol Hematol.* **43**, 33 (2002).
[24] E. A. Périgo *et al.*, *Appl. Phys. Rev.* **2**, 041302 (2015).
[25] S. v. Jadhav *et al.*, *Mater. Charact.* **102**, 209 (2015).
[26] Y. Chen *et al.*, *Nanoscale Res Lett.* **11**, 1 (2016).
[27] Galloway K. V. and Sammes N. M., "Encyclopedia of Electrochemical Power Sources," *Elsevier Science*, (2009).
[28] M. C. Weber *et al.*, *Phys. Rev. B* **85**, 054303 (2012).
[29] Boulay D J, "Structure, vibration and electron density in Neodymium-Iron-Boride and some rare-earth perovskite oxide.," *PhD thesis, The University of Western Australia*, (1996).
[30] O. Muller and R. Roy, *Science* **188**, 143 (1974).
[31] J. L. Garcia-Munoz *et al.*, *Phys. Rev. B.* **46***,* 4414 (1992).
[32] J. E. Greedan et. al., *J. Solid State Chem.* **116**, 118 (1995).
[33] S. Geller, P. Homo, and J. P. Remeika, *Z. Kristallogr. Cryst. Mater*. **124**, 136 (1967).
[34] A. D. Jodlowski et. al., *Adv. Energy Mater.* **8**, 1703120 (2018).
[35] S. Blundell, "Magnetism in Condensed Matter", Oxford University Press (2001).
[36] H. A. Jahn and E. Teller, (1937).
[37] F. Steglich, et. al., *Phys. Rev. Lett.* **43**, 1892 (1979).
[38] E. Dagotto, and Y. Tokura, (2008).
[39] J. M. D. Coey, "Magnetism and Magnetic Materials", Oxford University Press (2009).
[40] P. W. Anderson, *Phys. Rev.* **115**, 2 (1959).
[41] R. M. White, "Quantum Theory of Magnetism", Springer Science & Business Media (2007)
[42] W. Nolting and A. Ramakanth, "Quantum Theory of Magnetism" *Springer Science & Business Media*, (2009).
[43] I. E. Dzyaloshinski, *J. Exptl. Theoret. Phys.* **37**, 881 (1959).
[44] T. Moriya, *Phys. Rev.* **120**, 91 (1960).
[45] W. Thomson and J. P Nichol, "Encyclopedia of the Phys. Sciences Ed. 2nd," *Richard Green and Company: London*, 838 (1860).
[46] G. V. Brown, *J. Appl. Phys.* **47**, 3673 (1976).
[47] A. H. Morrish, "The Physical Principles of Magnetism," *Wiley New York* (1965).
[48] W. H. Meiklejohn and C. P. Bean, *Phys. Rev.* **105**, 904 (1957).
[49] J. N. Nogues et. al., *Phys. Rev. B.* **59**, 6984 (1999).

[50] S. M. Wu, *et. al.*, *Nat. Mater* **9**, 756 (2010).
[51] D. Deng. *et. al.*, *Appl. Phys. Lett.* **107**, 102404 (2015).
[52] R. K. Dokala *et. al.*, *J. Phys.: Condens. Matt.* **34**, 065801 (2022).
[53] L. Néel, *Ann. Phys.* **12**, 137 (1948).
[54] S. Biswas and S. Pal, *Rev. Adv. Mater. Science* **53**, 206 (2018).
[55] S. Chikazumi, "Physics of Ferromagnetism," *Oxford University Press London*, (1997).
[56] K. Yoshii, *J. Solid State Chem.* **159**, 204 (2001).
[57] B. D. Cullity, and C. D. Graham, "Introduction to Magnetic Materials," *IEEE Press Wiley New York* (2009).
[58] G. Zhou *et. al.*, *Appl. Mater. Inter.* **10**, 1463 (2018).
[59] G. Zhou, *et al.*, *Appl. Mater. Inter.* **9**, 3156 (2017).
[60] A. Urushibara *et al.*, *Physical review. B, Condensed matter*. **51**, 14103 (1995).
[61] D. S. L. Pontes *et al.*, *Ceram. Int.* **39**, 8025 (2013).
[62] A. D. Rataa *et al.*, *European Phys. J.* **76**, 215 (2010).
[63] V. V. Mehta *et al.*, *J. Appl. Phys.* **105**, 07E503 (2009).
[64] A. M. Durand, *et al.*, *J. Phys.: Condens. Matt.* **25**, 382203 (2013).
[65] Y. Cao, *et al.*, *Appl. Phys. Lett.,* **104**, 232405 (2014).
[66] A. McDannald, L. Kuna, and M. Jain, *J. Appl. Phys.* **114**, (2013).
[67] S. Mahana, U. Manju, and D. Topwal, *J. Phys. D Appl. Phys.* **51**, 305002 (2018).
[68] P. Gupta, R. Bhargava, and P. Poddar, *J. Phys. D Appl. Phys.* **48**, 025004 (2015).
[69] S. Rajendiran, "Plasma enhanced pulsed laser deposition," University of York (2017).
[70] K. Charles, "Introduction to Solid State Physics," *John Wiley & Sons, Inc*, 8th Edition, (2005).
[71] D. Graef and M. E. McHenry, "Structure of Materials: An Introduction to Crystallography, Diffraction, and Symmetry," *Cambridge University Press* (2007).
[72] A. T. Fromhold, "Quantum Mechanics for Applied Physics and Engineering," *Courier Dover Publications* (1991).
[73] D. A. Skoog, F. J. Holler, and T. A. Nieman, "Principles of Instrumental Analysis," *Saunders College Pub. Science* (1998).
[74] J. R. Ferraro, K. Nakamoto, and C. W. Brown, "Introductory Raman Spectroscopy," *Elsevier*, 2003.
[75] R. L. Fagaly, "Superconducting quantum interference device instruments and applications," *Review of Scientific Instruments* **77**, (2006).
[76] A. Kraft, C. Rupprecht, and Y. C. Yam, "Superconducting Quantum Interference Device (SQUID)," (2017).
[77] STAR Cryoelectronics, "Mr. SQUID ® User's Guide," (1996).
[78] Grundlagen and Anwendungen, "Supraleitung," *Wiley VCH* (1993).
[79] F. Hellman *et al.*, *Rev. Mod. Phys.* **89**, 025006 (2017).
[80] C. Sun, J. A. Alonso, and J. Bian, *Advan. Energy Mater.* **11**, 2000459 (2021).
[81] M. D. McDaniel *et al.*, *Appl. Phys. Rev* **2**, 054101 (2015).
[82] Y. Wang *et al.*, *Phys. Rev. Mater.* **2**, 021201(R) (2018).
[83] G. Tang *et al.*, *Adv. Mater.* **3**1, 1807689 (2019).
[84] Y. A. Izyumov and Y. N. Skryabin, *Physics-Uspekhi* **44**, 109, (2001).
[85] S. Thota *et al.*, *Appl. Phys. Lett.* **113**, 122405 (2018).
[86] V. V. Demidov *et al.*, *J. Appl. Phys.* **113**, 163909 (2013).
[87] M. Ziese, *Rep. Prog. Phys.* **65**, 143 (2002).
[88] I. Z. Utic, J. Fabian, and S. D. Sarma, *Rev. Mod. Phys.* **76**, 323 (2004).
[89] W. Prellier, P. Lecoeur, and B. Mercey, *J. Phys.: Condens. Matter.* **13**, R915 (2001).
[90] S. Ghosh, *et al.*, *Phys. Rev. B.* **99**, 195134 (2019).
[91] S. Thota *et al.*, *J. Appl. Phys.* **122**, 124304 (2017).
[92] S. Das *et al.*, *J. Phys. D Appl. Phys.* **51**, 325001 (2018).
[93] S. Thota, *et al.*, *Appl. Phys. Lett.* **97**, 112506 (2010).
[94] Q. Zhang, *et al.*, *J. Phys.: Condens. Matt.* **23**, 052201 (2011).
[95] D. Fuchs *et al.*, *Phys. Rev. B* **77**, 014434 (2008).
[96] P. M. Raccah, and J. B. Goodenough, *Phys. Rev.* **155**, 932 (1967).
[97] M. Izquierdo *et al.*, *Phys. Rev. B* **90**, 235128 (2014).
[98] B. Geisler and R. Pentcheva, *Phys. Rev. B*. **101**, 165108 (2020).
[99] M. A. Korotin *et al.*, *Phys. Rev. B.* **54**, 5309 (1996).
[100] M. W. Haverkort, *et al.*, *Phys. Rev. Lett.* **97**, 176405 (2006).

[101] D. Fuchs *et al.*, *Phys. Rev. B.* **75**, 144402 (2007).
[102] Y. Yokoyama *et al.*, *Phys. Rev. Lett.* **120**, 257001 (2018).
[103] A. Mizuno *et al.*, *Phys. Rev. Lett.* **119**, 057201 (2017).
[104] B. Chakrabarti, T. Birol, and K. Haule, *Phys. Rev. Mater.* **1**, 064403 (2017).
[105] V. V. Mehta *et al.*, *Phys. Rev. B.* **91**, 144418 (2015).
[106] N. Biškup *et al.*, *Phys. Rev. Lett.* **112**, 087202 (2014).
[107] H. L. Ju *et al.*, *Appl. Phys. Lett.* **65**, 2108 (1994).
[108] A. Kadigrobov *et al.*, *Euro. Phys. Lett.* **67**, 948 (2004).
[109] M. Merz *et al.*, *Phys. Rev. B.* **82**, 174416 (2010).
[110] A. Kushima, S. Yip, and B. Yildiz, *Phys. Rev. B.* **82**, 115435 (2010).
[111] Y. P. Zhang *et al.*, *R. Soc. Open Sci.* **5**, 171376 (2018).
[112] H. Zhang, *et al.*, *Appl. Mater. Int.* **8**, 18328 (2016).
[113] L. Wang, *et al.*, *Front. Mater. Front. Mater.* **7**, 60 (2020).
[114] A. M. Durand, *et. al.*, *J. Phys.: Condens. Matt.* **27**, 176003 (2015).
[115] Z. Liu, *et al.*, *Cryst. Eng. Comm.* **21**, 1534 (2019).
[116] B. Raveau, *Phil. Trans. Royal Soc. A: Math. Phys. Eng. Sci.* **366**, 83 (2008).
[117] G. Bergerhoff, R. Hundt, and R. Sievers, *J. Chem. Inf. Comput. Sci.* **23**, 66 (1983).
[118] N. Hauptmann, J. W. Gerritsen, D. Wegner, and A. A. Khajetoorians, *Nano Lett.* **17**, 5660 (2017).
[119] A. Thompson, "X-ray Data Booklet (Lawrence Livermore Lab)," (2009).
[120] Å. F. Monsen *et al.*, *Surf. Sci.* **606**, 1360 (2012).
[121] H. Xie, H. Huang *et al.*, *Phys. B: Condens. Matt.* **477**, 14 (2015).
[122] Q. Wang and L. Ma, *New J. Chem.* **43**, 2974 (2019).
[123] A. v Berenov, J. L. Macmanus-Driscoll, and J. A. Kilner, *Solid State Ion.* **122**, 41 (1999).
[124] S. Singh *et al.*, *Appl. Phys. Lett.* **114**, 222403 (2019).
[125] Q. Qin *et al.*, *Appl. Phys. Lett.* **110**, 112401 (2017).
[126] U. Shashank, *et al.*, *Adv Quantum Tech.* **4**, 2000112 (2021).
[127] C. Hauser *et al.*, *Phys. Status Solidi B Basic Res*, **257**, 1900606 (2020).
[128] C. Thiele *et al.*, *Phys. Rev. B Condens Matter Mater Phys*, **75**, 054408 (2007).
[129] M. Huijben *et al.*, *Phys. Rev. B Condens Matter Mater Phys.*, **78**, 094413 (2008).
[130] C. Adamo *et al.*, *Appl. Phys. Lett.* **95**, 11, (2009).
[131] S. v Andreev *et al.*, *J. Alloys Compd.* **260**, 196 (1997).
[132] R. K. Dokala *et al.*, *J Appl. Phys.*, **127**, 175303 (2020).
[133] P. Audehm *et al.*, *Sci Rep.* **6**, 25517 (2016).
[134] Å. Monsen *et al.*, *J Magn Magn Mater*, **369**, 197 (2014).
[135] Y. Suzuki *et al.*, *J Appl. Phys.*, **83**, 706 (1998).
[136] K. Poulsen and N. T. Zinner, *Phys. Rev. Lett.,* **126**, 077203 (2021).
[137] M. Naka, Y. Motome, and H. Seo, *Phys. Rev. B*, **103**, 125114 (2021).
[138] Z. Liu, L. Deng, and B. Peng, *Nano Research*, **14**, 1802 (2021).
[139] Y. Xu, D. D. Awschalom, and J. Nitta, "Handbook of Spintronics." Springer Dordrecht Heidelberg New York London (2015).
[140] J. J. F. Heitz *et al.*, *Phys. Rev. Appl.* **16**, 064047 (2021).
[141] L. D. Yuan, Z. Wang, J. W. Luo, and A. Zunger, *Phys. Rev. B*, **103**, 224410 (2021).
[142] H. Seo and M. Naka, *J. Phys. Soc. Jpn.* **90**, 064713 (2021).
[143] B. Ensign *et al., J Magn Magn Mater.* **509**, 166882 (2020).
[144] T. Wu and J. F. Mitchell, *Phys. Rev. B Condens Matter Mater Phys.*, **74**, 21 (2006).
[145] G. Zhou *et al.*, *ACS Appl. Mater Interfaces*. **9**, 3156 (2017).
[146] H. Pahlavani and F. Arezoumandi, *Modern Phys. ics Letters B*. **26**, 9 (2012).
[147] Z. Y. Ren *et al.*, *Phys. Rev. Appl*, **13**, 024044 (2020).
[148] Z. Huang *et al.*, *Adv Mater.* **30**, 1802439 (2018).
[149] M. Gibert *et al.*, *Nat Commun*, **7**, 11227 (2016).
[150] F. Sanchez *et al.*, *Thin Solid Films.* **384**, 2052001 (2001).
[151] M. Moreau, S. M. Selbach, and T. Tybell, *J Appl. Phys.*, **124**, 185301 (2018).
[152] J. D. Hoffman *et al.*, *Phys. Rev. X.* **6**, 041038 (2016).
[153] G. Fabbris *et al.*, *Phys. Rev. B*. **98**, 180401(R) (2018).
[154] J. D. Hoffman *et al.*, *Phys. Rev. Appl.* **9**, 044041 (2018).
[155] H. Chang *et al.*, *Appl. Phys. Lett.* **113**, 061602 (2018).

[156] N. Mottaghi *et al.*, *J Appl. Phys.* **128**, 073903 (2020).
[157] V. K. Vlasko-Vlasov *et al.*, *Phys. Rev. Lett.* **84**, 2239 (2000).
[158] M. Ziese, *et al.*, *New J Phys.* **10**, 063024 (2008).
[159] M. Egilmez *et al.*, *Phys. Rev. B.* **78**, 172405 (2008).
[160] D. Pesquera *et al.*, *Phys. Rev. B Condens Matter Mater Phys.* **84**, 184412 (2011).
[161] A. Tsukazaki *et al.*, *Nat Mater.* **9**, 889 (2010).
[162] L. Li *et al., Nat Phys.* **7**, 762 (2011).
[163] J. A. Bert *et al.*, *Nat Phys.*, **7**, 767 (2011).
[164] Arthur P. Ramirez, *Applied Phys. Ics*. **315**, 1377 (2007).
[165] A. Brinkman *et al.*, *Nat Mater.* **6**, 493 (2007).
[166] D. Xiao *et al.*, *Nat Commun*. **2**, 1 (2011).
[167] A. Rüegg *et al.*, *Phys. Rev. B* **85**, 245131 (2012).
[168] Y. Jia *et al.*, *Phys. Rev. B.* **92**, 094407 (2015).
[169] G. Zhou *et al.*, *ACS Appl. Mater Interfaces*, **10**, 1463 (2018).
[170] A. X. Gray *et al.*, *Phys. Rev. B.* **82**, 205116 (2010).
[171] M. Granada, J. C. Rojas Sánchez, and L. B. Steren, *Appl. Phys. Lett.,* **91**, 7 (2007).
[172] M. Granada *et al.*, *Phys. ica B Condens Matter*, **384**, 68 (2006).
[173] S. Ghosh, A. Y. Borisevich, and S. T. Pantelides, *Phys. Rev. Lett.,* **119**, 17 (2017).
[174] G. Zhou *et al.*, *J Mater Chem C Mater*, **6**, 582 (2018).
[175] G. Zhou *et al.*, *Nanoscale Res Lett.,* **12**, 1 (2017).
[176] H. Bhatt *et al.*, *Adv. Mater. Interfaces*, **7**, 21 (2020).
[177] P. P. Balakrishnan *et al.*, *AIP Adv*. **11**, 2 (2021).
[178] T. Wang *et al.*, *J Cryst Growth*. **310**, 3029 (2008).
[179] Y. K. Chan *et al.*, *IEEE Trans Magn*, **50**, 7 (2014).
[180] R. Ali, M. Yashima, *J. Solid State Chem.* **178**, 2867 (2005).
[181] P. A. Langjahr, *Mat. Res. Soc. Symp. Proc.* **401** (1996).
[182] H. Y. Lee *et al.*, *Thin Solid Films*. **494**, 325 (2006).
[183] M. Shen *et al.*, *Journal of Rare Earths*. **31**, 119 (2013).
[184] P. Przyslupski *et al.*, *Phys. Rev. B Condens Matter Mater Phys.* **69**, 13 (2004).
[185] L. Wu *et al.*, *ACS Appl. Mater Interfaces*. **9**, 44931 (2017).
[186] X. R. Wang et. al., *Science* **349**, 719 (1979).
[187] Z. T. Xu *et al.*, *Small*. **8**, 1279 (2012).
[188] W. Li *et al., Sci Rep*. **4**, 6641 (2014).
[189] A. J. Nelson, J. J. Adams, and K. I. Schaffers, *J Appl. Phys.* **94**, 7493 (2003).
[190] M. Saghayezhian *et al., Phys. Rev. B*. **95**, 16 (2017).
[191] L. Qiao and X. Bi, *EPL*. **93**, 5 (2011).
[192] D. C. Joshi *et al.,*, *Phys. Status Solidi B Basic Res*. **252**, 2323 (2015).
[193] P. Liu and X. Ning, *Physica B Condens Matter.* **589**, 412199 (2020).
[194] S. Mickevičius *et al.*, *J Alloys Compd*. **423**, 107 (2006).
[195] H. Wei *et al.*, *Appl. Phys. Lett.* **110**, 10 (2017).
[196] G. Tang, Y. Yu, W. Chen, and Y. Cao, *J Alloys Compd*. **461**, 486 (2008).
[197] C. Moreno *et al.*, *Nano Lett.* **10**, 3828 (2010).
[198] B. Raveau, A. Maignan, and C. Martin, *J. Solid State Chem.* **130**, 162 (1997).
[199] K. Sreedhar *et al.*, *Phys. Rev. B* **46**, 6382 (1992).
[200] J. Son *et al.*, *Appl. Phys. Lett.,* **96**, 6 (2010).
[201] X.-J. Meng *et al.*, Ferroelectrics **357**, 53 (2007).
[202] Z. J. Razi, S. A. Sebt, and A. Khajehnezhad, *Journal of Theoretical and Applied Physics*, **12**, 243 (2018).
[203] S. Y. Yang *et al.*, *J Magn Magn Mater*, **268**, 326 (2004).
[204] X. Ning, Z. Wang, and Z. Zhang, *Sci Rep*. **5**, 8460 (2015).
[205] R. Scherwitzl *et al.*, *Phys. Rev. Lett.,* **106**, 24 (2011).
[206] W. Noun *et al.*, *J Appl. Phys.* **102**, 6 (2007).
[207] H. Guo *et al.*, *Nat Commun*. **9**, 1 (2018).
[208] J. Song *et al.*, *Phys. Rev. Appl*. **14**, 2 (2020).
[209] M. M. Schwickert *et al.*, *Phys. Rev. B.* **57**, 13681 (1998).
[210] M. Ahlberg *et al.*, *Phys. Rev. B Condens Matter Mater Phys.* **81**, 21 (2010).

[211] S. V. Komogortsev and R. S. Iskhakov, *J Magn Magn Mater*. **440**, 213 (2017).
[212] W. F. Brown, *J Appl. Phys.* **30**, S62 (1959).
[213] X. Zhang and J. P. Wang, *Appl. Phys. Lett.* **114**, 15 (2019).
[214] E. C. Devi and I. Soibam, *J Alloys Compd*. **772**, 920 (2019).
[215] Y. Suzuki *et al.*, *Appl. Phys. Lett.* **71**, 140 (1997).
[216] N. Mottaghi *et al.*, *AIP Adv*. **8**, 5 (2018).
[217] M. Cabero *et al.*, *APL Mater*. **5**, 9 (2017).
[218] J. A. Alonso *et al.*, *Inorg Chem.* **39**, 917 (2000).
[219] S. Ghosh *et al.*, *Phys. Rev. B*. **99**, 11 (2019).
[220] A. Rajapitamahuni *et al.*, *Phys. Rev. Lett.,* **116**, 18 (2016).
[221] L. M. Berndt, V. Balbarin, and Y. Suzuki, *Appl. Phys. Lett.* **77**, 2903 (2000).
[222] M. Mathews *et al.*, *J Appl. Phys.* **107**, 1 (2010).
[223] K. Steenbeck and R. Hiergeist, *Appl. Phys. Lett.* **75**, 1778 (1999).
[224] D. Yi *et al.*, *Phys. Rev. Appl*. **15**, 2 (2021).
[225] B. C. Behera *et al.*, *Appl. Phys. Lett.* **104**, 9 (2014).
[226] A. Urushibara *et al.*, *Phys. Rev. B.* **51**, 14103 (1995).
[227] N. Chaban *et al.*, *Appl. Phys. Lett.,* **97**, 3 (2010).
[228] M. Agarwal and E. G. Mishchenko, *Phys. Rev. B*. **99**, 8 (2019).
[229] T. Bolstad *et al.*, *J. Condens. Matter Phys.* **30**, 25 (2018).
[230] D. Khomskii, "*Transition metal compounds*", Cambridge University Press (2014).
[231] A. Antonakos *et al.*, *J. Condens. Matter Phys.* **20**, 434232 (2008).
[232] A. A. El-Aziem *et al.*, *J. mater. sci. eng. B.* **6**, 5 (2016).
[233] M. N. Iliev *et al.*, *Phys. Rev. B*. **57**, 2872 (1998).
[234] M. N. Iliev *et al.*, *Phys. Rev. B Condens Matter Mater Phys.***73**, 6 (2006).
[235] A. Congeduti *et al.*, *Phys. Rev. Lett.* **86**, 1251 (2001).
[236] W. G. Nilsen and J. G. Skinner, *J Chem Phys.* **48**, 2240 (1968).
[237] J. M. D. Coey *et al.*, *Phys. Rev. Lett.* **75**, 3910 (1995).
[238] B. C. Behera, P. Padhan, and W. Prellier, *J Magn Magn Mater*. **388**, 22 (2015).
[239] T. Kimura *et al.*, Nature. **426**, 55 (2003).
[240] Fuyuhiko Sugawara *et al., J. Phys. Soc. Japan*, **25**, 1553 (1968).
[241] K. Miura and K. Terakura, *Phys. Rev. B*. **63**, 104402 (2001).
[242] J. R. Sahu *et al., J Mater Chem*. **17**, 42 (2007).
[243] S. A. Wolf *et al.*, *Science.* **294**, 1488 (2001).
[244] A. Mcdannald, "Investigations on Magnetoelectric Bulk and Nanocomposite Materials," University of Connecticut (2016).
[245] M. Imada, A. Fujimori, and Y. Tokura, *Rev. Mod. Phys.* **70**, 1039 (1998).
[246] M. Ni *et al.*, *Phys. Lett. A.* **397**, 127258 (2021).
[247] T. Kimura, *Annu. Rev. Mater. Res.* **37**, 387 (2007).
[248] Y. Tokura and S. Seki, *Adv. Mater.* **22**, 1554 (2010).
[249] B. H. Devmunde *et al.*, *J. Phys. Conf. Ser.* **1644**, 1 (2020).
[250] A. Jordens, Y. P. Cheng, and K. E. Waters, *Miner. Eng.* **41**. 97 (2013).
[251] Y. Zhu *et. al.*, *iScience*. **25**, 4 (2022).
[252] B. Paudel *et al.*, *Mater Res Lett.* **10**, 29 (2022).
[253] M. Siemons and U. Simon, *Sens Actuators B Chem*, **126**, 181 (2007).
[254] G. Kotnana and S. N. Jammalamadaka, *J Appl. Phys.* **118**, 124101 (2015).
[255] B. Tiwari *et al.*, *Mater Res Express.* **2**, 2 (2015).
[256] S. Yin and M. Jain, *J Appl. Phys.* **120**, 4 (2016).
[257] L. H. Yin *et al.*, *J Appl. Phys.* **117**, 13 (2015).
[258] R. Ahsan *et al.*, *RSC Adv.* **8**, 14258 (2018).
[259] B. Rajeswaran *et al.*, *Phys. Rev. B.* **86**, 21 (2012).
[260] L. H. Yin *et al.*, *Phys. Rev. B*. **98**, 5 (2018).
[261] A. McDannald *et al., Phys. Rev. B Condens Matter Mater Phys.* **91**, 22 (2015).
[262] Tsuyoshi Yamaguchi, *J. Phys.Soc. Japan.* **38**, 1270 (1975).
[263] L. H. Yin *et al.*, *J Mater Chem C Mater*. **4**, 11198 (2016).
[264] R. M. Hornreich, *J. Magn. Magn. Mater.* **7**, 280 (1978).
[265] T. Moriya, *Phys. Rev.***120**, 91 (1960).
[266] A. McDannald *et al., Phys. Rev. B*. **93**, 18 (2016).

[267] J. P. Bolletta *et al.*, *Phys. Rev. B*, **98**, 13 (2018).
[268] S. Huang *et al.*, *Ceram Int*. **43**, 12258 (2017).
[269] A. McDannald and M. Jain, *J Appl. Phys*.**118**, 4 (2015).
[270] R. Shukla *et al.*, *J. Phys. Chem. C.* **113**, 12663 (2009).
[271] M. Taheri *et al.*, *Phys. Rev. B*. **99**, 5 (2019).
[272] M. Yadav and C. Rath, *J Magn Magn Mater*. **543**, 168610 (2022).
[273] S. Yin *et al.*, *Phys. Rev. B*. **95**, 18 (2017).
[274] M. Zaghrioui *et al.*, *Phys. Rev. B.* **64**, 811021 (2001).
[275] M. C. Weber *et al.*, *Phys. Rev. B.* **85**, 5 (2012).
[276] S. Sasart, C. E. T. Pnnwnr, and R. C. Ltesenmann, *Am Min.* **68**, 1189 (1983).
[277] K. Sardar *et al.*, *Chem. Mater.* **23**, 48 (2011).
[278] M. R. Levy, "Crystal Structure and Defect Property Predictions in Ceramic Materials", Imperial College of Science, Technology and Medicine (2005).
[279] R. Shukla *et al., Inorg Chem*, **48**, 11691 (2009).
[280] S. Wang *et al.*, *Inorg Chem*. **58**, 2315 (2019).
[281] P. Gupta *et al.*, *RSC Adv*. **3**, 26427 (2013).
[282] T. M. Pan and C. H. Lu, *Appl. Phys. Lett.* **99**, 11 (2011).
[283] M. Taheri, M. Konuma, and F. S. Razavi, *Surf. Interface Anal.* **49**, 122 (2017).
[284] H. Schuchert, S. Hufner, and R. Faulhaber, *Z. Physik*. **222**, 105 (1969).
[285] L. M. Holmes *et al., Phys. Rev. B.* **5,** 138 (1972).
[286] T. Yamaguchi and K. Tsushima, *Phys. Rev. B*. **8**, 5187 (1973).
[287] K. Tsushima, T. Tamaki, and Y. Yamaguchi, *AIP Conf. Proc.* **24**, 69 (1975).
[288] A. Durán *et al.*, *Phys. Rev. Mater*. **2**, 1 (2018).
[289] A. T. Apostolov, I. N. Apostolova, and J. M. Wesselinowa, *Mod. Phys. Lett. B.* **31**, 3 (2017).
[290] X. Qian, L. Chen, S. Cao, and J. Zhang, *Solid State Commun*, **195**, 21 (2014).
[291] O. Peña *et al.*, *Phys. B: Condens. Matter.* **384**, 57 (2006).
[292] E. F. Bertaut *et al.*, *J Appl. Phys.* **37**, 1038 (1966).
[293] A. Durán *et al.*, *J. Condens. Matter Phys.* **20**, 8 (2008).
[294] L. B. Mendelsohn, F. Biggs, and J. B. Mann, *Phys. Rev. A.* **2**, 1130 (1970).
[295] S. V. Komogortsev and R. S. Iskhakov, *J Magn Magn Mater.* **440**, 213 (2017).
[296] W. Fuller Brown, *Phys. Rev*. **60**, 139 (1941).
[297] Y. Su *et al.*, *Journal of Rare Earths*. **29**, 1060 (2011).
[298] P. Pramanik *et al.*, *J. Condens. Matter Phys.* **32**, 24 (2020).
[299] S. Kumar *et al.*, *J. Condens. Matter Phys.* **29**, 19 (2017).
[300] Y. Du *et al.*, *J Appl. Phys.* **108**, 9 (2010).
[301] M. Taheri *et al.*, *Phys. Rev. B*, **93**, 10 (2016).
[302] F. Bartolomé and *et al.*, *Phys. Rev. B*. **62**, 1058 (2000).
[303] P. Gupta and P. Poddar, *RSC Adv.* **6**, 82014 (2016).
[304] M. N. Iliev *et al.*, *Phys. Rev. B.* **57**, 2872 (1998).
[305] A. A. A. Qahtan *et al.*, *J. Mater. Sci.: Mater. Electron.* **32**, 15108 (2021).
[306] V. K. Tripathi and R. Nagarajan, *ACS Omega*. **2**, 2657 (2017).
[307] N. D. Todorov *et al.*, *Phys. Rev. B.* **83**, 22 (2011).
[308] C. R. Serrao *et al.*, *Phys. Rev. B.* **72**, 22 (2005).
[309] N. Shamir, H. Shaked, and S. Shtrlkman, *Phys. Rev. B.* **24**, 6642 (1981).
[310] K. R. S. Preethi Meher *et al.*, *Phys. Rev. B.* **89**, 14 (2014).
[311] B. Rajeswaran *et al.*, *Phys. Rev. B. Condens Matter Mater Phys.* **86**, 21 (2012).
[312] A. Kumar and S. M. Yusuf, *Phys. Rep.* **556**, 1 (2015).
[313] A. Pal *et al.*, *Phys. Rev. Mater.* **4**, 4, (2020).
[314] M. Tripathi *et al.*, *Phys. Rev. B*. **99**, 1 (2019).
[315] K. Yoshii, *J Solid State Chem*. **159**, 204 (2001).
[316] T. Sau *et al.*, *Phys. Rev. B*. **103**, 14 (2021).
[317] M. Ohkoshi *et al.*, *IEEE Trans Magn.* **13**, 1158 (1977).
[318] T. Sarkar, V. Pralong, and B. Raveau, *Phys. Rev. B.* **83**, 21 (2011).
[319] P. Chaddah, K. Kumar, and A. Banerjee, *Phys. Rev. B.* **77**, 10 (2008).
[320] M. Manekar, M. K. Chattopadhyay, and S. B. Roy, *J. Condens. Matter Phys.* **23**, 8 (2011).
[321] M. K. Chattopadhyay, S. B. Roy, and P. Chaddah, *Phys. Rev.* **72**, 18 (2005).
[322] S. B. Roy *et al.*, *Phys. Rev. B.* **74**, 012403 (2006).

[323] E. Sato *et al.*, *RSC Adv*. **6**, 56475 (2016).
[324] G. Gorodetsky *et al.*, *Phys. Rev. B.* **16**, 515 (1977).
[325] R. D. Shannon, *Acta Crystallogr. Sect. A*. **32**, 751 (1976).
[326] A. Durán *et al.*, *Phys. Rev. Mater*. **2**, 1 (2018).
[327] A. Nashim and K. M. Parida, *J. Chem. Eng.* **215**, 608 (2013).
[328] V. K. Petersona *et al.*, NIST Center for Neutron Research, National Institute of Standards and Technbology, Gaithersburg, MD 20899 (2006).
[329] S. Das *et al.*, *J. Condens. Matter Phys.* **34**, 345803 (2022).
[330] A. Jaiswal *et al.*, *J Nanopart Res.* **13**, 1019 (2011).
[331] H. Zhang *et al.*, *J. Supercond. Novel. Mag.* **34**, 1415 (2021).
[332] A. M. Glazer, *Acta Crystallogr B.* **28**, 3384 (1972).
[333] A. A. A. Qahtan *et al.*, *J. Mater. Sci. Mater.* **31**, 9335 (2020).
[334] P. Gupta and P. Poddar, *RSC Adv.* **5**, 10094 (2015).
[335] M. el Amrani *et al.*, *J Magn Magn Mater.* **361**, 1 (2014).
[336] S. Mahana *et al.*, *Phys. Rev. B*. **96**, 10 (2017).
[337] A. Sarkar, B. Dalal, and S. K. De, *J. Condens. Matter Phys.* **31**, 50 (2019).
[338] M. C. Weber *et al.*, *Phys. Rev. B Condens. Matter Mater. Phys.* **85**, 5 (2012).
[339] J. Andreasson *et al.*, *Phys. Rev. B. Condens Matter Mater Phys.* **75**, 10 (2007).
[340] E. Granado *et al.*, *Phys. Rev. B.* **60**, 11879 (1999).
[341] Y. Sharma *et al.*, *J Appl. Phys.* **115**, 18 (2014).
[342] J. Guo *et al.*, *J Supercond Nov Magn.* **35**, 711 (2022).
[343] I. Dzyaloshinsky, *J. Phys. . Chem. Solids* **4**, 241 (1958).
[344] A. Banerjee *et al.*, *Phys. Rev. B. Condens Matter Mater Phys.* **74**, 22 (2006).
[345] K. Yoshii, *Mater Res Bull.* **47**, 3243 (2012).
[346] X. L. Qian *et al.*, *J Appl. Phys.* **115**, 19 (2014).
[347] M. Tripathi, R. J. Choudhary, and D. M. Phase, *RSC Adv*. **6**, 90255 (2016).
[348] J. Mao *et al.*, *Appl. Phys. Lett.,* **98**, 19 (2011).